OPTIMIZATION OF ToF-SIMS DEPTH PROFILING IN LOW-PRESSURE H_2, C_2H_2, CO AND O_2 ATMOSPHERE

Jernej Ekar

Doctoral Dissertation
Jožef Stefan International Postgraduate School
Ljubljana, Slovenia

Supervisor: Prof. Dr. Janez Kovač

Evaluation Board:
Prof. Dr. Primož Pelicon, Chair, MPŠ and Jožef Stefan Institute, Ljubljana, Slovenia
Prof. Dr. Miran Mozetič, Member, MPŠ and Jožef Stefan Institute, Ljubljana, Slovenia
Prof. Dr. Zdravko Siketić, Member, Rudjer Bošković Institute, Zagreb, Croatia

MEDNARODNA PODIPLOMSKA ŠOLA JOŽEFA STEFANA
JOŽEF STEFAN INTERNATIONAL POSTGRADUATE SCHOOL

Jernej Ekar

OPTIMIZATION OF ToF-SIMS DEPTH PROFILING IN LOW-PRESSURE H_2, C_2H_2, CO AND O_2 ATMOSPHERE

Doctoral Dissertation

OPTIMIZACIJA ToF-SIMS PROFILNE ANALIZE V NIZKOTLAČNI ATMOSFERI H_2, C_2H_2, CO IN O_2

Doktorska disertacija

Supervisor: Prof. Dr. Janez Kovač

Ljubljana, Slovenia, February 2024

Finding a purpose is easy. Finding a sense, not that much.

Acknowledgments

Firstly, I would like to thank my supervisor Janez Kovač who introduced me to the world of surface analysis, which I now enjoy very much. The combination of his guidance and experience together with the research freedom he provided was perfect for my style of work. I am also thankful for all the connections he helped me make, which pose a great advantage for my future career. Secondly, I would like to thank Tatjana Filipič, who helped me in the laboratory when I needed any kind of assistance.

I shall not forget other members of the F4 department, who helped me with bits of advice and made me feel appreciated, valued, and accepted. This goes to my boss Alenka Vesel as well as to Metka Benčina, Ita Junkar, Dane Lojen, Miran Mozetič, Domen Paul, Gregor Primc, Nina Recek, Pia Starič, Maja Šukarov, Janez Trtnik, Rok Zaplotnik, and Mark Zver. Furthermore, I would like to thank researchers from other departments who helped with my publications, Peter Panjan and Sandra Drev. For sharing their knowledge and broadening my horizons, I would also like to thank some other researchers I met on my way, mainly Miha Čekada, Katsuhisa Kitano, Matjaž Panjan, Primož Pelicon, and Zdravko Siketić.

Special thanks go to my girlfriend Saša Kos, who is now also finishing her Ph.D. studies and is even a coauthor of one of my articles. I am thankful for all her support, debates, and understanding of my late working hours. I am also thankful to my closest family, mother Janja Ivančič, and aunt Mirka Ivančič, who have supported me and my career decisions already from the beginning of my studies, and to my father Vili Ekar, who is nevertheless happy with me finding a place in this world, although it is in a public sector.

Finally, I would like to acknowledge cats Mic, Ska, and Muri. I am thankful for them being parts of my life as they made me smile even when no one else could.

From the financial part of view, I must also mention the Slovenian Research and Innovation Agency (ARIS), crucial for the successful study. Financial support was granted via program P2-0082 and project PR-09757.

Abstract

Time-of-flight secondary ion mass spectrometry (ToF-SIMS) is a versatile analytical method widely used in the field of surface science and thin films. Although it gives elemental, molecular, and isotopic information, it has a very low detection limit and high lateral resolution, is fast and works with all the vacuum-compatible samples, and can be used for the analysis of the topmost few atomic monolayers, depth profiling, and imaging, it also has some limitations. One of the limitations is the matrix effect which is the nonlinear effect of the substrate containing the compound of interest on the intensity of the secondary ion signals from this compound. The effect is strong enough to significantly influence detection limits, prevent quantitative analysis, and even cause problems in differentiation between similar compounds.

Different approaches to matrix effect reduction were developed because of its significance, and in this study, we studied gas-flooding. The introduction of the reactive gases in the analytical chamber during the SIMS analysis notably changes the ionization yields of secondary ions and causes the formation of cluster secondary ions. However, most of the previous research was done with the O_2 while the use of other reactive gases was almost never considered. In the first part of our study, we studied the influence of the H_2, C_2H_2, CO, and O_2 flooding during depth profiling of different thin metal, metal oxide, and alloy layers. The application of the H_2, C_2H_2, and CO is a novelty in the field of SIMS studies and was introduced by our research group. The largest improvements compared to the ultra-high vacuum (UHV) were observed when analyses were done in the H_2 atmosphere. Differentiation of layers became easier, and their identification unambiguous, interfaces were sharper, and depth resolution improved. There was even no decrease in the sputter rate which can be observed in the cases of all the other gases. An improved analysis was possible via measurements of negative metal (M_n^-), metal hydride ($M_nH_m^-$), and metal oxide ($M_nO_m^-$) cluster secondary ions. H_2 flooding adequately optimized ToF-SIMS depth profiling in a way that this approach can be applied for routine analyses.

We further investigated processes occurring during sputtering in UHV and H_2 atmosphere. Atomic force microscopy (AFM) measurements of surface topography confirmed that some of the improvements in the field of SIMS depth profiling are caused by the reduced surface roughening observed in the H_2 atmosphere. Namely, the continuous removal of material caused by the prolonged bombardment with primary ions, that is, the process taking place during depth profiling, causes the initially smooth surface to develop a higher degree of surface roughness. This process is in many cases reduced if H_2 flooding is applied instead of the UHV environment. We also observed that samples with initially rough surfaces can become smoother after sputtering with the 1 keV Cs^+ ion beam.

In the final study, we compared the quantification capabilities of the SIMS method to measure the chemical composition in UHV, O_2, and H_2 atmospheres. Pure metals and different alloys containing these metals were included in the analysis. The results indicate that the UHV environment offers the worst conditions for potential quantification. Flooding with O_2 improved results significantly, but deviations of measured intensities of SIMS signals from true values of chemical composition were still non-optimal.

Improvements achieved with the H_2 atmosphere provided additional optimization especially when analyzing transition metals, which in our study were Ti, Cr, Fe, Co, and Ni. Analyses of these transition metals in H_2 showed deviations from the true atomic ratio in alloys of only 46% at maximum. O_2 atmosphere and UHV environment gave deviations of 66 and 228%, respectively.

Our findings indicate that gas adsorbs to the surface and forms a new matrix, which reduces the differences between initial chemical environments and electronic structures of the surface. The quantitative aspects of the SIMS method can be due to a new matrix at the surface improved, especially with the help of H_2 flooding.

Povzetek

Masna spektrometrija sekundarnih ionov z analizatorjem na čas preleta (ToF-SIMS) je vsestransko uporabna metoda, namenjena analizi površin in tankih plasti. Daje informacije o elementarni, molekularni in izotopski sestavi, ima zelo nizko mejo detekcije in visoko lateralno ločljivost, je hitra in uporabna za vse vzorce, ki so kompatibilni z vakuumom, in omogoča analizo zgornjih nekaj atomskih plasti, globinsko profiliranje ter določanje razporeditve analitov po površini vzorca. Kljub temu ima tudi pomanjkljivosti, med katerimi prevladuje matrični efekt. Gre za vpliv substrata, v katerem se analit nahaja, na intenziteto signalov sekundarnih ionov, ki izvirajo iz analita. Efekt je dovolj močan, da vpliva na meje detekcije, preprečuje izvedbo kvantitativne analize in povzroča probleme pri razlikovanju sorodnih spojin.

Zaradi problematičnosti matričnega efekta je bilo razvitih več pristopov k zmanjševanju tega efekta. Mednje sodi vpuščanje plinov v analitsko komoro in ta pristop smo v okviru študije raziskali. Prisotnost reaktivnih plinov med SIMS analizo namreč znatno spremeni izkoristke ionizacije različnih sekundarnih ionov, kot tudi povzroči nastanek klastrskih sekundarnih ionov. Večina predhodnih raziskav pa je vključevala zgolj vpuščanje O_2, medtem ko drugih plinov skoraj niso uporabljali. V prvem delu raziskave smo preučili vpliv H_2, C_2H_2, CO in O_2 na rezultate globinskega profiliranja tankih plasti kovin, kovinskih oksidov in zlitin. Uporaba H_2, C_2H_2 in CO je novost na področju metode SIMS, ki jo je vpeljala naša raziskovalna skupina. Največje izboljšave v primerjavi z ultra-visokim vakuumom (UHV) smo opazili ob uporabi H_2. Razlikovanje med različnimi plastmi je postalo lažje in identifikacija teh plasti nedvoumna; meje med plastmi so postale ostrejše in izboljšala se je globinska ločljivost. Poleg tega ni bilo prisotnega zmanjšanja hitrosti odprševanja, ki smo jo zaznali pri vseh drugih plinih. Optimalne rezultate smo dobili prek analize kovinskih klastrskih ionov (M_n^-), kovinskih hidridov ($M_nH_m^-$) in kovinskih oksidov ($M_nO_m^-$). Vpuščanje H_2 v analitsko komoro med analizo je metodo ToF-SIMS izboljšalo v dovoljšni meri, da lahko ta pristop apliciramo za rutinske meritve.

Nadalje smo raziskali tudi druge procese, do katerih pride med odprševanjem delcev v UHV in H_2 atmosferi. Topografske meritve z mikroskopom na atomsko silo (AFM) so potrdile, da so nekatere izboljšave na področju SIMS profiliranja dosežene zaradi zmanjšane stopnje povečevanja hrapavosti površine med globinskim profiliranjem v atmosferi H_2. Med globinskim profiliranjem namreč pride do kontinuirnega odstranjevanja delcev, ki ga povzroči dolgotrajno obstreljevanje s primarnimi ioni. Posledica tega je pretvorba začetno gladke površine v bolj hrapavo in ta proces lahko v precej primerih upočasnimo, če med globinskim profiliranjem v analitsko komoro vpuščamo H_2. Opazili pa smo tudi, da jedkanje s snopom Cs^+ ionov z energijo 1 keV lahko začetno hrapavo površino naredi ob dovolj dolgotrajnem jedkanju bolj gladko.

V zadnjem koraku smo raziskali še sposobnost kvantifikacije kemične sestave vzorcev s SIMS metodo v UHV in O_2 ter H_2 atmosferah. Analizirali smo čiste kovine in različne zlitine, ki so te kovine vsebovale. Rezultati, dobljeni v UHV, so pokazali najmanjši potencial za kvantifikacijo. Vpuščanje O_2 je rezultate znatno izboljšalo, vendar odstopanja intenzitet izmerjenih SIMS signalov od točnih vrednosti kemične sestave še niso bila

optimalna. Izboljšave, dosežene z uporabo H_2, so omogočile nadaljnjo optimizacijo predvsem v primeru prehodnih kovin, ki so bile v primeru naše raziskave Ti, Cr, Fe, Co in Ni. Analize teh kovin v atmosferi H_2 so pokazale največ 46 % odstopanje od točnih vrednosti elementarne sestave zlitin. V primeru atmosfere O_2 je bilo maksimalno odstopanje 66 % in v primeru UHV 228 %.

Naši rezultati tako nakazujejo, da se prek adsorpcije molekul plina na površino vzorca ustvari novo kemijsko okolje, ki zmanjša začetne razlike med kovinami in različnimi zlitinami ter s tem elektronskimi lastnostmi površine. S pomočjo vpuščanja H_2 lahko tako izboljšamo kvantitativne lastnosti metode SIMS.

Contents

List of Figures

List of Tables

Abbreviations

AES	...	Auger electron spectroscopy
AFM	...	atomic force microscopy
DC	...	direct current
DESI	...	desorption electrospray ionization
DHEM	...	differential hall effect metrology
DRI	...	dynamic reactive ionization
EBSD	...	electron backscatter diffraction
EDI	...	electrospray droplet impact
EDXS	...	energy-dispersive X-ray spectroscopy
EELS	...	electron energy loss spectroscopy
EI	...	electron ionization
ESA	...	electro static analyzer
ESCA	...	electron spectroscopy for chemical analysis
FEG	...	field emission gun
FIB	...	focused ion beam
FT-ICR	...	Furrier transform ion cyclotron resonance
FWHM	...	full width at half maximum
GDOES	...	glow-discharge optical emission spectroscopy
IPES	...	inverse photoemission spectroscopy
IR	...	infrared
LA-ICP-MS	...	laser ablation inductively coupled plasma mass spectrometry
LEED	...	low-energy electron diffraction
LEIS	...	low-energy ion scattering spectroscopy
LIBS	...	laser-induced breakdown spectroscopy
LMIG	...	liquid metal ion gun
MALDI	...	matrix-assisted laser desorption/ionization
MCP	...	microchannel plate
MRI	...	mixing-roughness-information depth
MS	...	mass spectrometry
PECVD	...	plasma-enhanced chemical vapor deposition
PIXE	...	proton/particle-induced X-ray emission
ppb	...	parts per billion
ppm	...	parts per million
PVD	...	physical vapor deposition
RBS	...	Rutherford backscattering spectrometry
RF	...	radio frequency
RMS	...	root mean square
RSF	...	relative sensitivity factor
SEM	...	scanning electron microscopy
SIMS	...	secondary ion mass spectrometry

SNMS	...	secondary neutral mass spectrometry
SNOM	...	scanning near-field optical microscopy
STM	...	scanning tunneling microscopy
TEM	...	transmission electron microscopy
ToF	...	time of flight
TXRF	...	total reflection X-ray fluorescence
UHV	...	ultra-high vacuum
UPS	...	ultraviolet photoelectron spectroscopy
UV	...	ultraviolet
WDXS	...	wavelength-dispersive X-ray spectroscopy
XPS	...	X-ray photoelectron spectroscopy
XRD	...	X-ray diffraction
XRR	...	X-ray reflectivity

Chapter 1

Introduction

It needs to be mentioned that a notable part of the Introduction section was summarized, expanded, and copied from my original work done for the study subject Seminar I, which is a part of the Ph.D. program Nanosciences and Nanotechnologies at the Jozef Stefan International Postgraduate School. This note is present to prevent claims of undisclosed self-plagiarism.

1.1 Methods of Surface Analysis

There are several methods used for surface analysis. We can use them to identify the elemental, molecular, and isotopic composition, electronic states and electron distribution, oxidation states, crystal structure, and orientation, as well as topology and morphology. Information of interest is obtained by analyzing electrons, ions, and electromagnetic radiation, and measuring the currents and forces between the probe and the sample. These methods can be divided into categories of microscopic and spectroscopic techniques and mass spectrometry.

The most common microscopic method is electron microscopy. Electrons analyzed can be scattered or emitted back into the direction of the electron beam or the beam can pass through the sample. In the first case, we talk about scanning electron microscopy (SEM), and in the second case about transmission electron microscopy (TEM). [1], [2] Instead of the electrons, we can also use ions, analyzing both secondary electrons and transmitted ions. Such ion microscopes are most commonly used with the He^+ ions or with the focused ion beam (FIB) gun with Ga^+ ions. [3] Finally, the surface can be analyzed at the atomic level with different probe methods. The most common are scanning tunneling microscopy (STM) where the tunneling current between the probe and the sample is measured and atomic force microscopy (AFM) utilizing the measurements of different forces that are present when the probe and the sample are in proximity of less than hundreds of nm. AFM can be also coupled with methods, such as infrared (IR) and Raman spectroscopy, as well as modified to perform scanning near-field optical microscopy (SNOM). [4]–[8]

Among spectroscopic methods, many can be combined with the electron microscope since hitting a sample with an electron beam causes many different processes. Auger electron spectroscopy (AES) gives us elemental and chemical information about the sample. [9] The quantitative elemental composition can be also obtained with electron energy loss spectroscopy (EELS). [10], [11] Energy and wavelengths-dispersive X-ray spectroscopy (EDXS and WDXS, respectively) are the other two methods used for the elemental analysis, although these techniques are not as surface sensitive as others with the information depth of between 1 and 2 μm. [12] The electron beam can furthermore provide crystallographic information via methods, such as electron backscatter diffraction (EBSD)

and low-energy electron diffraction (LEED). [13], [14] Quantitative elemental information can be, similarly to with electron beam, obtained also with the ion beam. Methods utilizing this approach are proton/particle-induced X-ray emission (PIXE), low-energy ion scattering spectroscopy (LEIS), and Rutherford backscattering spectrometry (RBS). LEIS also gives some information about the sample structure and RBS about the depth distribution. [15]–[17]One can apply electromagnetic radiation to induce changes and get information about the samples as well. A very often used method in this group is X-ray photoelectron spectroscopy (XPS), also called electron spectroscopy for chemical analysis (ESCA). Information obtained with XPS is very similar to the AES. [18] Methods similar and complementary to the XPS are ultraviolet photoelectron spectroscopy (UPS) and inverse photoemission spectroscopy (IPES). They both give information about the electronic structures of the surface, although IPES actually uses an electron beam for the excitation while electromagnetic waves irradiated are analyzed. [19], [20] X-rays can be used also in the surface-sensitive version of fluorescence, that is total reflection X-ray fluorescence (TXRF) which gives us quantitative elemental information. [21] The same information can be also obtained using an IR laser of high intensity. Laser-induced breakdown spectroscopy (LIBS) works by the principle of laser ablation and formation of plasma, which during cooling process emits elemental-specific photons. [22]

A similar approach utilizing a laser can be also applied in the field of mass spectrometry. Laser ablation inductively coupled plasma mass spectrometry (LA-ICP-MS) uses different lasers and post-ionization with plasma to obtain elemental and isotopic information. [23] On the other hand, in the case of secondary ion mass spectrometry (SIMS), the sample is bombarded with the primary ions. Usage of the ion beam, in some cases similar to FIB, gives besides elemental and isotopic also molecular information. [24] Electrospray droplet impact (EDI) works in a very similar way, only instead of the ion beam, droplets of water are used for the bombardment of the surface. They can be used also in combination with the desorption electrospray ionization (DESI) mass spectrometry method, which is based on dissolving the analyte in these droplets. [25], [26] In a specific configuration, even matrix-assisted laser desorption/ionization (MALDI) can be used for the analysis of large molecules on the surface. [27], [28]

Among the number of different properties typical for the listed methods are also detection limits and lateral resolution. Detection limits are important because they indicate the concentration of analyte possibly detected and the choice of the method. On the other hand, lateral resolution is important when surface heterogeneity of the analyte is present and its distribution is of interest. The smaller the lateral resolution that can be achieved, the better are imaging capabilities of this technique. Figure 1 presents a majority of methods described above in terms of their detection limit and lateral resolution.

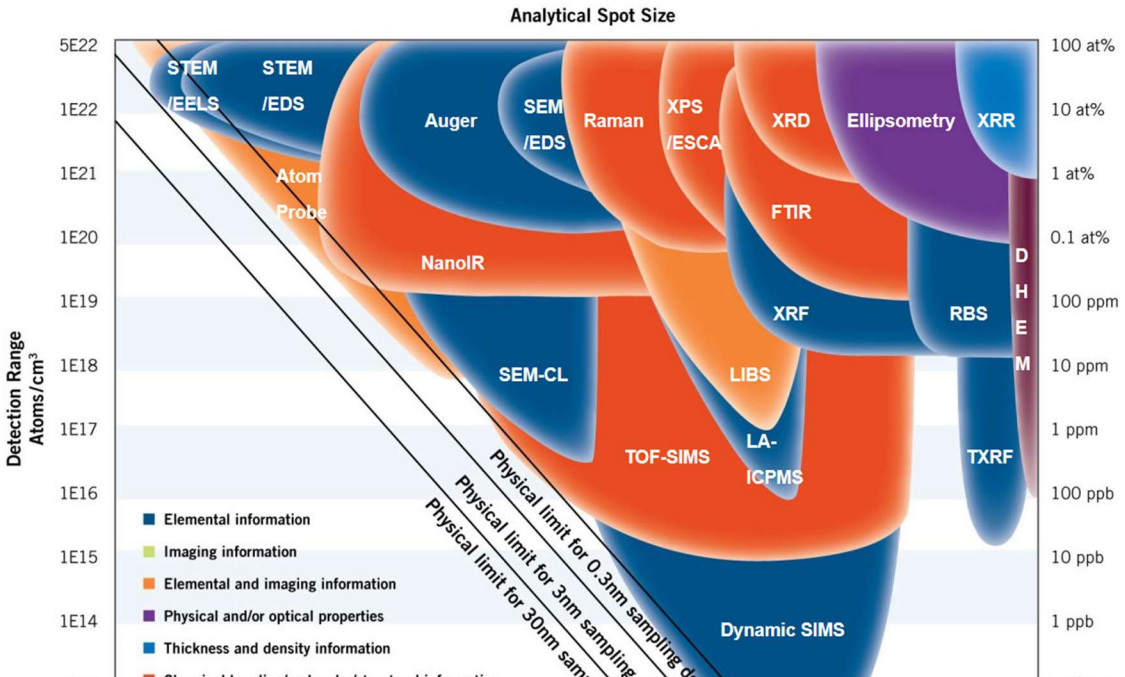

Figure 1: Comparison of detection limits and lateral resolution of different surface-sensitive analytical methods. (EAG Laboratories, https://www.eag.com/techniques/, 22nd December 2023).

1.2 Overview of SIMS

SIMS offers a very wide range of information like molecular structure, chemical composition, and distribution of chemical species to be acquired in the forms of surface mass spectra, depth profiles, and 2D and 3D mapping. [29] As such is the most commonly and widely used surface-sensitive mass spectrometry method with even a few of its subvariants developed for specific types of measurements. With its good lateral resolution and unsurpassed detection limit, it is applicable in many fields such as studies of metals, alloys, and their properties [30], [31], corrosion inhibition [32], [33], isotope research [34], [35], analysis of thin films and multilayers [36]–[38], investigation of nanoparticles [39], [40], microelectronics and photovoltaics [41], [42], batteries [43]–[45], catalysis [46], geological research of minerals [34], [35], cosmochemistry [47]–[49], studies of organic compounds and polymers [50], [51], photographic materials [52], detection of dopants and impurities [53], [54], analysis of biological material including cells and tissues [55], [56], and more.

In the SIMS method, we use primary ions, generated in an ion gun and focused with the electrostatic lenses, to sputter secondary ions which are analyzed giving the information about atomic, molecular, and isotopic structure of a surface. [24], [57], [58] Secondary ions are formed upon their emission from the surface and their signal is influenced by five parameters. These are the current density of the primary ions (I_p), the sputter yield (Y_m), the ionization probability ($\alpha^{+/-}$), the concentration of an analyzed compound on the surface (θ_m), and the transmission of the analytical system (η). They are related to the secondary ion current (I_m) as denoted by Equation 1. [24] Subscript m relates to the analyzed compound and subscript p to the primary ions.

$$I_m = I_p Y_m \, \alpha^{+/-} \theta_m \eta \tag{1}$$

The main advantages of a SIMS method are excellent lateral resolution and surface sensitivity as information is gathered only from the top 2 nm or, in some specific cases, even less. It also has very low detection limits in the range of ppm (parts per million) and ppb (parts per billion). The sample does not need to be modified and therefore chemical and topographical information remains unaltered. [24] However, there are also negative aspects of the SIMS method. In the cases of most primary ions, it is considered a hard

ionization technique, defined by a large degree of fragmentation caused by the high-energy primary ions. Therefore, molecules can be severely damaged during analysis, and species-specific fragments, as well as molecular peaks with high molar mass, are difficult to detect. Vacuum needed can be also a problem for some, especially biological samples. [24], [59]

Secondary ions emitted from the surface are extracted with the electrostatic lenses into the analyzer. Generally, any analyzer can be coupled with the SIMS instrument, but some are more frequent than others. [60] Due to their capabilities, time of flight (ToF) analyzers become very popular. SIMS instrument combined with the ToF analyzer is denoted as ToF-SIMS. [24] The main advantage of ToF analyzers is their ability to simultaneously analyze all the ions from m/z 0 to the selected m/z value. To improve mass resolution, now reaching above the $m/\Delta m$ value of 15,000, most of the ToF analyzers are equipped with the reflectron (ion mirror). Another advantage of ToF analyzers is also their very high transmission of the secondary ions, reaching almost 100%. [60], [61] An example of a ToF analyzer is shown in Figure 2. Some SIMS instruments, especially those intended for an isotopic analysis, which requires a very high mass resolution even around 30,000, are equipped with magnetic sectors. There are also still a lot of instruments with quadrupole analyzers because these are the cheapest and do not require pulsed primary ion beams as it is with the ToF analyzers. However, their mass resolution is significantly lower and they are generally only capable of distinguishing nominal/unit masses. Similar or slightly better performance can be observed with ion traps. [60], [62] Modern instruments can be also equipped with the orbitrap or even FT-ICR (Furrier transform ion cyclotron resonance) analyzers. Their main advantage is their exceptional mass resolution, for orbitrap reaching $m/\Delta m > 200\,000$ and for FT-ICR even $m/\Delta m > 1\,000\,000$. However, they are also by far the most expensive ones. [60], [63]

Another important part of the SIMS instrument is a low-energy electron gun. When analyzing isolating materials, the use of cations as the primary ions leads to charge accumulation. The consequence is the formation of the inhomogeneous electrostatic field which negatively affects transmission of secondary ions into the analyzer. The application of a low-energy electron beam partially solves this problem. [24] Electrons need to have a low energy so that the sample surface remains undamaged. Finally, strong vacuum pumps, usually turbomolecular ones combined with Ti sublimation pumps, are needed as SIMS analyses are conducted in the ultra-high vacuum (UHV) environment with a pressure range between 10^{-6} and 10^{-10} mbar. UHV is needed to prevent excess collisions between the primary ions and gas molecules leading to their scattering. There would be also a lower transmission of secondary ions and decreased primary ion beam focus, which would significantly worsen lateral resolution. [24], [64]

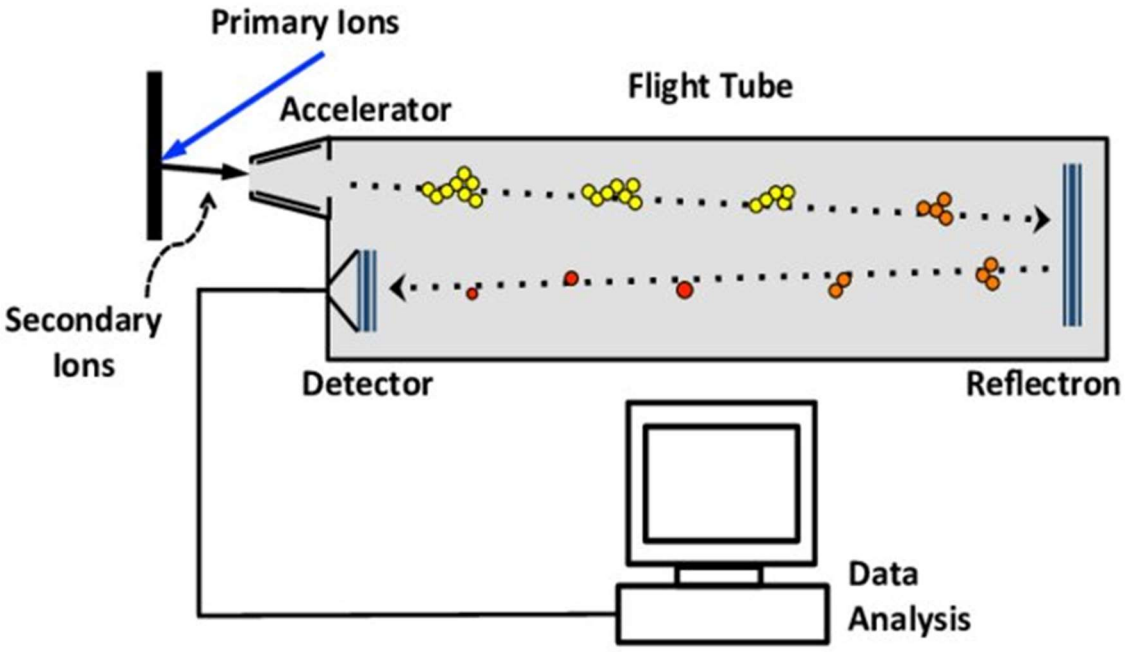

Figure 2: A ToF analyzer with a reflectron and depicted principle of operation. (P. Johansson: Characterization of Protein Surface Interaction: Collagen and Osteocalcin, *Master's degree thesis*, **2013**).

One of the measurement parameters is the type of the primary ions as different ones are suitable for different applications. These are divided into monoatomic, polyatomic, and cluster ions. The best lateral resolution is achieved using mono- or polyatomic metal cations (Ga^+, Bi^+, Au^+, Bi_3^+, Au_3^+) generated in an LMIG ion source (liquid metal ion gun). In this case, ions are generated in the field-ionization source. With LMIG lateral resolution even below 100 nm can be achieved. [24], [59], [65] More basic SIMS instruments are generally equipped with the ion gun for noble gases, most commonly Ar^+ and Xe^+. Reactive sputtering with the O_2^+ and Cs^+ ion beams is also frequently used. [65]–[68] Cs^+ ions increase the yield of negative secondary ions due to their incorporation into the surface of the sample with a consequent reduction of the work function. [65] On the other hand, O_2^+ ions increase the yield of positive secondary ions. [69] Unfortunately, monoatomic ions and polyatomic ones with a small number of constituting atoms cause severe damage to the surface when analyzing organic compounds and biological material. The reason is the low stability of such samples as molecules are easily broken down and their structure changed. Because of this, the desorption of whole molecules (molecular signal) can be very quickly lost especially during depth profiling. They also penetrate much deeper into the sample than polyatomic ions. [24], [63], [65] Therefore, polyatomic primary ions with many constituting atoms and clusters can be used instead. Such polyatomic ions are SF_5^+ and C_{60}^+ (fullerene). The most notable examples of cluster ions are Ar as well as O_2, CO_2, H_2O, and SF_6 clusters and Au_{400}^{4+}. [63], [70]–[73] A Comparison of a simulation of monoatomic and polyatomic primary ion impact is presented in Figure 3. The H_2O clusters approach can be developed even further by using droplets with up to 100,000 molecules of water or similar solvents with a charge of around 100+, essentially turning into the EDI method. [74] However, the bigger the primary ion is, the lower the focus. The reason for polyatomic and cluster ions to cause less damage is in the energy distribution as the energy of a whole ion is divided between the constituting particles. [63], [74]–[76] Most of these primary ions have an energy between a few 100 eV and a few 10 keV. [71], [77]–[79]

However, there is a special type of SIMS called MeV-SIMS which utilizes primary ions with an energy between 0.5 and 20 MeV. There are also less common types of primary ions used in MeV-SIMS, such as Cl^{n+} and Cu^{n+}. [80]–[83] The main difference between keV and MeV SIMS is in the mechanism via which primary ions are stopped when they hit the sample. In the case of keV SIMS, the prevalent stopping occurs via nuclear collisions, resulting in significant molecular fragmentation. For MeV SIMS, electronic stopping and electronic excitations are dominant. [81], [84], [85] Electronic excitations can be described as potential sputtering using models, such as heat/thermal spikes. The main characteristic of this type of sputtering is the desorption of whole organic molecules and a low degree of fragmentation. MeV SIMS can be consequently successfully applied for imaging and spectra measurements of organic and biological materials. [84], [85]

Connected with the process of ion bombardment and consequential sputtering are two concepts defined as ''*damage*'' and *''disappearance cross-section*''. The first one describes an accumulation of damage and the second one dose of primary ions (current density) needed for a molecular signal to disappear. Polyatomic and cluster ions cause less damage and increase sputter yield as seen in Figure 3. *''Disappearance cross section*'' is therefore also increased. Accumulation of damage and therefore *''damage cross section*'' are, on the other hand, reduced because most of the damaged molecules are removed from the surface. [63], [74] However, polyatomic and cluster primary ions are not an appropriate choice mainly for metals and inorganic compounds, because the low energy of the constituent particles severely extends the time of measurement. Therefore, Bi^+, Au^+, Bi_3^+, and Au_3^+ are generated in an LMIG source, or more conventional Ar^+, Xe^+, Cs^+, and O_2^+ ions are used for the analysis. [24], [59], [63], [76]

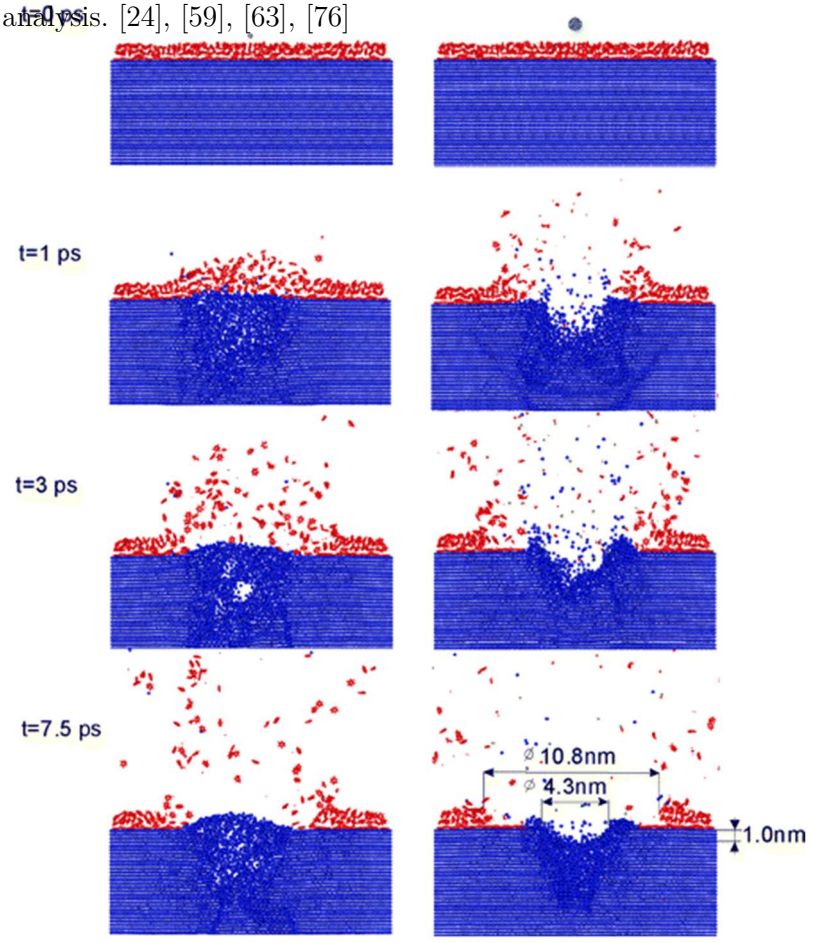

Figure 3: Computer simulation representing a cross-sectional view of 15 keV Ga and C_{60} particles upon collision (normal incidence angle) with a sample of the 3 benzene layers (red) deposited on the Ag{111} substrate (blue) (Z. Postawa et al.: Microscopic Insights into the Sputtering of Thin Organic Films on Ag{111} Induced by C_{60} and Ga Bombardment. *J. Phys. Chem. B.* **2005**).

The current density and, to some degree, also the type of primary ions furthermore determine the static or dynamic operational modes of SIMS. In the static SIMS, two primary ions must not hit the same area or, in other words, the *''damage cross section''* area must not be sputtered again. The reasons are the accumulation of damage and molecular changes in the affected area caused by the impinging particles with high energy. The static SIMS regime is limited with a primary ion density dose of approximately 10^{13} cm^{-2}. [24], [59] Majority of the static SIMS instruments are equipped with the pulsed primary ion gun, most commonly LMIG and ToF analyzers. Such ion guns are optimized to achieve the best focus and sufficient secondary ion yield in the shortest ion beam pulse possible. Since short-pulsed ion guns (1 – 100 ns) have a very low current density (approximately 1 pA), such instruments require another ion gun to perform depth profiling (dual beam approach), which operates somewhere between pulsed and DC (direct current) modes. Namely, to perform depth profiling, high enough currents of primary ions are needed for continuous removal of material because depth profiling can only be performed in dynamic SIMS mode. [24], [61], [86], [87] The structure of a ToF-SIMS instrument, equipped with two ion guns, one for the analysis and one for the depth profiling, is shown in Figure 4. However, many less sophisticated SIMS instruments have the same ion gun, mostly emitting Ar^+, Xe^+, Cs^+, and O_2^+ ions, used for both surface analysis and depth profiling. Such instruments are considered dynamic SIMS. [87] Their disadvantage is the fact that a high current of mono- or diatomic primary ions causes extensive damage on the surface and detection of molecular peaks and higher-mass fragments is consequently difficult. These instruments are therefore mainly used for elemental analysis in the field of the semiconductor industry for the quantitative analyses of dopants. On the other hand, much lower damage caused by the polyatomic and cluster ions offers the possibility of dynamic SIMS also in terms of molecular analysis as these primary ions do not cause damage accumulation. Even more so, they can even remove pre-existing damage caused by primary ions from monoatomic ion sources. [74], [88] Dynamic SIMS also has some advantages with the main being simultaneous analysis and depth profiling, causing all sputtered material to be available for the analysis. Secondary ion yields are consequently higher, detection limits lower, and analysis faster. The possibility of operating in the DC mode furthermore significantly reduces the complexity of the ion gun in comparison to the pulsed ones. [63], [87], [89]

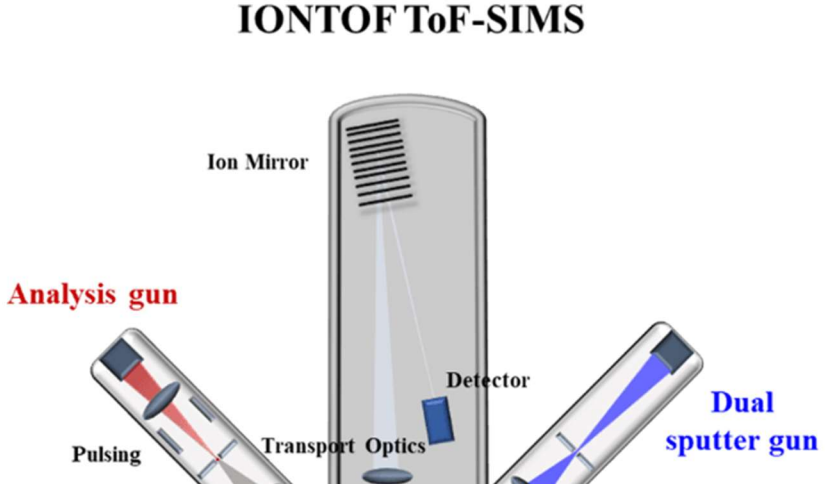

Figure 4: Structure of a ToF-SIMS instrument equipped with two ion guns and an electron flood gun. (Rice University, http://simslab.rice.edu/surface-analysis-lab/teaching-activities-resources/time-of-flight-secondary-ion-mass-spectrometry/, 29th December 2023).

With the dual-beam approach, only material sputtered with the pulsed analysis gun that represents less than 10% of all the ions is used for the analysis. Additionally, mass resolution achieved with the ToF analyzers is connected with a pulse duration because a secondary ion can be formed at any time during the pulse. The consequence is a deviation in time of flight for ions with the same m/z value broadening the peaks. To achieve the highest mass resolution, pulses should be as short as possible, further lowering the portion of secondary ions available for the analysis. [60], [61], [89] Even greater compromise needs to be done when performing imaging. In this case, long pulses are needed for good lateral resolution because focusing the beam on a small area results in low primary ion currents and, therefore, low yields of secondary ions. To achieve desirable detection limits, enough material must be sputtered and the yield should not be small. Longer pulses become a substitution for higher primary ion current. We are therefore trading between good mass and lateral resolution. [61], [89]

Other important analysis parameters besides the type of primary ions are the primary ion energy, the incident angle of an ion beam, sample rotation, sample temperature, and the atmosphere inside an analysis chamber. [90] With the ion energy changes, we influence the accumulation of damage on the sample surface (higher energy, more damage) and the amount of material sputtered (higher energy, higher sputter yield). The incident angle of an ion beam affects the depth to which ions penetrate inside a sample. The greater the angle regarding normal to the sample, the shallower ion trajectories inside a sample will be and more damage will be accumulated on the surface instead of the bulk. However, grazing angles can also negatively affect surface topography as micro-tranches, ripples, and ridges-like structures can be formed. Such roughening can be prevented by applying sample rotation. In this way, the direction from which primary ions hit the sample is randomized, damage averaged, and topographical changes less prominent. [90], [91] Temperature can affect the stability and physical properties of the sample and, therefore, the amount of damage accumulated, mixing of different compounds and amount of material sputtered. [90]

Finally, some gases, most often noble gases or oxygen, can be released into the analytical chamber during analysis. They can reduce charge buildup on the insulating samples and change the yield of positive and negative secondary ions. When using reactive gases, even adducts composed of the analyzed material and the gas molecules can form, resulting in

the detection of new secondary ions. [74], [90], [91] The gas flooding approach is described in a separate subsection number 1.2.4.4 in greater detail.

1.2.1 Operating conditions for the acquisition of mass surface spectra

One of the most important parameters of the surface spectra is mass resolution as it needs to be high enough to identify the compounds of interest with a high enough degree of certainty. Good mass resolution becomes the most important at the higher masses of the secondary ions since there are numerous possible combinations of elements forming molecules with approximately the same mass. This is the main reason that most of the SIMS instruments equipped with the quadrupole analyzer are used only for elemental analysis. [24], [60], [92] ToF analyzers provide the equipment with extensively improved mass resolution, in modern instruments exceeding the $m/\Delta m$ value of 15,000. However, to identify organic molecules with the m/z of a few hundred or to distinguish between different metal clusters, even better mass resolution is needed. Magnetic sector analyzers can achieve this but since they are unable to simultaneously analyze the whole m/z range from 0 to the chosen value, they are mainly used just for isotopic analysis. [60], [61], [92] Namely, when analyzing a sample, especially if composed of organic compounds, all the ions over the selected m/z range need to be detected to perform a reliable analysis, identifying both the molecular ions and their fragments. Measuring mass spectra of positive and negative secondary ions provides an additional degree of certainty. In the cases of more common ionization techniques, such as electron ionization (EI), fragmentation patterns are known and much more predictable than during SIMS measurements. This property is extensively used in the form of tandem mass spectrometry (MS/MS) when two, most commonly ToF analyzers, are used simultaneously. Secondary ions are separated in the first ToF analyzer; the ion of interest is selected and extraction optics are used to guide into the second ToF analyzer. Prior to the separation in the second ToF, ion is fragmented via EI and in this way, despite lower mass resolution, its composition can be determined with high degree of certainty by considering known fragmentation patterns. [24], [61], [93] Finally, application of the MS/MS can be avoided by introducing mass analyzers with a very high mass resolution, such as orbitrap, although they are also used in the tandem versions in combination with ToF. Regardless of the type of mass filters, energy filters are also required to achieve optimal results. They are needed to reduce the energy dispersion that occurs during secondary ion extraction. Therefore, the higher degree of energy filtering applied means lowering the extraction optics transmission. Examples of energy filters are reflectron combined with the ToF analyzer and electro static analyzer (ESA) combined with magnetic sectors. [60]

Besides mass resolution, other parameters need to be considered as well. Another two examples are surface sensitivity and lateral resolution. For SIMS to be a truly surface-sensitive analytical method, this property should be considered concerning primary ions. Samples need to be sputtered in a way in which secondary ions are emitted only from the topmost atomic layers. This can be achieved by optimizing the type, energy, and incidence angle of the primary ions. [74], [91] Bigger primary ions with higher mass mostly penetrate less into the sample. However, care should be taken when analyzing materials composed mainly of low-mass elements. In these cases, high-mass monoatomic primary ions can penetrate deep because of the low resistance of the small atoms composing the sample, and the application of primary ions, such as C_{60}^{+} and Ar clusters, can be a better choice. [93] Information depth can be further reduced by lowering the energy of the primary ions and applying the sputtering under the grazing angles. It is furthermore advisable to perform measurements in the static SIMS mode when only surface composition is of interest. Finally, a sample can be also optimized to reduce the penetration depth of primary ions.

This can be done in some cases by the sample cooling. [87], [91] Considering all of the above, we can achieve an information depth of approximately 1 nm, that is, around 5 atomic monolayers. Last but not least, a lateral resolution should not be disregarded because we are sometimes interested in a composition of very small structures on the surfaces, especially in cases of failure and contamination analysis. The primary ion beam must have a significantly lower focus than the size of the object of interest. [24]

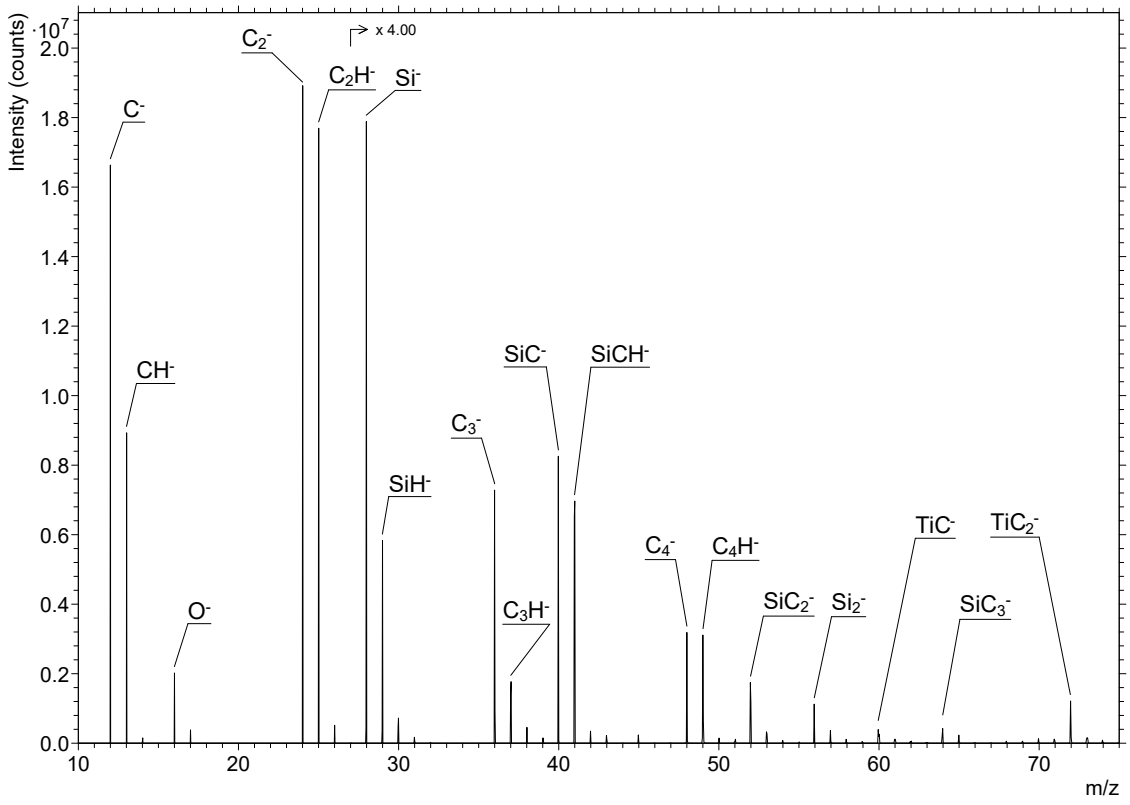

Figure 5: Mass spectra of negative secondary ions originating from the TiSi alloy. Measurements were performed in the atmosphere of C_2H_2. Shown are ions over the m/z range from 10 to 75 with the most intense ones identified and assigned. The intensities of the ions are magnified 4 times from the m/z value 27 on.

The majority of surfaces are exposed to air contamination as these can only be avoided if samples are constantly under vacuum. Contaminations are known to show a very similar pattern of secondary ion signals regardless of the type of the sample. However, it is possible to avoid detecting these contaminations if a sample is cleaned before the analysis. Mostly it is not advisable to use solvents as a sample can be damaged or modified. Ar cluster ions are an optimal solution in such cases as very big clusters with low energy can be also used for surface cleaning and not only for the analysis. [63], [75], [94] An example of the mass spectra without the presence of contaminations is shown in Figure 5. It represents the TiSi alloy measured in the atmosphere of C_2H_2.

1.2.2 Operating conditions for 2D mapping

To acquire the 2D distribution of different compounds and elements, the primary ion beam needs to scan the surface. The intensity of the secondary ions is measured in each pixel.

The resulting 2D map represents the intensity distribution of analyzed secondary ions for each ion separately. By ascribing secondary ions to the compounds they originate from, one can evaluate the homogeneity or heterogeneity of these compounds on the surface of the sample. The most important characteristics of micrographs are lateral resolution and image contrast. Namely, when imaging very small particles, only good enough lateral resolution offers useful results. In the imaging mode, the lateral resolution of the LMIG source is mostly between 100 and 200 nm while state-of-the-art instruments achieve lateral resolution between 50 and 100 nm. To accommodate for so high lateral resolution, the dimensions of the pixels need to be even smaller. However, increasing lateral resolution and lowering pixel size also decreases the number of molecules available for the analysis in each pixel leading to a worsened contrast. [95], [96] Therefore, we have a trade-off between the lateral resolution and the contrast.

This relationship was to some degree improved with the Bi_3^+ and Au_3^+ primary ions. They are generated in an LMIG source offering excellent lateral resolution but also greater ionization yields and lower *damage cross sections* than monoatomic primary ions, especially for the organic materials and biomolecules. Even better ionization yield and less damage accumulation can be achieved with SF_5^+ and C_{60}^+ but these ions do not offer so good lateral resolution. [95], [96] *Damage cross section* below 10^{-15} cm^2 can be achieved when using SF_5^+ and C_{60}^+ primary ions [24] while with the Bi_3^+ and Au_3^+ ions, it is between 10^{-12} and 10^{-13} cm^2 [97], [98]. However, it should be emphasized that damage cross-section also depends on the energy of the primary ions. [99] The number of secondary ions can be enhanced also with an extension of the primary ion pulse but as already explained, the mass resolution is severely worsened in this way. Ions with the same nominal mass, for example, frequently present K^+ and $C_3H_3^+$ ions, and consequently can no longer be distinguished. [24], [95], [96]

Another important factor that needs to be considered when performing imaging is surface topography. As the primary ion beam is generally directed to the sample surface at an incident angle of around 45°, topographic features are consequently distorted and elongated in the direction of the ion beam. There is also an area behind these features that receives no impacts from the primary ions at all as it is shadowed and therefore no secondary ions are emitted. As already mentioned, the angle of the primary ions affects ionization yield being the highest at the normal incidence angle. Topography changes lead to the change of the primary ion beam incidence angle and, therefore, to the different ionization yields. Finally, topographic features also cause distortions in the electrostatic field of the extraction lenses. The consequence is the change in the energy of the secondary ions, lowering mass resolution. [91], [95]

Micrographs can be after imaging is completed, analyzed, and modified in different ways. There are de-noising processes as well as multivariate analysis approaches. [95] The most basic data processing can be done with a summation and overlaying of micrographs of different ions showing correspondence or exclusion of the intensities of their signals. An example of such an approach is shown in Figure 6, presenting an imaging analysis of the Cu substrate covered with the corrosion inhibitor 2-mercaptobenzimidazole.

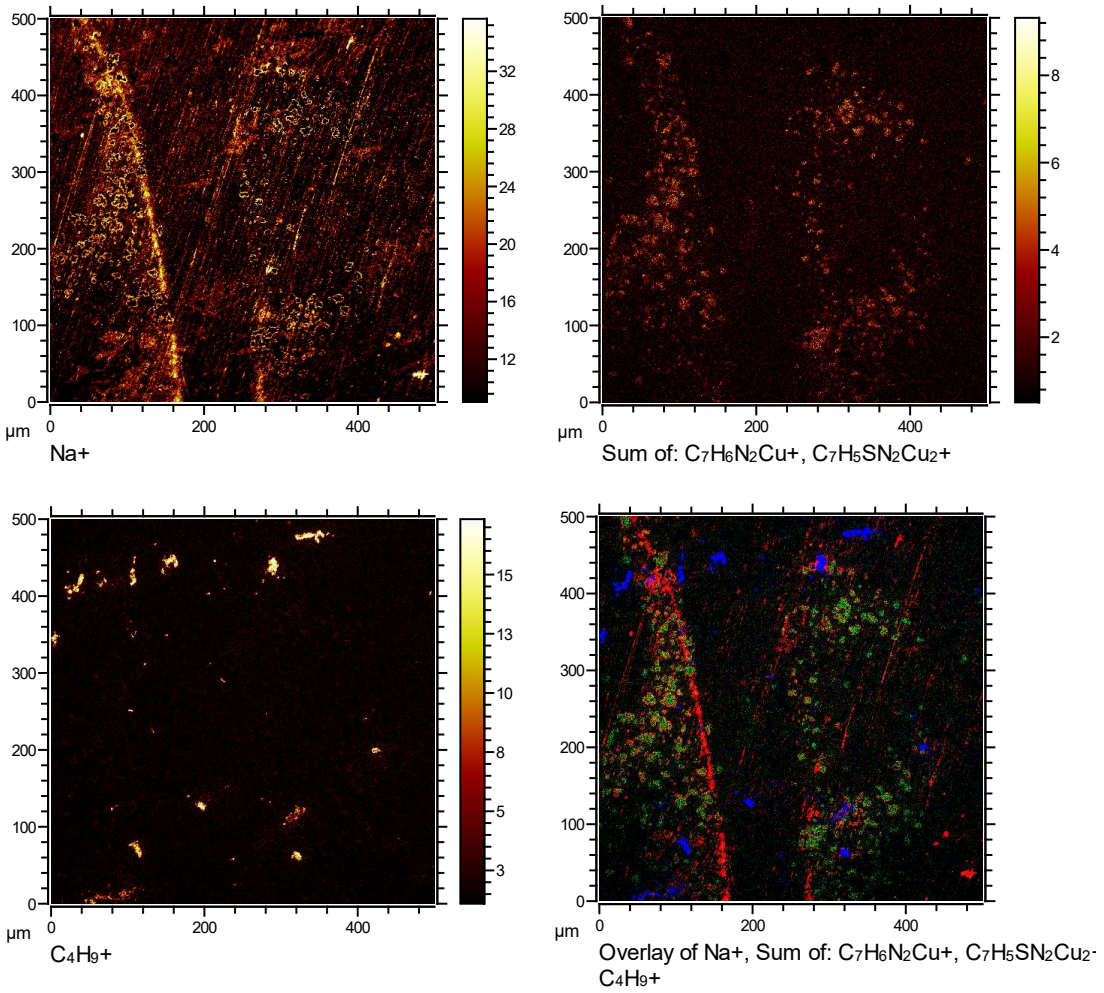

Figure 6: SIMS 2D mapping of the Cu substrate covered with the corrosion inhibitor 2-mercaptobenzimidazole. The upper left is an intensity distribution of Na^+ ions, the upper right is a sum of an intensity distribution of the specific fragment and the molecular ion of 2-mercaptobenzimidazole, the bottom left is an intensity distribution of the $C_4H_9^+$ ion, and the bottom right is an overlay of Na^+ (red), 2-mercaptobenzimidazole (green) and $C_4H_9^+$ fragment (blue).

1.2.3 Operating conditions for the acquisition of depth profiles

When performing depth profiling, the bulk of the sample is analyzed beside the surface. This is achieved by the continuous removal of the consecutive layers of the material in dynamic SIMS mode. The result is a depth profile, showing us the distribution of the compounds as a function of the sputter depth. Experimental parameters (primary ion type and energy, ion beam incident angle, sample rotation, sample temperature, and atmosphere) are important when performing depth profiling. This is especially true for the incident angle and rotation. The main reason is the significantly larger total dose of primary ions needed for the material to be sputtered away compared to the surface spectra measurement or imaging. During depth profiling, the primary ion dose is in the range of 10^{18} ions $cm^{-2}h^{-1}$ while during surface spectra measurement or imaging is in the range of 10^{13} ions $cm^{-2}h^{-1}$. This is directly connected with the fact that depth profiling can be only conducted in a dynamic SIMS mode which causes the greatest amount of sample damage and structure modifications. Consequently, changing these parameters can greatly improve an analysis outcome as well as the quality and accuracy of gathered data. [90], [100]

ToF-SIMS instruments are equipped with two ion guns used for a dual beam depth profiling approach with the instrument configuration presented in Figure 4. The main advantage is the optimization of both beams for their primary purpose. [90] Analysis beam is generally emitted from the LMIG source emitting monoatomic (e.g. Bi^+) or polyatomic (e.g. Bi_3^+) primary ions. Monoatomic ions are mostly used for the inorganic and polyatomic for the organic and biological materials. As sputtering caused by the analytical ion beam represents less than 10% of all sputtering, damage caused by the metal cations can be repaired during etching if using an appropriate type of ions. It was shown that large Ar clusters can recover molecular signals of a surface damaged with the mono or polyatomic metal primary ions and are therefore appropriate for the etching of organic and biological materials. [97] However, Ar clusters can be also used for both depth profiling and analysis but this is not a common approach. Single beam depth profiling is more common with SIMS instruments equipped only with the Ar^+, Xe^+, Cs^+, and/or O_2^+ ion guns. The main advantage of this approach is the availability of all the sputtered material for the analysis and it is the most appropriate for the analysis of the inorganic samples. [87], [90]

There is a specific problem connected with a molecular damage accumulation observed especially during depth profiling with the mono- or diatomic primary ions in the case of polymers. Namely, many polymers become heavily cross-linked, forming graphite-like structures, when irradiated by the large enough dose of primary ions. The point when cross-linking becomes so extensive that the 3D structure is formed and further etching is heavily limited or even no longer possible is called the gel point. [74] Surface damage can be minimized if a cluster ion beam is used both for the etching and the analysis. However, cluster pulses are difficult to focus and because of a low current (low brightness of an ion source), their time width is much longer, resulting in a lower mass resolution. The alternative is an application of a DC primary ion beam and pulsed secondary ion beam in the ToF analyzer but in this case, instrument transmission becomes much lower. [97]

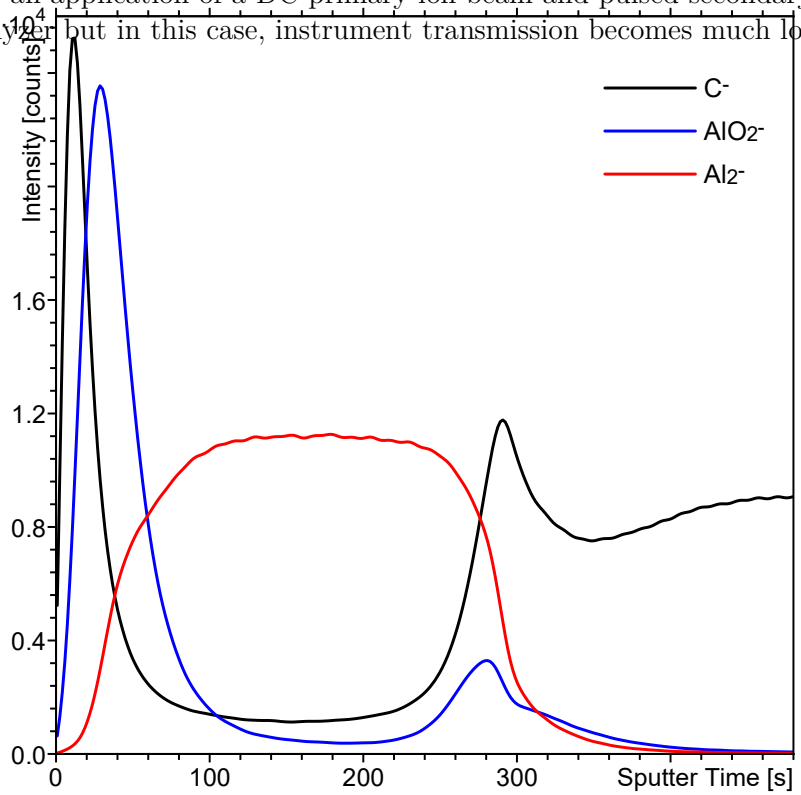

Figure 7: SIMS depth profile of negative secondary ions from the sample of a thin Al foil of thickness between 50 and 100 nm on a polymer substrate.

Minimized surface damage is favorable also from the point of achieving good depth resolution during the analysis of thin films. Depth resolution is most commonly defined as the depth interval over which the signal intensity rises from 16 % to 84 % or drops for the same value when crossing an interface between two layers and is usually measured using thin delta layers inside another material. MRI model (mixing-roughness-information depth) is often used to evaluate depth resolution and it relates these three parameters to the depth resolution. The upslope of a delta layer signal is connected with an information depth of analysis, for SIMS being between 1 and 2 nm, but if appropriately tuned, it can even drop below 1 nm. The full width at half maximum (FWHM) depends on a surface roughness being either previously present or caused by the sputtering process. Surface roughening during prolonged sputtering can be influenced by the modifications in the energy and the incident angle of the primary ions, with the latter accompanied by sample rotation. Finally, we have the (atomic) mixing, that is, the relocation of the atoms, ions, and molecules caused by the primary ion impacts. It is represented as the decay length or downslope of the delta layer signal and is most significantly affected by the measurement parameters, mainly the type and energy of the primary ions, as well as the sample temperature. [66]

Worth mentioning is also a typical shape of a depth profile. It starts with the transient region with an extensive drop in the signal intensity. In the case of organic and biological samples, it is directly related to the damage accumulation and in the case of inorganic materials, it is mostly a matrix effect consequence. Furthermore, the transient region can be also a result of a surface layer of contaminations. The transient region is followed by the steady state region where the signal intensity is constant. If the intensity is still slowly decaying, this region is called a quasi-steady state. Finally, it ends with the interfacial region where we reach a new compound if a multilayered sample is analyzed. [90] An example of such a depth profile is shown in Figure 7, corresponding to the sample of a thin Al foil of approximate thickness between 50 and 100 nm on a polymer substrate. The presented depth profile shape is most clearly seen while observing the intensity of a C^- signal. Its transient region is between 0 and 80 s (surface contamination) and between 290 and 400 s (polymer surface). A steady state region is from 400 s on in a pure polymer and also between 80 and 240 s in an Al layer. The interfacial region is observed in the time interval between 240 and 290 s. There is also a maximum of the AlO_2^- signal on the sample surface below the contaminations caused by the aluminum passivation.

By combining the results of depth profiling and 2D imaging, 3D reconstructions of the sample can be created as well. In this case, pixels are replaced by voxels and both lateral and in-depth heterogeneity are shown simultaneously with lateral and depth resolutions being important for a representative measurement. Furthermore, surface roughness must be carefully considered because, without software alterations, the 3D representation will be shown as having a perfectly smooth surface. Protruding structures on the surface layer will be consequently presented as indentations and holes in the substrate, and vice versa. Despite these limitations, knowing them offers a very powerful method for a detailed 3D assessment of the sample structure and composition. [95] An example of a 3D representation is shown in Figure 8 as a distribution of Na in a perovskite solar cell. The cell was composed of layers of Cu (100 nm), SnO_2 (20 nm), C_{60} (23 nm), perovskite (600 nm), and indium tin oxide (120 nm) on top of the glass substrate. Na^+ ions travel from the underlying glass into the layers of the solar cell and sodium channels are formed during this process. [42]

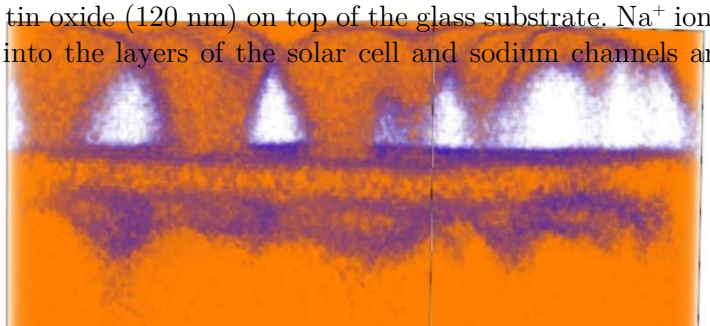

Figure 8: 3D distribution of the Na^+ ions inside a perovskite solar cell after prolonged operation under high voltage. Orange color represents the maximum and purple the minimum intensity of the Na^+. The surface of the cube is 100 μm × 100 μm and its thickness is approximately 1 μm.

1.2.4 Matrix effect and ionization yield

The negative aspect of the SIMS method is the extensive fragmentation of sputtered molecules which was to some degree improved with polyatomic and cluster ion beams. The UHV environment, required for the measurements, poses some limitations regarding the type of samples appropriate for the analysis but cannot be changed due to the physical background. However, the matrix effect and low ionization yield are two other problems that still need to be addressed.

The matrix effect is a direct consequence of a sample composition and is caused by the matrix in which the analyzed molecule is embedded. Some matrices enhance the formation of the positive ions by most commonly proton donation while others enhance negative ions formation. A typical example of an enhanced yield of the negative secondary ions is caused by the reduction of the work function which happens when Cs^+ ions become incorporated in the surface of the sample. [24], [59], [101] Another example of the matrix effect related to the presence of a specific element is connected to the differences in ionization yields between metals and metal oxides. The intensity of the positive monoatomic metal ion can be enhanced for up to three orders of magnitude when the metal cation originates from the metal oxide substrate compared to the pure metal. [24] There is also an effect of the analyzed molecule as some are good proton acceptors forming $[M + H]^+$ ions while others are much more easily ionized into anions as they have a highly electronegative nature. [24], [59], [101]–[103] Two quantities, related to the matrix effect, are ionization energy and electron affinity. First ionization energy E_i is defined as the minimum energy needed for the removal of a valence electron of a neutral atom in the gaseous phase. [104] It changes through the periodic table of elements as depicted in Figure 9. Elements with the smallest E_i will be most easily cationised and their signals in the positive SIMS spectrum the strongest. Electron affinity E_{ea} is defined as an energy released when an electron is attached to a neutral atom in the gaseous state. It is measured in a negative sign so elements that release the highest amount of energy will have the largest, most positive value of E_{ea}. Their

signals in the negative SIMS spectrum will be the most intense. [104] E_{ea} trend through the periodic table is shown in Figure 10.

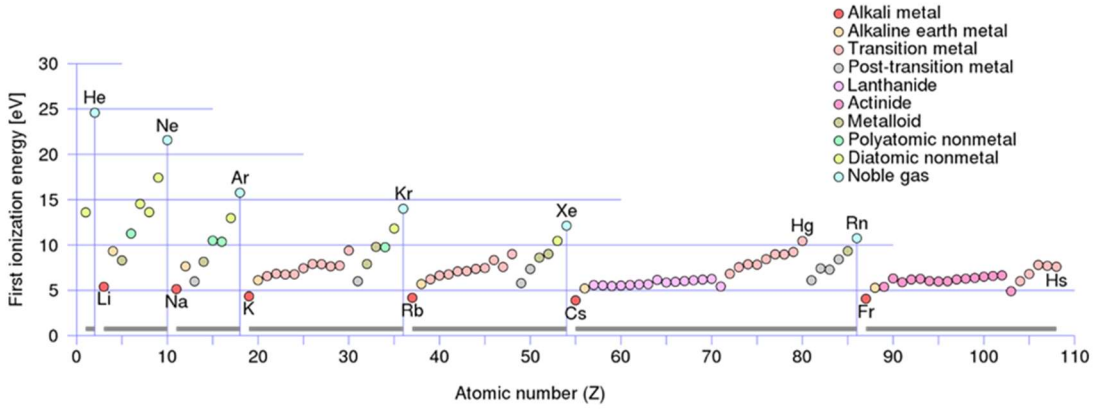

Figure 9: First ionization energies as a function of the atomic number. (Wikipedia, The Free Encyclopedia, https://en.wikipedia.org/wiki/Ionization_energy, 3rd January 2024).

The consequence of the described effects and their combination is a heavily influenced intensity of signals in SIMS spectra regarding the type of sample analyzed. The E_i and E_{ea} are not problematic per se because, without the substrate in which elements and molecules of interest are located, these physical quantities would remain constant and element-specific. However, changes in electronic properties caused by the surrounding compounds influence E_i and E_{ea} and, therefore, ionization probabilities. [101] The matrix can affect ionization so severely that the intensity of a chosen signal will differ for even a few orders of magnitude when comparing two very different samples with the same concentration of the analyte measured under the same conditions. The matrix effect also severely limits the quantitative capabilities of the SIMS technique. The only quantitative approach is comparing the concentration of the same analyte in the samples with a very similar chemical constitution, which means that standards cannot be used universally. [24], [59], [102], [103] Due to the preferential sputtering of generally lighter elements, the matrix effect can limit isotopic analyses as well, although differences caused by this phenomenon are significantly smaller than in the case of different ionization yields of the same material in different substrates. Nevertheless, the matrix effect can be also used to benefit the analysis, mostly via ionization yield enhancement. The most common example of such an approach is the MALDI technique. [101]

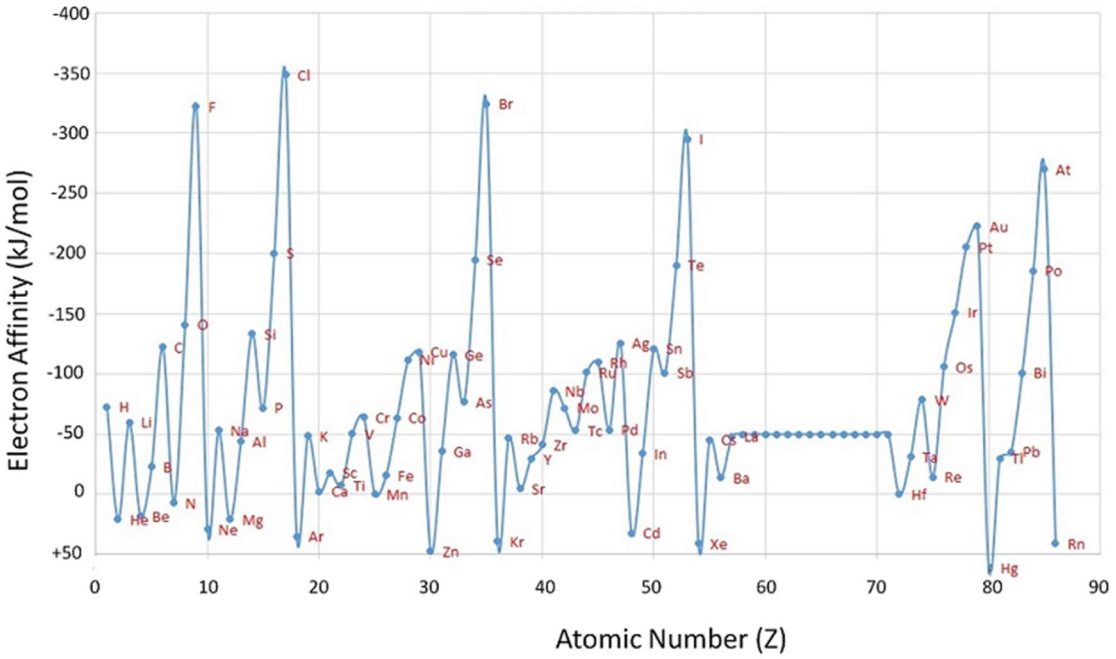

Figure 10: Electron affinities as a function of the atomic number. (University Pressbooks, https://university.pressbooks.pub/chemistryucf/chapter/8-8-electron-affinities-and-metallic-character-chemistry-libretexts/, 3rd January 2024).

Ionization yield is defined by the proportion of ionized particles in a gas phase after desorption from the surface concerning the number of all sputtered particles. Most of the sputtered particles remain neutral and they cannot be extracted by the electrostatic lenses. Sputter yields were significantly increased for organic and biological samples with the cluster primary ions but ionization yields remain under 10% of all sputtered material, some studies noting to be even under 0.1%. [105]–[107] With improved ionization yield, SIMS would become a more sensitive technique and lateral resolution could be improved as smaller areas would be acceptable producing large enough quantities of secondary ions for the analysis. [24], [59], [103] As the matrix effect and low ionization yields present such a limitation, different approaches were developed to improve the outcome. Most common are laser and electron post-ionization of sputtered neutrals, matrix-enhanced and metal-assisted SIMS, gas flooding, analysis of cluster secondary ions, and dynamic reactive ionization.

1.2.4.1 Sputtering process and ionization models

Although considering sputtering and ionization as two separate processes described by different time frames simplifies models used for their explanation, it is not fully correct as they are generally coupled. The reason for this is the efficiency of ionization taking place on the surface or slightly above it, approximately at a distance of 10 nm. The density of particles anywhere in this area is high enough for successful electron transfer. On the other hand, when particles are further from the surface, UHV conditions significantly limit processes that can take place. Two phenomena, that can still happen, are the dissociation of an already ionized molecule and the emission of an electron via a process, such as a combination of core electron hole and Auger emission. [58], [62], [108]

Already the sputtering itself can happen via different routes. Atomic secondary ions are considered to be emitted by the knock-on sputtering by the primary ion inducing the (linear) collision cascade. This process, referred to as kinetic sputtering, can result in the formation of new molecules on the surface, but molecular secondary ions are very rarely

emitted in this way. Their formation can be described with the overlap of the collision cascades that create a wave-like motion. Whole molecules are desorbed if enough energy is present during this process. Since sputtering is a highly energetic process, a significant increase in temperature occurs in the area hit by the primary ion beam and one of the consequences is also electronic excitation. This type of sputtering is consequently regarded as kinetically assisted potential sputtering or heat/thermal spike sputtering. Finally, potential sputtering is the least common as it does not include any momentum transfer. It is a high-energy phenomenon connected with different inelastic processes that occur when a primary ion comes in very close proximity to the surface. Potential sputtering is accompanied by electron excitations and results only in atomic emission. [57], [108] Electron excitations, as the most pronounced type of inelastic process, were extensively studied and found to be responsible for ionization in some specific cases. Mechanisms of the electronic excitations were further divided into core-level and valence-level excitations as well as plasmon formation in the case of Ag. [58]

The ionization process is affected by the different properties of the samples and it is significantly different for the atomic and molecular secondary ions. As already described, ionization energy and electron affinity crucially determine the probability of ionization. Another important factor is the work function and with it connected Fermi level as well as the mass and speed of the sputtered particle. [58], [62] When ions interact with the surface of the sample, charge can be transferred via different mechanisms. The most common one is resonant charge transfer which happens when electron tunnels between electronic states of the same energy present in the atom/ion on the surface and atom/ion in its close vicinity. Valence electrons are included in the charge transfer and for the process to occur, the particles need to be in a distance of less than 1 nm. Quasi-resonant charge transfer is similar but core electrons are included in this case. This process is much less common because core holes are energetically unfavorable and core electrons require even closer proximity of the particles. Auger electron transfer is a mix of both processes as valence electron fills the core hole in this case. [58]

Different models of ionization were developed for both atomic and molecular secondary ions. Four major models were widely accepted in the case of monoatomic ionization while some others, less recognized ones, exist as well. The local thermal equilibrium model describes the ionization of metals, alloys, and oxides as a consequence of the plasma formation during a sputtering event. E_i, E_{ea}, and work function are included in its description. The bond-breaking model was developed to describe the ionization of ionic solids. It applies resonant charge transfer between ions to explain the ionization process and is also connected with the E_i and E_{ea} of ionized species. The Electron tunneling model similarly applies resonant charge transfer but it is used to describe the ionization of conductors and semiconductors. Finally, the kinetic emission model is used to describe the formation of multiply charged ions and atomic ions of elements lighter than phosphorus. This model applies the mechanism of core holes and subsequent Auger electron emission, that is ion-induced Auger electrons. Only light elements can be ionized in this way because they are fast enough to travel a sufficient distance from the surface before other electron transfer processes (including neutralization) that occur when desorbed ions are in close proximity to the solid. [58]

In the case of molecular secondary ions, mechanisms are even more complicated to explain. However, they are important as not only molecular ion formation but also recombination processes can be explained in this way. [58], [108] Amongst different models developed, probably the most widely applicable is the pre-cursor model. It describes the emission of molecular ions at the edges of the crater formed by the impact of the primary ion while molecules directly hit by the primary ion experience fragmentation. The selvedge model is based on the formation of the diffuse boundary between the solid and the gas

phases where ionization takes place. The nascent emission model predicts the formation of molecular ions just after they are desorbed from the surface by dissociation. The desorption/ionization model is based on vibrational excitation. The gas flow model is similar to the selvedge concept but is only applicable to frozen surfaces. [24], [58] When considering molecular secondary ions, cationization is another important aspect that needs to be addressed. Cations can form when molecules bind with the positive metallic ions ($M + Me^+$), the most common being alkali metals but also Cu, Ag, and Au. The simplest cationization process is protonation, the formation of $(M + H)^+$ molecular cation. However, deprotonation can occur as well and molecular anion $(M - H)^-$ is formed in this way. Loss of different functional groups can also cause formation of molecular cations and anions while formation of M^+ and M^- molecular ions is mostly connected with the presence of pre-charged centers in the molecule. [102]

1.2.4.2 Post-ionization of neutrals in SNMS

The abbreviation SNMS stands for secondary neutral mass spectrometry. As more than 90% of the sputtered material is in the form of neutral particles, ionization yield would be significantly increased if we were able to ionize them. This is possible using a laser or an electron beam. Different types of lasers are applied, most commonly divided into resonant and non-resonant laser SNMS. In the non-resonant SNMS intense lasers with high energy, typically ArF excimer with a wavelength of 193 nm, are used. They nonselectively ionize all of the molecules and elements with a low enough ionization energy. To achieve a high enough power density, they need to be focused at the point of ionization as shown in Figure 11. On the other hand, resonant lasers ionize only species with excitation states in resonance with the laser energy. We can therefore eliminate isobaric interferences from the mass spectra as only targeted species, determined by the laser wavelength, will get ionized. [109]–[112]

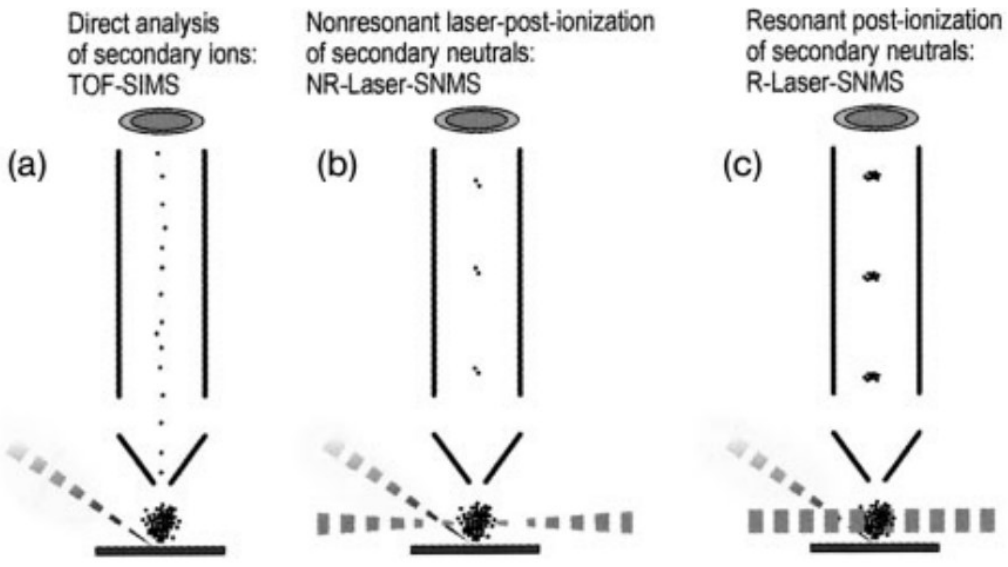

Figure 11: Schematic representation of the ionization approach in (a) SIMS, (b) non-resonant laser SNMS, and (c) resonant laser SNMS. (H. F. Arlinghaus: Surface and Thin Film Analysis: A Compendium of Principles, Instrumentation, and Applications, Second Edition. Wiley, 2011. pp. 179–189).

Resonant post-ionization was applied in the study of a uranium and plutonium sample. Using SIMS, uranium and plutonium signals were severely altered by the background caused by the other species. There is also an overlap of ^{238}U and ^{238}Pu signals. Using resonant laser frequencies specific for each element, these interferences were removed and the analysis greatly improved as can be seen in Figure 12. [113] This phenomenon has its drawbacks as only one element or only one type of molecule can be ionized and therefore analyzed at the same time. Resonant laser SNMS also has a much greater ionization efficiency than the non-resonant approach and the laser beam consequently does not need to be focused on a single point in space (Figure 11). This is the consequence of every photon transfer leading to another excited state until ionization is achieved. Contrary, when applying non-resonant post-ionization, multiple photon transition takes place without intermediate states leading to a much smaller ionization cross-section. Multi photon transition can only be avoided if ionization can be achieved with the single photon absorption, that is if the ionization potential is low enough and/or photon energy high enough. The most commonly used sources for resonant post-ionization are Nd:YAG lasers with the working wavelengths in the UV, visible, and IR fields. [109], [111]

Ionization taking place in the gas phase does not only improve ionization yield but also eliminates the matrix effect as the latter is not present if the matrix is non-existent, that is, a vacuum. To successfully achieve potential quantitative analysis, two conditions must be met. Firstly, all secondary ions formed by the impacts of the primary ions must be eliminated. This is usually done by the application of an electric field that retards secondary ions during a primary ion beam pulse. [111] The other requirement is the saturation of an ionization process. Different molecules have different ionization potentials and, therefore, some are more easily ionized than others. If the laser power is not high enough, only specific compounds will be ionized completely. Therefore, ionization saturation is needed if we want to conduct any type of quantitative analysis. Otherwise, we only substitute the matrix effect with the discrimination based on an ionization potential. The effect of the ionization saturation must be most carefully considered in the case of non-resonant laser SNMS as all compounds need to be ionized and the ionization cross-section is small. A large number of particles and low ionization yields pose additional challenges in this case. [109]–[111]

A focused laser beam leads us to the first major drawback of the laser SNMS approach. Material is sputtered in different directions and only part of it ends in the volume where the laser beam is focused. We are, therefore, far away from ionizing all of the sputtered neutrals. [105], [109], [110] It was estimated that ionization yield is two orders of magnitude greater for laser SNMS than for SIMS. This approximation was done while summarizing spectra recorded in the consecutive experiments over the whole volume of sputtered material correctly representing ionization probability but not the actual number of ionized molecules being limited by the ionization volume. Dimensions of the plum of gaseous sputtered neutrals can be reduced by lowering the sample temperature. [105] Besides volume focusing problems, particles are sputtered away from the surface with different velocities, smaller particles being faster. Applying the laser beam pulse at a certain time after the primary ion pulse can therefore discriminate either against smaller or larger particles. This problem can be solved by the application of a continuous primary ion beam to some degree but such an approach requires pulsed secondary ions if a ToF analyzer is used. [109], [110] Instruments built in this way are more complex than conventional SIMS instruments leading to the more complicated computer control of all the parameters and, of course, a higher price.

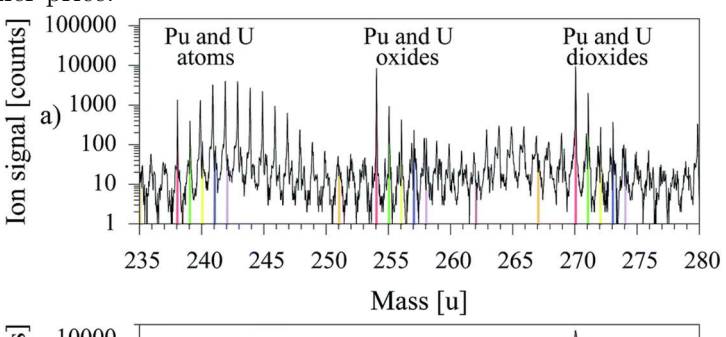

Figure 12: Mass spectra recorded with (a) conventional SIMS, (b) laser SNMS with a resonant ionization of U, and (c) laser SNMS with a resonant ionization of Pu. (M. Franzmann et al.: Resonant Laser–SNMS for Spatially Resolved and Element Selective Ultra-Trace Analysis of Radionuclides. *J. Anal. At. Spectrom.* **2018**).

Another problem is the repetition rate of laser pulses. Although newer lasers were improved, they still have much slower repetition frequency than ion guns. Therefore, fewer cycles can be conducted in a second, making the analysis process for the same factor longer. The intensity, energy, and duration of a laser beam pulse also affect the fragmentation accompanying ionization. We can minimize fragmentation with extremely short, femtosecond pulses of low intensity. But lowering these values too much will lead to unsaturated ionization and consequently a selective and incomplete post-ionization process. The fragmentation problem is the most prominent with a non-resonant ionization process as intensities are high and wavelengths low. However, with the laser post-ionization, we can improve spatial resolution as the percentage of ionized sputtered material is higher and, therefore, the sputtered area can be smaller. But combined ion and laser pulses last longer and consequent time extension causes reduced mass resolution as can be seen in Figure 12 when comparing spectra recorded with the SIMS and laser SNMS methods. [109]–[111]

Although resonant laser post-ionization avoids some of the problems connected with the non-resonant one, such as low ionization cross-section, severe fragmentation, and highly focused laser beam, it still has one major drawback. As resonant energy is acquired, we also need to choose the corresponding laser wavelength and we, therefore, analyze only selected species. Such an approach is only appropriate for the analysis of samples with a known composition as we otherwise cannot know the appropriate laser wavelength. [109]

However, issues related to light-induced ionization can be avoided if photons are substituted with electrons. Secondary neutrals are bombarded with electrons in an ionization cage, essentially making this electron ionization mass spectrometry. Even if problems with ionization cross-sections are avoided, it is still necessary to discriminate against secondary ions and also residual gases. [112], [114]–[117] Since electron bombardments ionize unselectively, it was shown that electron post-ionization SNMS can be used for quantitative analysis. EI post-ionization is also suited for a DC ion beam and instruments made were consequently equipped with the quadrupole analyzers. It would be also possible to use magnetic sectors but much more difficult to implement this type of post-ionization in the ToF-SIMS instrument. [112], [114] Finally, it should be mentioned that post-ionization was also achieved with high-frequency plasma. Since it worked by a principle of ionization inside an electron gas, it can be still considered electron-based post-ionization. [112]

1.2.4.3 Matrix-enhanced and metal-assisted SIMS

The matrix effect can be favorable if it enhances the ionization of species we are interested in. One of the first attempts in this direction was closely mimicking the approach used in MALDI spectrometry where a laser is used for desorption and ionization of the analyzed material. The analyte was dissolved with the matrix being the same as substances used in the MALDI technique and then co-crystalized together. The most effective matrix was 2,5-dihydroxybenzoic acid. Compounds of interest with masses of up to 10 kDa were successfully analyzed making such an approach suitable for the analyses of proteins, nucleic acids, and synthetic polymers. Signal intensities of a positive molecular ion measured with the matrix-enhanced SIMS were up to three orders of magnitude greater than in the case of conventional SIMS. [118] A similar study reports an 8-fold increase in the negative molecular ion intensity while applying sinapinic acid as a matrix. On the other hand, the intensity of CN^- ions resulting from the analyte fragmentation dropped with the increasing amount of sinapinic acid. [119] With analytes being dissolved, this approach is no longer surface sensitive posing a great disadvantage compared to the conventional SIMS. Ionic liquids based on the α-cyano-4-hydroxycinnamic acid, another MALDI matrix compound, were applied as ionization enhancements for the SIMS imaging. Samples were coated with the ionic liquids and then analyzed. Micrographs with the correlated ions showing increased intensity on the coated areas were recorded while these ions were undetected using conventional SIMS imaging. [120] As such, matrix-enhanced SIMS can be also used as a surface-sensitive technique but it remains out of the scope of depth profiling.

As with ionic liquids, samples can be also covered with a thin, at most a few nm thick film of metals. The most commonly used are silver and gold, the latter showing greater enhancement for both positive and negative secondary ion yields. [102], [121]–[124] Different samples can be analyzed in such a way, notable being polymers [121], [123] and small molecules inside biological materials [122]. The positive sides of metal-assisted SIMS are reduced fragmentation as the sample is protected by the metal film and suppressed background noise [122]. Unfortunately, metal coating is effective only in specific cases as it can lead to the signal intensity fall as well. Besides this, enhancement in the signal intensity compared to the conventional SIMS is not as prominent as with the application of matrices ranging from statistically insignificant to 3 or 4-fold at its best. [121], [122] Enhanced secondary ions can be both molecular (M^+) or clusters of these molecules and metal used for the sample coverage ($M + Me^+$). [102] The type of the primary ions is also important as it was shown that signal intensity increases when Bi^+ [121], Ga^+ [123], and C_{60}^+ [122] primary ions are used while it decreases when the sample is targeted with the Au_{400}^{4+} ions [121]. The reason behind the intensity drop for Au_{400}^{4+} ions is metal deposition from the

large gold clusters forming a thick metal film over already deposited Au or Ag and making the surface therefore inaccessible for the analysis. It was also found that for polymers better results and greater signal intensities are achieved when targeting unmodified samples with Au_{400}^{4+} primary ions than for Ag or Au-coated samples bombarded with the Bi^+ ions. [121] On the other hand, an important improvement compared to the matrix-enhanced SIMS is the possibility of depth profiling. A specific approach was developed for the metal-assisted SIMS changing conventional etching with so-called 'shave-off sectioning'. [123]

Greater enhancements of the secondary ion yields can be observed if instead of depositing thin layers of Ag or Au on the sample surface, a thin layer of analyte is dissolved and deposited on the Ag or Au foil. [102] Besides deposition on the top of the metal foil, there is also an option of adding alkali metal salts to the solution of the analyte. After co-crystallization, a solid sample is analyzed and ionization yields are enhanced by the detection of cluster secondary ions composed of analyte molecule and alkali metals (M + $alkali^+$). As with matrix co-crystallization, both of these approaches are not suitable for the analysis of the sample surface since the analyte needs to be dissolved. [102], [125]

1.2.4.4 Gas flooding and co-sputtering

The main idea behind gas flooding is related to the adsorption of gas molecules to the sample surface which modify the initial matrix effect. A monolayer of adsorbed molecules presents a universal matrix, which is the same regardless of the type of the sample, and, therefore, an initial matrix effect of the substrate is reduced. [126]–[129] The most commonly used gas is O_2. [126], [127] Noble gases are frequently used as well but since they are inert, they do not influence the matrix effect. They are mainly flooded to reduce surface charging during the analyses of insulating samples. [130] However, yields of secondary ions can be enhanced with different gases. For example, a successful study was performed with the H_2O and fluorine (via XeF_2) flooding. [129]

Although O_2 flooding generally improves ionization yields of the positive secondary ions, there are also reports about the decreased work function of the materials analyzed in the O_2 atmosphere. An example is a Si sample for which an increase in the yields of some negative secondary ions (B^-, P^-, As^-, Sb^-) originating from the dopants was observed while the intensity of the Si^- signal from the Si substrate decreased. [126] This can be explained by the different affinities of different elements to preferentially form either positive or negative ions. It was found that the decrease in a work function is the greatest at the specific O_2 pressure. The work function increases again when the pressure is further elevated. [126] Similar observations, but in this case for positive secondary ions, were found in the case of analyses of implanted noble gases in different samples. The most notable changes were observed at the particular O_2 pressures but signal intensities were in some cases increased and in others decreased. [127] Another notable impact of the gas flooding, unrelated to the matrix effect, is a decreased surface roughening. An O_2 flooding accompanying depth profiling of a silicon sample with 1 keV O_2^+ primary ions caused reduced surface roughening in comparison to the analysis in the UHV. O_2 flooding results in the formation of a thicker and more uniform layer of SiO_2, causing a decreased formation of unwanted surface topography. [128]

Low energy (0.25 – 2 keV) Cs^+ ion beam is used for the sample etching in a depth profile analysis but it simultaneously implants cesium ions into the sample creating a partial Cs matrix. The consequence is a formation of MCs_n^+ secondary ions, M being a metal, which are less sensitive to the matrix effect than pure M^+ ions. [131], [132] The lower the energy of the beam, the greater the amount of implanted Cs^+ ions. The consequence is a decrease in signal intensity of the positive analyte ions while the intensity of the adducts with cesium increases. When the Cs surface concentration becomes too high,

however, yields of the MCs_n^+ cluster ions decrease. To prevent this, the primary ion beam can be diluted with another type of ions, generally originating from noble gases. An example of such an approach is Cs/Xe co-sputtering. [132], [133] Adducts signal intensity has a maximum for Cs^+ beam concentration in the Cs/Xe mixture between 5 % (250 eV) and 25 % (2 keV), therefore shifting towards higher Cs/Xe mixtures with their increasing energy. The intensity of all the ions of interest, both of pure analyte and its adducts with Cs is greater when using a Cs/Xe ion beam with higher energy. [132], [133]

1.2.4.5 Dynamic reactive ionization by the proton transfer

A novel and innovative approach is the application of dynamic reactive ionization (DRI). It utilizes argon cluster primary ions (Ar_n^+, n = 1000 – 10 000) with O_2, CO_2, CH_4 or similar small gas molecules doped into the clusters. Recently, HCl was tested as it is a good proton donor and can therefore increase the percentage of protonated molecules of the analyte. [134] The formation of Ar clusters themselves under different conditions is depicted in Figure 13. HCl itself, however, was shown to be unable to increase protonation efficiency so the sample surface was coated with water in the form of ice. In the other approach, water vapor was leaked into the analysis chamber through the leak valve while the sample was being cooled. As protolysis between HCl and H_2O (or D_2O) molecules is exothermic and protons become more readily accessible. [134] It was shown that up to 10 or even 20-fold increase in the protonated molecules can be achieved using HCl-doped Ar clusters combined with the water flooding or ice film on the sample surface. [134], [135] Similar increase in ionization can be also seen when water clusters $(H_2O)_n^+$ (n = 1000 – 10 000) are used for the sputtering instead of the Ar ones. It was discovered that Ar cluster sputtering indeed causes low damage but also a low ionization yield. In many cases, it is in a range of ionization yields achieved with the monoatomic metal primary ions. By utilizing DRI via Ar clusters doped with HCl accompanied by the H_2O flooding, the ionization yield becomes similar or even notably better than the ionization yield of C_{60}^+ ion sputtering. [134], [136]

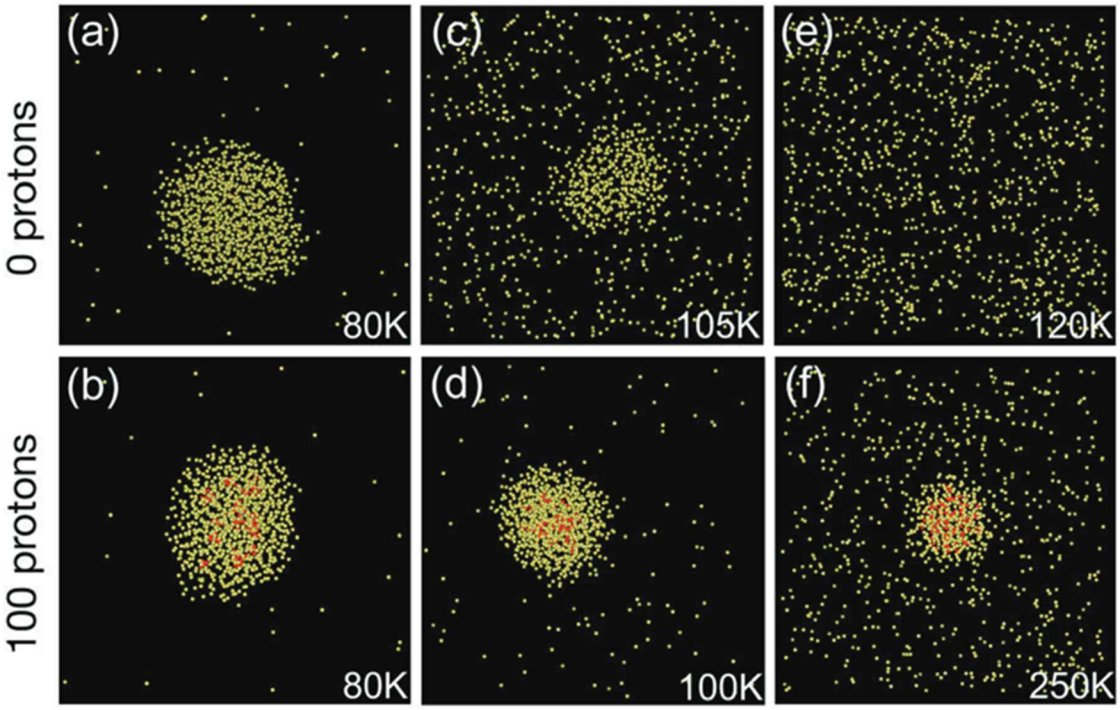

Figure 13: Theoretical modeling of the formation of Ar clusters with and without proton seeding at different temperatures. Yellow particles are Ar atoms and red particles are

protons. (O. C. F. Brown et al.: Formation of argon cluster with proton seeding. *Mol. Phys.* **2020**).

DRI was shown to be effective not only for the ionization yield increase but also for the reduction of the matrix effect when depth profiling Irganox multilayer films composed of two types of this polymer. Depth profiling using C_{60}^+ primary ions, Ar clusters, and Ar clusters doped with HCl without H_2O flooding led to the profiles of positive secondary ions without any information about the sequence and thickness of the layers. When applying DRI sputtering with the use of Ar clusters doped with HCl accompanied by the H_2O flooding, protonated molecular signals not only greatly increased in intensity but also multilayer structure was completely resolved. A larger increase in protonated ion intensity was observed for the Irganox type whose signals were without DRI suppressed in comparison with the other polymer. Therefore, the DRI approach led to the closer similarity in molecular ion intensities of both polymers, showing that the matrix effect was reduced. Finally, it is worth mentioning that the matrix effect was much less prominent when negative secondary ions were analyzed, regardless of the primary ion type. Such findings show promising possibilities in the direction of the SIMS analyses of negative secondary ions. [136]

As water is needed for a successful ionization via proton transfer, frozen biological samples are very suitable for the DRI analysis. An example of a successful study in this field is the imaging of lipids concentration in sliced tissue samples as these molecules are easily protonated. It was found that regardless of the already present water inside a biological tissue, an additional ice layer over the sample enhances the DRI effect even further. [135] Worth noting is an observation that only protonated ions intensity is increased with the DRI approach while the intensity of the adducts with metal cations remains unaltered or even shows a decrease. [134], [135]

1.2.4.6 Other approaches for matrix effect reduction

Another way of considering the matrix effect is data post-processing using different computational models. Such a computational approach is also the MRI modeling used to simulate the SIMS depth profiles of multilayered systems. [137], [138] An example of a successful application of the MRI model can be seen in the case of the Ag/Ni multilayered sample where the enhanced ionization of metal atoms due to the oxygen present at the interfaces was suppressed during postprocessing. [137]

There are also other computational models but they are in general time-consuming and require prior knowledge about the sample. Firstly, analysis of samples with a known composition, chemically as similar as possible to the one we are interested in, has to be done. Besides this, different signals corresponding to the analyzed molecule must be included in the model as it was shown that the matrix effect can act in a way of changing signal intensity ratios between different fragments from the same molecule with its changing concentration. [139]

There is also an approach for quantification of chemical composition using the relative sensitivity factors (RSF). This technique is much simpler than the computational methods and is more often applied. The RSF method requires all of the samples to contain a common element or compound, a type of internal standard. The concentration of the analyte is calculated via Equation 2 where c represents the atomic or molar concentration, I the intensity of the secondary ion signal, and the subscripts i and r are the analyte of interest and the internal reference, respectively. However, the main drawback of the RSF method is its applicability only for chemically very similar samples. Not only an internal standard

is needed but it also should be analyzed in the reference sample with a composition as similar as possible to the sample with the unknown composition. [140]–[143]

$$c_i \,/\, c_r = RSF\ (I_i \,/\, I_r) \tag{2}$$

As extensive fragmentation is characteristic of the SIMS method, most of the detected secondary ions are low-mass species. These are not of great interest as they are not characteristic of the analyzed molecule but rather common for many different species. Therefore, improved ionization yield of the higher mass fragments and molecular ions is desirable. It can be achieved utilizing polyatomic and cluster primary ions. The reason behind their suitability is the lower chemical damage they cause, but not an enhancement of ionization itself. The latter can be achieved with the application of reactive clusters made of O_2, SF_6, or H_2O molecules. [106] More surprisingly, an even greater yield of unfragmented molecular ions is achieved using MeV-SIMS. A different sputtering mechanism occurring during the bombardment of the sample with the primary ions with the energy of a few MeV is the most probable reason for this phenomenon. Any kind of fragmentation in the MeV-SIMS is poorly presented and signals in the low-mass end of the spectra are much less prominent. [81], [84], [85], [144]

1.2.5 Development of surface roughness due to ion sputtering

The chemical composition of multilayered structures and thin films can be characterized by SIMS depth profiling where extensive ion sputtering takes place. Depth resolution is an important parameter that needs to be considered during depth profiling. It is most commonly defined as the depth interval over which the signal intensity rises from 16% to 84% or drops for the same value when crossing an interface between two layers. It depends on the surface roughness, atom mixing due to ion bombardment, and information depth of analyses. Atom mixing and information depth are connected with the analytical method and are mainly defined by the energy and incident angle of the primary ion beam. In the case of SIMS, we can achieve a depth resolution of even less than 1 nm when optimally prepared samples are analyzed. On the other hand, surface roughness is influenced by different factors. It develops during ion sputtering as well but it is primarily connected with the sample preparation. [66] When very rough samples are analyzed, depth resolution can be more than 100 nm with the interface widened so much, that in some cases it cannot be unambiguously defined. With so bad depth resolution, differentiation between consecutive layers can become difficult or even impossible. Reduced sharpness of the interfaces and their potential disappearance can also occur if prolonged ion sputtering causes extensive surface roughening and particle redistribution so that layers of different compositions become mixed and indistinguishable by the SIMS analyses. This process can be described by the MRI model. [66]

During depth profiling, surface roughness increases with the prolonged sputtering time. Development of the roughness depends also on the energy of the primary ion beam and the sputter ion beam. Primary ions with high energy can penetrate deeper into the sample, causing more particle rearrangements and damage, and consequently more sputter-induced topographical changes than low-energy primary ions. [69], [145]–[147] Incident angle under which primary ions are bombarding the sample is important as well. It was shown that less surface roughening is observed if the primary ion beam is directed to the sample under grazing angles, that is, large incident angles with respect to the surface normal. [148]–[150] However, these conditions can further promote the formation of different topographical structures, such as ripples, ridges, valleys, cones, and pyramids. [145], [151], [152] To avoid

their formation, sample rotation can be applied. Sample rotation was developed by Anton Zalar at Jožef Stefan Institute, and it is regularly used in XPS, AES, and SIMS depth profiling of thin films to improve depth resolution. [153], [154] In the cases of the organic and biological materials, the application of polyatomic and cluster primary ions instead of monoatomic ones appeared beneficial for the quality of the depth profiles as well. [79], [90], [155] For such samples, surface roughening was also reduced if samples were cooled. [151], [156], [157] Finally, reduced surface roughening was observed if samples were analyzed in the O_2 atmosphere. These observations were attributed to the formation of the oxides on the sputtered surface. [128], [158]

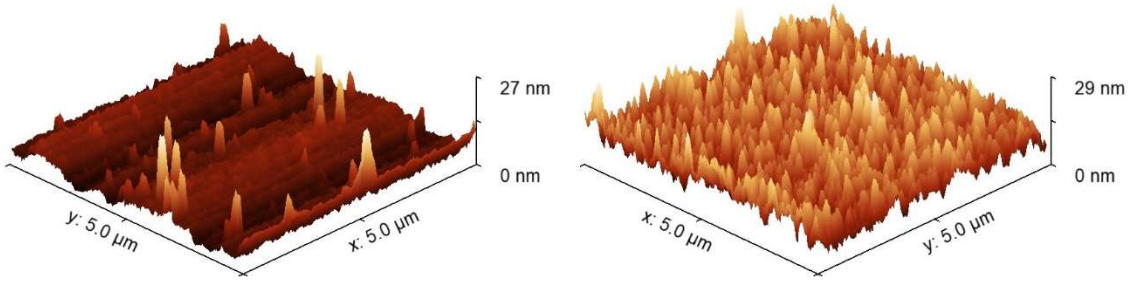

Figure 14: 3D representation of the surface roughness of the metallic sample measured before (left) and after ion sputtering (right).

Surface roughness is commonly measured with the AFM microscope. [159], [160] Roughness measured in this way can be expressed with different parameters. The most commonly used descriptions are S_a and S_q. The roughness average S_a is defined as the mean of the positive and negative absolute deviations of the height in each point from the mean plane within the analyzed area. The root mean square (RMS) roughness S_q, on the other hand, is obtained by taking the square root of the mean of the squares of all heights measured over the analyzed area. There are also some other parameters, for example, surface skewness (S_{sk}) defined as the asymmetry of the height measurements from the mean plane of the analyzed area but they are used only in special cases and for specific purposes. [161] An example of the 3D representation of the surface morphology on metallic sample with different roughness is shown in Figure 14.

Chapter 2

Instrumentation Used in Experimental Work

The SIMS analyses were performed with a ToF SIMS spectrometer, model TOF.SIMS 5, produced by ION TOF, Münster, Germany shown in Figure 15. The spectrometer is used to measure the mass spectra at the surface, depth profiles of thin films and layers with a thickness of up to approximately 1 μm, and to acquire two and three-dimensional mappings.

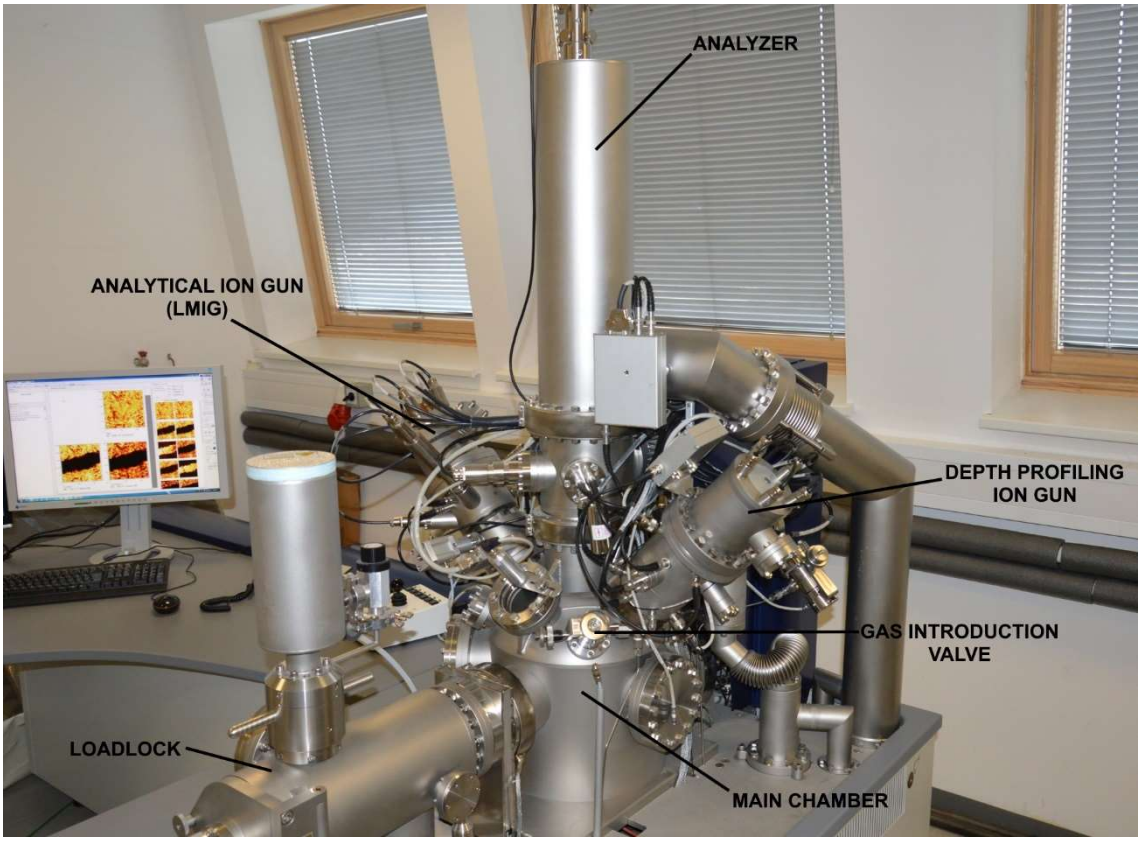

Figure 15: The TOF.SIMS 5 instrument. The main components are identified and assigned.

The instrument is equipped with two ion guns used for dual-beam depth profiling, a time-of-flight (ToF) analyzer with a reflectron, a microchannel plate (MCP) detector, a low-energy electron gun, a detector of the secondary electrons, a gas introduction system, a movable, rotatable and tilting stage for the sample holder, two video cameras with and without magnification and pre-chamber for fast introduction of the samples (loadlock). The system is pumped with six turbomolecular pumps, one for each component (main chamber, loadlock, both ion guns and analyzer) and one turbomolecular pump pumping all five of them. Between the last turbomolecular pump and the atmosphere pressure is a fore-pump. The main/analytical chamber is additionally equipped with a titanium sublimation pump. With such a pumping system, the lowest pressure achievable in the main chamber is in the range of 10^{-11} mbar. The instrument also offers the possibilities of sample rotation during the analysis, sample heating, and sample cooling. The latter is done with the liquid N_2 via contact through the cold finger.

Analytical ion gun provides a beam for analyses consisting of Bi primary ions originating from a BiMn liquid metal source (LMIG) and formed by field ionization. This type of ionization produces a small spot and bright ion beam similarly as this is done with the FEG emitter in the electron microscopy. [86] Primary ions accelerated with the potential of 30 kV can be selected between Bi^+, Bi_3^+, and Bi_3^{2+}. Therefore, they have an energy of 30 keV for single-charged ions and 60 keV for double-charged ones. The SIMS spectrometer can operate either in a high-mass resolution mode or in a high-lateral resolution mode. When high mass resolution is required, a Bi ion beam is pulsed with a pulse length of approximately 5 ns. However, lateral resolution in this case is approximately 5 μm. In the case of imaging, when high-lateral resolution is required, the pulse length is prolonged to 100 ns resulting in nominal mass resolution. However, the lateral resolution of less than 100 nm. The average ion current of Bi^+ ions in high mass resolution mode is approximately 1 pA while in the high lateral resolution, it is approximately 0.2 pA. An ion gun used for ion sputtering for crater etching during depth profiling utilizes ions of Cs, O_2, and noble gases. Cs^+ is ionized in a surface ionization source while O_2^+ and cations of noble gases are ionized in the electron impact source that operates via electron bombardment. [86] The energy of the sputtering ions is between 0.5 and 2 keV while in the case of Cs^+, 250 eV is also an option. Ion currents are in the range from approximately 30 to 700 nA with the higher currents achieved at the higher accelerating voltages.

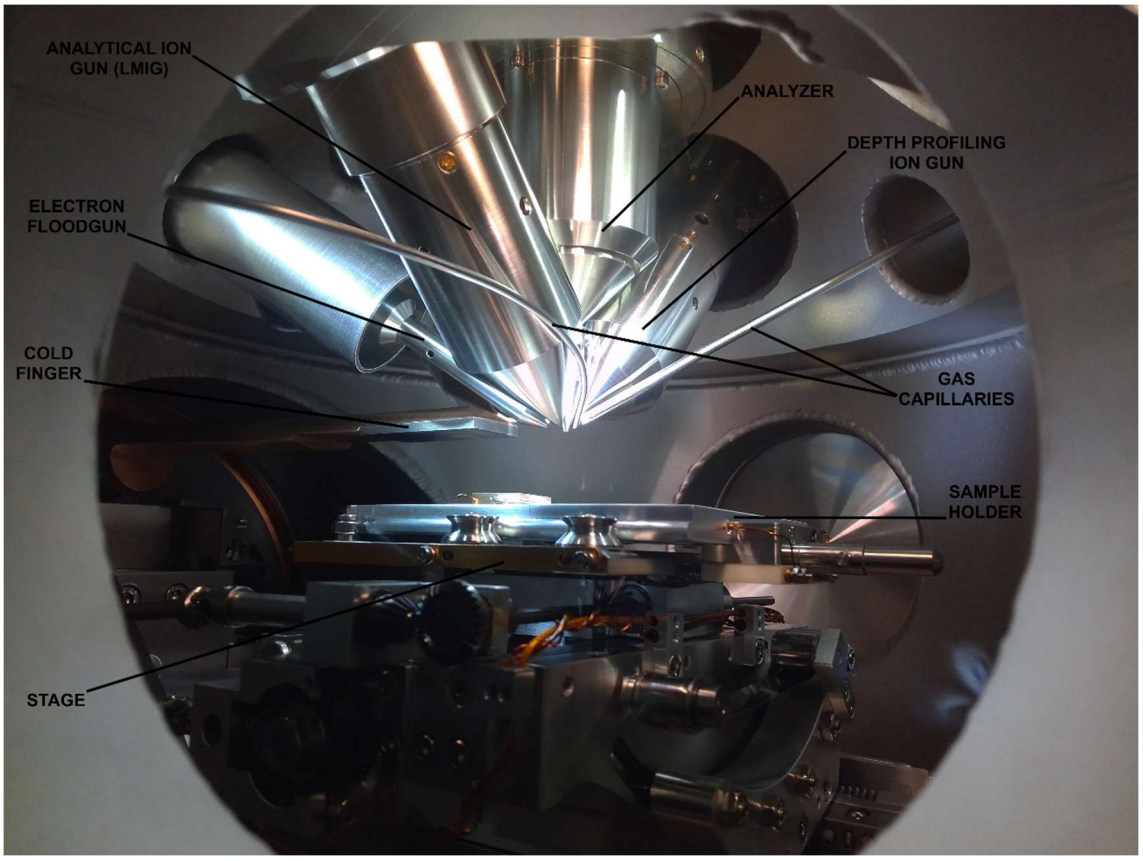

Figure 16: The internal parts of the modified TOF.SIMS 5 spectrometer. Nozzles, gas capillaries, cold finger, stage, and sample holder are identified and assigned.

Positive and negative secondary ions are analyzed in a single ToF analyzer with a reflectron. The sample holder is kept at the ground potential while the extraction optics of the analyzer have a potential of +2000 V for secondary anions and -2000 V for secondary cations. In the case of non-conductive samples, transmission, and mass resolution can be further improved by applying a bias to the sample holder with the maximal values of +/- 500 V. However, the surface charging is primarily reduced by the application of the low-energy electron gun. During depth profiling of nonconductive samples, we can choose the time gap between the sputtering cycle and the analysis cycles during which the electron gun is turned on and neutralization of the surface charge takes place. Mass resolution $m/\Delta m$ between 5,000 and 10,000 can be generally achieved in high mass resolution mode when the above-mentioned measures are considered. However, with the specialized settings targeting only the highest mass resolution possible, $m/\Delta m$ can exceed 15,000. In the high lateral resolution mode, the mass resolution is only a few hundred. Two-dimensional micrographs can be acquired with up to 2,048 $\times$ 2,048 pixels. The mass range m/z achievable with this analyzer is between 0 and 15,000 Da.

For the purpose of this thesis, the standard configuration of this instrument was modified. For the application of gas flooding, the instrument was equipped with additional leak valves for precise gas dosing and piping. The gases used during analyses are introduced into the analysis chamber in close vicinity to the analyzed region at a distance of less than 1 cm with the help of capillary. The reason for this is the optimization of the gas flow directly affecting the sample at the smallest possible contamination of the instrument. The internal parts of the SIMS spectrometer after modification together with two separate gas inlet capillaries are shown in Figure 16. The introduction of the gas is controlled with a precise gas leak valve type UDV 040 or UDV 140 produced by Pfeiffer Vacuum Company. A Swagelok-type installation is used to connect the gas leak valve and the gas bottle.

Chapter 3

Motivations and Hypotheses

The purpose of the dissertation is the optimization of the ToF-SIMS quantification and depth profiling of thin films and multilayers in terms of reduction of matrix effect and reduction of surface roughening. Due to the matrix effect combined with the different ionization probability of different metals, the identification of different layers in the multilayer structures composed of metals, metal oxides, and alloys can be very problematic. Even more problematic is the quantification of the chemical composition of alloys again caused by the matrix effect that significantly influences the ionization yield. In the field of depth profiling, there are also problems with the determination of the position of the interfaces, which can be caused by both the matrix effect and the reduction of the depth resolution. The depth resolution decreases because of the surface roughening and atomic mixing, both caused by the ion bombardment. Such physical and chemical phenomena pose limitations in the field of ToF-SIMS depth profiling, both as an analysis tool with a limited interpretation of the results and as a time-consuming process since often, multiple profiles are needed for the unambiguous analysis of the results. Similarly, quantitative analysis is possible only when standardized reference samples with compositions very similar to that of the analyzed sample are available. Reduction or even elimination of listed limitations would greatly improve the quantitative capability, applicability, usefulness, and efficiency of the ToF-SIMS method combined with depth profiling.

We followed these goals with the help of reactive gases, such as H_2, C_2H_2, CO, and O_2, which were introduced into the SIMS analytical chamber during the depth profiling process or quantitative measurements. These gases were used to improve ToF-SIMS depth profiling of multilayered structures and thin films, reduce matrix effect and surface roughening, improve ionization yields, and optimize quantitative aspects of the SIMS method. Our hypotheses, which were mostly confirmed, were established based on these ideas.

1. Reactive gases will adsorb to the surface of the samples when introduced in the analytical chamber in the pressure range between 10^{-8} and 10^{-6} mbar. Cluster secondary ions composed of elements from the sample surface, preferentially metallic, and adsorbed gases will be formed and emitted during ToF-SIMS measurements in quantities relevant to the analyses.

2. Intensities of emitted cluster secondary ions formed during the reaction between the metals and adsorbed gas will resemble the chemical composition of the surface more accurately than the intensities of the monoatomic secondary ions. In this way, the quantitative comparison of profoundly different samples concerning the common elements that these samples contain will be improved.

3. Depth profiles of multilayered structures and thin films will be improved with the use of H_2, C_2H_2, CO, and O_2 gases via matrix effect reduction. Identification of separate layers with different compositions will be easier, differentiation between successive layers more straightforward, and interfaces will be sharper.

4. The majority of the cluster secondary ions originating from both the compounds in the sample and adsorbed gases are supposed to be the most efficiently ionized in the negative polarity, causing depth profiling with the Cs^+ ion beam to be an optimal approach.

5. Gas flooding of the samples with the reactive gases during depth profiling may also affect the surface roughening. We assume a reduction of the surface roughness due to the formation of amorphous species on the surface and partial protection of the sample from bombardment with the primary ions via the adsorption of gas molecules.

Chapter 4

Article 1: Improvements in ToF-SIMS Depth Profiling of Metals, Alloys, and Metal Oxides with the Use of Reactive Gases

Depth profiling of thin films and multilayers is one of the most important applications of secondary ion mass spectrometry. However, in some cases, due to the matrix effect, differentiation of chemically similar layers is difficult. To avoid uncertainties, depth profiles of both positive and negative secondary ions can be measured but this significantly prolongs SIMS analysis. Furthermore, the matrix effect can substantially compromise the clear identification and determination of interfaces between the layers. However, there are different approaches toward matrix effect reduction like matrix-enhanced and metal-assisted SIMS, and laser and electron beam post-ionization of sputtered neutrals (SNMS). The first two are almost impossible to apply in depth profiling while SNMS can be easily combined with it but require significant modifications of the instrument. Dynamic reactive ionization presents a similar solution but it can be only used with the Ar cluster ion gun. Furthermore, Ar clusters are only appropriate for the depth profiling of organic and biological materials and are not suitable for inorganic materials due to low sputtering yield. Finally, we have an option of gas flooding, which may be applied for all types of samples, is compatible with depth profiling analyses, and does not require an extensive modification of the SIMS instrument. Considering these facts, we decided to investigate the influence of reactive gas flooding on the depth profiling of metals, metal oxides, and alloys.

We studied the influence of different gases that are reactive enough to react with the sample but not so reactive to harm the instrument. H_2, C_2H_2, CO, and O_2 were selected for our study, with only the O_2 being previously applied in the SIMS analyses. The application of H_2, C_2H_2, and CO was the novelty of our research, yet untested by any other research group. The gases were introduced in the SIMS analytical chamber through a capillary close to the sample surface. Different multilayer structures composed of consecutive thin layers of metals and their oxides, different metals, and different alloys were analyzed with positive and negative secondary ions. As an analytical ion beam, we used Bi^+ ions with an energy of 30 keV. The results were compared with the results obtained during depth profiling in ultra-high vacuum (UHV). Three different samples with the composition of Fe_2O_3/Fe/Ag/Ni/NiO/<Si>, Cr_2O_3/Cr/Ti/TiO_2/Al_2O_3/Al/<Si>, and $(Ti/Si)_5$/Ti:Si=3:1/Ti:Si=1:1/<Si> were analyzed. The thickness of the thin layers was between 2 and 60 nm. Si was used as a substrate in all three samples. The main challenge

concerning TiSi alloys was related to the differentiation between alloys containing the same elements in different ratios (Ti:Si=3:1 and Ti:Si=1:1). Cluster secondary ions in the form of metal hydrides, carbides, and oxides are formed when exposing metals to above-mentioned gases. Since these secondary ions most easily ionize in the negative polarity, depth profiling was performed with the Cs^+ ion beam because cesium implantation enhances the yield of negative secondary ions. Depth profiling in UHV was also performed with the O_2^+ and Ar^+ ion sputtering beams but no significant improvements were obtained. UHV measurements were done in the pressure range of 10^{-10} to 10^{-9} mbar while pressures of the reactive gases were determined in the manner of achieving the largest yields of cluster secondary ions. These were 7×10^{-7} mbar for H_2, 2×10^{-7} mbar for C_2H_2, 2×10^{-7} mbar for CO and 8×10^{-8} mbar for O_2.

Depth profiling with an Ar^+ ion beam in the UHV gave modest results because the intensities of both positive and negative secondary ions were very low. The application of the O_2^+ ions for sputtering significantly increased the yield of positive secondary ions but the quality of depth profiles was only partially improved. Differentiation between metals and their oxides was essentially impossible as well as the determination of the composition of TiSi alloys. However, differentiation between different metals was good but applicability for thin layers was not ideal due to quick degradation of depth resolution. Depth resolution was improved using the Cs^+ ion beam but since cesium implantation enhances the yield of negative secondary ions, issues connected with the general low ionization yields of negative metal ions arose. Despite good depth resolution, differentiation between metals was difficult while improvements were observed in connection with metal/metal oxide interfaces. Determination of the composition of TiSi alloys using Cs^+ ions was also improved. While performing Cs^+ sputtering, positive MCs^+ cluster ions (M = metal) were analyzed in addition to negative ions. To obtain adequate results, the intensities of these secondary ions needed to be normalized. Since the Cs^+ signal was constantly saturated, only normalization by the Cs_2^+ ion was possible. In this way, the differentiation between specific metals and their oxides and determination of the composition of alloys was possible to some degree but the main problem of this approach was the very low intensities of normalized MCs^+ signals often hindered by noise.

Considering all types of atmospheres we tested, optimal results were obtained with the H_2 flooding. The identification of all interfaces between the layers was unambiguous and different types of layers were easily distinguished from each other. The composition of TiSi alloys was determined with a high degree of certainty. While analyzing thin metallic layers, the matrix effect was further reduced by normalizing the intensities of secondary ions by the intensity of the H^- ions. This approach improved the resolving power needed for the clear differentiation between thin layers and resulted in sharp interfaces. The main reason for the quality of the results obtained in the H_2 atmosphere, especially in connection with the metal/metal oxide interfaces, is the formation of the metal hydride (MH_n^-) secondary ions which exclusively happens in the layers of unoxidized metals. Another important advantage of the H_2 flooding in comparison to the other atmospheres is no reduction of the sputter rate. On the other hand, all other gases significantly reduce the sputter rate.

This was not the case with the other gases. C_2H_2 and CO are furthermore composed of two different elements causing complications in the SIMS analysis. Since the affinity of carbon toward the formation of metal carbides is higher than the affinity of hydrogen toward the formation of metal hydrides, the intensity of the first was significantly higher in the case of C_2H_2 flooding. However, metal carbide secondary ions formed extensively also in the layers of metal oxides, preventing clear determination of interfaces between the metal/metal-oxide layers. C_2H_2 flooding was unsuccessful when analyzing thin metal layers as well. The expected results were obtained only for the TiSi alloy evaluation. Surprisingly, metal carbide signals were more strictly confined to the layers of pure metals when CO

was used. However, the presence of oxygen in the CO molecule caused the enhancement of metal oxide signals in the layers of pure metals. Consequently, there were no notable improvements concerning the metal/metal oxide interface determination in comparison to the C_2H_2 atmosphere. The situation with thin metal layers and alloys was also similar to with the C_2H_2. Results obtained during O_2 flooding were more following expectations as they closely resembled sputtering with the O_2^+ ion beam in the UHV, especially considering metals and metal oxides. Differentiation between thin metal layers was unclear and certainly worse than during O_2^+ sputtering but the determination of alloys was improved and unambiguous when combining Cs^+ sputtering with the O_2 flooding.

Finally, considering previous studies, we assume that the formation of cluster secondary ions composed of metals from the sample and gases from the atmosphere occurs after the adsorption of gases to the sample surface. Cluster secondary ions are formed during the sputtering process most probably on the surface or recombined just above the surface. The intensities of these cluster signals resemble the chemical composition of analyzed materials more correctly than the signals of monoatomic secondary ions. Results obtained in this study confirmed the hypotheses 1, 3, and 4.

Contributions of the Ph.D. dissertation author: conceptualization and visualization of the experiment, methodology, investigation via ToF-SIMS depth profiling, interpretation of the results, writing the original draft, reviewing and editing, and project administration.

ACS Partner Journal

Journal of the American Society for Mass Spectrometry

pubs.acs.org/jasms

Research Article

ToF-SIMS Depth Profiling of Metal, Metal Oxide, and Alloy Multilayers in Atmospheres of H_2, C_2H_2, CO, and O_2

Jernej Ekar, Peter Panjan, Sandra Drev, and Janez Kovač*

Cite This: J. Am. Soc. Mass Spectrom. 2022, 33, 31−44

Read Online

ACCESS | Metrics & More | Article Recommendations | Supporting Information

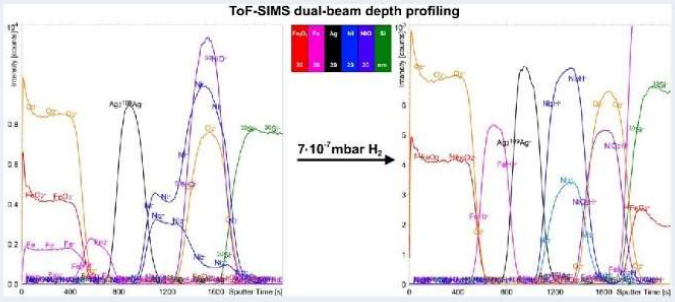

ABSTRACT: The influence of the flooding gas during ToF-SIMS depth profiling was studied to reduce the matrix effect and improve the quality of the depth profiles. The profiles were measured on three multilayered samples prepared by PVD. They were composed of metal, metal oxide, and alloy layers. Dual-beam depth profiling was performed with 1 keV Cs^+ and 1 keV O_2^+ sputter beams and analyzed with a Bi^+ primary beam. The novelty of this work was the application of H_2, C_2H_2, CO, and O_2 atmospheres during SIMS depth profiling. Negative cluster secondary ions, formed from sputtered metals/metal oxides and the flooding gases, were analyzed. A systematic comparison and evaluation of the ToF-SIMS depth profiles were performed regarding the matrix effect, ionization probability, chemical sensitivity, sputtering rate, and depth resolution. We found that depth profiling in the C_2H_2, CO, and O_2 atmospheres has some advantages over UHV depth profiling, but it still lacks some of the information needed for an unambiguous determination of multilayered structures. The ToF-SIMS depth profiles were significantly improved during H_2 flooding in terms of matrix-effect reduction. The structures of all the samples were clearly resolved while measuring the intensity of the $M_nH_m^-$, $M_nO_m^-$, $M_nO_mH^-$, and M_n^- cluster secondary ions. A further decrease in the matrix effect was obtained by normalization of the measured signals. The use of H_2 is proposed for the depth profiling of metal/metal oxide multilayers and alloys.

KEYWORDS: *SIMS depth profiling, H_2, C_2H_2, CO and O_2 atmosphere, gas flooding, cluster secondary ions, matrix effect*

INTRODUCTION

Thin layers are often depth profiled when we want to analyze the chemical composition and thickness of a single layer or a multilayer structure. In this way, corrosion properties,[1−4] diffusion mechanisms,[5] native or artificially prepared oxide layers,[6,7] layers that compose integrated circuits,[8−11] and the composition of nanoparticles, nanolayers, and nanocomposite coatings,[12,13] paints,[14] adhesives,[15] catalysts,[16,17] thin polymer films,[18] biological compounds[19,20] and even cells and tissues[21,22] can be studied. Such analyses can be performed using a variety of surface-sensitive analytical techniques such as SIMS (secondary ion mass spectrometry), XPS (X-ray photoelectron spectroscopy) or AES (Auger electron spectroscopy) in combination with ion sputtering for material removal.[23−25] Laser ablation or plasma etching is also an option,[10] but these approaches are less commonly applied. While depth profiling with ion sputtering is destructive, we can also use nondestructive methods such as RBS spectroscopy,[26] ellipsometry, X-ray reflectometry,[27] or angle-resolved analyses such as AR-XPS. When thicker layers are of interest, sectioning of the material either via mechanical means, such as a microtome[28] or with a focused-ion beam (FIB),[29] is preferred. Cross sections prepared in this way can be analyzed using, for example, a scanning electron microscope (SEM)[29] or SIMS imaging.[28]

With ion-sputtering methods, there are many possible ions to choose between. Ar^+ ions are the most frequently

Received: July 15, 2021
Revised: December 8, 2021
Accepted: December 13, 2021
Published: December 22, 2021

https://doi.org/10.1021/jasms.1c00218
J. Am. Soc. Mass Spectrom. 2022, 33, 31−44

used.[25,30−32] Other options include Xe^+ ions[20,33,34] and the reactive Cs^+ and O_2^+ ions.[30,31] Cs^+ ions increase the yield of negative secondary ions in SIMS spectrometry due to their incorporation into the surface of the sample with a consequent reduction of the work function.[31] Cs^+ ions also make possible the analysis of cluster secondary ions, which are mainly formed as MCs_n^+,[35,36] where M stands for any metal atoms. On the other hand, O_2^+ ions increase the yield of positive secondary ions during SIMS depth profiling.[37] If appropriate ion sources are used, O^- primary ions can also be used for sputtering, but this method is not often practiced.[31]

As these mono- or diatomic primary ions penetrate deep into the sample, causing extensive damage to the chemical bonds and the mixing of atomic/molecular layers, larger molecular as well as cluster primary ions were introduced, especially for molecular depth profiling.[19,38−41] The energy of the monatomic primary ions is focused on a small radius crater and deep in the subsurface layers, damaging and breaking molecules yet to be analyzed.[19,25,39] The energy of the polyatomic and cluster primary ions is distributed among all its constituent atoms and deposited mainly on the surface, resulting in less damage.[39−41] Consequently, the most commonly applied energies for monatomic primary ions are in the range of a few 100 eV up to a few keV,[11,37,42] while for polyatomic ions they are in the range of a few keV up to a few 10 keV, mainly depending on their type.[19,22,25,40] The first widely applied polyatomic source was SF_5^+, closely followed by the fullerenes, C_{60}^+.[19,22,40] More recently, Ar cluster ions have gained popularity due to their versatility, both in terms of energy (a few keV to a few 10 keV) and size, as they can be made up of 100−5000 Ar atoms.[25,40,43] Also worth mentioning are the experiments with H_2O,[40] CO_2,[43] and O_2 clusters.[44]

Since we are focusing on SIMS depth profiling, we should first distinguish between single-beam and dual-beam depth profiling. In single-beam depth profiling, the same ion beam is used for the etching process and analysis, while in dual-beam depth profiling, different ion beams are used for the analysis and ion etching.[41,45] The analysis is most commonly performed with a liquid metal ion gun (LMIG) using Bi^+, Bi_3^+, Au^+, Au_3^+, Ga^+, or In^+ primary ions.[31] Dual-beam depth profiling offers an advantage because the ion beam is optimized for the analysis. On the other hand, all of the material sputtered during the etching process is lost.[41] In addition to the deterioration of the depth resolution and ion-bombardment-induced damage, the application of SIMS is also limited by the matrix effect and the nonconstant ionization yields.[46−49] The matrix effect is the effect of the substrate on the ionization probability of the particles emitted from the surface, both increasing or decreasing the ionization yield of either positive or negative secondary ions depending on the substrate from which they originate.[46−50] The matrix effect is particularly critical for (semi)quantitative analyses.[48,50,51]

Fortunately, there are many ways of reducing the matrix effect. One commonly applied approach is laser postionization of the neutral sputtered particles (laser-SNMS).[52−54] Since the particles are ionized in the plume, there is no matrix around them to affect the ionization.[53] Laser-SNMS can be used in depth profiling,[55] thereby improving the ionization yield.[56,57] With this method, we can selectively ionize only some of the neutral particles (resonant laser-SNMS)[58] or nonselectively ionize all of them (nonresonant).[52] In the case of resonant laser-SNMS, we must know exactly what is being analyzed, and in the case of the nonresonant approach, we must make sure that the laser intensity is high enough to ionize all the particles.[59] The sputtered neutrals can also be postionized with an electron beam, similar to a laser.[60−63] We can also intentionally exploit the matrix effect by depositing a thin metal layer, usually Au or Ag.[64,65] However, depth profiling combined with metal-assisted SIMS can only be performed while using a nonconventional experimental setup.[66] The ionization yield can also be increased by depositing ionic liquids[67] or graphene oxide[68] on the sample surface. Furthermore, the samples can be mixed with specific matrices,[69−71] but with this approach we lose the surface sensitivity. Results similar to those using metal-assisted SIMS, but also applicable for depth profiling, offer sputtering with Cs^+ or cosputtering with Cs^+ and Xe^+.[36,72] The metal that increases the ionization yield in this case is cesium, which opens the possibility of analyzing the MCs_n^+ secondary-ion clusters.[36,72] More recently, dynamic reactive ionization (DRI) has been developed in which reactive HCl molecules are incorporated into the Ar cluster primary ions.[73−75] Water on the sample surface introduced into the analysis chamber through the gas valve enhances the protonation and consequently increases the ionization yield while reducing the matrix effect.[73,74] DRI is compatible with depth profiling.[75] Finally, it is also possible to flood different gases into the analysis chamber during both surface analysis and depth profiling, thus introducing a gaseous matrix that is universal, regardless of the sample used.[76−79] The most commonly used gas is O_2, leading to higher ionization yields for positive secondary ions[76,77] or improving the depth resolution while reducing surface roughening.[78] The ionization yield can also be affected by the introduction of some other compounds, such as water or fluorine (via XeF_2), which also change the sputtering rate.[79]

The aim of our research was to investigate the influence of different gases on the quality of the SIMS depth profiles of different multilayer structures. Our study was performed on a ToF-SIMS instrument with a dual-beam configuration. Using Bi^+ ions for the analysis and Cs^+, O_2^+, or Ar^+ for the etching process, we aimed to optimize the depth profiles recorded while changing the atmosphere in the analysis chamber. For our study, we selected three different multilayer structures similar to those we frequently analyze in our laboratory for industrial and academic partners. Our goal was to find a way to clearly and unambiguously resolve the layered structure of the samples mainly by manipulating the atmosphere in the analysis chamber. Using this process, the ionization yield of the secondary ions and the matrix effect would be turned in our favor. In our study, we compared the effects of O_2, CO, C_2H_2, and H_2. The results of our experiments show that the introduction of H_2 gas during the SIMS depth profiling improves the chemical sensitivity of the SIMS method, provides a clear distinction between the metallic and metal-oxide layers, allowing the easier identification of elements and their oxides in thin films, and improves the depth resolution.

EXPERIMENTAL SECTION

Preparation of Multilayered Samples. All of the metals and metal oxides were deposited in a Sputron triode sputtering system (Balzers Oerlikon). The background pressure was better than 1×10^{-6} mbar. The partial pressure of the argon working gas in the vacuum chamber was 2×10^{-3} mbar for all the processes. A maximum substrate temperature of less than 100 °C was maintained during the deposition. A quartz-crystal microbalance was used to calibrate the deposition rates. The

https://doi.org/10.1021/jasms.1c00218
J. Am. Soc. Mass Spectrom. 2022, 33, 31−44

Journal of the American Society for Mass Spectrometry pubs.acs.org/jasms Research Article

deposition rates and thickness reproducibility were better than 2%.

The 60 mm diameter targets are interchangeable *in situ*, allowing us to easily prepare multilayer structures without interrupting the vacuum from one deposition to the next. All the targets were initially cleaned for 5 min to remove the native oxide and other impurities on their surfaces. High-purity targets were used as the sputtering source. With an average DC power of 60 W/cm^2 (1700 V/0.6 A) on the pure metal target (Al, Fe, Ti, Cr, Ni), deposition rates in the range 10−12.5 nm/min were achieved. At the same target power, the deposition rate of the TiSi (50/50) was slightly lower (7.6 nm/min). At half the target power, the deposition rate of Ag was much higher (around 16 nm/min). Silicon was RF sputtered onto the target at 36.5 W/cm^2 ,and a deposition rate of 3.1 nm/min was achieved. For depositing the layers of Ti−Si alloys, composite targets were used with 3:1 and 1:1 atomic ratios between the Ti and Si.

Metal oxide layers (Cr_2O_3, TiO_2, Al_2O_3, Fe_2O_3, NiO) were prepared by reactive sputtering. In this process, thin oxide films were deposited on substrates by sputtering metallic targets in the presence of oxygen mixed with an argon working gas. The composition of the deposited layers and the deposition rate are very sensitive to the supply of oxygen; therefore, the flow rate of the oxygen (99.998%) was controlled with a flowmeter. Prior to the deposition, the targets were cleaned and conditioned in pure Ar plasma and Ar/O_2 plasma at a closed shutter, respectively. Due to the lower density of the oxide layers, the deposition rates were higher than for pure metal layers at the same power on the target (from 11.4 nm/min for Al_2O_3 to 26.5 nm/min for NiO).

SIMS Measurements. The ToF-SIMS analyses were made using a TOF.SIMS 5 instrument from ION TOF. The instrument has two ion guns (dual-beam depth profiling), a ToF analyzer with a reflectron, a microchannel plate (MCP) detector and a low-energy electron gun. We used Bi^+ primary ions from a BiMn LMIG field-ionization source as the analysis beam with an energy of 30 keV and a current between 0.9 and 1.2 pA, depending on the measurement. The Bi^+ primary ion beam was pulsed with a pulse length of 5.9 ns. With the settings used, the analyzed depth was about 2 nm, the detection limits around 1 ppm, and the mass resolution $m/\Delta m$ between 8000 and 20000, depending on the peak of interest. Only the mass resolution of the H^- signal was lower, around 3000. For the depth profiling we used a Cs^+ or O_2^+ sputter ion beam with an energy of 1 keV for both ion species. In the case of the Cs^+ sputter beam, the ion current ranged from 42 to 58 nA, while in the case of the O_2^+ it ranged from 107 to 116 nA, depending on the measurement. The surface-ionization-based ion source and the electron-impact ion source were used for the generation of the Cs^+ and O_2^+ ions, respectively. The analyses with the Bi^+ primary ions were performed over a 50 × 50 μm scanning area (128 × 128 pixels), located in the center of the 400 × 400 μm etching crater created by the Cs^+ or O_2^+ sputter ion beam. Secondary ions were analyzed over the m/z range from 0 to 875.

The gases used during the depth profiling were introduced into the analysis chamber close to the analyzed region (a distance of less than 1 cm). The introduction of the gas was manually controlled with a precise gas-leak valve that had a Swagelok installation and a capillary leading toward the analyzed area. We used gases with different purity levels, i.e., 6.0 H_2, industrial grade C_2H_2, 3.0 CO, and 5.0 O_2. The applied pressures were 7×10^{-7} mbar for H_2, 2×10^{-7} mbar for C_2H_2, 2×10^{-7} mbar for CO, and 8×10^{-8} mbar for O_2. These were approximately the lowest pressures needed to saturate the formation of cluster secondary ions from the metals and the respective gas. Since optimizing the gas pressures was not the main goal of our study, we emphasize that it is probably possible to further reduce the pressures of the gases.

Cross-Section Sample Preparation and TEM Measurements. The sample was cut into blocks and mounted face to face in a brass ring with epoxy glue. The TEM specimen was ground to a thickness of 100 μm and dimpled down to 15 μm at the disc center (Dimple grinder, Gatan, Inc., Warrendale, PA). The TEM specimen was finally ion-milled (PIPS, Precision Ion Polishing System, Gatan, Inc., Warrendale, PA) using 3 kV Ar^+ ions at an incidence angle of 8° until perforation. Detailed structural investigations of the sample were performed using a 200 kV transmission electron microscope with field emission electron gun (JEM-2010F, Jeol Ltd., Tokyo, Japan).

RESULTS AND DISCUSSION

Samples. We conducted our study on the influence of different gases during SIMS depth profiling on three different samples. Samples 1 (FeAgNi) and 2 (CrTiAl) were multilayer structures of Fe_2O_3/Fe/Ag/Ni/NiO and Cr_2O_3/Cr/Ti/TiO_2/Al_2O_3/Al, respectively. Both were prepared on mirror-like polished silicon wafers. All the layers had a thickness between 15 and 30 nm, with the exact values given in Figure 1. The thicknesses of the layers were determined by TEM imaging, with the corresponding images presented in Figure S2. The third sample (TiSi), also shown in Figure 1, consisted of 10 alternating layers of Ti and Si, only 5.5 and 2.5 nm thick, respectively. They were followed by two layers of Ti−Si alloy

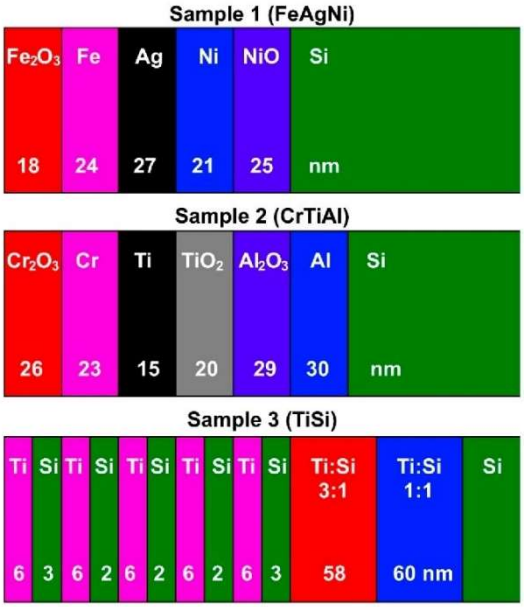

Figure 1. Schematic presentation of sample 1 (FeAgNi), sample 2 (CrTiAl), and sample 3 (TiSi).

https://doi.org/10.1021/jasms.1c00218
J. Am. Soc. Mass Spectrom. 2022, 33, 31−44

Journal of the American Society for Mass Spectrometry pubs.acs.org/jasms Research Article

with a thickness of almost 60 nm. In the first TiSi layer, the atomic ratio between Ti and Si was 3:1 with the higher concentration being titanium, while in the second TiSi layer this ratio was 1:1. A multilayer structure was again deposited on the silicon wafer.

In the first part of our study, we measured the SIMS depth profiles of the three samples described using a dual-beam depth profiling technique without the presence of an additional gas. In the second part, we introduced gases such as O_2, CO, C_2H_2, and H_2 and qualitatively compared the acquired depth profiles.

O_2^+ Sputtering. For the initial depth analyses we used an O_2^+ beam for etching. Figure 2 shows the depth profiles of the positive secondary ions of the FeAgNi and CrTiAl samples using a 1 keV O_2^+ sputter beam. As is evident from Figure 2, the difference in the intensity of the metal oxide secondary-ion signals (MO^+) between the layers of pure metal and metal oxide of the same element can only be seen for Fe and Cr. For the other elements (Ni, Ti and Al), the intensity of their MO^+ signal is relatively constant through both the metal and its oxide layers due to the oxidation caused by the O_2^+ ions. Additionally, due to the matrix effect, the M^+ signals either show a higher intensity in the layer of their oxide rather than in the layer of the pure metal (Fe, Ni, and Cr) or have a constant intensity through both layers (Ti) (Figure 2). However, this is not the case for the Al^+ signal, which was saturated in our measurements. The M_2^+ signals are much less affected by the matrix and therefore give a somewhat more representative picture, but they still do not provide an adequate description of the composition of the layers. For some metals, such as Ti, the Ti_2^+ signal is also too weak to be considered relevant. From the depth profiles recorded when using O_2^+ ions, only different metal layers can be distinguished from each other, but not the layers of the pure metal and its oxide.

The use of O_2^+ ions for etching was partially successful in the analysis of the TiSi sample, where we can recognize the multilayer structure of this sample (Figure S2a). Both the M^+ and MO^+ signals are correctly positioned and exhibit relatively intense maxima and minima. But we encounter a problem when we compare Ti−Si alloy layers with different Ti/Si concentration ratios. As the relative concentration of Si increases, we also observe an increase in the intensity of the Si^+ and SiO^+ signals, as shown in Figure S2b. On the other hand, as the relative concentration of Ti decreases, there is no clear decrease in the intensity of the Ti^+ signal, while the intensity of the TiO^+ signal decreases only slightly. Therefore, the application of O_2^+ ions for sputtering is not suitable when analyzing multilayer structures composed of metal layers and their oxides as well as when analyzing multilayer structures composed of alloy layers with different compositions.

Cs^+ Sputtering. In the next experiments, the 1 keV Cs^+ ion beam was used for etching. Figure 3 shows the depth profiles of the negative secondary ions sputtered from the FeAgNi and CrTiAl samples. From the depth profiles measured using Cs^+ ions, oxide layers can be identified from both the O_2^- and MO_n^- signals. However, there are still problems with the identification of metal layers. Indeed, the analysis of the depth profiles in Figure 3 shows that all of the M^- signals have maxima in the respective oxide layer, except for Ti. The intensities of both the Ti^- and Ti_n^- signals are too low to treat them as relevant for the analysis. The M_n^- secondary ions are much less affected by the matrix effect than the M^- ions and show maxima in the layers of the pure metals (Figure 3). This

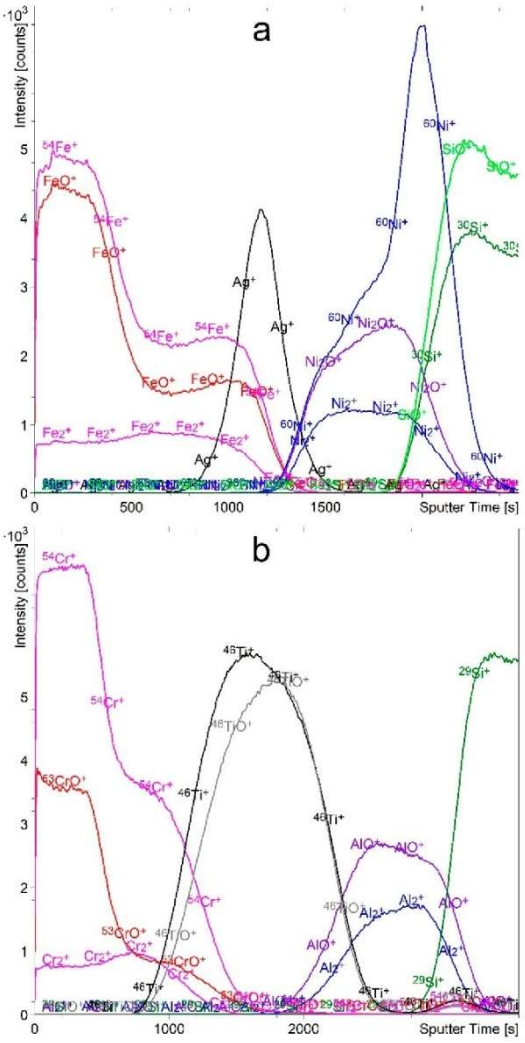

Figure 2. Depth profiles of FeAgNi (a) and CrTiAl (b) samples recorded using a 1-keV O_2^+ sputtering beam. Intensities of some signals were multiplied by a specific factor as a way of reducing the intensity scale interval (0.6 for $^{54}Fe^+$, 0.5 for $^{60}Ni^+$, 0.7 for SiO^+, 0.7 for $^{54}Cr^+$, 0.3 for $^{46}Ti^+$, and 0.3 for $^{46}TiO^+$).

observation implies that the matrix has a greater effect on the monatomic secondary ions than on the cluster secondary ions. However, the intensity of the M_n^- ions is still significant in the oxide layers. Moreover, with the exception of Al_n^-, their average intensity is very low so that the signal-to-noise ratio is also low.

The application of the Cs^+ beam for sputtering the TiSi sample also showed some problems regarding the interpretation of the measured depth profiles. The Si layers in the multilayer structure can be easily identified via the Si_3^- signal (Figure 4a). The TiO^- signal, on the other hand, has a disproportionately intense maximum in the first Ti layer and an additional maximum in the last Si layer. But the TiH^- signal

https://doi.org/10.1021/jasms.1c00218
J. Am. Soc. Mass Spectrom. 2022, 33, 31−44

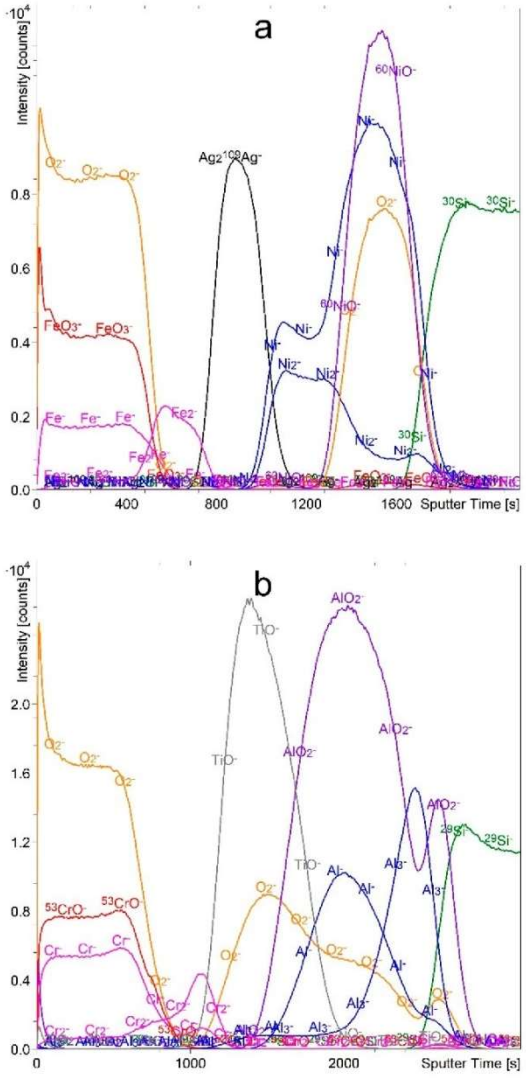

Figure 3. Depth profiles of FeAgNi (a) and CrTiAl (b) samples recorded using a 1 keV Cs^+ sputtering beam. The intensity-multiplication factors are 0.3 for O_2^-, 2.0 for Fe_2^-, 0.4 for Ni^-, 0.3 for $^{60}NiO^-$, 4.0 for Cr_2^-, and 0.5 for TiO^-.

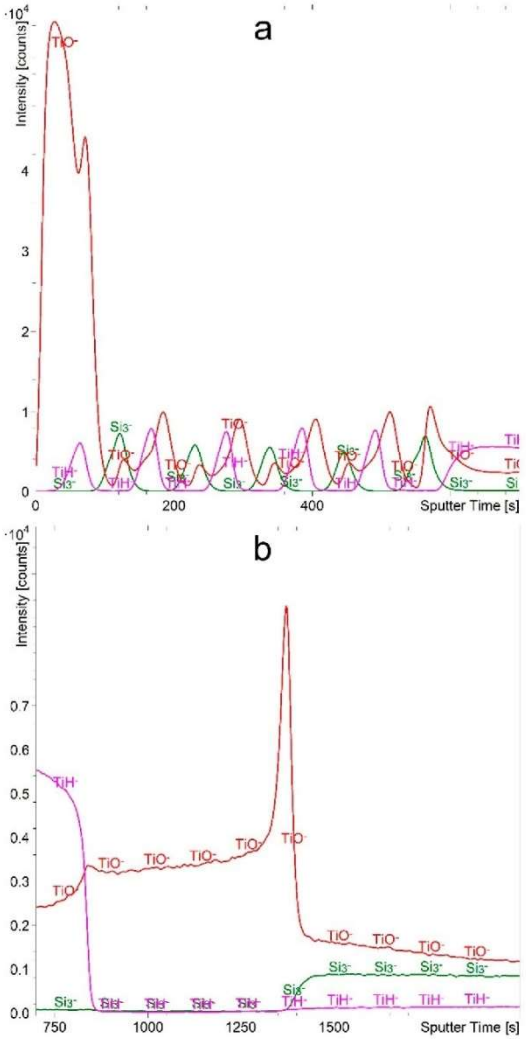

Figure 4. Depth profile of TiSi sample recorded using a 1 keV Cs^+ sputtering beam. The depth profile (a) presents the first 700 s of etching time, while the profile (b) presents the etching time interval between 700 and 2000 s.

resolves the multilayer structure more clearly. This presents the only case of an intense hydride signal formation, even without the presence of H_2 during the analysis. Namely, other metals and even Si in the TiSi sample form different and much more intense hydride signals when H_2 gas flooding is applied. Furthermore, even the Ti in the CrTiAl sample does not form hydride signals without H_2 being present in the analysis chamber. We can therefore conclude that the thin Ti and Si layers are permeable to the hydrogen, while the Cr and Cr_2O_3 layers protect the underlying Ti from the hydrogen. Since we observed TiH^- formation for two different sample series while they were exposed only to the ambient conditions, we can conclude that measurable amounts of hydrogen dissolve in the thin Ti layers even when the only source of hydrogen is the air. This phenomenon can be explained by the good solubility of hydrogen in titanium.[80,81] The ambient source of the hydrogen can even be water, as studies have shown that water forms a metal oxide layer on the surface while hydrogen atoms diffuse deeper into the metal, forming hydrides.[82,83] It should be also mentioned that hydrogen, either from the H_2O or H_2 molecule, dissociates into atoms before it diffuses into the metal.[84,85]

Furthermore, the layers of the Ti−Si alloys show unsatisfactory results as well (Figure 4b). It appears that the hydrogen is dissolved at the beginning of the first alloy layer as well, but the abrupt fall in the intensity of the TiH^- signal at

https://doi.org/10.1021/jasms.1c00218
J. Am. Soc. Mass Spectrom. 2022, 33, 31−44

around 840 s of sputtering (Figure 4b) indicates that the hydrogen cannot penetrate deeper. Furthermore, with a decreasing relative concentration of Ti, the intensity of the TiO^- signal also decreases, but the prominent TiO^- maximum at the interface between the alloys severely alters the depth profile. Only the Si_3^- (and Si_2^-) signals correctly describe both alloys. Namely, with an increasing relative concentration of Si, the intensity of both the Si_3^- and Si_2^- signals also increases. Some anomalies and artifacts seen in Figure 4 can also be explained with the change in the concentration of implanted Cs atoms when crossing interfaces as well as with the oxidized species at the interfaces originating from the sample preparation. Both of these phenomena strongly influence the ionization probability.

If Cs^+ ions were used for the etching, the positive secondary ions have a very low intensity and are strongly influenced by the matrix effect originating from the Cs implantation and the sample oxidation during preparation. On the other hand, Cs_2M^+ and Cs_2MO^+ cluster ions show better results and are often used in the so-called MCs^+ approach.[35,36] These signals can be normalized to the Cs^+ or Cs_2^+ signals. In our case, normalization to the Cs^+ signal is not effective because the Cs^+ signal is saturated. The correct multilayer structure of the FeAgNi sample can be determined from the depth profiles based on the Cs_2M^+ and Cs_2MO^+ secondary ions (Figure 5a). The O^+ ions provide additional confirmation. The CrTiAl sample, on the other hand, appears to be much more problematic (Figure 5b). Namely, the Cs_2Cr^+ signal shows two maxima, the $CsTi^+$ and $CsTiO^+$ signals do not offer a clear distinction between the pure Ti and TiO_2, and the much-less-intense Cs_2Ti^+ and Cs_2TiO^+ signals do not offer much better results. Finally, neither the $CsAlO^+$ nor Cs_2AlO^+ signals provide a clear insight into the Al_2O_3/Al layers. There are also issues that occur with both the FeAgNi and CrTiAl samples. Namely, the CsM^+ signals are not representative because they are strongly affected by the matrix effect and thus show maxima in the oxide layer. Moreover, the Cs_2M^+ signals also do not disappear in the oxide layers. Last but not least, most of the Cs^+ cluster signals are of very low intensity. They are one to two orders of magnitude weaker than the signals of the positive secondary ions recorded while etching with O_2^+ ions or the negative secondary ions recorded while etching with Cs^+.

Significant problems were encountered in the analysis of the TiSi sample, too. The Cs_2Ti^+ and Cs_2Si^+ signals show only partial and unclear differentiation of the Ti and Si thin layers, while the $CsTi^+$ shows no clear maxima or rather too many of them (Figure S3a). The $CsSi^+$ signal shows the same pattern as the Cs_2Si^+ signal, only it is less intense. Due to the very low intensity of the Cs_2Ti^+ signal in particular, we are faced with many artifacts as well as with secondary misplaced maxima. The discrimination between the Ti−Si alloy layers with different Ti/Si atomic ratios is slightly better, as the intensity of the Cs_2Ti^+ signal decreases when the relative concentration of the Ti decreases and the intensity of the Cs_2Si^+ signal increases when the relative concentration of the Si increases (Figure S3b). This is not true for the $CsTi^+$ and $CsSi^+$ signals, as their intensity remains more or less constant. Additionally, we again observe an increase in the intensity of both the Cs_2Ti^+ and Cs_2Si^+ signals for an etching time of about 1100 s caused by the abrupt fall in the concentration of the dissolved hydrogen. Finally, the consequence of the very low intensity of all these signals is a significant presence of noise in the lines of the depth profile.

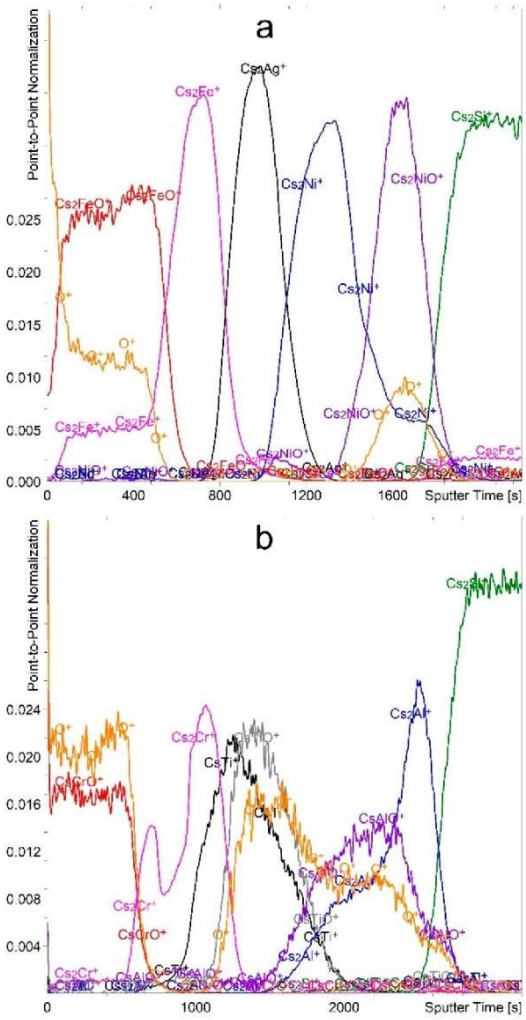

Figure 5. Depth profiles of FeAgNi (a) and CrTiAl (b) samples with the scale normalized to the intensity of the Cs_2^+ signal recorded using a 1-keV Cs^+ sputtering beam. The intensity-multiplication factors are 3.0 for O^+, 2.0 for Cs_2FeO^+, 0.15 for Cs_2Ag^+, 0.3 for Cs_2Ni^+, 3.0 for Cs_2NiO^+, 0.2 for Cs_2Cr^+, 2.0 for $CsTiO^+$, 2.0 for $CsAlO^+$, and 0.4 for Cs_2Al^+.

Gas Flooding: General and O_2. From the results shown above, we can conclude that upon sputtering with only O_2^+ or Cs^+ ions, we cannot unambiguously determine the layered structure of multilayer samples composed of metals and their oxides nor can we find the differences between alloys of the same constituents with their different relative concentrations. Even a combination of the depth profiles of positive secondary ions (recorded during sputtering with O_2^+ or as MCs_n^+ clusters during sputtering with Cs^+) and negative secondary ions (recorded during sputtering with Cs^+) does not always provide enough results to be able to draw unambiguous conclusions. We should emphasize that we also used Ar^+ ions for etching, but O_2^+ and Cs^+ ions appeared to be the better choice. For the

https://doi.org/10.1021/jasms.1c00218
J. Am. Soc. Mass Spectrom. 2022, 33, 31−44

FeAgNi and CrTiAl samples, etching with Ar^+ is not suitable because of the problems with the low intensity of the positive secondary ions. Moreover, the positions of their maxima with respect to the metal and metal oxide layers are not correct, similar to the O_2^+ etching. The intensities of the negative secondary ions are even lower and, in some cases, indistinguishable from the noise. In the case of Ar^+ etching of the TiSi sample, both elements have their maxima in the same layers, so it is impossible to distinguish them.

To improve our depth-profiling results, we decided to proceed with gas flooding. Gas flooding with oxygen has often been applied during SIMS analyses to increase the ionization probability of the particles emitted from the surface into positive secondary ions.[76,77] Besides O_2, we also introduced gases such as CO, C_2H_2, and H_2 into the analysis chamber. The use of O_2 gas for flooding in SIMS analyses is a common practice, whereas the application of CO, C_2H_2, and H_2 gases is a novelty of this work, to the best of our knowledge. Our main goals were to minimize the sample-induced matrix effect, increase the secondary-ion yield, and unambiguously resolve the structure of our multilayer samples while recording only one depth profile. Since we wanted to distinguish metals from their oxide layers, etching with O_2^+ ions was not acceptable because the metal layer oxidizes during the etching process. O_2^+ in combination with gas flooding also introduces two other problems. First, O_2^+ can react with many gases, in our case with all those we used (CO, C_2H_2, and H_2). Second, sputtering with O_2^+ increases the pressure in the analysis chamber by an order of magnitude, reducing the pressure range in which the flooding gas can be tested.

Nonetheless, we performed the depth profiling of our samples with a Cs^+ sputtering beam in the presence of O_2. For the FeAgNi and CrTiAl samples, the O_2 flooding provides no advantage over Cs^+ or O_2^+ sputtering in a vacuum. For the TiSi sample, slightly larger and more important differences were observed. We chose to analyze the negative secondary ions (Figure S4) since Cs^+ sputtering enhances the formation of negative ions more than O_2 flooding enhances the formation of positive ions. Furthermore, as seen in Figure S4, we mainly focused on the oxide species, which ionize better in the negative polarity. Figure S4a shows us that the multilayer structure of the Ti and Si thin layers is resolved, but not ideally since multimaxima structures appear. An important improvement can be seen when analyzing the Ti−Si alloy layers. Namely, the difference between layers with different Ti/Si atomic ratios is now clear. The intensity of the TiO^- and TiO_2^- signals decreases as the relative concentration of the Ti decreases and the intensity of the Si^- and SiO_2^- signals increases as the relative concentration of the Si increases (Figure S4b). From Figure S4 we can also observe another important feature of O_2 flooding. This is a significant decrease in the sputtering rate. When other analyzed samples are also included in the consideration, this decrease appears to be between 70 and 300% with respect to measurements without gas flooding.

The main idea of the O_2 flooding, which has often been applied by various research groups, is to increase the ionization yield. We have extended such studies to the use of other gases such as CO, C_2H_2, and H_2. Inert gases are not suitable for such purposes, so we chose reactive ones. CO is reactive because of the partial negative charge on the C atom and the partial positive charge on the O atom, C_2H_2 because of its two π bonds, and H_2 because of the weak σ bond. We also considered that the species formed should ionize well into the anions because etching with Cs^+ ions increases the yield of negative secondary ions. When choosing the reactive gas, we also need to make sure that it is not too reactive (e.g., F_2) to avoid damaging the components of the spectrometer. Besides the increased ionization, our main goal was to exploit the matrix effect in our favor by applying a specific atmosphere, which is the universal matrix independent of the sample to be analyzed. Namely, when the samples are sputtered and the emitted particles are ionized in a vacuum, the only matrix comes from the sample itself and is, therefore, sample specific. However, when we introduce the reactive gas into the analysis chamber, we create an artificial gaseous matrix that is under our control. Such a matrix affects different samples in the same way.

CO Flooding. We performed depth profiling of the FeAgNi and CrTiAl samples using the Cs^+ sputter beam in an atmosphere of 2×10^{-7} mbar CO (Figure 6). The analysis of the depth profiles of the MC_2^- and MO_n^- signals showed improved depth profiles with moderate depth resolution. In the case of the FeAgNi sample (Figure 6a), all the layers are resolved and the multilayer structure of the sample can be derived from this profile alone, with only minor uncertainties. It should be noted that only weak AgC_n^- signals could be detected due to the inertness of the Ag. The depth profile of the CrTiAl sample (Figure 6b) was not successful. The Ti and TiO_2 layers are difficult to distinguish because there is no sharp interface between them. The AlC_2^- signal has its maximum in the Al_2O_3 layer, so the Al and Al_2O_3 layers cannot be correctly identified. The AlC^- signal shows the same pattern as AlC_2^-. As a reactive gas, CO is a suitable choice, but its main drawback is the fact that it consists of C as well as O atoms. The related problems can be seen in Figure 6, where we can see that the signals of the O_2^- and MO^- species do not drop to zero in the layers of pure metal. This could mean that the metal layer is partially oxidized, which is not the case.

The results in the case of depth profiling for the TiSi sample with Cs^+ ions in the CO atmosphere were slightly worse than those obtained in the O_2 atmosphere. As shown in Figure S5a, the TiO^- peak has two local maxima located at the Si/Ti and Ti/Si interfaces. This indicates the presence of an extensive matrix effect at the interfaces, which has a negative effect on the profile structure. The SiO_2^- signal similarly shows an unclear multimaxima structure. The TiC_2^- signal is very weak and also does not clearly resolve the multilayer structure. The Ti−Si alloy layers in the TiSi sample offer a slightly better result. As the relative concentration of silicon increases, the intensity of the SiC^- and SiO_2^- signals increases as well. As the relative concentration of titanium decreases, the intensity of the TiO^- signal also decreases, while the intensity of the TiC_2^- signal remains more or less constant (Figure S5b). Nevertheless, we should emphasize that the CO flooding reduces the sputtering rate by 20−90% (depending on the sample), which is much less than in the case of the O_2 atmosphere.

C_2H_2 Flooding. The presence of acetylene in the analysis chamber results in depth profiles similar to those recorded when using CO. Positive results are obtained as the intensity of the MO_n^- secondary ions decreases in the layers of pure metal, compared to the CO flooding (Figure S6), due to the absence of oxygen in the C_2H_2 molecule. An exception is seen for Al in the CrTiAl sample. The layer of "pure" Al is a mixture of Al and Al_2O_3 because aluminum is partially oxidized during the sample preparation due to its reactivity (Figure S6b). Oxide layers can therefore be identified from the O^-, OH^-, $C_nO_m^-$,

https://doi.org/10.1021/jasms.1c00218
J. Am. Soc. Mass Spectrom. 2022, 33, 31−44

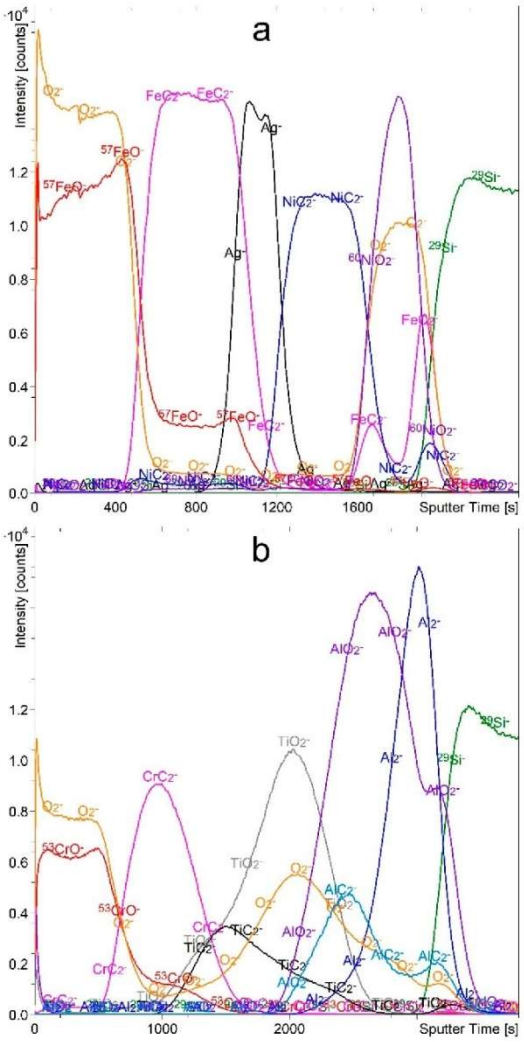

Figure 6. Depth profiles of FeAgNi (a) and CrTiAl (b) samples recorded using a 1 keV Cs^+ sputtering beam and an atmosphere of 2 × 10^{-7} mbar CO. The intensity-multiplication factors are 0.5 for O_2^-, 2.0 for $^{57}FeO^-$, 0.6 for $^{60}NiO_2^-$, 0.7 for AlO_2^-, 3.0 for AlC_2^-, and 0.5 for Al_2^-. The reason for the two additional FeC_2^- maxima in the profile of the FeAgNi sample is that Ti contamination on the Si surface as TiO_2^- presents an isobaric interference for the FeC_2^- signal.

and $C_nO_mH^-$ species. However, in contrast to the application of CO, no significant reduction of the MC_2^- signal's intensities is observed in the oxide layers in the case of C_2H_2 flooding. Additionally, the AlC_2^- signal again shows its maximum in the Al_2O_3 layer (Figure S6b). Even worse results are obtained when observing the MC^-, MH_n^-, and MC_nH^- signals, since their intensities are more or less constant through both the pure metal and its oxide layers. Al is again an exception, with the maxima in the Al_2O_3 layer. From the comparison of the depth profiles in Figures 6 and S6, it appears that, at least for the FeAgNi and CrTiAl samples, the CO atmosphere is a better choice than the C_2H_2 atmosphere, since the layers are much more clearly resolved. An improvement in the case of the C_2H_2 atmosphere can only be seen when discriminating between the Ti and TiO_2 layers.

There is also not much difference or improvement for the TiSi sample compared to the CO flooding. As can be seen in Figure S7a, both the SiC^- and SiH^- signals clearly indicate the positions of the Si layers. The depth profile of the TiC_2^- signal has its maxima in the Ti layers, but they are not as pronounced as in the case of the Si species. Moreover, additional smaller local maxima from the TiC_2^- signal can be observed in the Si layers. The intensity of both the SiC^- and SiH^- signals increases with an increase in the relative concentration of the Si in the Ti−Si alloy layers (Figure S7b). We can also observe that the intensity of the TiC_2^- signal decreases as the relative Ti concentration decreases. Therefore, a C_2H_2 atmosphere is more suitable for the analysis of Ti−Si alloys than CO. Nevertheless, we also observe a larger decrease in the sputtering rate compared to the CO flooding (between 30 and 150%, depending on the sample). Based on these measurements, we can conclude that neither O_2, CO, or C_2H_2 is an ideal choice that would provide excellent layer resolution with a clearly resolved multilayer structure for our samples.

H_2 Flooding. Finally, we performed depth profiling with H_2 flooding at a pressure of 7 × 10^{-7} mbar. By using hydrogen, we eliminate the presence of oxygen and simplify the analysis by introducing only one new element. This also means that we can perform a reliable analysis of all the elements except hydrogen. Indeed, the results for both the FeAgNi and CrTiAl samples are very promising. As shown in Figure 7, when the H_2 gas was introduced into the analysis chamber, we were able to record depth profiles that correctly and unambiguously represent the exact multilayer structure of our samples. The maxima of all the $M_nH_m^-$ signals are located in the layers of pure metal, so we can preferentially choose the most intense of them. M_n^- metallic cluster signals also have maxima in the metal layers. The metal oxide layer can be identified from either MO_n^- or MO_nH^- signals. We should also emphasize that the depth resolution is improved compared to all the other atmospheres. As mentioned before, the presence of the AlO_2^- signal in the Al layer (Figure 7b) is due to the unwanted oxidation that occurred during the sample preparation. It should also be mentioned that most metals form very intense $M_nH_m^-$ signals. Exceptions are Ag, which is inert and does not form clusters with any of the gases used, and Al, whose AlH_n^- signals are much weaker than those of the other elements. They are also not as representative of the exact structure as the Al_n^- signals.

While flooded with H_2, very good results were also obtained for the TiSi sample. Figure S8a shows the depth profile of the alternating Ti and Si thin layers. The TiH^- and Si_3^- signals are completely separate and resolve all the thin layers as the intensity of both the TiH^- in the Si layers and the Si_3^- in the Ti layers decreases close to zero—like during the Cs^+ sputtering in a vacuum (Figure 4a), where the reason is dissolved hydrogen in the Ti layers. However, the SiH_n^- signals (SiH^- shown in Figure S8) being the most intense in the Ti layers and having double maxima at both interfaces are problematic due to the matrix effect. The same can be observed, however, for the SiH_n^- signals during the Cs^+ sputtering without gas flooding. Such results can again be

https://doi.org/10.1021/jasms.1c00218
J. Am. Soc. Mass Spectrom. 2022, 33, 31−44

Journal of the American Society for Mass Spectrometry pubs.acs.org/jasms Research Article

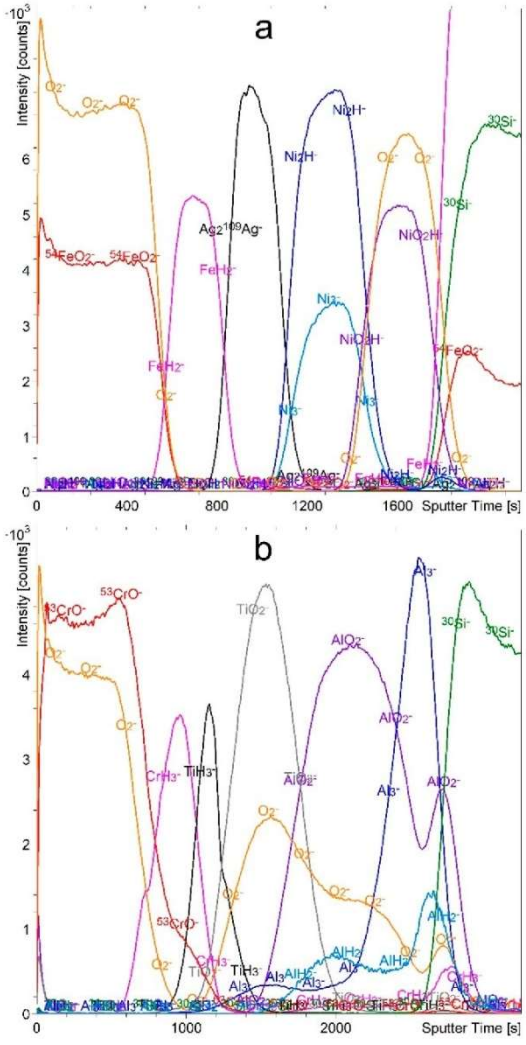

Figure 7. Depth profiles of FeAgNi (a) and CrTiAl (b) samples recorded using a 1 keV Cs^+ sputtering beam and an atmosphere of 7 × 10^{-7} mbar H_2. The intensity-multiplication factors are 0.3 for O_2^-, 0.4 for Ni_2H^-, 0.4 for NiO_2H^-, 0.7 for $^{53}CrO^-$, 0.6 for TiO_2^-, 0.2 for AlO_2^-, 5.0 for AlH_2^-, 0.5 for Al_3^-, and 0.7 for $^{30}Si^-$. The reason for the intensity increase of the FeH_2^- and $^{54}FeO_2^-$ signals in the Si substrate for the profile of the FeAgNi sample is the overlapping of these signals with the Si_n^- signals of different silicon isotopes.

explained by the good solubility of hydrogen in titanium.[80,81] Namely, as seen in Figure S8, the H^- signal also has its maxima in the Ti layers, indicating an elevated concentration. Observations of dissolved hydrogen in the Ti layers even in the TiSi samples exposed only to the ambient conditions (Figure 4a) proves this hypothesis even further. Since ion sputtering causes atom mixing, some Si atoms enter the Ti layers, where they can form SiH_n^- cluster ions with the hydrogen dissolved in titanium. Furthermore, the first SiH_n^- maximum is at the interface between the first Ti and the first Si layer, as no silicon could enter the first Ti layer, which is directly at the sample surface, further supporting the theory of the combined effects of dissolved hydrogen in the Ti layers and sputtering-induced atom mixing. The Si_2H^- signal, however, has three-maxima-shaped signals with the two maxima at each interface and one in the middle of the Si layer. This phenomenon can be explained in a similar way to the previous one. Namely, for the Si_2H^- ion formation, a higher concentration of silicon is needed, and the maxima therefore appear in the middle of the Si layer, where the concentration of silicon is the highest and, on each interface, where the silicon concentration is still sufficient, while the hydrogen concentration starts to rise abruptly due to its solubility in titanium. Nevertheless, the Si_2H^- intensity also remains above zero in the Ti layers. Similarly, the correct as well as the matrix-influenced results for the Ti−Si alloy layers are shown in Figure S8b. As the relative concentration of titanium decreases, the intensity of the TiH^- signal decreases as well. As the relative concentration of Si increases, the intensity of the Si_3^- and Si_2H^- signals also increases, while the intensity of the SiH^- signal decreases. This happens because of the elevated concentration of hydrogen in the layer with a higher concentration of titanium, also causing the intensity rise of the SiH^- signal.

As already mentioned, the matrix effect strongly affects the intensity of the H^- ions as well. Therefore, in the next step we considered the normalization of the SIMS signals to the H^- signal, as shown in Figure 8. After such a normalization, we obtain an improved profile for the alternating Ti and Si multilayer structure with correctly positioned maxima for all the signals (TiH^-, Si_3^-, SiH^-, and Si_2H^-). The only drawback of this approach is that after such a normalization the intensity of the TiH^- signal in the Si layers and the SiH^- signal in the Ti layers does not drop to zero. A similar improvement is seen at the interface between the Ti−Si alloy layers, as shown in Figure 8b. As the relative Ti concentration decreases, the intensity of the TiH^- signal decreases as well. However, as the relative Si concentration increases, the intensity of all the Si-related signals (Si_3^-, Si_2H^-, and SiH^-) also increases.

Therefore, we can conclude that by introducing the H_2 gas into the analysis chamber in the pressure range of 10^{-7} mbar the multilayer structure of all our samples can be clearly and unambiguously resolved. Moreover, we achieved this while analyzing only a depth profile of negative secondary ions recorded during etching with Cs^+ ions. We must also emphasize that flooding with H_2 gas does not significantly affect the sputtering rate for any of our samples, suggesting yet another advantage of hydrogen flooding.

We also tried to use Ar^+ ions for etching in a H_2 atmosphere, but the results were again significantly worse than those obtained by sputtering with Cs^+ ions. Namely, the intensity of the negative secondary ions is too low, similar to that obtained for Ar^+ sputtering without gas flooding. The intensity of the positive secondary ions is slightly higher, but still around 2 orders of magnitude lower than the intensity of the negative secondary ions recorded while sputtering with Cs^+. Also, the multilayer structure is less pronounced and the differentiation between layers less clear than in the depth profiles recorded with the Cs^+ sputter ion beam.

Cluster Secondary-Ion Formation. A recent study has shown that the adsorption of gaseous species on a sample surface is very fast and happens during the ion-etching process as well.[86] We believe, therefore, that the O_2, CO, C_2H_2, and H_2

https://doi.org/10.1021/jasms.1c00218
J. Am. Soc. Mass Spectrom. 2022, 33, 31−44

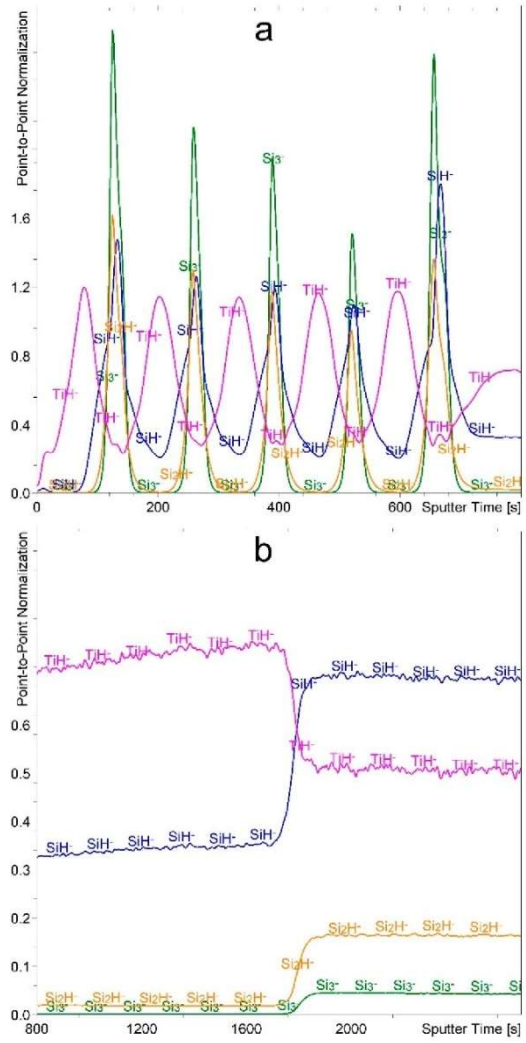

Figure 8. Depth profile of TiSi sample with the scale normalized to the intensity of the H^- signal recorded using a 1 keV Cs^+ sputtering beam and an atmosphere of 7×10^{-7} mbar H_2. The depth profile (a) presents the first 800 s of etching time, while the profile (b) presents the etching time interval between 800 and 2650 s. The intensity-multiplication factor for TiH^- is 15.0.

become adsorbed on the freshly exposed sample surface between the Cs^+ sputtering cycles but do not penetrate extensively into the bulk. The exception is the TiSi sample in a H_2 atmosphere, as in this case, as already presented (Figure 4), hydrogen becomes dissolved in all the thin Ti layers, even when the sample is only exposed to ambient conditions. Such claims are supported by three observations. Namely, if we lower the gas pressure in the analysis chamber, the intensity of the cluster secondary-ion species such as hydrides or carbides will immediately decrease in proportion to the pressure reduction. If the gases were to penetrate deeper into the bulk, as seen for hydrogen and the TiSi sample, the decrease would not be so sudden. Furthermore, a significant decrease in the sputter rate during O_2 flooding can be explained via the O_2 adsorption and the formation of thin oxide layers. As seen in Figure 3, the sputter rate of the metal is greater than the sputter rate of its oxide, since all the layers are of similar thickness. The oxide layers formed on the surfaces of the metals in the O_2 atmosphere have a lower sputter rate, and consequently, the analysis time is prolonged, indicating a reduced sputter rate. The greatest prolongation of the analysis time was seen for the case of the TiSi sample, which initially has no oxide layers. Since the sputter rate changes for the metal layers, but not for the metal oxide layers, this observation confirms our explanation. Figures 6 and S6 indicate that metal carbides have a lower sputter rate compared to the pure metal as well, explaining the moderate reduction in sputter rate during CO and C_2H_2 flooding. Nevertheless, Figure 7 indicates that metal hydrides do not differ significantly from the metals in terms of the sputter rate, so no significant change in the sputter rate for any of our samples is expected while flooding with the H_2 gas, matching our experimental results. Observations made during H_2 flooding are supported by the well-known embrittlement of metals resulting from hydrogen adsorption because the structure of the hydride is less stable.[81,87,88]

Finally, we also noticed that the intensity of many secondary ions, which are not formed as a consequence of the recombination with the gas molecules (Fe^-, Ni^-, Cr^-, Al^-, Al_2^-, Al_3^-, Si^-, Si_2^-, Si_3^-), does not change significantly in comparison with the Cs^+ sputtering in vacuum, regardless of the gas used. Therefore, the processes responsible for the cluster secondary-ion formation observed in our analyses most probably take place exclusively on the surface or just above the surface, in both cases specifically during ion sputtering. Major chemical changes caused by the absorption would probably also cause the changes in the intensity of the mentioned secondary ions, which is not the case. The intensity change of the secondary-ion species connected with the hydrogen dissolved in the TiSi sample provides additional support for such a hypothesis. Our prediction about the cluster-ion origin is further supported by extensive studies concerning the mechanism of their formation, proved by both the computer simulations and the experimental findings. As we were bombarding metallic and ionic (oxide) surfaces with monatomic ions, a collision cascade is the appropriate approximation of the processes involved.[89] Cluster ions formed during a collision cascade are mainly formed from the atoms that were initially first or second neighbors at the surface.[89,90] During ion sputtering, they move as a bound cluster in the selvedge region of the surface, followed by desorption into the gas phase.[91,92] Another, yet similar, explanation is that the cluster-ion formation happens in the near-surface region,[90,93,94] probably as the recombination of a neutral atom and a sputtered ion.[94] Recombination above the sample surface is also the supposed reason for the matrix effect's reduction.[94] Both of described mechanisms correspond to our hypothesis that cluster secondary ions composed of metals and flooding gases are formed on the topmost surface layers or just above the surface after the gas molecule's adsorption, always during the ion-sputtering process.

Last but not least, the reasons behind the greatest improvement in the depth profiles achieved during H_2 flooding have not been proven yet. Nevertheless, we believe that the specificity of the chemical reactions of the different gases is at

https://doi.org/10.1021/jasms.1c00218
J. Am. Soc. Mass Spectrom. 2022, 33, 31−44

play, at least to some degree. Figures S6 and S7 show a significant intensity decrease in the metal oxide signals in the metal layers during the C_2H_2 and H_2 flooding. The same can be seen for the Cs^+ sputtering without gas flooding (Figure 3). Such observations are expected since no oxygen source is present. In contrast, during the CO flooding (Figure 6), the metal oxide signal's intensity stays significant in the metal layers as well due to the CO being a source of both carbon and oxygen. Even more important is the observation of the intensity of the signals in the metal oxide layers. Namely, the intensity of the metal hydride signals decreases to near-zero in the metal oxide layers (Figure 7), while this is not the case for the metal-carbide signals (Figures 6 and S6). The most probable explanation for this is a different mechanism for the reactions with hydrogen and carbon. It appears that hydrogen preferentially forms hydroxides with metal oxides, while carbon rather substitutes for oxygen in the metal oxides, forming metal carbides in a similar manner as in the layers of pure metals. The greatest difference between the intensity of the secondary ions in metal and metal oxide layers in the presence of H_2 among all the atmospheres tested is therefore a consequence of the different reaction mechanisms. Nevertheless, these processes cannot fully explain the improved interface resolution observed during H_2 flooding.

CONCLUSION

Our study shows that introducing different gases into the analysis chamber during SIMS depth profiling can lead to very different depth profiles with respect to the type of gas used. As a result, new information has been obtained. We have found that when using O_2, CO, or C_2H_2 there is an improvement with respect to a vacuum, but only in some specific cases. Therefore, at least two separate depth profiles are needed to explain the results of the analysis correctly and with sufficient confidence. However, since the introduction of these gases also reduces the sputtering rate, the time required for such an analysis is even greater than when two profiles are recorded with two different types of etching ions. In contrast, the introduction of H_2 does not reduce the sputtering rate and shows improved results for all the samples we tested. By only recording the depth profile of the negative secondary ions while using the Cs^+ sputter ion beam and H_2 flooding, we were able to determine the compositional depth of FeAgNi, CrTiAl and TiSi samples while clearly distinguishing between successive layers.

SIMS dual-beam depth profiling in a hydrogen atmosphere in the range of 10^{-7} mbar thus appears to be a successful approach for the analysis of metal, metal oxide, and alloy multilayers. In this way, the interfaces between different metals, metals and their oxides, and different alloys can be determined with a satisfactory depth resolution. It also offers the potential for the analysis of other elements with sufficiently intense secondary anions. Since only one new, nonharmful element is introduced, the analysis does not become complicated. With this approach, sufficient information for the sample's structure determination can be obtained with only a single depth profile. Further studies are necessary to analyze the influence of the hydrogen atmosphere on the chemistry and topography of the crater formed during ion etching and also in relation to the depth resolution.

ASSOCIATED CONTENT

Supporting Information

The Supporting Information is available free of charge at https://pubs.acs.org/doi/10.1021/jasms.1c00218.

TEM images, depth profiles (Figures S1−S8) (PDF)

AUTHOR INFORMATION

Corresponding Author

Janez Kovač − *Jožef Stefan Institute, SI-1000 Ljubljana, Slovenia;* orcid.org/0000-0002-4324-246X; Email: janez.kovac@ijs.si

Authors

Jernej Ekar − *Jožef Stefan Institute, SI-1000 Ljubljana, Slovenia; Jožef Stefan International Postgraduate School, SI-1000 Ljubljana, Slovenia;* orcid.org/0000-0001-8895-4746

Peter Panjan − *Jožef Stefan Institute, SI-1000 Ljubljana, Slovenia*

Sandra Drev − *Jožef Stefan Institute, SI-1000 Ljubljana, Slovenia; Center for Electron Microscopy and Microanalysis, SI-1000 Ljubljana, Slovenia*

Complete contact information is available at: https://pubs.acs.org/10.1021/jasms.1c00218

Author Contributions

All authors have given approval to the final version of the manuscript.

Notes

The authors declare no competing financial interest.

ACKNOWLEDGMENTS

We thank Prof. Siegfried Hofmann for suggestions for the TiSi sample structure and composition. This work was supported by the Slovenian Research Agency (ARRS) through the Program P2-0082.

REFERENCES

(1) Kovač, J.; Finšgar, M. Analysis of the Thermal Stability of Very Thin Surface Layers of Corrosion Inhibitors by Time-of-Flight Secondary Ion Mass Spectrometry. *J. Am. Soc. Mass Spectrom.* **2018**, *29*, 2305−2316.

(2) Kozlica, D. K.; Ekar, J.; Kovač, J.; Milošev, I. Roles of Chloride Ions in the Formation of Corrosion Protective Films on Copper. *J. Electrochem. Soc.* **2021**, *168*, 031504.

(3) Abe, Y.; Komatsu, M.; Okuhira, H. Estimation of ToF-SIMS information depth in micro-corrosion analysis. *Appl. Surf. Sci.* **2003**, *203−204*, 859−862.

(4) Maharjan, N.; Murugan, V. K.; Zhou, W.; Seita, M. Corrosion behavior of laser hardened 50CrMo4 (AISI 4150) steel: A depth-wise analysis. *Appl. Surf. Sci.* **2019**, *494*, 941−951.

(5) Biswas, A.; Abharana, N.; Jha, S. N.; Bhattacharyya, D. Non-destructive elemental depth profiling of Ni/Ti multilayers by GIXRF technique. *Appl. Surf. Sci.* **2021**, *542*, 148733.

(6) Kovač, J.; Bizjak, M.; Praček, B.; Zalar, A. Auger electron spectroscopy depth profiling of Fe-oxide layers on electromagnetic sheets prepared by low temperature oxidation. *Appl. Surf. Sci.* **2007**, *253*, 4132−4136.

(7) Chasoglou, D.; Hryha, E.; Norell, M.; Nyborg, L. Characterization of surface oxides on water-atomized steel powder by XPS/AES depth profiling and nano-scale lateral surface analysis. *Appl. Surf. Sci.* **2013**, *268*, 496−506.

(8) Guryanov, G.; St. Clair, T. P.; Bhat, R.; Caneau, C.; Nikishin, S.; Borisov, B.; Budrevich, A. SIMS quantitative depth profiling of matrix

elements in semiconductor layers. *Appl. Surf. Sci.* **2006**, *252*, 7208−7210.
(9) Ronsheim, P. A. Depth profiling of emerging materials for semiconductor devices. *Appl. Surf. Sci.* **2006**, *252*, 7201−7204.
(10) Sykes, D. Depth profiling techniques for the elemental analysis of semiconductor layers. *Vacuum* **1990**, *40*, 347−349.
(11) Noël, C.; Houssiau, L. Hybrid Organic/Inorganic Materials Depth Profiling Using Low Energy Cesium Ions. *J. Am. Soc. Mass Spectrom.* **2016**, *27*, 908−916.
(12) Gulin, A.; Shakhov, A.; Vasin, A.; Astafiev, A.; Antonova, O.; Kochev, S.; Kabachii, Y.; Golub, A.; Nadtochenko, V. ToF-SIMS depth profiling of nanoparticles: Chemical structure of core-shell quantum dots. *Appl. Surf. Sci.* **2019**, *481*, 144−150.
(13) Krishnan, R.; Swart, H. C.; Thirumalai, J.; Kumar, P. Depth profiling and photometric characteristics of Pr^{3+} doped $BaMoO_4$ thin phosphor films grown using (266 nm Nd-YAG laser) pulsed laser deposition. *Appl. Surf. Sci.* **2019**, *488*, 783−790.
(14) Reiche, I.; Müller, K.; Eveno, M.; Itié, E.; Menu, M. Depth profiling reveals multiple paint layers of Louvre Renaissance paintings using non-invasive compact confocal micro-X-ray fluorescence. *J. Anal. At. Spectrom.* **2012**, *27*, 1715−1724.
(15) Hammer, G. E.; Shemenski, R. M.; Hunt, J. D. Brass-rubber adhesive interphase investigated via depth profiling by using Auger electron spectroscopy. *J. Vac. Sci. Technol., A* **1994**, *12*, 2388−2391.
(16) González-Elipe, A. R.; Holgado, J. P.; Alvarez, R.; Espinós, J. P.; Fernández, A.; Munuera, G. Depth Profiling of Rh/CeO_2 Catalysts: An Alternative Method for Dispersion Analysis. *NATO ASI Ser. B, Physics* **1991**, *265*, 227−235.
(17) González-Elipe, A. R.; Espinós, J. P.; Fernandez, A.; Munuera, G. Depth profiling of catalyst samples: An XPS-based model for the sputtering behavior of powder materials. *J. Catal.* **1991**, *130*, 627−641.
(18) Wagner, M. S. Molecular depth profiling of multilayer polymer films using time-of-flight secondary ion mass spectrometry. *Anal. Chem.* **2005**, *77*, 911−922.
(19) Fletcher, J. S.; Conlan, X. A.; Lockyer, N. P.; Vickerman, J. C. Molecular depth profiling of organic and biological materials. *Appl. Surf. Sci.* **2006**, *252*, 6513−6516.
(20) Brison, J.; Mine, N.; Wehbe, N.; Gillon, X.; Tabarrant, T.; Sporken, R.; Houssiau, L. Molecular depth profiling of model biological films using low energy monoatomic ions. *Int. J. Mass Spectrom.* **2012**, *321*−*322*, 1−7.
(21) Jenčič, B.; Vavpetič, P.; Kelemen, M.; Vencelj, M.; Vogel-Mikuš, K.; Kavčič, A.; Pelicon, P. MeV-SIMS TOF Imaging of Organic Tissue with Continuous Primary Beam. *J. Am. Soc. Mass Spectrom.* **2019**, *30*, 1801−1812.
(22) Malmberg, P.; Kriegeskotte, C.; Arlinghaus, H. F.; Hagenhoff, B.; Holmgren, J.; Nilsson, M.; Nygren, H. Depth profiling of cells and tissues by using C_{60}^+ and SF_5^+ as sputter ions. *Appl. Surf. Sci.* **2008**, *255*, 926−928.
(23) Gilbert, J. B.; Rubner, M. F.; Cohen, R. E. Depth-profiling X-ray photoelectron spectroscopy (XPS) analysis of interlayer diffusion in polyelectrolyte multilayers. *Proc. Natl. Acad. Sci. U. S. A.* **2013**, *110*, 6651−6656.
(24) Zalar, A.; Panjan, P.; Kraševec, V.; Hofmann, S. Alternative model multilayer structures for depth profiling studies. *Surf. Interface Anal.* **1992**, *19*, 50−54.
(25) Theodosiou, A.; Spencer, B. F.; Counsell, J.; Jones, A. N. An XPS/UPS study of the surface/near-surface bonding in nuclear grade graphites: A comparison of monatomic and cluster depth-profiling techniques. *Appl. Surf. Sci.* **2020**, *508*, 144764.
(26) Han, B.; Wang, Z.; Devi, N.; Kondamareddy, K. K.; Wang, Z.; Li, N.; Zuo, W.; Fu, D.; Liu, C. RBS Depth Profiling Analysis of (Ti, Al)N/MoN and CrN/MoN Multilayers. *Nanoscale Res. Lett.* **2017**, DOI: 10.1186/s11671-017-1921-3.
(27) Kessels, M. J. H.; Bijkerk, F.; Tichelaar, F. D.; Verhoeven, J. Determination of in-depth density profiles of multilayer structures. *J. Appl. Phys.* **2005**, *97*, 093513.
(28) Noun, M.; Van Elslande, E.; Touboul, D.; Glanville, H.; Bucklow, S.; Walter, P.; Brunelle, A. High mass and spatial resolution mass spectrometry imaging of Nicolas Poussin painting cross section by cluster TOF-SIMS. *J. Mass Spectrom.* **2016**, *51*, 1196−1210.
(29) Ishitani, T.; Yaguchi, T. Cross-sectional sample preparation by focused ion beam: A review of ion-sample interaction. *Microsc. Res. Tech.* **1996**, *35*, 320−333.
(30) Niehuis, E., Grehl, T.: Depth profiling of inorganic materials. In *ToF-SIMS: Materials Analysis by Mass Spectrometry*, 2nd ed.; IM Publications LLP and Surface Spectra Limited: Chichester, 2013; pp 613−635..
(31) van der Heide, P.: Ion Sources. In *Secondary Ion Mass Spectrometry: An Introduction to Principles and Practices*; John Wiley and Sons: Hoboken, NJ, 2014; pp 161−167.
(32) Steinberger, R.; Walter, J.; Greunz, T.; Duchoslav, J.; Arndt, M.; Molodtsov, S.; Meyer, D. C.; Stifter, D. XPS study of the effects of long-term Ar^+ ion and Ar cluster sputtering on the chemical degradation of hydrozincite and iron oxide. *Corros. Sci.* **2015**, *99*, 66−75.
(33) Houssiau, L.; Mine, N. Molecular depth profiling of polymers with very low energy reactive ions. *Surf. Interface Anal.* **2010**, *42*, 1402−1408.
(34) Wehbe, N.; Houssiau, L. Comparative study of the usefulness of low energy Cs^+, Xe^+, and O_2^+ ions for depth profiling amino-acid and sugar films. *Anal. Chem.* **2010**, *82*, 10052−10059.
(35) Kudriavtsev, Y.; Asomoza, R.; Mansurova, M.; Perez, L. A.; Korol', V. M. Sputtering of the target surface by Cs^+ ions: Steady-state concentration of implanted cesium and emission of CsM^+ cluster ions. *Tech. Phys.* **2013**, *58*, 735−743.
(36) Brison, J.; Houssiau, L. Study of ionization processes during TOF-SIMS analysis by co-sputtering cesium and xenon. *Nucl. Instrum. Methods Phys. Res., Sect. B* **2007**, *259*, 984−988.
(37) Yan, X. L.; Duvenhage, M. M.; Wang, J. Y.; Swart, H. C.; Terblans, J. J. Evaluation of sputtering induced surface roughness development of Ni/Cu multilayers thin films by Time-of-Flight Secondary Ion Mass Spectrometry depth profiling with different energies O_2^+ ion bombardment. *Thin Solid Films* **2019**, *669*, 188−197.
(38) Zhu, Z.; Nachimuthu, P.; Lea, A. S. Molecular depth profiling of sucrose films: A comparative study of C_{60}^{n+} ions and traditional Cs^+ and O_2^+ ions. *Anal. Chem.* **2009**, *81*, 8272−8279.
(39) Shard, A.; Gilmore, I.; Wucher, A. Molecular depth profiling. In *ToF-SIMS: Materials Analysis by Mass Spectrometry*, 2nd ed.; IM Publications LLP and Surface Spectra Limited: Chichester, 2013; pp 311−334.
(40) Delcorte, A., Restrepo, O. A., Czerwinski, B. Cluster SIMS of Organic Materials: Theoretical Insights. In *Cluster Secondary Ion Mass Spectrometry: Principles and Applications*; John Wiley and Sons, 2013; pp 13−55.
(41) Mahoney, C. M., Wucher, A. Molecular Depth Profiling with Cluster Ion Beams. In *Cluster Secondary Ion Mass Spectrometry: Principles and Applications*; John Wiley and Sons, 2013; pp 117−205.
(42) Houssiau, L.; Douhard, B.; Mine, N. Molecular depth profiling of polymers with very low energy ions. *Appl. Surf. Sci.* **2008**, *255*, 970−972.
(43) Tian, H.; Maciążek, D.; Postawa, Z.; Garrison, B. J.; Winograd, N. CO_2 Cluster Ion Beam, an Alternative Projectile for Secondary Ion Mass Spectrometry. *J. Am. Soc. Mass Spectrom.* **2016**, *27*, 1476−1482.
(44) Holzer, S.; Krivec, S.; Kayser, S.; Zakel, J.; Hutter, H. Large O_2 Cluster Ions as Sputter Beam for ToF-SIMS Depth Profiling of Alkali Metals in Thin SiO_2 Films. *Anal. Chem.* **2017**, *89*, 2377−2382.
(45) Brison, J.; Muramoto, S.; Castner, D. G. ToF-SIMS depth profiling of organic films: A comparison between single-beam and dual-beam analysis. *J. Phys. Chem. C* **2010**, *114*, 5565−5573.
(46) Vickerman, J. C. Prologue: ToF-SIMS—An evolving mass spectrometry of materials. In *ToF-SIMS: Materials Analysis by Mass Spectrometry*, 2nd ed.; IM Publications LLP and Surface Spectra Limited: Chichester, 2013; pp 1−37.
(47) Delcorte, A. Fundamentals of organic SIMS: insights from experiments and models. In *ToF-SIMS: Materials Analysis by Mass*

https://doi.org/10.1021/jasms.1c00218
J. Am. Soc. Mass Spectrom. 2022, 33, 31−44

Spectrometry, 2nd ed.; IM Publications LLP and Surface Spectra Limited: Chichester, 2013; pp 87−123.
(48) Priebe, A.; Xie, T.; Bürki, G.; Pethö, L.; Michler, J. The matrix effect in TOF-SIMS analysis of two-element inorganic thin films. *J. Anal. At. Spectrom.* **2020**, *35*, 1156−1166.
(49) Jurewicz, A. J. G.; Olinger, C. T.; Burnett, D. S.; Guan, Y.; Hervig, R.; Rieck, K. D.; Woolum, D. S. Quantifying low fluence ion implants in diamond-like carbon film by secondary ion mass spectrometry by understanding matrix effects. *J. Anal. At. Spectrom.* **2021**, *36*, 194−209.
(50) Gelb, L. D.; Walker, A. V. Toward understanding weak matrix effects in TOF SIMS. *J. Vac. Sci. Technol., B: Nanotechnol. Microelectron.: Mater., Process., Meas., Phenom.* **2018**, *36*, 03F127.
(51) Seah, M. P.; Havelund, R.; Spencer, S. J.; Gilmore, I. S. Quantifying SIMS of Organic Mixtures and Depth Profiles—Characterizing Matrix Effects of Fragment Ions. *J. Am. Soc. Mass Spectrom.* **2019**, *30*, 309−320.
(52) Breuer, L.; Ernst, P.; Herder, M.; Meinerzhagen, F.; Bender, M.; Severin, D.; Wucher, A. Mass spectrometric investigation of material sputtered under swift heavy ion bombardment. *Nucl. Instrum. Methods Phys. Res., Sect. B* **2018**, *435*, 101−110.
(53) Breuer, L.; Tian, H.; Wucher, A.; Winograd, N. Molecular SIMS Ionization Probability Studied with Laser Postionization: Influence of the Projectile Cluster. *J. Phys. Chem. C* **2019**, *123*, 565−574.
(54) Breuer, L.; Popczun, N. J.; Wucher, A.; Winograd, N. Reducing the Matrix Effect in Molecular Secondary Ion Mass Spectrometry by Laser Post-Ionization. *J. Phys. Chem. C* **2017**, *121*, 19705−19715.
(55) Popczun, N. J.; Breuer, L.; Wucher, A.; Winograd, N. Effect of SIMS ionization probability on depth resolution for organic/inorganic interfaces. *Surf. Interface Anal.* **2017**, *49*, 933−939.
(56) Popczun, N. J.; Breuer, L.; Wucher, A.; Winograd, N. Ionization Probability in Molecular Secondary Ion Mass Spectrometry: Protonation Efficiency of Sputtered Guanine Molecules Studied by Laser Postionization. *J. Phys. Chem. C* **2017**, *121*, 8931−8937.
(57) Popczun, N. J.; Breuer, L.; Wucher, A.; Winograd, N. On the SIMS Ionization Probability of Organic Molecules. *J. Am. Soc. Mass Spectrom.* **2017**, *28*, 1182−1191.
(58) Franzmann, M.; Bosco, H.; Hamann, L.; Walther, C.; Wendt, K. Resonant laser−SNMS for spatially resolved and element selective ultra-trace analysis of radionuclides. *J. Anal. At. Spectrom.* **2018**, *33*, 730−737.
(59) Laser post-ionisation—fundamentals. In *ToF-SIMS: Materials Analysis by Mass Spectrometry*, 2nd ed.; IM Publications LLP and Surface Spectra Limited: Chichester, 2013; pp 217−246.
(60) Kopnarski, M., Jenett, H. Electron-Impact (EI) Secondary Neutral Mass Spectrometry (SNMS). In *Surface and Thin Film Analysis*; Wiley-VCH Verlag: Weinheim, 2011; pp 161−177.
(61) Oechsner, H. Electron Gas SNMS. In *Secondary Ion Mass Spectrometry SIMS V*; Springer: Berlin, 1986; pp 70−74.
(62) Wilson, R.; Van Den Berg, J. A.; Vickerman, J. C. Quantitative surface analysis using electron beam SNMS: Calibrations and applications. *Surf. Interface Anal.* **1989**, *14*, 393−400.
(63) Wilson, R.; Van den Berg, J. A.; Vickerman, J. C. Surface analysis using electron beam SNMS, applications and investigations of sputter yields. *Vacuum* **1989**, *39*, 1089−1093.
(64) Debord, J. D.; Prabhakaran, A.; Eller, M. J.; Verkhoturov, S. V.; Delcorte, A.; Schweikert, E. A. Metal-assisted SIMS with hypervelocity gold cluster projectiles. *Int. J. Mass Spectrom.* **2013**, *343*−*344*, 28−36.
(65) Dunham, S. J. B.; Comi, T. J.; Ko, K.; Li, B.; Baig, N. F.; Morales-Soto, N.; Shrout, J. D.; Bohn, P. W.; Sweedler, J. V. Metal-assisted polyatomic SIMS and laser desorption/ionization for enhanced small molecule imaging of bacterial biofilms. *Biointerphases* **2016**, *11*, 02A325.
(66) Yamazaki, A., Tobe, T., Akiba, S., Owari, M. Metal-Assisted SIMS for three-dimensional analysis using shave-off section processing. In *Surf. Interface Anal.*; John Wiley and Sons Ltd., 2014; pp 1215−1218.
(67) Fitzgerald, J. J. D.; Kunnath, P.; Walker, A. V. Matrix-enhanced secondary ion mass spectrometry (ME SIMS) using room temperature ionic liquid matrices. *Anal. Chem.* **2010**, *82*, 4413−4419.
(68) Cai, L.; Sheng, L.; Xia, M.; Li, Z.; Zhang, S.; Zhang, X.; Chen, H. Graphene Oxide as a Novel Evenly Continuous Phase Matrix for TOF-SIMS. *J. Am. Soc. Mass Spectrom.* **2017**, *28*, 399−408.
(69) Locklear, J. E.; Guillermier, C.; Verkhoturov, S. V.; Schweikert, E. A. Matrix-enhanced cluster-SIMS. *Appl. Surf. Sci.* **2006**, *252*, 6624−6627.
(70) Wu, K. J.; Odom, R. W. Matrix-enhanced secondary ion mass spectrometry: A method for molecular analysis of solid surfaces. *Anal. Chem.* **1996**, *68*, 873−882.
(71) Lanni, E. J.; Dunham, S. J. B.; Nemes, P.; Rubakhin, S. S.; Sweedler, J. V. Biomolecular imaging with a C_{60}-SIMS/MALDI dual ion source hybrid mass spectrometer: Instrumentation, matrix enhancement, and single cell analysis. *J. Am. Soc. Mass Spectrom.* **2014**, *25*, 1897−1907.
(72) Brison, J.; Vitchev, R. G.; Houssiau, L. Cesium/xenon co-sputtering at different energies during ToF-SIMS depth profiling. *Nucl. Instrum. Methods Phys. Res., Sect. B* **2008**, *266*, 5159−5165.
(73) Tian, H.; Wucher, A.; Winograd, N. Dynamic Reactive Ionization with Cluster Secondary Ion Mass Spectrometry. *J. Am. Soc. Mass Spectrom.* **2016**, *27*, 285−292.
(74) Tian, H.; Wucher, A.; Winograd, N. Reduce the matrix effect in biological tissue imaging using dynamic reactive ionization and gas cluster ion beams. *Biointerphases* **2016**, *11*, 02A320.
(75) Tian, H.; Wucher, A.; Winograd, N. Reducing the Matrix Effect in Organic Cluster SIMS Using Dynamic Reactive Ionization. *J. Am. Soc. Mass Spectrom.* **2016**, *27*, 2014−2024.
(76) Kudriatsev, Y.; Villegas, A.; Gallardo, S.; Ramirez, G.; Asomoza, R.; Mishurnuy, V. Cesium ion sputtering with oxygen flooding: Experimental SIMS study of work function change. *Appl. Surf. Sci.* **2008**, *254*, 4961−4964.
(77) Williams, P.; Franzreb, K.; Sobers, R. C.; Lörinčík, J. On the effect of oxygen flooding on the detection of noble gas ions in a SIMS instrument. *Nucl. Instrum. Methods Phys. Res., Sect. B* **2010**, *268*, 2758−2765.
(78) Ng, C. M.; Wee, A. T. S.; Huan, C. H. A.; See, A. Effects of oxygen flooding on crater bottom composition and roughness in ultrashallow secondary ion mass spectrometry depth profiling. *J. Vac. Sci. Technol., B: Microelectron. Process. Phenom.* **2001**, *19*, 829−835.
(79) Priebe, A.; Utke, I.; Pethö, L.; Michler, J. Application of a Gas-Injection System during the FIB-TOF-SIMS Analysis - Influence of Water Vapor and Fluorine Gas on Secondary Ion Signals and Sputtering Rates. *Anal. Chem.* **2019**, *91*, 11712−11722.
(80) Wipf, H. Solubility and diffusion of hydrogen in pure metals and alloys. *Phys. Scr.* **2001**, *T94*, 43−51.
(81) Lewis, F. A. Solubility of hydrogen in metals. *Pure Appl. Chem.* **1990**, *62*, 2091−2096.
(82) Vigdorchik, S. A.; Kolachev, B. A.; Fishgoit, A. V. Absorption of hydrogen by titanium alloys in annealing in air. *Mater. Sci.* **1980**, *16*, 120−122.
(83) Saxena, S. K.; Drozd, V.; Durygin, A. Synthesis of metal hydride from water. *Int. J. Hydrogen Energy* **2007**, *32*, 2501−2503.
(84) Tanaka, T.; Keita, M.; Azofeifa, D. E. Theory of Hydrogen Absorption in Metal Hydrides. *Phys. Rev. B: Condens. Matter Mater. Phys.* **1981**, *24*, 1771−1776.
(85) Nanba, Y.; Tsutsumi, T.; Ishimoto, T.; Koyama, M. Theoretical Study of the Hydrogen Absorption Mechanism into a Palladium Nanocube Coated with a Metal−Organic Framework. *J. Phys. Chem. C* **2017**, *121*, 14611−14617.
(86) Sameshima, J.; Numao, S. Behavior and procedure of background signal formation of hydrogen, carbon, nitrogen and oxygen in silicon wafer during depth profiling using dual-beam TOF-SIMS. *Surf. Sci. Anal.* **2021**, DOI: 10.1002/sia.7035.
(87) Louthan, M. R., Jr.; Caskey, G. R., Jr.; Donovan, J. A.; Rawl, D. E., Jr. Hydrogen embrittlement of metals. *Mater. Sci. Eng.* **1972**, *10*, 357−368.

https://doi.org/10.1021/jasms.1c00218
J. Am. Soc. Mass Spectrom. 2022, 33, 31−44

(88) Bhadeshia, H. K. D. H. Prevention of hydrogen embrittlement in steels. *ISIJ Int.* **2016**, *56*, 24−36.
(89) Urbassek, H. M. Status of cascade theory. In *ToF-SIMS: Materials Analysis by Mass Spectrometry*, 2nd ed.; IM Publications LLP and Surface Spectra Limited: Chichester, 2013; pp 67−86.
(90) Vlekken, J.; D'Olieslaeger, M.; Knuyt, G.; Vandervorst, W.; De Schepper, L. Investigation of the formation process of MCs^+-molecular ions during sputtering. *J. Am. Soc. Mass Spectrom.* **2000**, *11*, 650−658.
(91) Honda, F.; Lancaster, G. M.; Fukuda, Y.; Rabalais, J. W. SIMS study of the mechanism of cluster formation during ion bombardment of alkali halides. *J. Chem. Phys.* **1978**, *69*, 4931−4937.
(92) Lancaster, G. M.; Honda, F.; Fukuda, Y.; Rabalais, J. W. Secondary ion mass spectrometry of molecular solids. Cluster formation during ion bombardment of frozen water, benzene, and cyclohexane. *J. Am. Chem. Soc.* **1979**, *101*, 1951−1958.
(93) Vlekken, J.; Wu, T. D.; D'Olieslaeger, M.; Knuyt, G.; De Schepper, L.; Stals, L. M. Monte Carlo simulation of the formation of MCs^+ molecular ions. *Int. J. Mass Spectrom. Ion Processes* **1996**, *156*, 61−66.
(94) Saha, B.; Chakraborty, P. Secondary ion mass spectrometry of MCs_n^+ molecular ion complexes. *Nucl. Instrum. Methods Phys. Res., Sect. B* **2007**, *258*, 218−225.

https://doi.org/10.1021/jasms.1c00218
J. Am. Soc. Mass Spectrom. 2022, 33, 31−44

Supporting information

ToF-SIMS Depth Profiling of Metal, Metal-Oxide and Alloy Multilayers in Atmospheres of H_2, C_2H_2, CO and O_2

Jernej Ekar,[1,2] Peter Panjan,[1] Sandra Drev,[1,3] Janez Kovač[1,*]

[1]Jožef Stefan Institute, Jamova cesta 39, SI-1000 Ljubljana, Slovenia
[2]Jožef Stefan International Postgraduate School, Jamova cesta 39, SI-1000 Ljubljana, Slovenia
[3]Center for electron microscopy and microanalysis, Jamova cesta 39, SI-1000 Ljubljana, Slovenia

Corresponding Author

* Janez Kovač
Jožef Stefan Institute, Jamova cesta 39, SI-1000 Ljubljana, Slovenia
email: janez.kovac@ijs.si

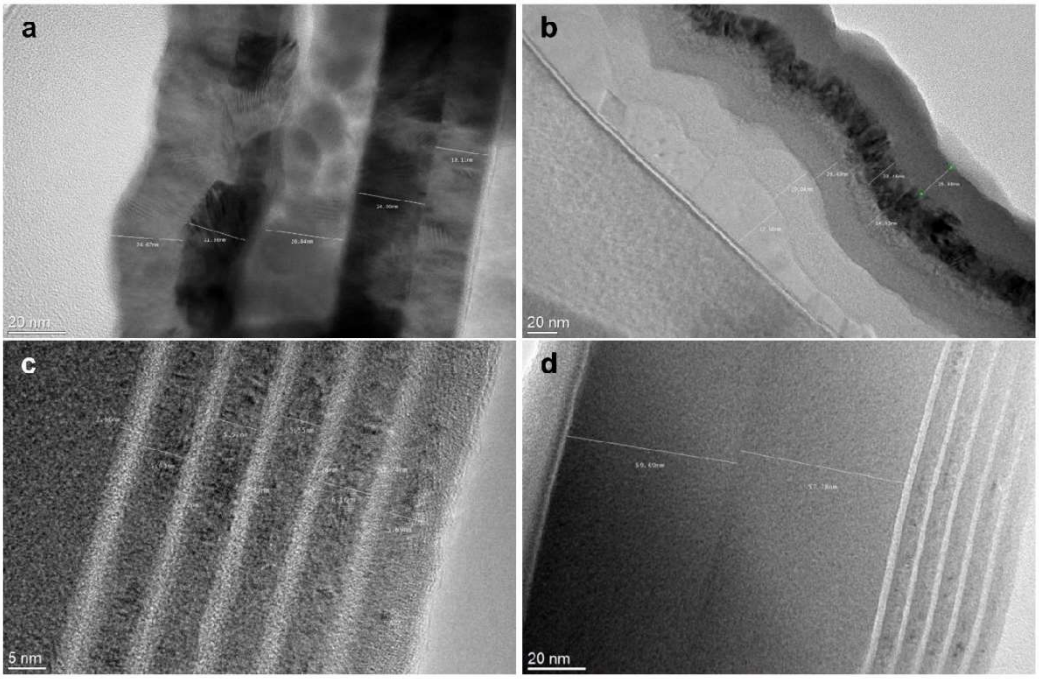

Figure S1. TEM images with the measured thicknesses of the cross sections of the FeAgNi sample (**a**), CrTiAl sample (**b**), thin alternating layers of Ti and Si in the TiSi sample (**c**), and the whole TiSi sample (**d**).

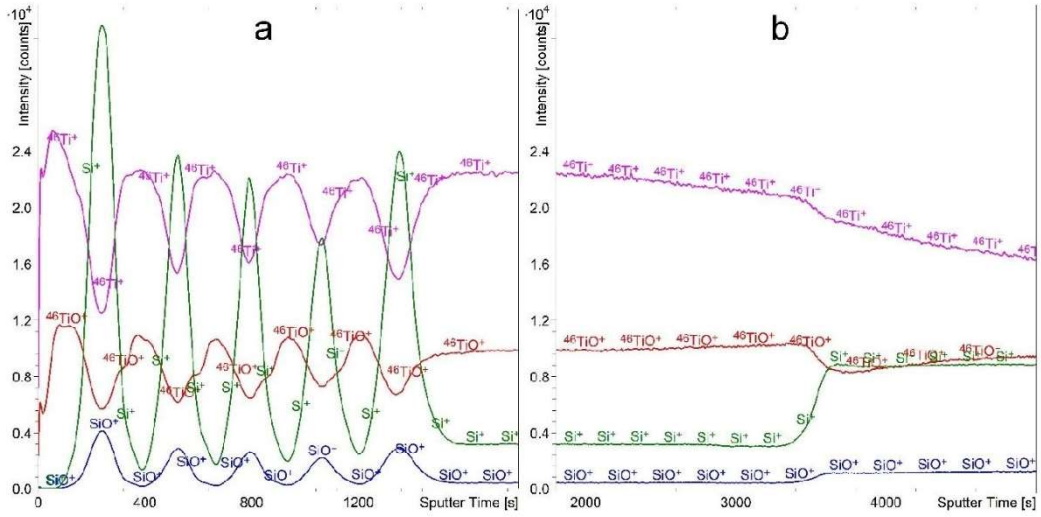

Figure S2. Depth profile of TiSi sample recorded using a 1-keV O_2^+ sputtering beam. The depth profile (**a**) presents the first 1800 s of etching time while the profile (**b**) presents the etching time interval between 1800 and 5000 s. The intensity-multiplication factor for Si^+ is 0.4.

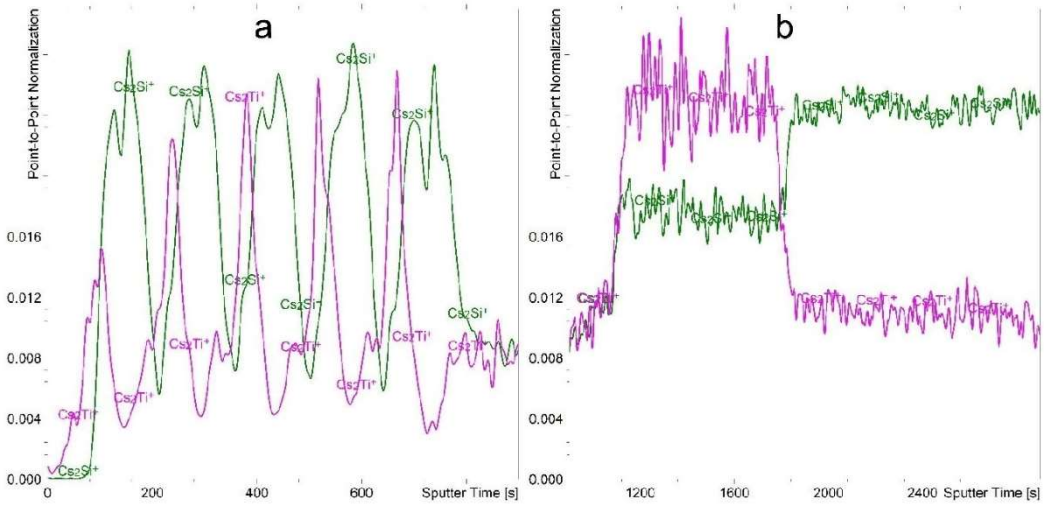

Figure S3. Depth profile of TiSi sample with the scale normalized to the intensity of the Cs_2^+ signal recorded using a 1-keV Cs^+ sputtering beam. The depth profile (**a**) presents the first 900 s of etching time while the profile (**b**) presents the etching time interval between 900 and 2900 s. The intensity-multiplication factor for Cs_2Ti^+ is 4.0.

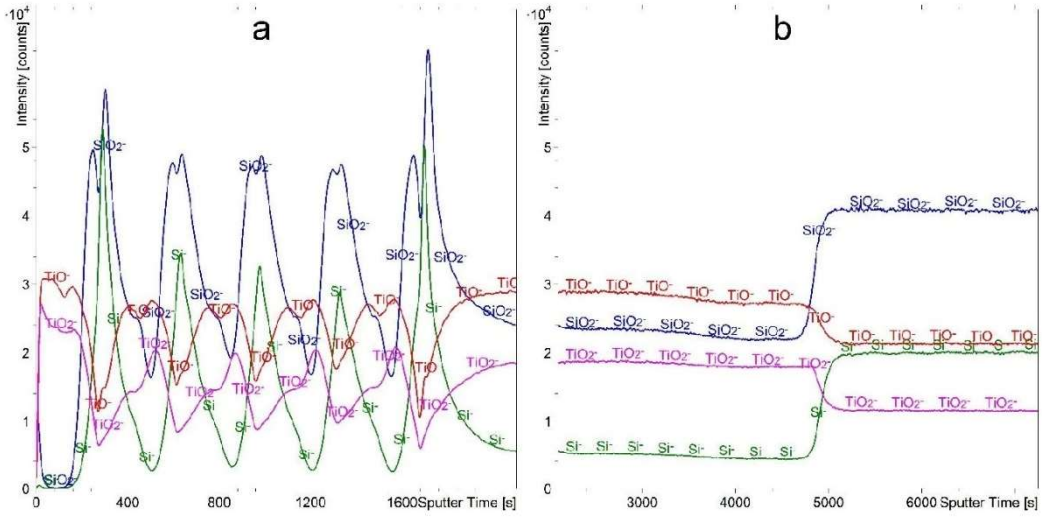

Figure S4. Depth profile of TiSi sample recorded using a 1-keV Cs^+ sputtering beam and an atmosphere of $8 \cdot 10^{-8}$ mbar O_2. The depth profile (**a**) presents the first 2100 s of etching time while the profile (**b**) presents the etching time interval between 2100 and 7250 s.

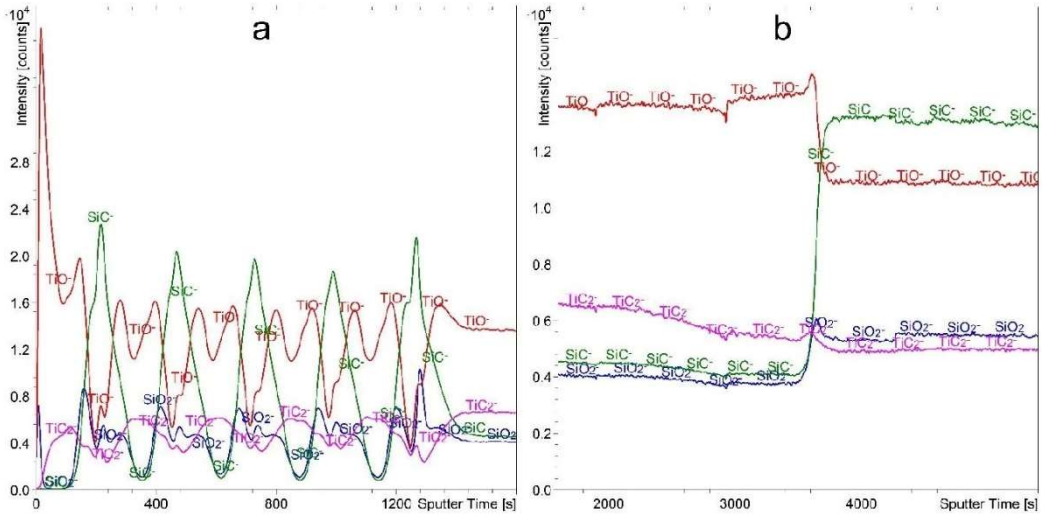

Figure S5. Depth profile of TiSi sample recorded using a 1-keV Cs^+ sputtering beam and an atmosphere of $2 \cdot 10^{-7}$ mbar CO. The depth profile (**a**) presents the first 1600 s of etching time while the profile (**b**) presents the etching time interval between 1600 and 5400 s. The intensity-multiplication factors are 1.5 for TiC_2^- and 0.5 for SiC^-.

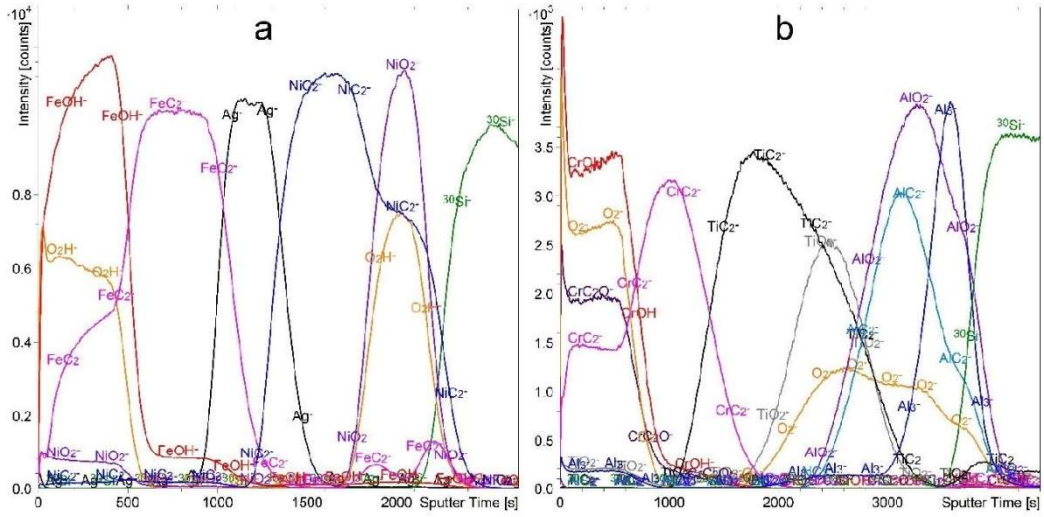

Figure S6. Depth profiles of FeAgNi (**a**) and CrTiAl (**b**) samples recorded using a 1-keV Cs^+ sputtering beam and an atmosphere of $2{\cdot}10^{-7}$ mbar C_2H_2. The intensity-multiplication factors are 0.4 for $FeOH^-$, 0.3 for FeC_2^-, 0.3 for NiC_2^-, 0.4 for O_2^-, 0.2 for CrC_2^-, 0.7 for TiC_2^-, 0.3 for AlO_2^-, 0.2 for AlC_2^-, 0.4 for Al_3^- and 0.4 for $^{30}Si^-$. The reason for the two additional FeC_2^- maxima in the profile of the FeAgNi sample is Ti contamination on the Si surface as TiO_2^- presents an isobaric interference for the FeC_2^- signal.

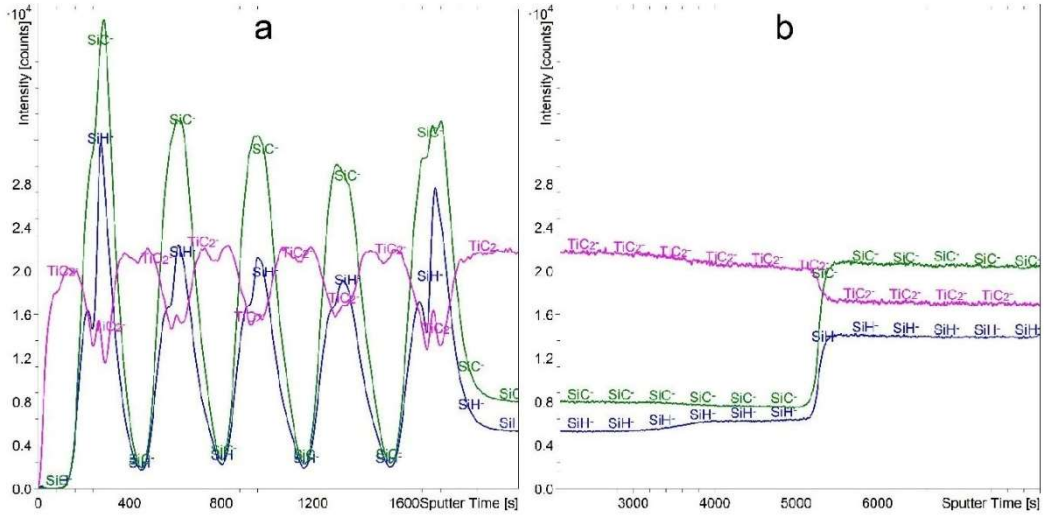

Figure S7. Depth profile of TiSi sample recorded using a 1-keV Cs^+ sputtering beam and an atmosphere of $2{\cdot}10^{-7}$ mbar C_2H_2. The depth profile (**a**) presents the first 2100 s of etching time while the profile (**b**) presents the etching time interval between 2100 and 8000 s. The intensity-multiplication factor for TiC_2^- is 4.0.

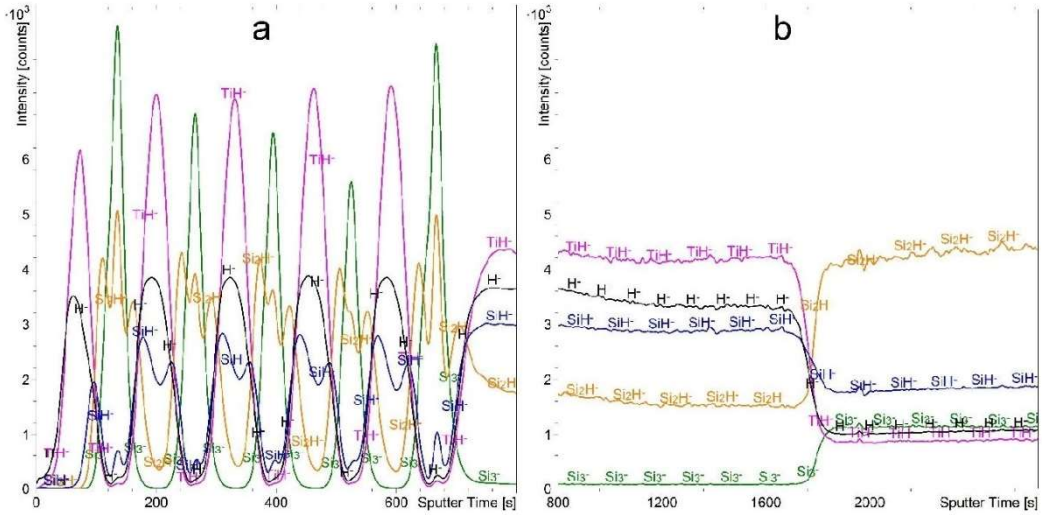

Figure S8. Depth profile of TiSi sample recorded using a 1-keV Cs^+ sputtering beam and an atmosphere of $7 \cdot 10^{-7}$ mbar H_2. The depth profile (**a**) presents the first 800 s of etching time while the profile (**b**) presents the etching time interval between 800 and 2650 s. The intensity-multiplication factors are 0.04 for H^- and 0.1 for SiH^-.

Chapter 5

Article 2: Comparison of Depth Profiling with GDOES in an Ar and Ar-O_2 Plasma, and SIMS Depth Profiling in an H_2 Atmosphere

Glow-discharge optical emission spectroscopy (GDOES) is a technique that is, similar to SIMS, used for depth profiling. However, there are quite a few differences between these two methods. GDOES works by sample etching induced by the glow-discharge plasma directed onto the sample surface. To obtain plasma, much higher pressure than in SIMS is needed, generally around 1 mbar. The results of higher pressure are also higher flux density of particles bombarding the sample and consequent higher sputter rates. They are one or two orders of magnitude higher than what is a standard for the ion guns used with methods like SIMS and XPS. Consequently, the GDOES method is more suitable for the depth profiling of thicker layers with a thickness between a few 100 nm and a few μm. In the case of GDOES, the information about the chemical composition is obtained by measuring the optical emission spectra of plasma-exited atoms sputtered from the sample surface. Therefore, GDOES only gives the elemental information. On the other hand, it offers better quantification possibilities than SIMS.

The purpose of this study was to apply GDOES depth profiling for the characterization of thin organic films on metallic substrate and compare such analyses with the SIMS and XPS analyses. For this purpose, polymerized amine films were initially deposited on the stainless steel samples. They were prepared by plasma-enhanced chemical vapor deposition (PECVD) while using a combination of Ar and cyclopropylamine precursor. Prepared samples were analyzed with the GDOES method using plasma sustained by an asymmetric radio-frequency (RF) capacitively coupled discharge. The use of the RF plasma was needed because polyamine films are insulating and classical direct-current (DC) discharge is incompatible with the samples that do not conduct electric current. Plasma was created in the pure Ar and the mixture of Ar with 4 vol% of O_2. When pure Ar plasma was used, GDOES depth profiles were not ideal especially concerning the polyamine film/stainless steel interface. Extensive retention of C and N signals was observed in the metallic substrate. The possible explanations are the redeposition of C and N atoms to the different parts of the GDOES instrument and also the sample itself, the formation of polyamine droplets due to the heating of the sample and consequent shrinkage and melting, and the formation of extensive surface roughness with notable topographical structures on the bottom of the profiling crater. The issue of the broadened interface was successfully solved

with the addition of 4 vol% of O_2 in Ar plasma. In this case, no C and N retention was observed which is probably due to the effects of the chemical etching caused by the reactive oxygen species. It was calculated that the probability of the oxygen atom from the plasma interacting with the carbon on the surface is close to 0.1. Although it appears that even more pronounced topographical structures are created when O_2 is added, there is no indication of material redeposition. Furthermore, combined Ar + O_2 etching substantially increases the sputter rate, from 3.3 nm/s when profiling in the pure Ar to 83 nm/s when using the combination of both gases.

SIMS and XPS methods were used in parallel to characterize the polymerized amine films on stainless steel substrates to compare the results obtained with the GDOES depth profiling. SIMS and XPS analyses confirmed the positive effect of the O_2 addition to the Ar plasma for the GDOES depth profiling of organic films and appropriate representation of the GDOES depth profiles. Accounting for the composition of the organic thin film, a 500 eV Cs^+ ion beam in the H_2 atmosphere was used for the sputtering during the SIMS depth profiling, promoting the formation of negative secondary ions. Analysis of these ions clearly shows the oxide layer on the top of the stainless steel substrate, which is much less pronounced in the GDOES and XPS profiles. To determine the oxide/metal interface unambiguously, our novel approach of H_2 flooding was successfully applied during SIMS measurements. Intense metal hydride ions like CrH_2^-, FeH^-, and NiH_2^- were formed in the metallic substrate while their intensities were close to zero in the metal oxide layer. This study is an example of the applicability of the H_2 flooding approach for the SIMS depth profiling of the different types of real-life samples composed of profoundly different layers. Results obtained in this study confirmed the hypotheses 1, 3, and 4.

Contributions of the Ph.D. dissertation author: investigation via ToF-SIMS depth profiling, and writing the parts of the manuscript describing the results of the SIMS analyses.

Applied Surface Science 581 (2022) 152292

Contents lists available at ScienceDirect

Applied Surface Science

journal homepage: www.elsevier.com/locate/apsusc

Full Length Article

Depth profiling of thin plasma-polymerized amine films using GDOES in an Ar-O_2 plasma

Janez Kovač [a,*], Jernej Ekar [a,b], Miha Čekada [c], Lenka Zajíčková [d,e], David Nečas [f], Lucie Blahová [d], Jiang Yong Wang [g], Miran Mozetič [a]

[a] Department for Surface Engineering, Jozef Stefan Institute, Jamova cesta 39, Ljubljana SI 1000, Slovenia
[b] Jozef Stefan International Postgraduate School, Jamova cesta 39, Ljubljana SI 1000, Slovenia
[c] Department of Thin Films and Surfaces, Jozef Stefan Institute, Jamova cesta 39, Ljubljana SI 1000, Slovenia
[d] Central European Institute of Technology – CEITEC, Brno University of Technology, Purkyňova 123, Brno 61200, Czech Republic
[e] Department of Condensed Matter Physics, Faculty of Science, Masaryk University, Kotlářská 2, Brno 61200, Czech Republic
[f] Central European Institute of Technology – CEITEC, Brno University of Technology, Purkyňova 123, Brno 61200, Czech Republic
[g] Department of Physics, Shantou University, 243 Daxue Road, Shantou, Guangdong 515063, China

ARTICLE INFO

Keywords:
GDOES
Depth profile
Amine plasma polymer
Ar-O_2 plasma

ABSTRACT

Thin polymer films were deposited on polished stainless-steel samples by PECVD from a cyclopropylamine precursor and characterized by X-ray photoelectron spectroscopy, secondary-ion mass spectrometry and glow-discharge optical emission spectroscopy (GDOES) depth profiling. These depth profiles exhibited reasonable agreement. The GDOES involved the erosion of the polymer films in plasma sustained by an asymmetric RF capacitively coupled discharge using both Ar and Ar-O_2 gases. The application of pure Ar caused unwanted effects, such as the broadening of the polymer-film/substrate interface, which were suppressed when using the mixture with oxygen. Another benefit of oxygen was a significant increase in the etching rate by a factor of about 15 as compared to pure argon. The mechanisms involved in the depth profiling using the mixture of gases were elaborated in some detail, taking into account plasma parameters typical for an asymmetric, capacitively coupled RF discharge in a small volume. The main benefit of using the Ar/O_2 GDOES profiling with respect to XPS and SIMS depth profiling is the increased sputtering rate for polymer films. Comparing the GDOES depth profiling with the Ar/O_2 mixture with profiling in pure Ar, the benefits are a higher sputtering rate and better depth resolution at the polymer/substrate interface.

1. Introduction

Glow-discharge optical emission spectroscopy (GDOES) is a technique used for the depth profiling of thin films. It was developed about 50 years ago [1], and the first commercial instrument was developed in the 1980 s. A review of this technique, summarizing developments up to 2005, was prepared by Hoffmann et al. [2]. GDOES enables the rapid depth profiling of a variety of samples. Compared to other techniques that only operate well in ultra-high-vacuum conditions, such as Auger electron spectroscopy (AES), X-ray photoelectron spectroscopy (XPS) and secondary-ion mass spectrometry or secondary-neutral mass spectrometry (SIMS and SNMS, respectively), GDOES operates well at a medium pressure of the order of 100 Pa. The ion current used for sputtering the samples is thus much larger in GDOES than in these other techniques, and so is the sputtering rate. The classic techniques for depth profiling involve a sputtering rate of the order of nm/s, while GDOES operates at an order of magnitude higher rate. The acquisition of optical lines arising from atomic transitions is almost instant due to the sophisticated optical spectrometer. Traditional GDOES instruments employ direct-current (DC) discharges as the ion sources, but advanced versions are equipped with radio-frequency (RF) discharges. The advantage of RF discharges is that an electric current in the frequency range of the order of MHz also flows through any dielectric material placed on the powered electrode, so such versions are also suitable for the depth profiling of insulators, providing their thickness is reasonable. Modern instruments allow for pulsed RF discharges.

Despite the possibility to etch dielectrics, the literature on the GDOES depth profiling of polymer films is scarce. Carquigny et al. [3]

* Corresponding author.
E-mail address: janez.kovac@ijs.si (J. Kovač).

https://doi.org/10.1016/j.apsusc.2021.152292
Received 6 July 2021; Received in revised form 1 December 2021; Accepted 18 December 2021
Available online 28 December 2021

used this technique for the characterization of thin polypyrrole films loaded with dopants for pharmaceutical applications. She employed a flush time of 500 s, an argon pressure of 400 Pa, and discharge power of 20 W. The thickness of the polymer films prepared by electrodeposition was of the order of 10 μm, and the acquisition of the GDOES depth profile took about 10 min. Similar material was deposited with a comparable technique by Cysewska et al. [4], and the depth-profile acquisition time was also about 10 min. Similar results with doped polypyrrole films were also reported by Sizun et al. [5]. Giaveri et al. [6] prepared thin films of doped polysiloxane-epoxy resin with a thickness of about 50 μm and determined the composition of such coatings, which are useful as high-temperature corrosion-protection coatings. A detailed study of the GDOES characterization of thin polymer films was reported by Moutarlier et al. [7]. They deposited polyaniline films by electrochemical methods and characterized them thoroughly by GDOES. They used a flush time of 60 s, a discharge power of 10 W, and discharge pressure of 400 Pa. They found these parameters to be the most suitable for depth profiling. The thickness of the deposited films as determined by profilometry was between 0.7 and 7 μm. Relatively porous polymer films were obtained with a roughness of approximately 100 nm. The depth profiles were acquired in a few minutes. Groza et al. studied different polymer-composite layers of doped hydroxyapatite polydimethylsiloxanes with a thickness below 1 μm using GDOES at a pressure of 650 Pa, a RF discharge power of 35 W in pulsed mode at a pulse frequency of 1 kHz and a duty cycle of 0.25 [8]. Surmeian et al. [9] applied both GDOES and glow-discharge time-of-flight mass spectrometry (GD-TOFMS) to study the depth profiles of polymer films. The films for GDOES were sputtered at a discharge pressure of 650 Pa, 25 W of RF power operating in pulsed mode at 3 kHz, and a duty cycle of 0.25. For GD-TOFMS the authors found suitable parameters, i.e., 700 Pa of pressure and 30 W of RF power in the pulsed mode with a pulse duration of 1 ms and a period of 4 ms. Mass spectra were recorded over the entire pulse duration and thereby also in the plasma afterglow. The above-cited researchers always sustained gaseous plasma in the GDOES in pure argon. GDOES depth profiling was applied by Y. Liu et al. to very thin organic films like a self-assembled thiourea layer on copper. The authors showed that by using the MRI (mixing-roughness-information depth) model for GDOES depth profiling, a very good depth resolution (Δz as low as 0.5 nm) could be obtained [10]. Although some GDOES devices also allow a mixture of argon and oxygen for the depth profiling of samples, there are not many scientific papers investigating this topic. In two papers, Fernandez et al. studied the influence of hydrogen, nitrogen, and oxygen additions to argon for RF-GDOES depth profiling [11,12]. They found a decrease in the sputtering rate when adding oxygen to argon, as compared with pure argon. They also reported a great potential to improve the depth resolution for thin-film depth profiling when using gas mixtures. Takahara et al. studied the influence of small quantities of oxygen and hydrogen to argon on GDOES depth profiling of graphite electrodes in lithium-ion batteries. They discussed profile analysis, both its speed and quality. They found that adding oxygen to argon plasma increased the sputtering rate on the graphite layer but the chemical etching was more inhomogeneous in this case [13]. Fischer et al. studied the influence of controlled addition of N_2 and of O_2 to Ar on the sputtering rate, the emission intensity of spectral lines in a DC glow discharge for bulk samples of the pure metals Al, Ti, Fe, Ni, Cu, and Ag. The effect of the gaseous addition was a decrease in the sputtering rate of metals with increasing concentrations of N_2 or O_2 [14].

The scientific literature on gaseous plasma created in oxygen-containing gas mixtures with a high-frequency discharge is abundant, and so is the literature on the interaction of such plasma with polymer materials. Recent review papers such as [15], [16] and [17] summarize the advances in both scientific niches and provide suitable references. Of particular relevance are papers reporting the behavior of plasma sustained in a mixture of argon and oxygen at a discharge power density similar to that applied in modern RF-driven GDOES instruments. A complete description of gaseous plasma sustained in a tube filled with Ar-O_2 was prepared by Kutasi et al. [18]. They included over 100 reactions occurring in the gas mixture depending on plasma conditions. The discharge tube was 5 mm in diameter and the power density of the order of 10 W/cm^3, similar to the discharges employed in RF-driven GDOES. They found the dissociation fraction of oxygen molecules close to 50% at a pressure of several 100 Pa and an oxygen concentration in the gas mixture of 4%. The dissociation fraction decreased with increasing probability for the heterogeneous surface recombination of O atoms to parent molecules. At a recombination coefficient of 0.01, the dissociation fraction was about 35% at a pressure of 267 Pa, with 5% of oxygen in the Ar-O_2 mixture. For a coefficient of 0.1, the dissociation fraction was much lower than about 5%. In general, the O-atom density was of the order of 10^{21} in this gas mixture. Therefore, orders of magnitude larger than the density of any ions. The ion densities were much lower, of the order of 10^{17} m^{-3} for Ar^+, 10^{16} m^{-3} for O^+, and 10^{15} m^{-3} for O_2^+. The density of Ar metastables was of the order of 10^{17} m^{-3}. These data represent an important estimation of the plasma parameters in the discharge tube of a modern GDOES driven by an RF discharge.

In this work, we addressed the important challenges in the field of plasma polymer interactions like the synergy of the ion sputtering and the reactive chemical etching of polymer by the oxygen addition in the Ar-plasma applied in GDOES configuration. We report experiments performed using both pure argon and a mixture of Ar + 4 vol% of O_2 for GDOES depth profiling at various discharge parameters like power and gas pressure. We discuss the results in terms of the scientific literature on the interaction of Ar-O_2 plasma with polymer materials. We also addressed artifacts and interface broadening observed by GDOES depth profiling of polymer layer in pure Ar and Ar/O_2 mixture. The beneficial results when using oxygen are emphasized. Further, we compare GDEOS depth profiling of the polymer layer with the ToF-SIMS and XPS depth profiling of such layer. We believe that such a systematic study of GDOES etching of polymer by the Ar/O_2 mixture has not yet been reported.

The polymer film characterized in our study is a plasma polymerized cyclopropylamine film. This film contains a high concentration of amine groups, and it is of high interest for tissue engineering. The PP-CPA-coated surfaces exhibited extremely high cell adhesion [19]. A possibility for many applications of CPA films was a reason to select this polymer for systematic investigation of GDOES depth profiling. We believe that the results of our study may also be applied to other types of polymers.

2. Experimental details

Thin films containing amino groups were prepared by plasma-enhanced chemical vapor deposition (PECVD) on commercially available, polished, stainless-steel substrates with a thickness of 0.75 mm. The substrates were cut into rectangular pieces with dimensions of 10 cm × 5 cm and carefully cleaned. They were put on the bottom electrode of a high-vacuum PECVD chamber in which a capacitively coupled plasma discharge was ignited at 13.56 MHz between two parallel-plate electrodes. The chamber was a stainless-steel cylinder, 490 mm in inner diameter and 246 mm in height, closed by two stainless-steel flanges. The bottom electrode, 420 mm in diameter, was connected to a radio-frequency (RF) generator via a matching unit containing a blocking capacitor. Thus, the bottom electrode with substrates was negatively DC self-biased depending on the applied RF power and the pressure. Details of this relation can be found in our previous publications [20,21,19]. The processing gas, either argon for the substrate cleaning or Ar with cyclopropylamine vapors (CPA, C_3H_7N) for the deposition, was fed into the chamber through a grounded upper showerhead electrode, 380 mm in diameter. The distance between the electrodes was 55 mm. A sketch of the experimental setup is shown in Ref. [19].

The PECVD chamber was evacuated with a turbomolecular pump backed with a two-stage rotary pump to an ultimate pressure of 1×10^{-4} Pa. The system was not baked but evacuated for 20 h before depositing

the coating. The pressure during both processes (the substrate cleaning and the thin-film deposition) was adjusted to 50 Pa with a valve between the chamber and the turbomolecular pump. The Ar flow rate of 28 sccm was regulated with an electronic flow controller, whereas the flow rate of CPA vapor was set to 2 sccm with a needle valve. Thus, the effective pumping speed during the deposition was only about 1 l/s, which was found to be helpful for increasing the residence time of gaseous precursors inside the reaction chamber and thus the optimal formation of radicals from CPA for the deposition of high-quality films. Before the deposition, the substrates were sputter-cleaned for 5 min with a pulsed Ar plasma at 100 W (33 % duty cycle, 500-Hz pulse repetition frequency). The plasma polymerization of CPA was also carried out in the pulsed mode (33 % duty cycle and 500-Hz repetition frequency) at 100 W on-time RF power. The applied optimized conditions of the CPA plasma polymerization yielded stable yet amine-rich films, as found previously [21]. Different deposition times were chosen (12, 24, and 96 min) to obtain thin films of different thicknesses. The films were characterized by spectroscopic ellipsometry, and the thicknesses obtained by the fitting were 70.2 ± 0.4 nm, 118.2 ± 1.3 nm, and 502 ± 3 nm, respectively. The deposition rate corresponding to these three films vary within the statistical variations observed for a large number of deposition experiments. However, the film composition was not influenced by these variations.

The samples were characterized by XPS, ToF-SIMS, AFM, and GDOES. The XPS analyses were carried out with the PHI-TFA XPS spectrometer (Physical Electronics Inc) using a monochromatized X-ray Al source. The analyzed area was 0.4 mm in diameter. The surface composition was quantified from the XPS peak intensities, taking into account the instrument manufacturer's relative sensitivity factors. The XPS analyses were performed in combination with ion sputtering to analyse the depth distribution of the elements in the sub-surface region. The Ar ions with an energy of 3 keV were used for rastering an area of 3 × 3 mm^2. During the XPS depth profiling, the signals of C 1 s, N 1 s, O 1 s, Fe 2p, Cr 2p, and Ni 2p were acquired. The pass energy of the electron analyser was 187 eV for the acquisition of the XPS spectra during the depth profiling and 29 eV for the acquisition of the XPS spectra from the surface.

ToF-SIMS analyses were performed using a ToF–SIMS 5 instrument (ION-TOF, Münster, Germany) equipped with a bismuth liquid–metal ion gun with a kinetic energy of 30 keV. The analyses were performed in an ultra-high vacuum of approximately 10^{-7} Pa. The SIMS spectra of the negative ions were measured by scanning a Bi^+ cluster ion beam over an area 100 × 100 μm^2 in size. The beam current was 0.6 pA, and the total measuring time to acquire the SIMS spectra was 500 s. The dose of the primary ions during the measurements was in the static regime. An electron gun was used to prevent charge compensation on the sample surfaces during the analysis. The SIMS depth profile was obtained in dual-beam mode using a Bi^+ beam as the analyzing beam and a Cs^+ beam at 0.5 keV for sputtering. The sputtering rate was about 0.42 nm/s. During the ToF-SIMS depth profiling, the analyses chamber was flooded by H_2 gas at the pressure of $7x10^{-5}$ Pa to reduce the matrix effect.

AFM measurements were made on polymer films that were sputtered to half of the film's thickness to reveal the surface morphology. A Dimension Icon AFM instrument, produced by Brucker, was employed in semi-contact mode for these measurements. The surface morphology of the bottom of the craters after GDOES depth profiling was examined by stylus profilometer (Taylor Hobson Talysurf).

The GDOES depth profiling was performed in the pulsed RF GDOES instrument, GD-Profiler 2 by Horiba Scientific. This instrument integrated the ultra-fast sputtering mode (UFS) based on applying a mixture of gases during the depth profiling, as patented by Horiba Scientific [22]. The GD plasma excited at 13.56 MHz was confined within the non-biased copper tube of 4 mm in diameter. The GDOES depth profiling was performed at different powers from 20 to 45 W and at different pressures from 400 to 700 Pa. The RF power was pulsed with a frequency of 2.5 kHz and a duty cycle of 25%. A pure Ar gas and a mixture of 96 vol% Ar and 4 vol% O_2 gases were used for the sputtering during the depth profiling. Optical transitions were recorded in the spectral range 100–800 nm.

The GDOES had a powerful plasma for sputtering the sample surface, so heating of the uppermost layer is expected during the depth profiling. The surface layer's temperature can be estimated from the known discharge power, taking into account some assumptions. The GDOES employs a highly asymmetrical, capacitively coupled RF discharge. Such discharges are characterized by an asymmetrical distribution of the power applied to the electrodes: the major fraction is dissipated at the smaller electrode. Such a configuration is beneficial since the voltage drop between the plasma and the smaller electrode is much higher than in the large electrode's plasma sheath. Consequently, the positive ions accelerate in the plasma sheath at the small electrode to high kinetic energy. They create collision cascades with atoms in the samples' surface layer, releasing their kinetic energy, i.e., heating the surface layer with a thickness of the order of the ion-penetration depth. The penetration depth of such ions is several nm, so one can assume all the available RF power is dissipated on the surface of the sample. A temperature gradient is thus established across the sample. Assuming further infinite thermal conductivity of the sample holder, the difference in temperature between the sample surface facing the plasma and the rear in steady conditions (i.e., neglecting the thermal capacity of the sample) is calculated using a simple equation

$$\Delta T = \frac{P}{S}\left(\frac{d_{steel}}{\lambda_{steel}} + \frac{d_{polymer}}{\lambda_{polymer}}\right) \quad (1)$$

Here, P is the discharge power, d is the sample thickness, λ is the thermal conductivity, and S is the area of the sample facing the plasma. Assuming the sample holder is kept at 300 K at all times, the temperature of the sample surface is shown versus the thickness of the polymer layer in Fig. 1 for the case of discharge power of 30 W, a sample diameter of 5 mm, and for a stainless-steel substrate with a thickness of 0.75 mm. Namely, our samples were polymer films on stainless-steel substrates. The thermal conductivities (λ) of the polymer film and the stainless-steel substrate were taken as 0.5 W/(m K) and 15 W/(m K), respectively.

The temperatures plotted in Fig. 1 are definitely overestimated since not all the discharge power is dissipated on the sample surface. Still, Fig. 1 is useful for estimating any thermal effects. As can be seen in Fig. 1, the expected surface temperature is between 100 and 400 °C. In our case, there is a thin film of polymer on the stainless-steel substrate with a thickness of 0.75 mm. Since the stainless steel has only moderate thermal conductivity, the surface temperature as calculated with equation (1) is not negligible – about 100 °C for the stainless-steel substrate with a thickness of 0.75 mm. The thickness of the polymer film in our case is up to 0.5 μm, so the temperature gradient across the polymer film

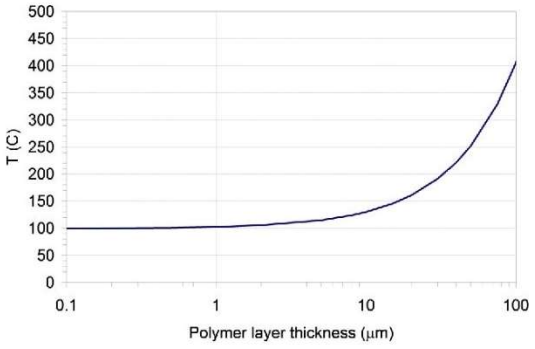

Fig. 1. The temperature of the sample surface consisting of the polymer layer of variable thickness on the steel foil of 0.75 mm in thickness upon depth profiling by GDOES at discharge power 30 W.

due to exposure to gaseous plasma is negligible – up to a couple of °C. In any case, the results of the simple calculation confirm that the surface of the polymer sample in our case does not heat to a temperature where the thermal decomposition of the polymer film would become significant. Still, we should be aware of thermal effects if thicker polymer films were used. For example, the surface of a polymer foil of thickness 0.1 mm would heat to over 400 °C. This has to be taken into account when probing thick samples that have poor thermal conductivity using the GDOES technique.

3. Results and discussion

Detailed XPS analyses of the surface of the plasma-polymerized polyamine film studied here have already been reported [19,23,24]. The film composition averaged over several deposition experiments was 79.5 ± 1.0 at.% of C, 17.2 ± 0.5 at.% of N and 3.3 ± 0.8 at.% of O, as measured maximum three days after the deposition. The XPS analyses performed in the present study were carried out more than one month after the deposition, and, therefore, the concentration of oxygen at the film surface was higher due to a film oxidation. Namely, the composition was 80 at.% C, 11 at.% N and 9 at.% O.

We focused on the XPS depth profiling of an amine film. Fig. 2 shows an XPS depth profile of the amine film with a thickness of 70 nm. The sputtering time to acquire the total depth profile was 1.5 h. We estimated the sputtering rate to be 2.0 nm/min for this polymer film. We did not attempt to acquire XPS depth profiles for thicker polymer films since the analysis time would be very long. For the 1-μm-thick films, the required analysis time would be almost one day.

The depth profile in Fig. 2 reveals some details that are worth discussing. First, the oxygen concentration dropped quickly to 2 at.% after starting to etch the polymer film. A decrease of nitrogen (to 6 at.%) was also observed. A possible explanation for these changes is a preferential sputtering of these two elements with Ar ions [25]. The artifact due to preferential etching of N and O upon depth profiling with a monoatomic Ar ion gun can be partially avoided using more sophisticated Ar-cluster ions optimized for etching the polymer films [26]. However, we believe that the significant decrease in the amount of oxygen, the concentration of which stabilized at 1–2 at.% through the polymer film's entire thickness, is also related to the depth-limited amine film oxidation. Here, it is worth mentioning that monochromatic Ar sputtering also causes partial de-hydrogenation of polymers, which may further influence the composition as deduced from XPS depth profiles.

The interface width between the polymer film and the stainless-steel substrate in the XPS depth profile shown in Fig. 2 is about 15 nm. The measured interface width may be related to the analyses depth of the XPS method, which may be up to 10 nm, or the atom mixing at the interface induced by the ion sputtering. The main reason for the interface width measured by XPS is probably related to the surface roughness of the steel substrate, considering that the as-received stainless-steel sheets were not additionally polished. The interface is enriched with oxygen that is explained by weak oxidation of the stainless-steel substrate. The cleaning by bombardment with Ar ions performed in-situ before polymer film deposition was not efficient enough to remove the native oxide film. Still, the concentration of oxygen within the interface is only several at.%.

The sample with the 70-nm-thick polymer films was also characterized by ToF-SIMS. A typical depth profile of negative secondary ions obtained by sputtering with the Cs^+ ions with 0.5 keV is shown in Fig. 3. It is similar to the XPS depth profile from Fig. 2, taking into account the specificity of both techniques for depth profiling. The selected signals of C_3N^-, CH^-, FeO_2^-, CrO^-, FeH^-, NiH_2^- and CrH_2^- are shown in Fig. 3 for simplicity. The interface width between the polymer film and the substrate is almost the same (about 15 nm) in both the XPS and SIMS depth profiles. As already mentioned, the interface thickness is explained by a

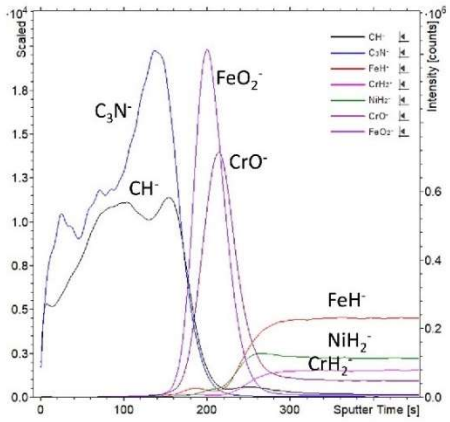

Fig. 3. ToF-SIMS depth profile of negative secondary ions across a polymer film of thickness 70 nm.

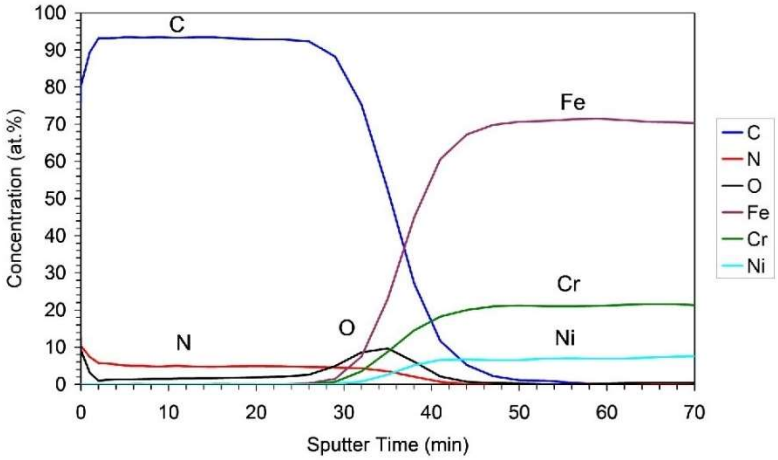

Fig. 2. XPS depth profile across the polymer film of thickness 70 nm.

rough stainless-steel surface due to incomplete polishing rather than the formation of a diffused layer. The ToF-SIMS profile clearly shows the presence of C_3N^- and CH^- signals related to the amine and hydrocarbon groups in the deposited film. Variation of these signals is probably related to a change of ionization due to the matrix effect. At the interface, it can be recognized a thin oxide layer from the FeO_2^-, CrO^- signals. A steel matrix beneath the oxide layer is evidenced in the SIMS profile by the FeH^-, NiH_2^- and CrH_2^- signals. These metal-hydrogen clusters are formed from the emitted metallic ions and hydrogen molecules introduced in the vacuum at the pressure range of 10^{-5} Pa. This is a new approach to reduce a matrix effect in ToF-SIMS depth profiling by flooding the analyses chamber with H_2 gas. We should note that ToF-SIMS is not a quantitative method and that the intensity of signals does not directly reflect the concentration of corresponding species.

The samples were also characterized by GDOES using two different gases introduced into the discharge unit, either pure Ar or a mixture of 96 vol% Ar and 4 vol% O_2. A typical GDOES depth profile of a 500-nm-thick polymer layer when using pure argon for the sample's plasma sputtering is shown in Fig. 4. The discharge parameters adopted for this depth profile were as follows: gas pressure of 450 Pa, discharge power of 20 W, a duty cycle of 0.25, and repetition frequency of 2500 Hz. The evolution of the optical signals for C, N, O, Fe, Cr, and Ni are shown in Fig. 4. The intensity of the Cr and Fe signals was much larger than any other spectral line, so the other elements were multiplied by 50–100 to better read the depth profile.

To evaluate the surface morphology developed during etching, we analyzed the surface of a sample with a polymer thickness of 500 nm after 50 s of etching in the GDOES instrument, when approximately half of the layer thickness was removed (Fig. 4). A typical AFM image is shown in Fig. 5. We can observe round pits of about 65 nm in diameter and 10 nm in height. The roughness on this surface was measured to be about 3.2 nm. A possible reason for such structure may be inhomogeneous plasma distribution above the dielectric layer of polymer on the nanoscale or internal heterogeneity of the polymer layer. At this point, we are not able to explain this in more detail, and this would require further research. The sputtering rate of the polymer layer was evaluated to be about 3.3 nm/s, much faster than for similar XPS and SIMS analysis. The concentrations of C and N were almost constant across the polymer film in accordance with observations by XPS (Fig. 2). The behavior of the elements at the interface between the polymer film and substrate, however, deviates significantly. While the interface thickness in the case of both the XPS and SIMS depth profiles was about 15 nm, it was well over 100 nm in the case of GDOES. Namely, both carbon and

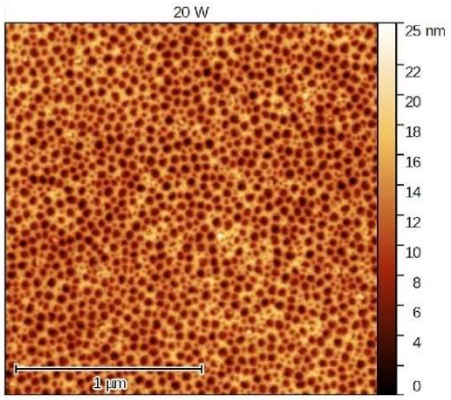

Fig. 5. A typical AFM image of a sample of polymer thickness 500 nm at 30 W and 50 s treatment time in Ar), when a half of the polymer layer was removed in order to reveal development of the surface morphology.

nitrogen lines remained intensive after the Fe and Cr lines prevailed in the optical spectrum. This effect could be attributed either to the retention of carbon and nitrogen in the discharge chamber of the GDOES or highly inhomogeneous etching of the polymer film upon depth profiling, or both. The version of the GDOES instrument used in this study is equipped with a sophisticated pumping system, so any gaseous molecules formed upon etching of the polymer film will be pumped from the discharge chamber quickly. The depth profile in Fig. 4, however, reveals that a substantial concentration of C and N remains about 100 s after the appearance of the Fe and Cr lines. There are two feasible explanations for the persistence of N and C in the optical spectra: 1 – carbon and nitrogen-containing molecules desorb from surfaces other than the substrate in plasma conditions, and 2 – some polymer persists on the sample surface well after a part of the surface was free from polymer.

Details about the discharge and plasma properties in the GDOES instrument adopted in this study are not available. The Ar ions are accelerated in the sheath between the bulk plasma and the sample and bombard the surface. The bombardment causes the depletion of hydrogen in the polymer film and sputtering of the surface atoms. The removed material enters the gaseous plasma, where the atoms are

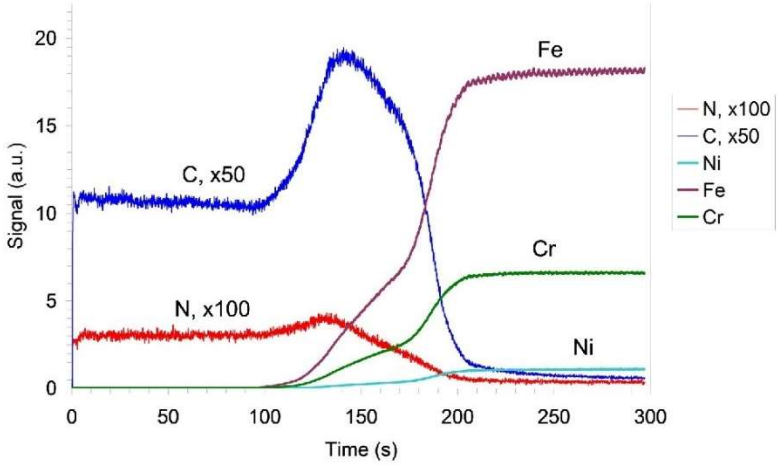

Fig. 4. GDOES depth profile across the polymer film of thickness 500 nm at 20 W using pure Ar.

excited in collisions with the plasma electrons or with the Ar metastables. Although the pressure in the discharge chamber is rather large (450 Pa in the case of the depth profile shown in Fig. 4), not all the removed molecules or atoms are pumped away. Some diffuse inside the gaseous plasma and eventually reach the surface of the counter-electrode. The mean free path of the gaseous molecules at a pressure of 450 Pa is below 0.1 mm, so the removed material suffers numerous collisions in the gas phase until it reaches the surface of the counter-electrode. Residual gases will not be retained significantly on the surface, but radicals such as CH_x ($x < 3$) will stick to any surface facing plasma, causing the formation of a hydrogenated carbon film. This film would remain on the counter-electrode surface forever unless the surface is subjected to bombardment with plasma ions. This effect cannot be evaluated due to the lack of information on discharge coupling and thus an inability to estimate the kinetic energy of ions bombarding the counter-electrode. Another reason for the removal of such unwanted deposits is desorption at very high temperatures, but this effect can be excluded since it is believed that the counter-electrode remains reasonably close to room temperature during the depth profiling.

Another explanation for persistent carbon in the optical spectra long after the Fe and Cr lines appeared is the laterally inhomogeneous etching of the polymer film under bombardment with Ar ions. It is well known that with a non-homogenous sputtering flux during the etching in the GDOES, a crater on the substrate may be formed with a non-flat bottom. This effect deteriorates the depth resolution and the sharpness of the measured interface for thin-film structures like in our case as it was modeled by one of the authors [10].

A third explanation could be a simple shrinkage of the polymer film upon depth profiling due to pure thermal effects. Elevated temperatures cause the melting of a thin polymer film and thus the formation of polymer droplets. As shown in Fig. 1, the polymer temperature is close to 100 °C during the GDOES depth profiling.

To evaluate the morphology at the interface between the polymer film and the steel substrate, the etching in pure Ar was stopped after reaching the interface. The micrograph obtained by the optical microscope and the line profile obtained by profilometry of the bottom of the crater after etching are presented in Figures S1 and S2. These data are shown for the 500-nm thick polymer film. The shape of the crater after pure Ar etching is relatively flat but contains many small dots of 200 – 400 nm in height. As supposed, the origin of the dots after pure Ar etching may be due to the redeposition of the sputtered material from the polymer film or from the deposit on the counter electrode.

Whatever the reason, the persistence of the C and N emission lines in the depth profiles well after the metal lines have appeared represents a serious drawback of GDOES compared to XPS or SIMS. Modern GDOES instruments are also equipped with other gases for the depth profiling of polymer films. The instrument used in this work enables depth profiling using a mixture of Ar and O_2, in particular 96 vol% Ar and 4 vol% O_2. Such a mixture was used as an alternative to pure Ar for the depth profiling of our samples. The addition of oxygen to the Ar plasma complicates the plasma kinetics since there are numerous additional gas-phase and surface reactions involved. The literature on plasma parameters in such gas mixtures is abundant, but we found no paper on plasma parameters in the discharge configuration as adopted by our GDOES instrument. The closest study in terms of similar discharge power density (power per unit volume), similar diameter and length of the discharge tube, and similar pressure and gas mixture was published by Kutasi et al. [18]. She found the most abundant species to be metastable neutral O_2 molecules in the singlet state, followed by neutral oxygen atoms in the ground state. The concentration of Ar^+ ions and Ar metastables was much smaller (the order of magnitude was 10^{17} m^{-3}), while the concentration of oxygen ions (molecular or atomic) was at least an order of magnitude lower. In any case, the flux of the reactive oxygen species suitable for chemical interaction with polymer films on any surface facing plasma is much larger than the flux of positive ions in discharge configurations similar to that of our GDOES instrument.

Fig. 6 shows a typical GDOES depth profile for plasma created in a mixture of 96% Ar + 4% O_2. As compared to Fig. 4, which shows the depth profile of the same sample under the same conditions but using Ar only, we observe two important differences: 1 – the removal of the polymer film is much faster, and 2 – neither carbon nor nitrogen persist in the optical spectra once the Fe and Cr lines have become significant. The sputtering rate was estimated to be about 83 nm/s in comparison to the sputtering rate of 3.3 nm/s when profiling in pure Ar. The fast sputtering of the polymer film in a mixture of Ar + O_2 gases is attributed to chemical etching of the carbon-containing material rather than sputtering and will be elaborated later in this paper. The interface is far less broad in the case of the oxygen admixture than when using only argon for the depth profiling. Therefore, the application of oxygen in the gaseous plasma suitable for etching of the sample for depth profiling eliminates both the nitrogen and carbon lines from the optical spectra once the signals from the metal ions become noticeable. As explained above, the carbon may persist in the spectra when only Ar is used for the depth profiling either due to the retention of carbon on the walls of the counter-electrode or due to highly inhomogeneous sputtering. Reactive oxygen species interact chemically with carbon-containing materials causing the formation of simple molecules that quickly desorb from the surfaces, predominantly H_2O, CO and CO_2. The application of oxygen for the depth profiling of thin polymer films on metallic substrates is therefore highly recommended.

To confirm further our assumption we analyzed morphology of the crater obtained by the Ar + O_2 etching by optical microscope and by profilometer what is shown in Figures S3 and S4. The crater shape is less flat than in the case of the pure Ar etching (Figures S1 and S2), but it does not show a presence of dots. The absence of the dots for etching with the Ar + O_2 mixture shows that the redeposition of the sputtered material does not occur. Similar behavior was observed by Takahara et al. performing GDOES etching on the graphite layer in the Ar + O_2 mixture in comparison to etching in pure Ar, where similar dots were observed [13]. The Figure S4 shows that the bottom of crater obtained by the Ar/O_2 mixture etching does not contain dots but there are present regions with pronounced convexity. This morphology may be related with inhomogeneous etching in the Ar/O_2 mixture due to the O_2 addition. Such effect on morphology was also reported by Fernandez et al. applying the Ar/O_2 mixture at similar conditions for etching steel and glass substrates [11].

In order to gain an insight into the mechanisms of interaction between the polymer films and plasma created in either pure Ar or an Ar-O_2 mixture, we performed more systematic depth profiling at various discharge parameters and compared the results with those obtained using Ar only. Fig. 7 compares the etching rate of the 500-nm-thick polymer film versus the gas pressure at a constant discharge power of 30 W for pure Ar and the Ar-O_2 mixture, as deduced from the corresponding GDOES depth profiles. Fig. 8 shows a similar comparison, but for etching rate versus power at a constant pressure of 400 Pa. The repetition frequency of the pulsed RF discharge was 2.5 kHz, and the duty cycle 0.25 for all conditions.

Fig. 7 indicates that the etching rate with gaseous plasma created in pure argon (lower curve) is about 6 nm/s and it remains almost constant in the range of pressures from 400 to 700 Pa. The etching mechanism, in this case, is sputtering by bombardment with Ar ions. The sputtering efficiency depends on the ions' kinetic energy and the flux of ions onto the surface. At low fluences, the sputtering yield decreases with increasing fluence due to various reactions in the surface layer of the polymer film affected by the Ar ions, but after receiving the fluence of about 10^{20} m^{-2} the yield assumes a rather constant value of roughly one carbon atom per incident Ar ion at an Ar^+ energy of 1 keV [27]. Such fluency is achieved in our case in the first second of plasma treatment, so we can assume a rather time-independent sputtering yield of the polymer film. Increasing the pressure causes an increase in the number of gaseous species available for ionization, which should be beneficial for increasing electron density. On the other hand, increasing the pressure

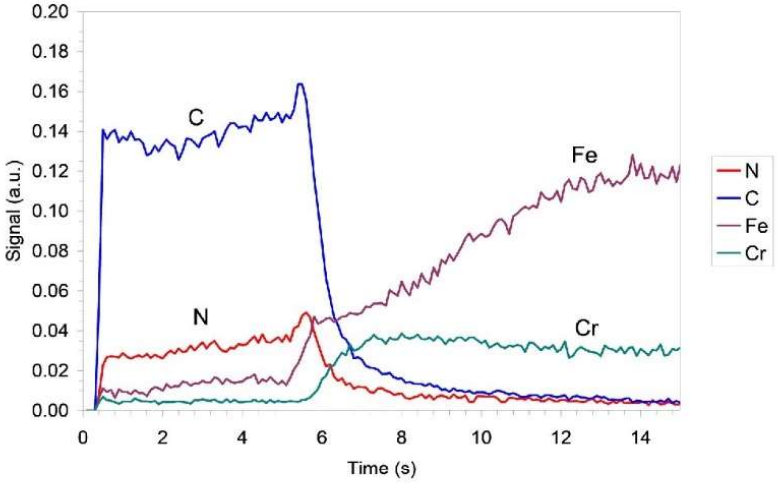

Fig. 6. GDOES depth profile across the polymer film of thickness 500 nm at 20 W using pure Ar + 4% O_2. Oxygen signal was also detected throughout the depth profile but not shown in this Figure.

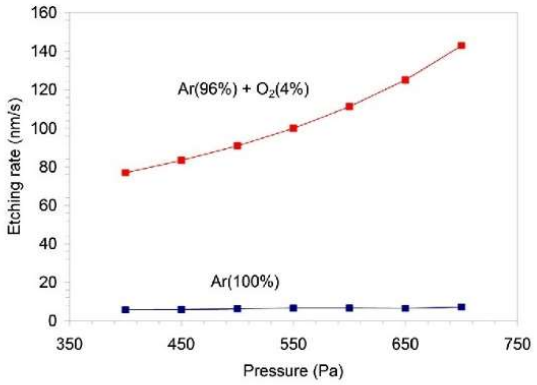

Fig. 7. The etching rate during GDOES depth profiling of the polymer film of thickness 500 nm versus gas pressure at discharge power 30 W using pure Ar (lower curve) and the Ar-4% O_2 mixture (upper curve).

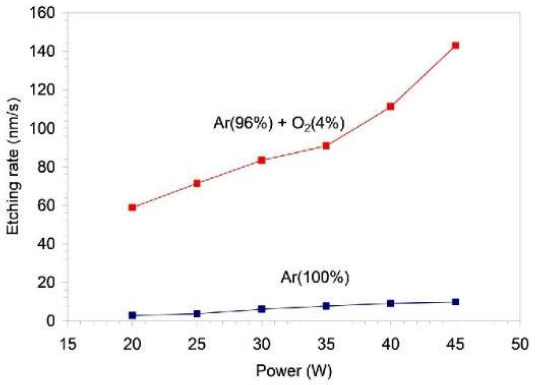

Fig. 8. The etching rate during GDOES depth profiling of the polymer film of thickness 500 nm versus discharge power at pressure 400 Pa using pure Ar (lower curve) and the Ar- 4% O_2 mixture (upper curve).

causes a decrease in the mean free path of the gaseous species, which in turn causes more frequent collisions of the plasma electrons and a higher probability of the loss of the electron energy and correspondingly lower electron temperature. This effect, however, becomes important at pressures much larger than those applied in our experiments, since the power density is large enough to sustain plasma even at an elevated pressure.

A standard presentation of the capacitively coupled plasma involves an equivalent circuit that includes at least two capacitive and a resistive component of the total impedance, although such a presentation may not always be completely accurate, especially when a thin dielectric film persists on the powered electrode [28]. The capacitive components reflect the impedances across the powered and grounded electrodes, and the resistive across the bulk plasma. The current carriers in the bulk plasma are predominantly electrons and, in the sheaths, ions. Since the electron mobility is much larger than the mobility of positive ions (mainly due to the mass differences), the resistive component is usually neglected for short distances between the electrodes like those in the discharge configuration of our GDOES instrument. The key feature of a capacitively coupled discharge as a source of Ar ions is DC self-biasing of the powered electrode that causes a high time-averaged negative bias of the electrode against the bulk plasma. The self-bias slightly decreases with increasing pressure in the range of several 100 Pa [29], but the electron density increases and so does the ion density (plasma is quasi-neutral), so the result of these competing effects is an almost pressure-independent etching rate, as shown in Fig. 7 for pure Ar.

The distribution of Ar ions impinging the sample surface over the kinetic energy is the parameter that governs the sputtering kinetics. Unfortunately, such information is not available. The kinetic energy could be deduced from the RF voltage, but it is not feasible to measure it in our GDOES instrument. The voltage should be large enough to enable gas breakdown. The necessary voltage is estimated from the Paschen curves [30]. Knowing the geometry of the RF discharge chamber in our GDOES instrument, it is possible to conclude that the instrument operates close to the minimum in the Paschen curve, which is just over 100 V for the case of pure argon discharges [30]. If the sheath next to the powered electrode were collisionless, the Ar ions would have been monochromatic at the kinetic energy, which corresponds to the applied voltage. The collision frequency and thus the deviation of the energy distribution from monochromatic could be estimated from the density

and the electron temperature in plasma. However, these parameters are not provided by the GDOES producer, and it is not feasible to measure them in our instrument. From the general knowledge about the behavior of such discharges, we can only speculate that the maximal kinetic energy of Ar ions impinging the samples should be within 100 and 200 eV, but a significant fraction of ions could be less energetic.

The interaction between gaseous plasma and polymer samples is different when oxygen is admixed with argon, as can be seen from the upper curve in Fig. 7. The etching rate versus pressure for the case of 4% O_2 admixture is in the range between 70 and 140 nm/s, and it is an order of magnitude larger than the rate for pure Ar. It is also an almost parabolic increase in the etching rate with increasing pressure for the Ar-O_2 mixture. The effects cannot be explained by more intensive sputtering, but the chemical interaction between reactive gaseous species in an Ar-O_2 plasma and the polymer surface must be taken into account. According to recent review papers [15,31], the major reactive oxygen species in oxygen-containing plasma are neutral oxygen atoms. The O-atoms interact with the polymer surface, causing the formation of oxygen functional groups on the surface. The saturation of the polymer surface with oxygen functional groups is accomplished after achieving a fluence of about 10^{21} m^{-2} [32,33]. The flux of O-atoms onto the polymer surface is

$$j_0 = \frac{1}{4} n_0 \langle v \rangle_0 \tag{2}$$

where n_O is the O-atom density in the plasma next to the polymer surface and $\langle v \rangle_O$ is the average random velocity of O atoms in a gaseous plasma, i.e.

$$\langle v \rangle_0 = \sqrt{\frac{8kT_0}{\pi m_0}} \tag{3}$$

Here, k is the Boltzmann constant, T_O is the temperature of O atoms in the gaseous plasma, and m_O is the mass of an oxygen atom. According to Kutasi et al., the density of O atoms in Ar + 4 vol% O_2 plasma created at the power density of several 10 W cm^{-3} is about 4×10^{20} m^{-3} [18]. The corresponding flux taking into account the gas temperature of 400 K is about 8×10^{22} $m^{-2}s^{-1}$. The time for saturation of the polymer surface with oxygen groups is thus close to 10 ms. Once the surface is saturated, the O-atoms cause chemical etching. The etching rate is

$$\frac{dx}{dt} = \frac{\eta j_O M}{\rho N_A} \tag{4}$$

where η is the probability that an impinging O-atom removes a carbon atom from the polymer surface, M is the molar mass of carbon (using the rough approximation that the entire polymer mass is carbon), ρ is the polymer density, and N_A is the Avogadro number. Taking into account the numerical values, i.e. $j_O = 8 \times 10^{22}$ $m^{-2}s^{-1}$, M = 12 kg $kmol^{-1}$, $\rho = 10^3$ kg m^{-3} and $N_A = 6 \times 10^{26}$ $kmol^{-1}$, and the reaction probability η = 1 we obtain an etching rate of 1.5 μm/s. The measured etching rate for the Ar-O_2 mixture is over an order of magnitude smaller than what can be explained with the above simplifications, so the reaction probability for O-atoms is well below 1. In fact, the reaction probability for O-atoms for a thin polyethylene terephthalate film on a quartz substrate as determined with a quartz-crystal microbalance at room temperature was of the order of 10^{-6} in the case that the polymer was exposed only to O-atoms [34], and between 10^{-4} and 10^{-3} when the polymer was exposed to a weakly ionized oxygen plasma of negligible ion kinetic energy [34]. So, orders of magnitude lower than in the case of our GDOES experiments, where the reaction probability is close to 0.1. The virtual discrepancy is explained by the synergy of the chemical interaction due to polymer oxidation with oxygen atoms and the simultaneous bombardment with Ar^+ ions. The technique is usually called "reactive ion etching" and was commercialized in microelectronics decades ago [35].

The almost parabolic increase of the etching rate with increasing pressure, as evident from Fig. 7 for the Ar-O_2 mixture, is difficult to explain. The etching rate with Ar only does not increase much with increasing pressure. The significant increase of the etching rate as observed in Fig. 7 for the Ar-O_2 mixture should be a consequence of the higher flux of the oxygen reactive species onto the polymer surface. The flux of these species, however, increases at most linearly with increasing pressure, so one would expect a rather linear curve for the Ar-O_2 mixture. In terms of numerical values, the discrepancy is not that dramatic. Although, when the pressure increases from 400 to 700 Pa (by a factor of 1.75), the etching rate increases from 78 to 148 nm/s (by a factor of 1.9).

The discharge power affects the etching rate much more than the pressure. Fig. 8 illustrates this effect for pure Ar and for the Ar-O_2 mixture. The etching rate increases rather linearly with increasing power, and it is about 15 times higher for the Ar-O_2 mixture compared to the pure Ar gas. This is a result of two effects: 1 – increasing self-bias of the powered electrode, and 2 – increasing ion density in plasma. The first effect causes increased Ar^+ kinetic energy when bombarding the sample, and the second an increased ion flux. Both contribute to more extensive etching and also heating of the polymer surface, but the latter effect does not cause a significant increase in the surface temperature for thin polymer films (see Fig. 1).

Here, it is worth mentioning that the exact mechanisms of oxygen plasma interaction with polymers are still not well understood. The main reactants in oxygen plasmas are usually neutral oxygen atoms. A useful theory on the interaction of O-atoms with a polymer was recently provided by Longo et al. [36]. The authors elaborated on almost 20 reaction paths that lead to surface functionalization at low atom fluence, and etching at larger fluencies. The etching causes bong cleavage, so it is likely that low-molecular-mass fragments are also formed on the polymer surface. The fragments may be released upon low-pressure conditions so that incomplete oxidation may occur. The theoretical predictions provided by Longo were recently confirmed by experiments using a broad range of O-atom fluences [37]. Gaseous plasma, sustained in a mixture of argon and oxygen, comprises other species but neutral atoms. The synergy between the reactive species is not understood, especially because such a plasma is a rich source of vacuum ultraviolet (VUV) radiation [38], which is renowned for its ability to break bonds in the surface film of organic materials [39].

4. Conclusions

Characterization of thin polymer films on stainless-steel substrates by GDOES using either pure argon or a mixture of argon with 4 vol% oxygen provided an insight into the phenomena that take place on the surface of samples during etching. The etching rates were by a factor of around 15 larger in the case that oxygen was added to the plasma created in the GDOES instrument, as compared to classic etching by sputtering of the polymer film with Ar ions. Such a pronounced effect was explained by a synergy between the reactive oxygen species that interact chemically with the polymer surface and the bombardment with Ar ions. A rough estimation of the plasma parameters taking into account the available scientific literature, made it possible to estimate the probability that an oxygen atom from the gas phase interacts with carbon on the surface of the polymer material. The probability was found to be close to 0.1, which is far larger than what was reported for the interaction of pure oxygen plasma of comparable O-atom density with polymer samples kept at a floating potential so that the kinetic effects caused by bombardment with positively charged ions were negligible.

A peculiarity of GDOES depth profiling when using argon only as the source of polymer etching is the virtual persistence of the carbon signal well after the signals from metallic atoms have become large. Possible explanations for this observation were presented in this paper and briefly discussed. A comparison with depth profiles obtained by XPS and SIMS proved that the persistence of carbon in the depth profiles obtained by GDOES was an artefact of the GDOES method. The problem was

solved effectively by using a mixture of Ar with 4 vol% oxygen, where we observed rather sharp interfaces between the polymer film and metallic substrate. The results, therefore, confirm the superior analytical results when using oxygen in GDOES depth profiles.

CRediT authorship contribution statement

Janez Kovač: Investigation, Writing – review & editing, Conceptualization. **Jernej Ekar:** Investigation. **Miha Čekada:** Investigation. **Lenka Zajíčková:** Investigation. **David Nečas:** Investigation. **Lucie Blahová:** Investigation. **Jiang Yong Wang:** Investigation, Resources. **Miran Mozetič:** Resources, Writing – review & editing, Conceptualization.

Declaration of Competing Interest

The authors declare that they have no known competing financial interests or personal relationships that could have appeared to influence the work reported in this paper.

Acknowledgement

The authors acknowledge the financial support from the Slovenian Research Agency (research core funding No. P2-0082 and project L2-1728), Slovenian-Chinese bilateral project BI-CN/17-18-003. We also acknowledge CzechNanoLab Research Infrastructure supported by MEYS CR (LM2018110) and the project 21-12132 J supported by the Czech Science Foundation

Appendix A. Supplementary material

Supplementary data to this article can be found online at https://doi.org/10.1016/j.apsusc.2021.152292.

References

[1] W. Grimm, Eine neue glimmentladungslampe für die optische emissionsspektralanalyse, Spectrochim. Acta, Part B 23 (7) (1968) 443–454.
[2] V. Hoffmann, M. Kasik, P.K. Robinson, C. Venzago, Glow discharge mass spectrometry, Anal. Bioanal. Chem. 381 (2005) 173–188.
[3] S. Carquigny, B. Lakard, S. Lakard, V. Moutarlier, J.-Y. Hihn, L. Viau, Investigation of pharmaceutically active ionic liquids as electrolyte for the electrosynthesis of polypyrrole and active component in controlled drug delivery, Electrochim. Acta 211 (2016) 950–961.
[4] K. Cysewska, L.F. Macía, P. Jasiński, A. Hubin, In-situ odd random phase electrochemical impedance spectroscopy study on the electropolymerization of pyrrole on iron in the presence of sodium salicylate – The influence of the monomer concentration, Electrochim. Acta 290 (2018) 520–532.
[5] T. Sizun, T. Patois, M. Bouvet, B. Lakard, Microstructured electrodeposited polypyrrole–phthalocyanine hybrid material, from morphology to ammonia sensing, J. Mater. Chem. 22 (2012) 25246–25253.
[6] S. Giaveri, P. Gronchi, A. Barzoni, IPN Polysiloxane-Epoxy Resin for High Temperature Coatings: Structure Effects on Layer Performance after 450 °C Treatment, Coatings 7 (2017) 213.
[7] V. Moutarlier, S. Lakard, T. Patois, B. Lakard, Glow discharge optical emission spectroscopy: a complementary technique to analyze thin electrodeposited polyaniline films, Thin Solid Films (2014) 27–35.
[8] A. Groza, C.S. Ciobanu, C.L. Popa, S.L. Iconaru, P. Chapon, C. Luculescu, M. Ganciu, D. Predoi, Structural Properties and Antifungal Activity against Candida albicans Biofilm of Different Composite Layers Based on Ag/Zn Doped Hydroxyapatite-Polydimethylsiloxanes, Polymers 8 (2016) 131.
[9] A. Surmeian, D.M. Maximean, B. Mihalcea, O. Stoican, B. Butoi, O. Danila, P. Dinca, I. Barbut, L. Tudor, A. Fazacas, GDOES and GDMS analytical systems, effective tools for characterization of conductive and nonconductive material surfaces, University Politehnica of Bucharest, Scientific Bulletin-Series A-Appl. Mathematics. Phys. 77 (2015) 273–280.
[10] Y. Liu, W. Jian, J.Y. Wang, S. Hofmann, K. Shimizu, Quantitative reconstruction of the GDOES sputter depth profile of a monomolecular layer structure of thiourea on copper, Appl. Surf. Sci. 331 (2015) 140–149.
[11] B. Fernández, N. Bordel, R. Pereiro, A. Sanz-Medel, Investigations of the effect of hydrogen, nitrogen or oxygen on the in-depth profile analysis by radiofrequency argon glow discharge-optical emission spectrometry, J. Anal. At. Spectrom. 18 (2) (2003) 151–156.
[12] B. Fernández, N. Bordel, C. Pérez, R. Pereiro, A. Sanz-Medel, The influence of hydrogen, nitrogen or oxygen additions to radiofrequency argon glow discharges for optical emission spectrometry, J. Anal. At. Spectrom. 17 (11) (2002) 1549–1555.
[13] H. Takahara, A. Kojyo, K. Kodama, T. Nakamura, K. Shono, Y.o. Kobayashi, M. Shikano, H. Kobayashi, Depth profiling of graphite electrode in lithium ion battery using glow discharge optical emission spectroscopy with small quantities of hydrogen or oxygen addition to argon, J. Anal. At. Spectrom. 29 (1) (2014) 95–104.
[14] W. Fischer, A. Naoumidis, H. Nickel, Effects of a controlled addition of nitrogen and oxygen to argon on the analytical parameters of glow discharge optical emission spectrometry, J. Anal. At. Spectrom. 9 (3) (1994) 375, https://doi.org/10.1039/ja9940900375.
[15] A. Vesel, M. Mozetic, New developments in surface functionalization of polymers using controlled plasma treatments, J. Phys. D Appl. Phys. 50 (29) (2017) 293001, https://doi.org/10.1088/1361-6463/aa748a.
[16] M. Mozetič, K. Ostrikov, D.N. Ruzic, D. Curreli, U. Cvelbar, A. Vesel, G. Primc, M. Leisch, K. Jousten, O.B. Malyshev, J.H. Hendricks, L. Kövér, A. Tagliaferro, O. Conde, A.J. Silvestre, J. Giapintzakis, M. Buljan, N. Radić, G. Dražić, S. Bernstorff, H. Biederman, O. Kylián, J. Hanuš, S. Milošević, A. Galtayries, P. Dietrich, W. Unger, M. Lehocky, V. Sedlarik, K. Stana-Kleinschek, A. Drmota-Petrič, J.J. Pireaux, J.W. Rogers, M. Anderle, Recent advances in vacuum sciences and applications, Journal of Physics D: Applied Physics 47 (2014) 153001.
[17] M. Mozetič, A. Vesel, G. Primc, C. Eisenmenger-Sittner, J. Bauer, A. Eder, G.H. S. Schmid, D.N. Ruzic, Z. Ahmed, D. Barker, K.O. Douglass, S. Eckel, J.A. Fedchak, J. Hendricks, N. Klimov, J. Ricker, J. Scherschligt, J. Stone, G. Strouse, I. Capan, M. Buljan, S. Milošević, C. Teichert, S.R. Cohen, A.G. Silva, M. Lehocky, P. Humpolíček, C. Rodriguez, J. Hernandez-Montelongo, D. Mercier, M. Manso-Silván, G. Ceccone, A. Galtayries, K. Stana-Kleinschek, I. Petrov, J.E. Greene, J. Avila, C.Y. Chen, B. Caja-Munoz, H. Yi, A. Boury, S. Lorcy, M.C. Asensio, J. Bredin, T. Gans, D. O'Connell, J. Brendin, F. Reniers, A. Vincze, M. Anderle, L. Montelius, Recent developments in surface science and engineering, thin films, nanoscience, biomaterials, plasma science, and vacuum technology, Thin Solid Films 660 (2018) 120–160.
[18] K. Kutasi, V. Guerra, P. Sá, Theoretical insight into Ar–O2surface-wave microwave discharges, J. Phys. D Appl. Phys. 43 (2010), 175201.
[19] A. Manakhov, M. Landová, J. Medalová, M. Michlíček, J. Polčák, D. Nečas, L. Zajíčková, Cyclopropylamine plasma polymers for increased cell adhesion and growth, Plasma Processes Polym. 14 (2017) 1600123.
[20] L. Zajíčková, V. Buršíková, Z. Kučerová, J. Franclová, P. Sťahel, V. Peřina, A. Macková, Organosilicon thin films deposited by plasma enhanced CVD: Thermal changes of chemical structure and mechanical properties, J. Phys. Chem. Solids 68 (2007) 1255–1259.
[21] L. Štrbková, A. Manakhov, L. Zajíčková, A. Stoica, P. Veselý, R. Chmelík, The adhesion of normal human dermal fibroblasts to the cyclopropylamine plasma polymers studied by holographic microscopy, Surf. Coat. Technol. 295 (2016) 70–77.
[22] A.T. Patrick Chapon, Célia Olivero, Tatsuhito Nakamura, Hiroko Nakamura, Akira Fujimoto, Method of measuring a solid organic or polymer sample by luminescent discharge spectrometry, in: E.P. Office (Ed.), 2016.
[23] M. Michlíček, L. Blahová, E. Dvořáková, D. Nečas, L. Zajíčková, Deposition penetration depth and sticking probability in plasma polymerization of cyclopropylamine, Appl. Surf. Sci. 540 (2021), 147979.
[24] I. Nemcakova, L. Blahova, P. Rysanek, A. Blanquer, L. Bacakova, L. Zajíčková, Behaviour of Vascular Smooth Muscle Cells on Amine Plasma-Coated Materials with Various Chemical Structures and Morphologies, Int. J. Mol. Sci. 21 (2020) 9467.
[25] A.M. Ektessabi, S. Hakamata, XPS study of ion beam modified polyimide films, Thin Solid Films 377–378 (2000) 621–625.
[26] T. Miyayama, N. Sanada, S.R. Bryan, J.S. Hammond, M. Suzuki, Removal of Ar+ beam-induced damaged layers from polyimide surfaces with argon gas cluster ion beams, Surf. Interface Anal. 42 (2010) 1453–1457.
[27] J. Zekonyte, V. Zaporojtchenko, F. Faupel, Investigation of the drastic change in the sputter rate of polymers at low ion fluence, Nucl. Instrum. Methods Phys. Res., Sect. B 236 (2005) 241–248.
[28] T.S. Ho, C. Charles, R. Boswell, Redefinition of the self-bias voltage in a dielectrically shielded thin sheath RF discharge, J. Appl. Phys. 123 (2018), 193301.
[29] P. Saikia, H. Bhuyan, M. Escalona, M. Favre, R.S. Rawat, E. Wyndham, A nonlinear global model of single frequency capacitively coupled plasma and its experimental validation, AIP Adv. 8 (2018), 045113.
[30] W. contributors, Paschen's law, in, Wikipedia, The Free Encyclopedia.
[31] M. Mozetič, G. Primc, A. Vesel, R. Zaplotnik, M. Modic, I. Junkar, N. Recek, M. Klanjšek-Gunde, L. Guhy, M.K. Sunkara, M.C. Assensio, S. Milošević, M. Lehocky, V. Sedlarik, M. Gorjanc, K. Kutasi, K. Stana-Kleinschek, Application of extremely non-equilibrium plasmas in the processing of nano and biomedical materials, Plasma Sources Sci. Technol. 24 (2015), 015026.
[32] T. Vukušić, A. Vesel, M. Holc, M. Šćetar, A.R. Jambrak, M. Mozetič, Modification of Physico-Chemical Properties of Acryl-Coated Polypropylene Foils for Food Packaging by Reactive Particles from Oxygen Plasma, Materials 11 (2018) 372.
[33] A. Vesel, R. Zaplotnik, J. Kovac, M. Mozetic, Initial stages in functionalization of polystyrene upon treatment with oxygen plasma late flowing afterglow, Plasma Sources Sci. Technol. 27 (2018), 094005.
[34] A. Vesel, M. Kolar, A. Doliska, K. Stana-Kleinschek, M. Mozetic, Etching of polyethylene terephthalate thin films by neutral oxygen atoms in the late flowing afterglow of oxygen plasma, Surf. Interface Anal. 44 (2012) 1565–1571.

[35] V.M. Donnelly, A. Kornblit, Plasma etching: Yesterday, today, and tomorrow, J. Vac. Sci. Technol., A 31 (5) (2013) 050825, https://doi.org/10.1116/1.4819316.
[36] R.C. Longo, A. Ranjan, P.L.G. Ventzek, Density Functional Theory Study of Oxygen Adsorption on Polymer Surfaces for Atomic-Layer Etching: Implications for Semiconductor Device Fabrication, ACS Appl. Nano Mater. 3 (6) (2020) 5189–5202.
[37] A. Vesel, R. Zaplotnik, M. Mozetič, G. Primc, Surface modification of PS polymer by oxygen-atom treatment from remote plasma: Initial kinetics of functional groups formation, Appl. Surf. Sci. 561 (2021), 150058.
[38] D. Popović, M. Mozetič, A. Vesel, G. Primc, R. Zaplotnik, Review on vacuum ultraviolet generation in low-pressure plasmas, Plasma Processes Polym. 18 (2021) 2100061.
[39] Y. Zhang, K. Ishikawa, M. Mozetič, T. Tsutsumi, H. Kondo, M. Sekine, M. Hori, Polyethylene terephthalate (PET) surface modification by VUV and neutral active species in remote oxygen or hydrogen plasmas, Plasma Processes Polym. 16 (2019) 1800175.

Supplementary information

Depth profiling of thin plasma-polymerized polyamine films using GDOES in an Ar-O_2 plasma

Janez Kovač [a, *], Jernej Ekar [a, b], Miha Čekada [c], Lenka Zajíčková [d, e], David Nečas [f], Lucie Blahová [d], Jiang Yong Wang [g], Miran Mozetič [a]

[*]Corrersponding author, e-mail address: janez.kovac@ijs.si

[a] Department for Surface Engineering, Jozef Stefan Institute, Jamova cesta 39, SI 1000 Ljubljana, Slovenia

[b] Jozef Stefan International Postgraduate School, Jamova cesta 39, SI 1000 Ljubljana, Slovenia

[c] Department of Thin Films and Surfaces, Jozef Stefan Institute, Jamova cesta 39, SI 1000 Ljubljana, Slovenia

[d] Central European Institute of Technology – CEITEC, Brno University of Technology, Purkyňova 123, 61200 Brno, Czech Republic

[e] Department of Condensed Matter Physics, Faculty of Science, Masaryk University, Kotlářská 2, 61137 Brno, Czech Republic

[f] Central European Institute of Technology – CEITEC, Brno University of Technology, Purkyňova 123, 61200 Brno, Czech Republic

[g] Department of Physics, Shantou University, 243 Daxue Road, Shantou, 515063 Guangdong, China

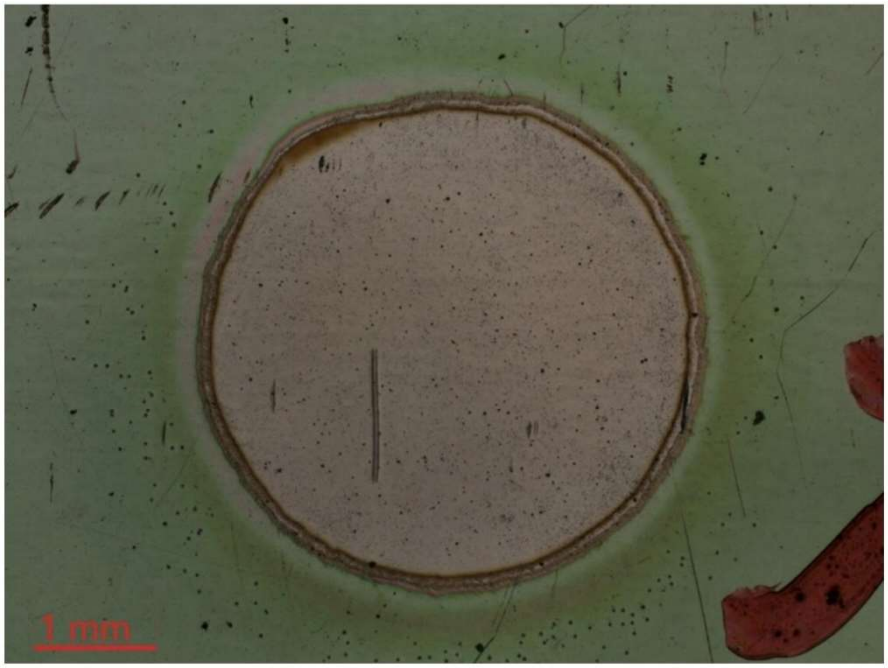

Figure S1. Bottom of the crater of the GDOES depth profile across a polymer film of thickness 500 nm using pure Ar.

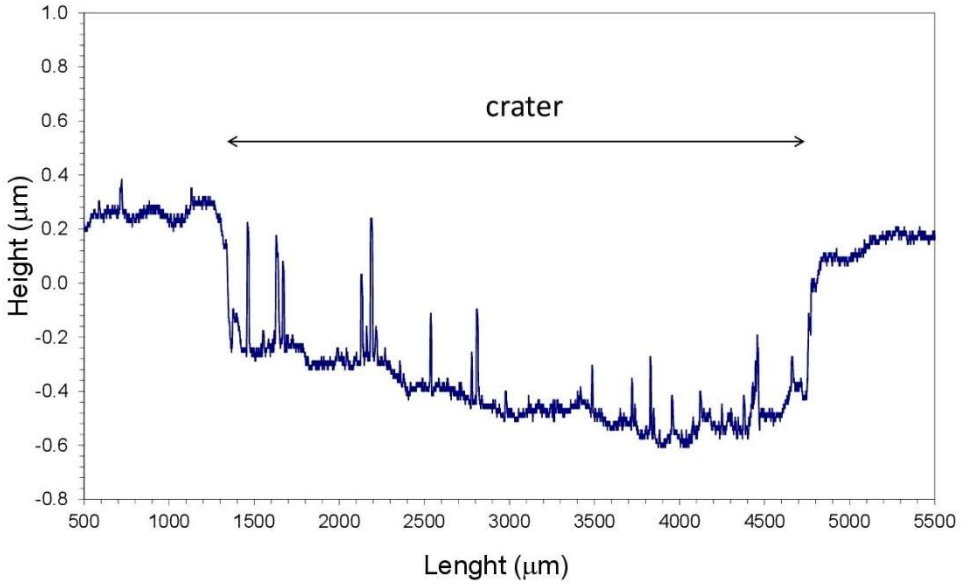

Figure S2. Line profile of the bottom of the crater of the GDOES depth profile across a polymer film of thickness 500 nm using pure Ar.

Figure S3. Bottom of the crater of the GDOES depth profile across a polymer film of thickness 500 nm using Ar + 4% O2.

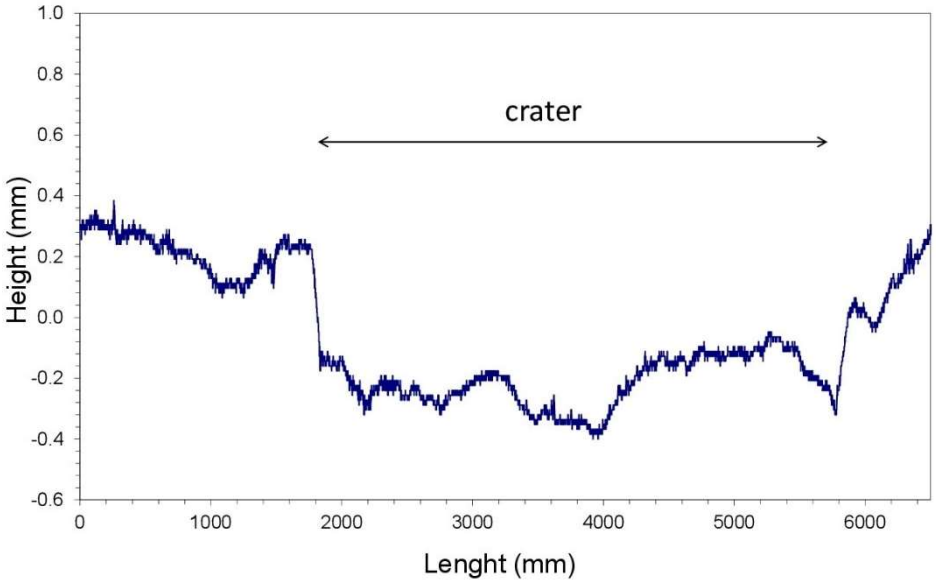

Figure S4. Line profile of the bottom of the crater of the GDOES depth profile across a polymer film of thickness 500 nm using Ar + 4% O2.

Chapter 6

Article 3: Reduction of Surface Roughening Caused by the Cs^+ Depth Profiling via H_2 Flooding

Surface roughening is present during all types of ion sputtering because of the damage accumulation caused by the ion bombardment. SIMS depth profiling is especially sensitive for roughness development. In this case, ion sputtering is prolonged and very intense with the total dose of sputtering ions much higher than during surface spectra measurements or imaging. In the case of depth profiling, a total dose of sputtering ions is in the range of 10^{18} ions $cm^{-2}h^{-1}$ while during surface spectra measurements or imaging, a total dose of primary ions is in the range of 10^{13} ions $cm^{-2}h^{-1}$. The most pronounced negative effect of surface roughening is reduced depth resolution needed for the high-quality analyses of thin films and multilayers. Thin layers can consequently become more difficult to distinguish. Increased surface roughness causes a broadening of the interfaces between layers. Since these effects are unwanted, different approaches toward reduced surface roughening during depth profiling were developed. The energy, type, and size of sputtering ions have an important role. The bigger the ions are and the lower their energy is, the less surface roughening they induce. The latter can be reduced also by the application of grazing angles under which ions bombard the surfaces. The further approach for roughness reduction is sample rotation during ion bombardment. Finally, less surface roughening can be observed when samples are cooled during the analysis and if gas flooding is applied.

Previous research showed good results obtained in the O_2 atmosphere. Therefore, we decided to test our novel approach of H_2 flooding. We performed depth profiling in the ToF-SIMS instrument on four different samples composed of thin layers of metals, metal oxides, and alloys. The compositions of the layered samples were $(Ni/Cr)_8$/<Si>, Fe_2O_3/Fe/Ag/Ni/NiO/<Si>, Cr_2O_3/Cr/Ti/TiO_2/Al_2O_3/Al/<Si>, and $(Ti/Si)_5$/Ti:Si=3:1/Ti:Si=1:1/<Si>. The thickness of the layers was between 2 and 60 nm. Si was used as a substrate in all four samples. Results obtained in the H_2 atmosphere with a pressure of 7×10^{-7} mbar were compared with the ultra-high vacuum (UHV) environment where pressure was in the range between 6×10^{-10} and 4×10^{-9} mbar. Since H_2 flooding is the most successful in combination with the Cs^+ ions, these ions were selected for the sputtering process. By following the signals in the SIMS profiles, the sputtering process was stopped at a specific depth, either in the middle of the layer or at the interface between layers. Samples were then taken out of the vacuum chamber and roughness average S_a at the bottom of the craters was measured with the atomic force microscope (AFM).

Measurements were done over the 2 μm × 2 μm and 5 μm × 5 μm scanning areas in a semicontact mode. Typical values of S_a in our study were between 0.6 and 5 nm.

We obtained quite a few different results. Some of them were expected. For example, it was shown that a Cs^+ ion beam with the energy of 2 keV induces more pronounced surface roughening than a Cs^+ ion beam with the energy of 1 keV. Such energy dependence has already been proven in previous studies. A gradual increase in surface roughness was observed with the prolonged depth profiling related to a higher dose of primary and sputtering ions. Less expected results were obtained when samples with high initial surface roughness S_a of approximately 5 nm were analyzed. For sputtering with the Cs^+ ions with the energy of 1 keV, a reduction of surface roughness was observed for some of these samples, indicating a reverse process, smoothing of the surface. Furthermore, it appeared that in some of the initially rough samples, S_a was more closely connected with the composition of the individual layers and not that much with the depth to which depth profiling was performed. This indicates different sensitivity of chemically different layers for roughness development as a consequence of ion sputtering. Finally, positive effects of the H_2 atmosphere on roughness reduction were observed as well. It appears that H_2 flooding causes a reduction in surface roughening for almost all the samples and all the layers and interfaces. However, due to the large differences in measured S_a values of initially rough samples, improvements caused by the H_2 were mostly statistically insignificant in these cases. Differences in these samples are so large because they have many trench and ripple-like structures that are randomly distributed over the surface and have a significant influence on the measured value of the S_a. On the other hand, when initially a very smooth sample with the S_a of approximately 1 nm was analyzed, improvements achieved with the H_2 flooding were statistically significant and unambiguously proven. It was observed that the H_2 atmosphere shows a larger effect when a Cs^+ ion beam with a higher energy is used. Differences between S_a measured after depth profiling in H_2 or UHV also increase with prolonged sputtering.

Effects caused by the H_2 atmosphere are probably connected with the formation of hydride species on the freshly sputtered surface. Different compounds show different tendencies toward crystallization and ion sputtering is known to induce amorphization of the material. Crystalline materials are generally rougher than amorphous ones because topographical structures, such as trenches, ripples, ridges, and cones/pyramids more easily form on crystalline surfaces. Amorphous materials have less of these structures because they relax more easily. Therefore, it can be anticipated that metal hydrides formed on top of the metal substrates during the sputtering process tend to remain amorphous to a larger extent than pure metals, causing reduced surface roughness when H_2 flooding is applied. Results obtained in this study confirmed the hypothesis 5.

Contributions of the Ph.D. dissertation author: conceptualization and visualization of the experiment, methodology, investigation via ToF-SIMS depth profiling and AFM measurements, performing calculations and interpreting the results, writing the original draft, reviewing and editing, and project administration.

LANGMUIR

pubs.acs.org/Langmuir Article

AFM Study of Roughness Development during ToF-SIMS Depth Profiling of Multilayers with a Cs^+ Ion Beam in a H_2 Atmosphere

Jernej Ekar and Janez Kovač*

Cite This: *Langmuir* 2022, 38, 12871−12880 Read Online

ACCESS | Metrics & More | Article Recommendations | Supporting Information

ABSTRACT: The influence of H_2 flooding on the development of surface roughness during time-of-flight secondary ion mass spectrometry (ToF-SIMS) depth profiling was studied to evaluate the different aspects of a H_2 atmosphere in comparison to an ultrahigh vacuum (UHV) environment. Multilayer samples, consisting of different combinations of metal, metal oxide, and alloy layers of different elements, were bombarded with 1 and 2 keV Cs^+ ion beams in UHV and a H_2 atmosphere of 7×10^{-7} mbar. The surface roughness S_a was measured with atomic force microscopy (AFM) on the initial surface and in the craters formed while sputtering, either in the middle of the layers or at the interfaces. We found that the roughness after Cs^+ sputtering depends on the chemical composition/structure of the individual layers, and it increases with the sputtering depth. However, the increase in the roughness was, in specific cases, approximately a few tens of percent lower when sputtering in the H_2 atmosphere compared to the UHV. In the other cases, the average surface roughness was generally still lower when H_2 flooding was applied, but the differences were statistically insignificant. Additionally, we observed that for the initially rough surfaces with an S_a of about 5 nm, sputtering with the 1 keV Cs^+ beam might have a smoothing effect, thereby reducing the initial roughness. Our observations also indicate that Cs^+ sputtering with ion energies of 1 and 2 keV has a similar effect on roughness development, except for the cases with initially very smooth samples. The results show the beneficial effect of H_2 flooding on surface roughness development during the ToF-SIMS depth profiling in addition to a reduction of the matrix effect and an improved identification of thin layers.

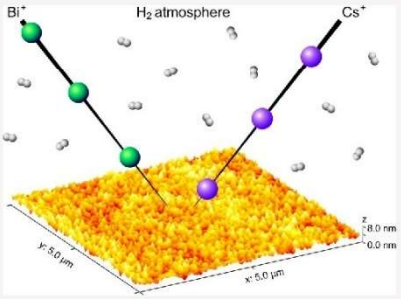

INTRODUCTION

Ion sputtering is the main process taking place during an analysis based on secondary ion mass spectrometry (SIMS).[1] It is also an essential process for depth profiling, combined with X-ray photoelectron spectroscopy (XPS) and Auger electron spectroscopy (AES).[2−4] All three methods employ ion guns for sputtering, although the sputtering process itself is also present in the case of glow-discharge optical emission spectroscopy (GDOES) or glow-discharge mass spectrometry (GDMS).[3,5−7] The main difference is the characteristic of the GDOES or GDMS processes, as ions are intrinsic to the plasma that flows toward the cathode, causing its surface to be sputtered away.[6,8] These methods are used in many areas of research, for example, during the analysis of oxide layers,[9] while studying corrosion properties,[10] polymer films,[11] mono- and multilayers,[12] biomaterials,[13] microelectronics,[14,15] power-storage materials,[16] solar cells,[17,18] and catalysts.[19] However, regardless of the exact process used for the ion sputtering, the ion beam generated by the ion gun or the plasma flow, some damage caused by the ion bombardment is always present.[20−22] The accumulation of damage is observed as surface roughening, which is most commonly determined with atomic force microscopy (AFM).[23,24] This technique is especially suitable for the characterization of nanostructures formed on the surface since it is optimized to achieve molecular and atomic resolutions.[25−27] However, AFM can also be used to study many other topographical characteristics of the sample, its conductivity at the nano level, and different forces using its spectroscopy mode.[27−31]

The general behavior related to sputter-induced damage and surface roughening is that sputtering ions with a higher energy[21,32,33] and a longer sputtering process[21,33−35] lead to a greater surface roughness being caused by the ions. Since surface roughening is an unwanted process in many applications, different approaches have been developed to reduce it as much as possible. Many investigations have looked at temperature manipulation, the type and size of the sputtering ions as well as adjusting the angle at which they bombard the surface, the use of sample rotation,[36,37] and finally gas flooding.[38,39] It was shown that the depth profiles of mainly polymeric, organic, and biological, but also inorganic compounds can be improved, as well as the sputter-induced

Received: July 13, 2022
Revised: October 4, 2022
Published: October 14, 2022

https://doi.org/10.1021/acs.langmuir.2c01837
Langmuir 2022, 38, 12871−12880

topography reduced, if the sample is cooled.[40−42] The depth profiling of organic materials was also improved by the application of larger, molecular sputter ions such as Bi_3^+, Au_3^+, SF_5^+, C_{60}^+ (fullerene), and Ar_n^+ (argon clusters with n being the number of Ar atoms, which is between a few hundred and a few thousand).[37,43,44] Furthermore, we can improve the depth resolution by bombarding the sample with ions at larger incident angles with respect to the surface normal (grazing angles).[45,46] But regardless of the angle of bombardment, topographical structures such as ripples, ridges, valleys, cones, and pyramids are formed during the sputtering process.[35,40,47] Their formation can be suppressed and the surface roughening reduced by sample rotation.[22,48,49] Last but not least, it was also shown that surface roughening can be reduced if an O_2 atmosphere is applied during the depth profiling, causing the sample to oxidize.[38,39]

As we have shown in our recent work, the time-of-flight secondary ion mass spectrometry (ToF-SIMS) depth profiling of metals, metal oxides, and alloys is improved in terms of sensitivity and a reduction of the matrix effect if a H_2 atmosphere is applied instead of ultrahigh vacuum (UHV).[12] Since H_2 flooding is a novelty in the field of atmosphere manipulation and has, at least to some degree, similar effects to O_2 flooding, we made AFM measurements of the sputtered craters and checked whether less surface roughening can be observed in the case of our experiments as well. In this study, we depth-profiled four different samples composed of metal, metal oxide, and alloy multilayers while sputtering with a Cs^+ ion beam in both UHV and H_2 environments. Furthermore, we tested different energies of Cs^+ sputtering ions and analyzed the surface roughness of the layers with different chemical compositions. Last but not least, the samples analyzed had different initial surface roughnesses, another factor that influenced the surface morphology during sputtering. We showed that a H_2 atmosphere generally reduces the surface roughening or leads to no statistically significant change.

EXPERIMENTAL SECTION

Preparation of the Samples. All of the metals and metal oxides were prepared using physical vapor deposition (PVD). They were deposited in a Sputron triode sputtering system (Balzers Oerlikon). The background pressure was lower than 1×10^{-6} mbar. The partial pressure of the argon working gas in the vacuum chamber was 2×10^{-3} mbar for all of the processes. A maximum substrate temperature of less than 100 °C was maintained during the deposition. A quartz-crystal microbalance was used to calibrate the deposition rates. The deposition rates and thickness reproducibility were better than 2%.

The 60 mm diameter targets were initially cleaned for 5 min to remove the native oxide and other impurities on their surfaces. High-purity targets were used as the sputtering source. Metal-oxide layers (Cr_2O_3, TiO_2, Al_2O_3, Fe_2O_3, NiO) were prepared by reactive sputtering. In this process, thin oxide films were deposited on the substrates by sputtering metallic targets in the presence of oxygen mixed with an argon working gas. The flow rate of the oxygen (99.998%) was controlled with a flowmeter.

Ion Sputtering of the Samples. Samples were sputtered using Cs^+ ions with energies of 1 and 2 keV and ion currents of 49−67 and 78−90 nA, respectively. The 1 keV Cs^+ was sputtered in pulses lasting 48.5 μs, while the 2 keV Cs^+ used pulses of 61.5 μs. Pulsed Bi^+ primary ions with an energy of 30 keV, a pulse length of 5.9 ns, and an ion current of 0.8−2.2 pA were used for the analysis. The Cs^+ and Bi^+ ions were generated in two separate ion guns (dual-beam depth profiling) mounted on a TOF.SIMS 5 instrument produced by IONTOF GmbH (Munster, Germany). The ion guns work interchangeably and sequentially. Namely, we have a cycle of ion-etching with the Cs^+ ions, which happens while the separation in the time-of-flight analyzer and detection takes place (70 μs). The Cs^+ cycle is shorter than the ToF analysis, so we also have a time interval without any sputtering. This is followed by the cycle of ion sputtering with the Bi^+ ions, being the basis for the next ToF analysis. Sputtering with the Bi^+ primary ions was performed over a 200 μm × 200 μm scanning area (128 pixels × 128 pixels), located in the center of the 400 μm × 400 μm etching crater created by the Cs^+ ion beam.

The H_2 used during the depth profiling was introduced into the analysis chamber close to the analyzed region (a distance of less than 1 cm). The gas introduction was manually controlled with a precise gas-leak valve through a capillary, leading toward the analyzed area. H_2 with a 6.0 purity was used and the pressure inside the analysis chamber during the gas flooding was approximately 7×10^{-7} mbar. Analyses in the UHV conditions were made in the pressure range between 6×10^{-10} and 4×10^{-9} mbar.

AFM Measurements. Surface roughness was determined with a Solver PRO 47 AFM microscope produced by NT-MDT (Russia) with AFM tips produced by the same company. The arithmetic average of the three-dimensional (3D) roughness (S_a) was chosen as the representative value. Images were measured on 2 μm × 2 μm and 5 μm × 5 μm scanning areas in semicontact mode. The recording frequency was 1.0 Hz. The resolution of the images was set to 256 pixels × 256 pixels. The plane subtraction of the AFM images due to the inclination of the samples involved a second-order polynomial correction.

RESULTS AND DISCUSSION

Composition of the Samples. Four different samples with multilayer structures of metals, metal oxides, and alloys were analyzed. All of the samples were prepared on mirror-like polished silicon wafers and had a different initial surface roughness. Sample 1 (FeAgNi) and sample 2 (CrTiAl) were composed of Fe_2O_3/Fe/Ag/Ni/NiO and Cr_2O_3/Cr/Ti/TiO_2/Al_2O_3/Al layers, respectively. Sample 3 (TiSi) consisted of 10 alternating layers of Ti and Si followed by two Ti−Si alloy layers. The first layer had a stoichiometric ratio of Ti and Si equal to 3:1, with the higher concentration being titanium, while the second layer had a Ti/Si ratio of 1:1. Sample 4 (NiCr) consisted of 16 alternating layers of Ni and Cr. The exact structure of each sample is shown in Figure 1, together with the thickness of each layer. The surface roughness was measured on the initial nonsputtered surface of all four samples, at different interfaces, and in the middle of the chosen layers. The analyzed interfaces were:

- Fe_2O_3/Fe interface (FeAgNi sample)
- 5th Ti/Si interface (TiSi sample)
- 2nd and 6th Cr/Ni interface (NiCr sample)

The layers for which we analyzed the surface roughness were:

- Ag and NiO (FeAgNi sample)
- Cr and Al_2O_3 (CrTiAl sample)
- Ti−Si alloy with the atomic ratio of 1:1 (TiSi sample)
- 3rd and 7th Ni layer (NiCr sample)

The depths where the analyses were made are also indicated in Figure 1 as white circles at the interfaces and in the middle of the layers.

SIMS Depth Profiles. Figure 2a shows the ToF-SIMS depth profile of the FeAgNi sample recorded in UHV conditions, and Figure 2b shows the depth profile of the same sample recorded during H_2 flooding. The signals of the different secondary ions are shown as a function of the sputtering time. In the ToF-SIMS depth profile shown in Figure 2a, different metal and metal oxide layers cannot be

https://doi.org/10.1021/acs.langmuir.2c01837
Langmuir 2022, 38, 12871−12880

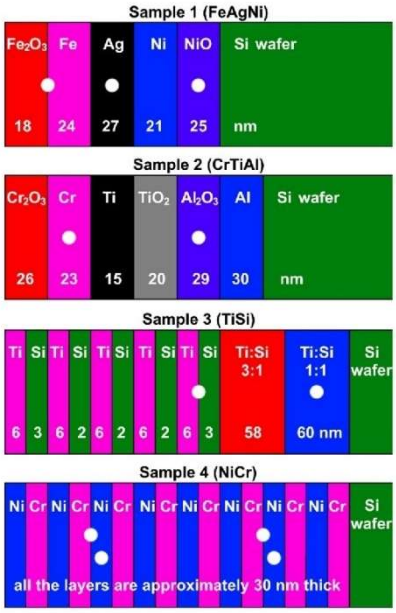

Figure 1. Schematic of four samples with layer thicknesses. White dots represent interfaces and layers where the analyses of the surface roughnesses were made. Adapted with permission from ref 12. Copyright 2022 creative commons.

clearly identified. On the other hand, the depth profile recorded during H_2 flooding (Figure 2b) unambiguously describes the exact structure of the FeAgNi sample. The roughness developed during ion sputtering is an important parameter since it can reduce the sharpness of the interfaces.

Surface Roughness Measurements. The craters where the surface roughnesses were measured were ion sputtered in the SIMS instrument with a 1 or 2 keV Cs^+ ion beam. An example of an optical image of such a crater is shown in Figure 3. Two craters were sputtered in UHV and two in a H_2

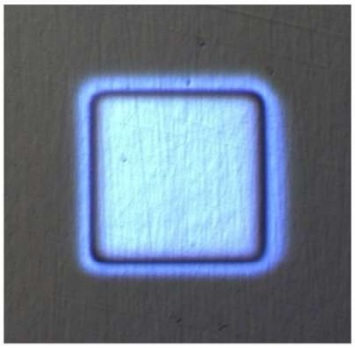

Figure 3. Crater caused by etching the CrTiAl sample with the 1 keV Cs^+ ion beam.

atmosphere of 7×10^{-7} mbar. During the crater sputtering a Bi^+ analysis ion beam was used as well, and we were able to see the multilayer structure that we were profiling. Following the SIMS signal evolution, we were therefore always able to stop the ion sputtering at the desired depth, either in the middle of the layer or exactly at the interface. In such a way the differences in the ion current, as well as sputtering rate, were considered, as slightly different times were needed to reach the

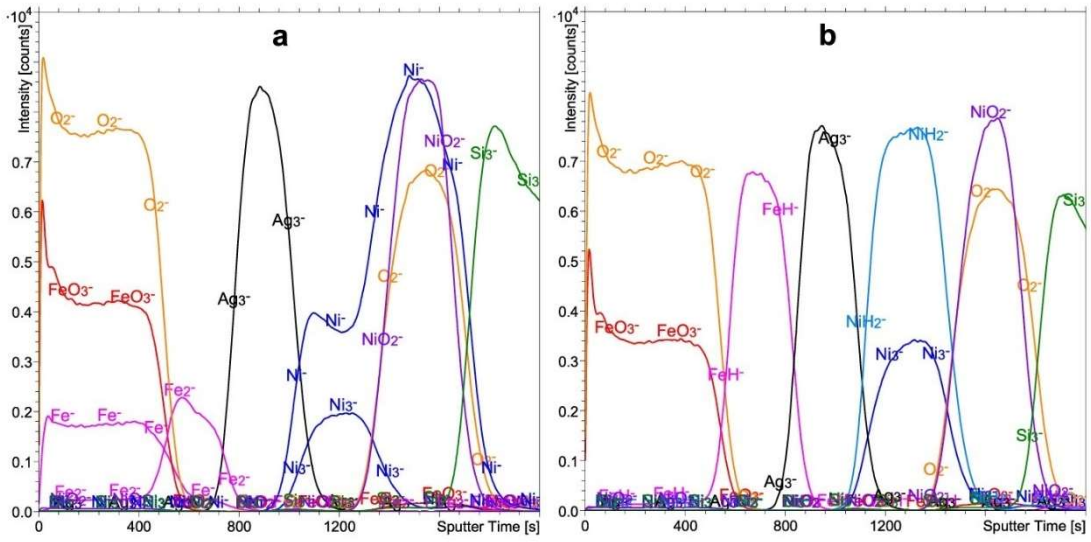

Figure 2. Depth profiles of the FeAgNi sample recorded using a 1 keV Cs^+ sputtering beam. Profile (a) was recorded in a UHV environment, while profile (b) was recorded during H_2 flooding. The presence of H_2 is the reason for the intense metal hydride signals in profile (b). The intensities of some signals were multiplied by a specific factor as a way of reducing the intensity scale interval and making the profile clearly readable. Adapted with permission from ref 12. Copyright 2022 creative commons.

https://doi.org/10.1021/acs.langmuir.2c01837
Langmuir 2022, 38, 12871−12880

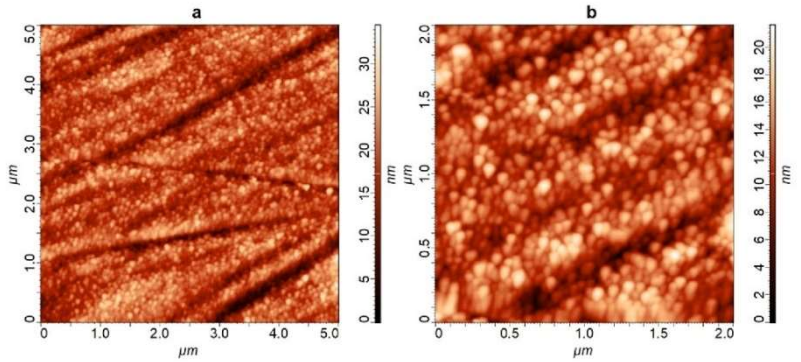

Figure 4. AFM images of the NiO layer at a depth of around 100 nm in the FeAgNi sample recorded inside the depth-profiling crater; 1 keV Cs^+ ions were used for sputtering in the H_2 atmosphere. Image (a) was taken over the 5 μm × 5 μm analysis area, while image (b) was measured inside the boundaries of this area over 2 μm × 2 μm while choosing the area with the least amount of large structural defects, such as ripples and ridges (seen in image (a)).

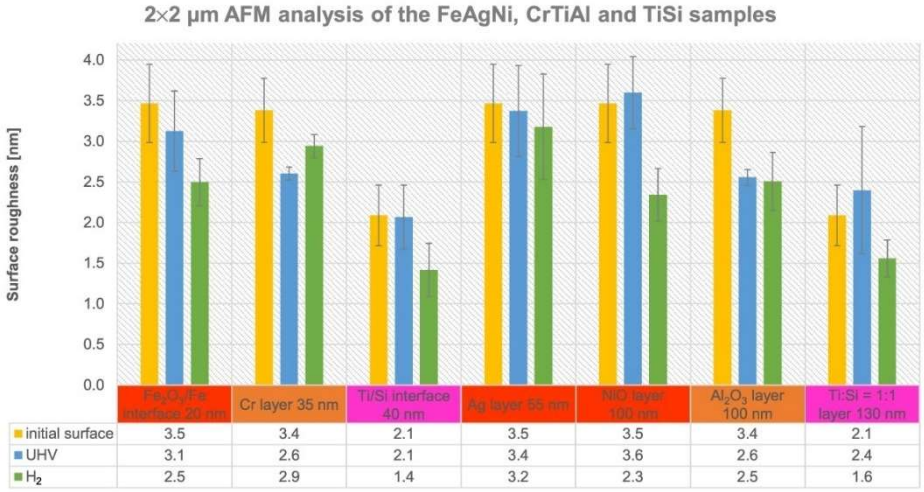

Figure 5. Surface roughness of the FeAgNi, CrTiAl, and TiSi samples with a table of the average surface roughness values. Surface roughness was measured over the 2 μm × 2 μm area. Yellow columns represent the initial surface roughness of the chosen sample, blue columns are the roughness of the craters sputtered in the UHV conditions, and green columns are the roughness after sputtering in the H_2 atmosphere. Sputtering was made with the 1 keV Cs^+ ion beam. The layers and interfaces measured on the FeAgNi sample are colored red, the ones from the CrTiAl sample are orange, and the ones from the TiSi sample are pink.

desired depth while ion sputtering the same sample. The AFM analyses were performed in ambient conditions after all four craters were sputtered. Two 5 μm × 5 μm images were measured in each of the craters, so overall four images for the UHV conditions and four for the H_2 atmosphere ion sputtering were made. The 2 μm × 2 μm images were recorded in the same manner. Analyses of the nonsputtered surface were made a few millimeters from the craters so that long-range differences did not affect the results. The analyses made too close to the crater are problematic as the debris originating from the ion sputtering could affect the measurements. The 2 μm × 2 μm areas were always analyzed inside the 5 μm × 5 μm areas, which were analyzed first.

AFM measurements showed that the FeAgNi, CrTiAl, and TiSi samples all have relatively large initial surface roughnesses. In the case of the FeAgNi and CrTiAl samples, it was 5 ± 1 nm, and in the case of the TiSi sample, it was 3.4 ± 0.5 nm for the 5 μm × 5 μm analysis area. When the 2 μm × 2 μm area was analyzed, the surface roughness values were slightly lower: 3.5 ± 0.5 nm for the FeAgNi, 3.4 ± 0.4 nm for the CrTiAl, and 2.1 ± 0.4 nm for the TiSi sample. Figure 4 shows AFM images of the NiO layer in the FeAgNi sample recorded over the 5 μm × 5 μm and 2 μm × 2 μm analyses areas inside a crater after depth profiling with the 1 keV Cs^+ ion beam in the H_2 atmosphere.

Figure 5 graphically presents the initial surface roughness of the first three samples (FeAgNi, CrTiAl, and TiSi) together with the surface roughness measured in the layers and interfaces noted previously after sputtering with the 1 keV Cs^+ ion beam in the UHV conditions and during H_2 flooding. The initial surface roughness is presented beside each layer and interface, with the sputtered depth increasing from left to right.

https://doi.org/10.1021/acs.langmuir.2c01837
Langmuir 2022, 38, 12871−12880

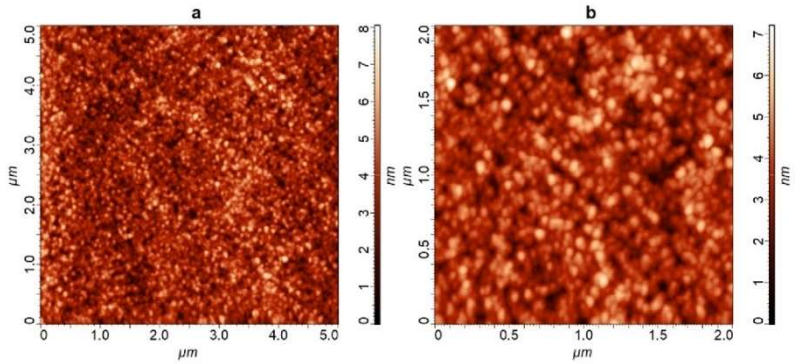

Figure 6. AFM images of the third Ni layer at a depth of around 135 nm in the NiCr sample recorded inside the depth-profiling crater; 1 keV Cs^+ ions were used for sputtering in the H_2 atmosphere. Image (a) was taken over a 5 μm × 5 μm analysis area, while image (b) was measured inside the boundaries of this area over 2 μm × 2 μm.

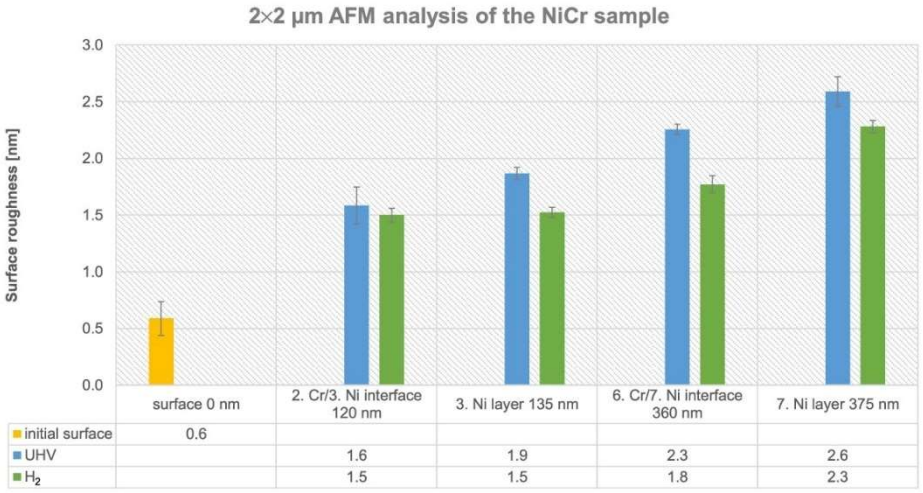

Figure 7. Surface roughness of the NiCr sample with a table of the average surface roughness values. Surface roughness was measured over the 2 μm × 2 μm area. Yellow column represents the initial surface roughness, blue columns the roughness of the craters sputtered in the UHV conditions, and green columns the roughness after sputtering in the H_2 atmosphere. Sputtering was made with the 2 keV Cs^+ ion beam.

The data presented in Figure 5 were measured over the 2 μm × 2 μm analysis area. We also added a table of the average surface roughness values below the graph to present our findings more clearly. The average surface roughness values for the 5 μm × 5 μm analysis area are between 3.1 ± 0.4 and 5.1 ± 0.5 nm and for the area of 2 μm × 2 μm, between 1.4 ± 0.3 and 3.6 ± 0.4 nm. All of the surface roughness values with standard deviations are listed in Supporting Information Tables S1−S3 for the FeAgNi, CrTiAl, and TiSi samples, respectively. A pronounced surfaced roughness is correlated with high standard deviation values and therefore many changes noticed during the depth profiling cannot be regarded as statistically significant. Nevertheless, we can still find and emphasize a few trends that are also statistically significant:

- Sputtering with the 1 keV Cs^+ ion beam in the UHV environment or H_2 atmosphere either does not change the initial surface roughness significantly (Ti/Si interface, Ag and Ti/Si = 1:1 layers) or can reduce it (Cr and Al_2O_3 layers, Fe_2O_3/Fe interface and NiO layer in the H_2 atmosphere).
- Surface roughness can be reduced when the ion sputtering is performed in a H_2 atmosphere compared to UHV conditions (significantly for the NiO layer and probably for the Ti/Si interface as well). Sputtering in UHV produces lower values of roughness than sputtering in H_2 only for the Cr layer.
- Surface roughness is less affected by the sputtering depth than by the chemical composition of the layer or the interface of interest. The differences are within the statistically accepted uncertainty; however, the average surface roughness values for the FeAgNi sample, as an example, sputtered in the H_2 atmosphere follow the trend of an initial decrease (Fe_2O_3/Fe interface), then an increase (Ag layer), and another decrease (NiO layer).

The surface roughness changes measured over the 5 μm × 5 μm area are shown in Figure S1. All of the main characteristics

https://doi.org/10.1021/acs.langmuir.2c01837
Langmuir 2022, 38, 12871−12880

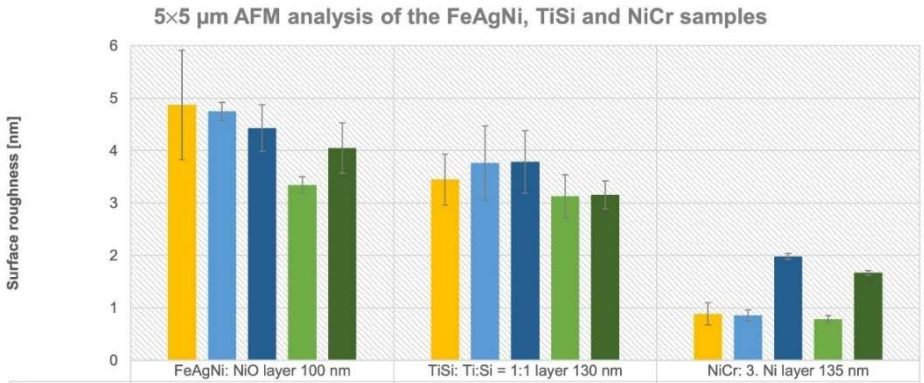

	FeAgNi: NiO layer 100 nm	TiSi: Ti:Si = 1:1 layer 130 nm	NiCr: 3. Ni layer 135 nm
initial surface	4.9	3.4	0.9
UHV 1 keV Cs^+	4.7	3.8	0.9
UHV 2 keV Cs^+	4.4	3.8	2.0
H_2 1 keV Cs^+	3.3	3.1	0.8
H_2 2 keV Cs^+	4.0	3.2	1.7

Figure 8. Surface roughness of the FeAgNi, TiSi, and NiCr samples after sputtering with the 1 and 2 keV Cs^+ ion beams. Added is the table of average surface roughness values. Surface roughness was measured over the 5 μm × 5 μm area. Yellow columns represent the initial surface roughness, light blue columns the roughness of the craters sputtered in UHV with the 1 keV Cs^+, dark blue columns the roughness of the craters sputtered in UHV with the 2 keV Cs^+, light green columns the roughness after sputtering with the 1 keV Cs^+ in the H_2 atmosphere, and dark green columns the roughness after sputtering with the 2 keV Cs^+ in the H_2 atmosphere. Analyses of the layers are assigned as "the sample: the layer of the sample being analyzed and the depth at which ion sputtering was stopped".

and trends are the same as for the 2 μm × 2 μm analysis area. There are only slightly changed average values for the differences between the surface roughness for the nonsputtered surface, the one sputtered in the UHV, and the one in the H_2 atmosphere. Small differences can also be seen when comparing the standard deviation values between the graphs for the 5 μm × 5 μm and 2 μm × 2 μm analyses areas.

The NiCr sample is, on the other hand, much smoother than the FeAgNi, CrTiAl, and TiSi samples. Its initial surface roughnesses are 0.9 ± 0.2 and 0.6 ± 0.1 nm for the 5 μm × 5 μm and 2 μm × 2 μm analyses areas, respectively. This can also be observed on the AFM images as there are no lines caused by the sample preparation. Such ripples are, on the other hand, present in the cases of the FeAgNi (Figure 4), CrTiAl, and TiSi samples. Figure 6 shows AFM images of the third Ni layer in the NiCr sample recorded over the 5 μm × 5 μm and 2 μm × 2 μm analyses areas after sputtering. The depth profiling was, as in Figure 4, performed with the 1 keV Cs^+ ion beam in the H_2 atmosphere.

Figure 7 presents the surface roughness of the NiCr sample measured over the 2 μm × 2 μm area. The roughness was measured on a nonsputtered surface and in the craters, etched with the 2 keV Cs^+ ion beam, at depths of approximately 120, 135, 360, and 375 nm. The layers and interfaces were again etched in the UHV and during H_2 flooding, with the results compared in Figure 7. The average surface roughness values with their standard deviations for both 5 μm × 5 μm and 2 μm × 2 μm analyses areas are listed in Table S4. The result is that the S_a measured over the 5 μm × 5 μm area increases from 0.9 ± 0.2 nm at the surface to 2.66 ± 0.05 nm (UHV) or 2.50 ± 0.05 nm (H_2) at a depth of 375 nm. The change of S_a observed over the 2 μm × 2 μm area is from 0.6 ± 0.1 to 2.6 ± 0.1 nm (UHV) or 2.28 ± 0.05 nm (H_2). The consequence of the much smoother surface of the NiCr sample is also a significantly lower standard deviation of the surface roughness compared to the FeAgNi, CrTiAl, and TiSi samples. Statistically significant conclusions are therefore easier to draw and more clearly pronounced:

- Surface roughness increases with a prolonged sputter time, and therefore with the depth of the crater being sputtered.
- H_2 flooding notably reduces the surface roughening caused by the Cs^+ ion sputtering.
- The effect of the H_2 atmosphere becomes more evident at greater depths, and therefore after a longer sputter time.

The first observation was, however, expected since it is well known that ion sputtering with small projectiles (mainly monoatomic ions) increases surface roughening. Therefore, the results regarding surface roughness changes during ion sputtering presented in Figure 5 are worthy of more attention, since "polishing" of the surface with the Cs^+ ion beam is not a well-known effect. Also, the surface roughness for the NiCr sample measured over the 5 μm × 5 μm analysis area shows the same pattern as the roughness measured over the 2 μm × 2 μm area. The graph showing the results from the 5 μm × 5 μm AFM analysis is shown in Figure S2.

Finally, we compared the surface roughening caused by Cs^+ ion beams with different energies, i.e., 1 and 2 keV. We must also emphasize that we tested only the Cs^+ ion beam since our previous study[12] showed that H_2 flooding works optimally when combined with Cs^+ sputtering. Since the main objective of this study is to show the effects of the H_2 atmosphere on surface roughening during depth profiling, we did not include other types of sputtering ions. Figure 8 shows a graph comparing the surface roughness of the specific layers of the FeAgNi, TiSi, and NiCr samples after etching with both the 1 and 2 keV Cs^+ ion beams in the UHV and H_2 atmosphere. The AFM analysis for Figure 8 was made over the 5 μm × 5 μm area. The results for the 2 μm × 2 μm analysis area shown in

https://doi.org/10.1021/acs.langmuir.2c01837
Langmuir 2022, 38, 12871−12880

Figure S3 reveal the same trends as the 5 μm × 5 μm AFM analysis. The average surface roughness values and their standard deviations used in Figures 8 and S3 are listed in Tables S1−S4. The results shown in Figure 8 confirm the findings from Figures 5 and 7, as well as offer some additional information:

- The 2 keV Cs^+ ion beam causes a more pronounced roughening than the 1 keV Cs^+ beam if the surface initially has a low surface roughness (NiCr sample). If the surface is initially rougher (FeAgNi and TiSi samples), then there is no statistical difference when sputtering with Cs^+ ions of different energies.
- The 1 keV Cs^+ sputtering either does not cause any significant change in the surface roughness (TiSi sample) or it can, for some layers and during H_2 flooding, reduce the roughness (FeAgNi and CrTiAl samples).
- H_2 flooding either reduces the roughening compared to the UHV conditions or does not affect the surface roughening. The positive H_2 effect is the most clearly seen for the NiO layer (FeAgNi sample) when sputtering with the 1 keV Cs^+ and for the third Ni layer (NiCr sample) when sputtering with the 2 keV Cs^+ ion beam.

Discussion. From the surface roughness measurements, we can conclude that the H_2 flooding during SIMS depth profiling potentially leads to reduced surface roughening caused by the ion sputtering. This can be clearly seen in Figures 5, 7, 8, and S1−S3. Namely, almost all of the AFM analyses of the layers and interfaces show reduced average surface roughness values when H_2 flooding was applied, compared to the UHV environment. The reduction in the surface roughness is sometimes statistically significant, while in other cases it cannot be confirmed. The only exception is the Cr layer in the CrTiAl sample (Figures 5 and S1), where the surface roughness during H_2 flooding increases compared to the UHV depth profiling. Such observations are positive, as they indicate that the H_2 atmosphere applied during the depth profiling of metals, metal oxides, and alloys not only improves the capability of the SIMS method to unambiguously distinguish different layers[12] but also potentially reduces the surface roughening caused by the ion-induced damage. The results are even better when we put them into the perspective of the sputter rate, which does not change significantly when the H_2 atmosphere and UHV are compared.[12] Namely, we anticipate that a very thin surface layer of metal hydride is formed during H_2 flooding, which also causes hydrogen-induced embrittlement of the metals.[50−52] The embrittlement explains the unchanged sputter rate, which is otherwise reduced if gases such as O_2, CO, or C_2H_2 are applied instead of the H_2.[12]

Another important observation is connected with the initial surface roughness of our samples. Namely, if the sample is very flat (NiCr sample with a surface roughness below 1 nm), ion sputtering either leads to a gradual surface roughening (2 keV Cs^+ ion beam, Figures 7, 8, S2, and S3) or the surface roughness remains more or less unchanged (1 keV Cs^+ ion beam, Figures 8 and S3). Such results are expected since the surface roughening caused by the ion-bombardment-induced damage is a well-known phenomenon.[20−22] The roughness of the surfaces increases during the ion sputtering due to the formation of different topographical structures such as ripples, ridges, and cones/pyramids.[35,40] It is, therefore, unexpected that especially the 1 keV Cs^+ ion beam offers the potential for smoothing the surface of a sample that is not very flat (surface roughness above 3 nm). Namely, as seen in Figures 5 and S1, the surface roughness of the specific layers of the FeAgNi and CrTiAl samples, which have a greater initial surface roughness, decreases after they are sputtered with the 1 keV Cs^+ ion beam, either during H_2 flooding and/or in the UHV environment. This is most clearly seen for the Fe_2O_3/Fe interface and the Cr, NiO, and Al_2O_3 layers. In these cases, we can observe a statistically significant decrease of the surface roughness in at least one of the measurement areas (2 μm × 2 μm or 5 μm × 5 μm) and during the depth profiling in at least one of the environments (H_2 atmosphere or UHV). The 1 keV Cs^+ depth profiling is therefore very suitable when surface roughening during a depth profiling is highly undesirable, as well as when polishing of the initially rough surface is desired. However, we must also emphasize that this is not the only example of surface smoothing achieved with ion sputtering. For example, a bombardment of a SiO_2 surface with an initial roughness of approximately 1 nm with the 0.2−1.0 keV H^+ ions resulted in a reduced surface roughness.[53]

As already mentioned, greater surface roughening can be seen when a Cs^+ ion beam of higher energy is used (Figures 8 and S3). Such results are expected since ions of higher energy cause greater damage to the surface during their impact and similar findings were already published.[21,32,33] We must, however, note that an increase in the surface roughening is not always correlated with an increase in the energy of the sputtering ions. O_2^+ sputtering is such an example, as the onset of the surface roughening during this process happens, in some specific cases defined by the incident angle of the ion beam, sooner and also to a greater extent if O_2^+ ions of lower energy are used.[54,55] We can, therefore, conclude that the results of our study can be applied only as a confirmation of the correlation between the surface roughening and the energy of the Cs^+ ion beam, but cannot be extended to the other types of sputter ions.

Our study, furthermore, shows a correlation between the sputtering depth (or the sputter time) and the surface roughness, but only in the case of an initially flat NiCr sample. As seen in Figures 7 and S2, the surface roughness of the NiCr sample increases with the increasing sputter depth reached during sputtering with the 2 keV Cs^+ ion beam, both when H_2 flooding or UHV conditions were applied. Such results are expected, as previous studies show the same correlation.[21,33−35] However, different results were found for the initially rougher FeAgNi, CrTiAl, and TiSi samples, where no correlation between the surface roughness and the sputtering depth can be determined when sputtering with 1 keV Cs^+ ions (Figures 5 and S1). We believe that different effects are behind such observations. Namely, as we already determined, sputtering with a 1 keV Cs^+ ion beam can reduce the surface roughness of initially rough samples. Therefore, increased roughening should not be expected. On the other hand, we also cannot observe any continuous decrease of the surface roughness, but rather random decreases and increases, which are in many cases statistically insignificant. As such, a layer that was lying deeper in the sample and needed a longer sputtering time could have a smaller surface roughness than the layer above it, or the other way around. These decreases and increases in the surface roughness are, however, correlated for the 2 μm × 2 μm and 5 μm × 5 μm analyses areas when the

https://doi.org/10.1021/acs.langmuir.2c01837
Langmuir 2022, 38, 12871−12880

same layer and the same profiling condition (H_2 atmosphere or UHV) are compared. The most probable explanation for this is the effect of the chemical composition and crystallographic structure of the layer. Namely, different layers can have different initial crystallinity and also exhibit different tendencies to form an amorphous layer on the surface as a consequence of the ion sputtering. It was already proven that many materials amorphize during ion sputtering.[32,34,56−58] Amorphization affects the surface roughness, generally reducing it as amorphous materials more easily relax and fewer topographical structures are formed.[34] Furthermore, hydrides and hydroxides, formed during depth profiling in the H_2 atmosphere, and mostly oxides, formed in the UHV, can exhibit different roughnesses depending on the metal they bind with. Mostly oxides are formed in UHV because some O_2 is still present, while during H_2 flooding, we observe the formation of hydrides when metals are being sputtered, and the formation of hydroxides when sputtering metal oxide layers. Flooding of the oxygen during depth profiling as well as the formation of the oxides in the profiling crater both reduce the surface roughening.[38,39] We believe that a similar effect can be observed for metallic hydrides and hydroxides.

CONCLUSIONS

The results of our study show that H_2 flooding applied during SIMS depth profiling with a Cs^+ ion beam positively affects many aspects of the measurements. Besides the improved resolving capability of SIMS due to the reduced matrix effect, also a reduced surface roughening can be observed in comparison to the UHV environment. Namely, the surface roughness of different metallic and metal oxide layers measured during AFM was lower when they were depth-profiled in the H_2 atmosphere instead of the UHV or there was no statistical difference. Only one exception was observed. Furthermore, our research posts another proof for the ion-energy-dependent roughening, as we have shown that the Cs^+ ion beam with an energy of 2 keV causes more damage and roughening than the 1 keV Cs^+ ion beam. We even observed smoothing capabilities with the 1 keV Cs^+ ions. If the surface of our samples was initially rough (more than 3 nm), sputtering with Cs^+ ions having an energy of 1 keV led either to a reduction of surface roughness in cases of some layers in the FeAgNi and CrTiAl samples, or there was no statistically significant difference before and after sputtering. Another important observation indicates that surface roughness is also dependent on the chemical composition of the layer, as a different surface roughness was measured for chemically different layers of the same sample regardless of their sputter depth. Since the only unchanged parameter was the chemical composition of the layers, we believe that the formation of hydrides, hydroxides, and oxides with different crystallinity is the reason for the different surface roughness values. Namely, a different degree of order in the structure of the material, i.e., the material being more crystalline or amorphous, can cause different surface roughnesses. Amorphization can also be caused by ion sputtering since different materials are differently prone to form amorphous phases. On the other hand, when the surface roughnesses of layers of the same chemical composition were measured through different depths (NiCr sample), their roughness continuously and gradually increased with increasing sputter depth. Such a result was expected since prolonged sputtering also leads to the accumulation of ion-bombardment-induced damage. Future studies will be performed to find the relationships between the surface morphology and the depth resolution, i.e., broadening of the interfaces observed in the ToF-SIMS depth profiles.

ASSOCIATED CONTENT

Supporting Information

The Supporting Information is available free of charge at https://pubs.acs.org/doi/10.1021/acs.langmuir.2c01837.

Additional graphs presenting surface roughness measured over the 2 μm × 2 μm or 5 μm × 5 μm analyses areas and tables of average surface roughness values with their standard deviations (PDF)

AUTHOR INFORMATION

Corresponding Author

Janez Kovač − *Jožef Stefan Institute, SI-1000 Ljubljana, Slovenia;* orcid.org/0000-0002-4324-246X; Phone: 00386-1-477-34-03; Email: janez.kovac@ijs.si

Author

Jernej Ekar − *Jožef Stefan Institute, SI-1000 Ljubljana, Slovenia; Jožef Stefan International Postgraduate School, SI-1000 Ljubljana, Slovenia;* orcid.org/0000-0001-8895-4746

Complete contact information is available at: https://pubs.acs.org/10.1021/acs.langmuir.2c01837

Author Contributions

The manuscript was written with the contributions of all of the authors. All of the authors have given approval to the final version of the manuscript.

Funding

The authors acknowledge also the financial support from the Slovenian Research Agency (ARRS) through the Program P2-0082 (thin-film structures and plasma surface engineering).

Notes

The authors declare no competing financial interest.

ACKNOWLEDGMENTS

The authors thank Dr. Peter Panjan for the sample preparation.

REFERENCES

(1) Vickerman, J. C. Prologue: ToF-SIMS—An Evolving Mass Spectrometry of Materials. In *ToF-SIMS: Materials Analysis by Mass Spectrometry*, 2nd ed.; Vickerman, J. C.; Briggs, D., Eds.; IM Publications LLP and SurfaceSpectra Limited: Chichester, Manchester, 2013; pp 1−37.

(2) Hofmann, S. Compositional Depth Profiling by Sputtering. *Prog. Surf. Sci.* **1991**, *36*, 35−87.

(3) Oswald, S.; Baunack, S. Comparison of Depth Profiling Techniques Using Ion Sputtering from the Practical Point of View. *Thin Solid Films* **2003**, *425*, 9−19.

(4) Zalar, A.; Panjan, P.; Kraševec, V.; Hofmann, S. Alternative Model Multilayer Structures for Depth Profiling Studies. *Surf. Interface Anal.* **1992**, *19*, 50−54.

(5) Cemin, F.; Bim, L. T.; Leidens, L. M.; Morales, M.; Baumvol, I. J. R.; Alvarez, F.; Figueroa, C. A. Identification of the Chemical Bonding Prompting Adhesion of A-C:H Thin Films on Ferrous Alloy Intermediated by a SiC_x:H Buffer Layer. *ACS Appl. Mater. Interfaces* **2015**, *7*, 15909−15917.

(6) Konarski, P.; Kaczorek, K.; Ćwil, M.; Marks, J. SIMS and GDMS Depth Profile Analysis of Hard Coatings. *Vacuum* **2008**, *82*, 1133−1136.
(7) Kovač, J.; Ekar, J.; Čekada, M.; Zajíčková, L.; Nečas, D.; Blahová, L.; Yong Wang, J.; Mozetič, M. Depth Profiling of Thin Plasma-Polymerized Amine Films Using GDOES in an Ar-O_2 Plasma. *Appl. Surf. Sci.* **2022**, *581*, No. 152292.
(8) Quarles, C. D., Jr.; Castro, J.; Marcus, R. K. Glow Discharge Mass Spectrometry. In *Encyclopedia of Spectroscopy and Spectrometry*; Lindon, J. C., Ed.; Elsevier Ltd.: Amsterdam, 2010; pp 762−769.
(9) Kovač, J.; Bizjak, M.; Praček, B.; Zalar, A. Auger Electron Spectroscopy Depth Profiling of Fe-Oxide Layers on Electromagnetic Sheets Prepared by Low Temperature Oxidation. *Appl. Surf. Sci.* **2007**, *253*, 4132−4136.
(10) Kovač, J.; Finšgar, M. Analysis of the Thermal Stability of Very Thin Surface Layers of Corrosion Inhibitors by Time-of-Flight Secondary Ion Mass Spectrometry. *J. Am. Soc. Mass Spectrom.* **2018**, *29*, 2305−2316.
(11) Wagner, M. S. Molecular Depth Profiling of Multilayer Polymer Films Using Time-of-Flight Secondary Ion Mass Spectrometry. *Anal. Chem.* **2005**, *77*, 911−922.
(12) Ekar, J.; Panjan, P.; Drev, S.; Kovač, J. ToF-SIMS Depth Profiling of Metal, Metal Oxide, and Alloy Multilayers in Atmospheres of H_2, C_2H_2, CO, and O_2. *J. Am. Soc. Mass Spectrom.* **2022**, *33*, 31−44.
(13) Brison, J.; Mine, N.; Wehbe, N.; Gillon, X.; Tabarrant, T.; Sporken, R.; Houssiau, L. Molecular Depth Profiling of Model Biological Films Using Low Energy Monoatomic Ions. *Int. J. Mass Spectrom.* **2012**, *321*−*322*, 1−7.
(14) Guryanov, G.; Clair, T. P. S.; Bhat, R.; Caneau, C.; Nikishin, S.; Borisov, B.; Budrevich, A. SIMS Quantitative Depth Profiling of Matrix Elements in Semiconductor Layers. *Appl. Surf. Sci.* **2006**, *252*, 7208−7210.
(15) Hammond, J.; Fisher, G.; Raman, S.; Moulder, J. Molecular Depth Profiling to 3D Molecular Imaging with XPS and TOF-SIMS. *Microsc. Microanal.* **2008**, *14*, 466−467.
(16) Niehoff, P.; Passerini, S.; Winter, M. Interface Investigations of a Commercial Lithium Ion Battery Graphite Anode Material by Sputter Depth Profile X-Ray Photoelectron Spectroscopy. *Langmuir* **2013**, *29*, 5806−5816.
(17) Brecl, K.; Jošt, M.; Bokalič, M.; Ekar, J.; Kovač, J.; Topič, M. Are Perovskite Solar Cell Potential-Induced Degradation Proof? *Sol. RRL* **2022**, *6*, No. 2100815.
(18) Harvey, S. P.; Zhang, F.; Palmstrom, A.; Luther, J. M.; Zhu, K.; Berry, J. J. Mitigating Measurement Artifacts in TOF-SIMS Analysis of Perovskite Solar Cells. *ACS Appl. Mater. Interfaces* **2019**, *11*, 30911−30918.
(19) González-Elipe, A. R.; Holgado, J. P.; Alvarez, R.; Espinós, J. P.; Fernández, A.; Munuera, G.Depth Profiling of Rh/CeO_2 Catalysts: An Alternative Method for Dispersion Analysis. In *Fundamental Aspects of Heterogeneous Catalysis Studied by Particle Beams*; Brongersma, H. H.; van Santen, R. A., Eds.; NATO ASI Series B; Springer: Boston, MA, 1991; Vol. *265*, pp 227−235.
(20) Hofmann, S. Approaching the Limits of High Resolution Depth Profiling. *Appl. Surf. Sci.* **1993**, *70*−*71*, 9−19.
(21) Marton, D.; Fine, J. Sputtering-Induced Surface Roughness of Metallic Thin Films. *Thin Solid Films* **1990**, *185*, 79−90.
(22) Wang, J. Y.; Hofmann, S.; Zalar, A.; Mittemeijer, E. J. Quantitative Evaluation of Sputtering Induced Surface Roughness in Depth Profiling of Polycrystalline Multilayers Using Auger Electron Spectroscopy. *Thin Solid Films* **2003**, *444*, 120−124.
(23) Chen, Z.; Luo, J.; Doudevski, I.; Erten, S.; Kim, S. H. Atomic Force Microscopy (AFM) Analysis of an Object Larger and Sharper than the AFM Tip. *Microsc. Microanal.* **2019**, *25*, 1106−1111.
(24) Poon, C. Y.; Bhushan, B. Comparison of Surface Roughness Measurements by Stylus Profiler, AFM and Non-Contact Optical Profiler. *Wear* **1995**, *190*, 76−88.
(25) Albrecht, T. R.; Quate, C. F. Atomic Resolution Imaging of a Nonconductor by Atomic Force Microscopy. *J. Appl. Phys.* **1987**, *62*, 2599−2602.
(26) Kaiser, K.; Gross, L.; Schulz, F. A Single-Molecule Chemical Reaction Studied by High-Resolution Atomic Force Microscopy and Scanning Tunneling Microscopy Induced Light Emission. *ACS Nano* **2019**, *13*, 6947−6954.
(27) Muller, D. J. AFM: A Nanotool in Membrane Biology. *Biochemistry* **2008**, *47*, 7986−7998.
(28) Giannazzo, F.; Fisichella, G.; Greco, G.; Di Franco, S.; Deretzis, I.; La Magna, A.; Bongiorno, C.; Nicotra, G.; Spinella, C.; Scopelliti, M.; Pignataro, B.; Agnello, S.; Roccaforte, F. Ambipolar MoS_2 Transistors by Nanoscale Tailoring of Schottky Barrier Using Oxygen Plasma Functionalization. *ACS Appl. Mater. Interfaces* **2017**, *9*, 23164−23174.
(29) Daniels, S. L.; Ngunjiri, J. N.; Garno, J. C. Investigation of the Magnetic Properties of Ferritin by AFM Imaging with Magnetic Sample Modulation. *Anal. Bioanal. Chem.* **2009**, *394*, 215−223.
(30) Patterson, B. A.; Galan, U.; Sodano, H. A. Adhesive Force Measurement between HOPG and Zinc Oxide as an Indicator for Interfacial Bonding of Carbon Fiber Composites. *ACS Appl. Mater. Interfaces* **2015**, *7*, 15380−15387.
(31) Yuan, Y.; Lenhoff, A. M. Characterization of Phase Separation in Mixed Surfactant Films by Liquid Tapping Mode Atomic Force Microscopy. *Langmuir* **1999**, *15*, 3021−3025.
(32) Barna, A.; Pécz, B.; Menyhard, M. Amorphisation and Surface Morphology Development at Low-Energy Ion Milling. *Ultramicroscopy* **1998**, *70*, 161−171.
(33) Yan, X. L.; Duvenhage, M. M.; Wang, J. Y.; Swart, H. C.; Terblans, J. J. Evaluation of Sputtering Induced Surface Roughness Development of Ni/Cu Multilayers Thin Films by Time-of-Flight Secondary Ion Mass Spectrometry Depth Profiling with Different Energies O_2^+ Ion Bombardment. *Thin Solid Films* **2019**, *669*, 188−197.
(34) Chason, E.; Mayer, T. M.; Kellerman, B. K.; McIlroy, D. T.; Howard, A. J. Roughening Instability and Evolution of the Ge(001) Surface during Ion Sputtering. *Phys. Rev. Lett.* **1994**, *72*, 3040−3043.
(35) Valbusa, U.; Boragno, C.; De Mongeot, F. B. Nanostructuring Surfaces by Ion Sputtering. *J. Phys.: Condens. Matter* **2002**, *14*, 8153−8175.
(36) Hofmann, S.; Zalar, A.; Cirlin, E.-H.; Vajo, J. J.; Mathieu, H. J.; Panjan, P. Interlaboratory Comparison of the Depth Resolution in Sputter Depth Profiling of Ni/Cr Multilayers with and without Sample Rotation Using AES, XPS, and SIMS. *Surf. Interface Anal.* **1993**, *20*, 621−626.
(37) Shard, A.; Gilmore, I.; Wucher, A. Molecular Depth Profiling. In *ToF-SIMS: Materials Analysis by Mass Spectrometry*, 2nd ed.; Vickerman, J. C.; Briggs, D., Eds.; IM Publications LLP and SurfaceSpectra Limited: Chichester, Manchester, 2013; pp 311−334.
(38) Ng, C. M.; Wee, A. T. S.; Huan, C. H. A.; See, A. Effects of Oxygen Flooding on Crater Bottom Composition and Roughness in Ultrashallow Secondary Ion Mass Spectrometry Depth Profiling. *J. Vac. Sci. Technol., B: Microelectron. Nanometer Struct.–Process., Meas., Phenom.* **2001**, *19*, 829−835.
(39) Wolff, M.; Schultze, J. W.; Strehblow, H.-H. Low-Energy Implantation and Sputtering of TiO_2 by Nitrogen and Argon and the Electrochemical Reoxidation. *Surf. Interface Anal.* **1991**, *17*, 726−736.
(40) MacLaren, S. W.; Baker, J. E.; Finnegan, N. L.; Loxton, C. M. Surface Roughness Development during Sputtering of GaAs and InP: Evidence for the Role of Surface Diffusion in Ripple Formation and Sputter Cone Development. *J. Vac. Sci. Technol., A* **1992**, *10*, 468−476.
(41) Mahoney, C. M.; Fahey, A. J.; Gillen, G.; Xu, C.; Batteas, J. D. Temperature-Controlled Depth Profiling in Polymeric Materials Using Cluster Secondary Ion Mass Spectrometry (SIMS). *Appl. Surf. Sci.* **2006**, *252*, 6502−6505.
(42) Mahoney, C. M.; Fahey, A. J.; Gillen, G.; Xu, C.; Batteas, J. D. Temperature-Controlled Depth Profiling of Poly(Methyl Methacrylate) Using Cluster Secondary Ion Mass Spectrometry. 2. Investigation of Sputter-Induced Topography, Chemical Damage, and Depolymerization Effects. *Anal. Chem.* **2007**, *79*, 837−845.

https://doi.org/10.1021/acs.langmuir.2c01837
Langmuir 2022, 38, 12871−12880

(43) Fletcher, J. S.; Conlan, X. A.; Lockyer, N. P.; Vickerman, J. C. Molecular Depth Profiling of Organic and Biological Materials. *Appl. Surf. Sci.* **2006**, *252*, 6513−6516.
(44) Carbone, M. E. E.; Castle, J. E.; Ciriello, R.; Salvi, A. M.; Treacy, J.; Zhdan, P. In Situ Electrochemical-AFM and Cluster-Ion-Profiled XPS Characterization of an Insulating Polymeric Membrane as a Substrate for Immobilizing Biomolecules. *Langmuir* **2017**, *33*, 2504−2513.
(45) Kozole, J.; Wucher, A.; Winograd, N. Energy Deposition during Molecular Depth Profiling Experiments with Cluster Ion Beams. *Anal. Chem.* **2008**, *80*, 5293−5301.
(46) Zalar, A.; Hofmann, S. Influence of Ion Energy, Incidence Angle and Surface Roughness on Depth Resolution in AES Sputter Profiling of Multilayer Cr/Ni Thin Films. *Nucl. Instrum. Methods Phys. Res., Sect. B* **1986**, *18*, 655−658.
(47) Bradley, R. M.; Harper, J. M. E. Theory of Ripple Topography Induced by Ion Bombardment. *J. Vac. Sci. Technol., A* **1988**, *6*, 2390−2395.
(48) Bradley, R. M.; Cirlin, E. H. Theory of Improved Resolution in Depth Profiling with Sample Rotation. *Appl. Phys. Lett.* **1996**, *68*, 3722−3724.
(49) Zalar, A. Improved Depth Resolution by Sample Rotation during Auger Electron Spectroscopy Depth Profiling. *Thin Solid Films* **1985**, *124*, 223−230.
(50) Bhadeshia, H. K. D. H. Prevention of Hydrogen Embrittlement in Steels. *ISIJ Int.* **2016**, *56*, 24−36.
(51) Lewis, F. A. Solubility of Hydrogen in Metals. *Pure Appl. Chem.* **1990**, *62*, 2091−2096.
(52) Louthan, M. R.; Caskey, G. R.; Donovan, J. A.; Rawl, D. E. Hydrogen Embrittlement of Metals. *Mater. Sci. Eng.* **1972**, *10*, 357−368.
(53) Chason, E.; Mayer, T. M. Low Energy Ion Bombardment Induced Roughening and Smoothing of SiO_2 Surfaces. *Appl. Phys. Lett.* **1993**, *62*, 363−365.
(54) Jiang, Z. X.; Alkemade, P. F. A. The Complex Formation of Ripples during Depth Profiling of Si with Low Energy, Grazing Oxygen Beams. *Appl. Phys. Lett.* **1998**, *73*, 315−317.
(55) Liu, R.; Ng, C. M.; Wee, A. T. S. Surface Roughening Effect in Sub-KeV SIMS Depth Profiling. *Appl. Surf. Sci.* **2003**, *203*−*204*, 256−259.
(56) Basnar, B.; Lugstein, A.; Wanzenboeck, H.; et al. Focused Ion Beam Induced Surface Amorphization and Sputter Processes. *J. Vac. Sci. Technol., B: Microelectron. Nanometer Struct.–Process., Meas., Phenom.* **2003**, *21*, 927−930.
(57) Ossi, P. M. Ion-Beam-Induced Amorphization. *Mater. Sci. Eng.* **1987**, *90*, 55−68.
(58) Pelaz, L.; Marqús, L. A.; Barbolla, J. Ion-Beam-Induced Amorphization and Recrystallization in Silicon. *J. Appl. Phys.* **2004**, *96*, 5947−5976.

https://doi.org/10.1021/acs.langmuir.2c01837
Langmuir 2022, 38, 12871−12880

Supporting information

AFM Study of Roughness Development during ToF-SIMS Depth Profiling of Multilayers with a Cs^+ Ion Beam in a H_2 Atmosphere

Jernej Ekar,[1,2] *Janez Kovač*[1,*]

[1]Jožef Stefan Institute, Jamova cesta 39, SI-1000 Ljubljana, Slovenia

[2]Jožef Stefan International Postgraduate School, Jamova cesta 39, SI-1000 Ljubljana, Slovenia

Corresponding author: * Janez Kovač (email: janez.kovac@ijs.si, phone: 00386 1 477 34 03)

Table S1. Measured surface roughness S_a values in nm with their standard deviations for the layers of the FeAgNi sample.

FeAgNi sample		Roughness S_a over 5 × 5 μm²		Roughness S_a over 2 × 2 μm²	
		1 keV Cs^+	2 keV Cs^+	1 keV Cs^+	2 keV Cs^+
initial surface roughness*		5 ± 1		3.5 ± 0.5	
Fe_2O_3/Fe interface at 20 nm	UHV	4.6 ± 0.6	/	3.1 ± 0.5	/
	H_2	4.3 ± 0.7	/	2.5 ± 0.3	/
Ag layer at 55 nm	UHV	5.1 ± 0.5	/	3.4 ± 0.6	/
	H_2	4.3 ± 0.6	/	3.2 ± 0.6	/
NiO layer at 100 nm	UHV	4.7 ± 0.2	4.4 ± 0.4	3.6 ± 0.4	3.1 ± 0.6
	H_2	3.3 ± 0.2	4.0 ± 0.5	2.3 ± 0.3	3.0 ± 0.5

Measured surface roughness values are for the 5 μm × 5 μm and 2 μm × 2 μm areas, UHV conditions and H_2 flooding, as well as for the 1 and 2 keV energies of the Cs^+ sputtering ions.

* Initial surface roughness values correspond only to the 5 μm × 5 μm and 2 μm × 2 μm analysis areas since no prior sputtering was done in cases of these AFM measurements.

Table S2. Measured surface roughness S_a values in nm with their standard deviations for the layers of the CrTiAl sample.

CrTiAl sample		Roughness S_a over 5 × 5 μm²		Roughness S_a over 2 × 2 μm²	
		1 keV Cs^+	2 keV Cs^+	1 keV Cs^+	2 keV Cs^+
initial surface roughness*		5 ± 1		3.4 ± 0.4	
Cr layer at 35 nm	UHV	3.4 ± 0.3	/	2.60 ± 0.08	/
	H_2	4.3 ± 0.2	/	2.9 ± 0.1	/
Al_2O_3 layer at 100 nm	UHV	4.6 ± 0.4	/	2.6 ± 0.1	/
	H_2	4.0 ± 0.4	/	2.5 ± 0.4	/

Measured surface roughness values are for the 5 μm × 5 μm and 2 μm × 2 μm areas, UHV conditions and H_2 flooding, measured after sputtering with the 1 keV Cs^+ ions.

* Initial surface roughness values correspond only to the 5 μm × 5 μm and 2 μm × 2 μm analysis areas since no prior sputtering was done in cases of these AFM measurements.

Table S3. Measured surface roughness S_a values in nm with their standard deviations for the layers of the TiSi sample.

TiSi sample		Roughness S_a over 5 × 5 μm²		Roughness S_a over 2 × 2 μm²	
		1 keV Cs^+	2 keV Cs^+	1 keV Cs^+	2 keV Cs^+
initial surface roughness*		3.4 ± 0.5		2.1 ± 0.4	
Ti/Si interface at 40 nm	UHV	4.1 ± 0.8	/	2.1 ± 0.4	/
	H_2	3.3 ± 0.9	/	1.4 ± 0.3	/
Ti:Si = 1:1 layer at 130 nm	UHV	3.8 ± 0.7	3.8 ± 0.6	2.4 ± 0.8	2.2 ± 0.4
	H_2	3.1 ± 0.4	3.2 ± 0.3	1.6 ± 0.2	2.0 ± 0.4

Measured surface roughness values are for the 5 μm × 5 μm and 2 μm × 2 μm areas, UHV conditions and H_2 flooding, as well as for the 1 and 2 keV energies of the Cs^+ sputtering ions.

* Initial surface roughness values correspond only to the 5 μm × 5 μm and 2 μm × 2 μm analysis areas since no prior sputtering was done in cases of these AFM measurements.

Table S4. Measured surface roughness S_a values in nm with their standard deviations for the layers of the NiCr sample.

NiCr sample		Roughness S_a over 5 × 5 μm²		Roughness S_a over 2 × 2 μm²	
		1 keV Cs^+	2 keV Cs^+	1 keV Cs^+	2 keV Cs^+
initial surface roughness*		0.9 ± 0.2		0.6 ± 0.1	
2. Cr/3. Ni interface at 120 nm	UHV	/	1.6 ± 0.2	/	1.6 ± 0.2
	H_2	/	1.61 ± 0.05	/	1.50 ± 0.06
3. Ni layer at 135 nm	UHV	0.9 ± 0.1	1.98 ± 0.06	0.8 ± 0.1	1.87 ± 0.05
	H_2	0.79 ± 0.07	1.67 ± 0.05	0.69 ± 0.08	1.52 ± 0.05

6. Cr/7. Ni interface at 360 nm	UHV	/	2.41 ± 0.06	/	2.26 ± 0.04
	H_2	/	2.07 ± 0.02	/	1.77 ± 0.08
7. Ni layer at 375 nm	UHV	/	2.66 ± 0.05	/	2.6 ± 0.1
	H_2	/	2.50 ± 0.05	/	2.28 ± 0.05

Measured surface roughness values are for the 5 μm × 5 μm and 2 μm × 2 μm areas, UHV conditions and H_2 flooding, as well as for the 1 and 2 keV energies of the Cs^+ sputtering ions.

* Initial surface roughness values correspond only to the 5 μm × 5 μm and 2 μm × 2 μm analysis areas since no prior sputtering was done in cases of these AFM measurements.

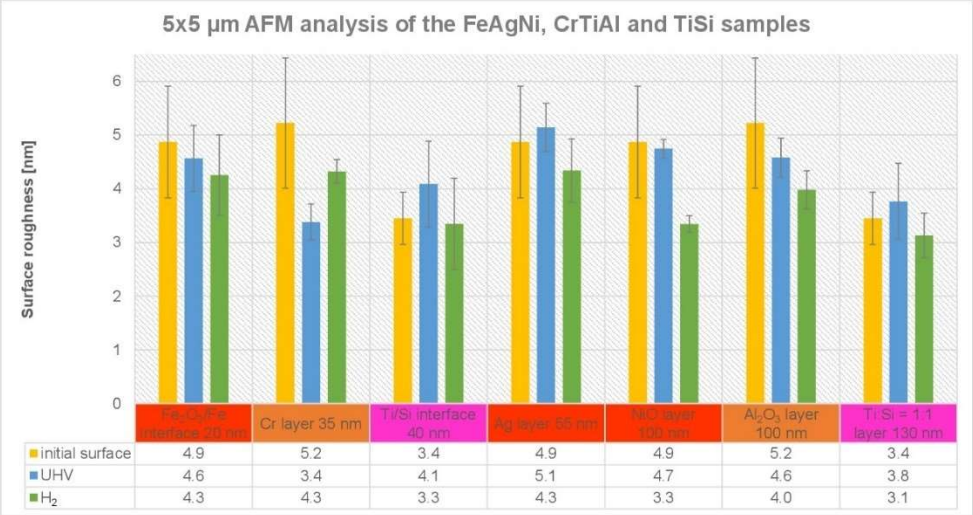

Figure S1. Surface roughness of the FeAgNi, CrTiAl, and TiSi samples with a table of the average surface roughness values. Surface roughness was measured over the 5 μm × 5 μm area. Yellow columns represent the initial surface roughness of the chosen sample, blue columns are the roughness of the craters sputtered in the UHV conditions, and green columns are the roughness after sputtering in the H_2 atmosphere. Sputtering was made with the 1 keV Cs^+ ion beam. The layers and interfaces measured on the FeAgNi sample are colored red, the ones from the CrTiAl sample are orange, and the ones from the TiSi sample are pink.

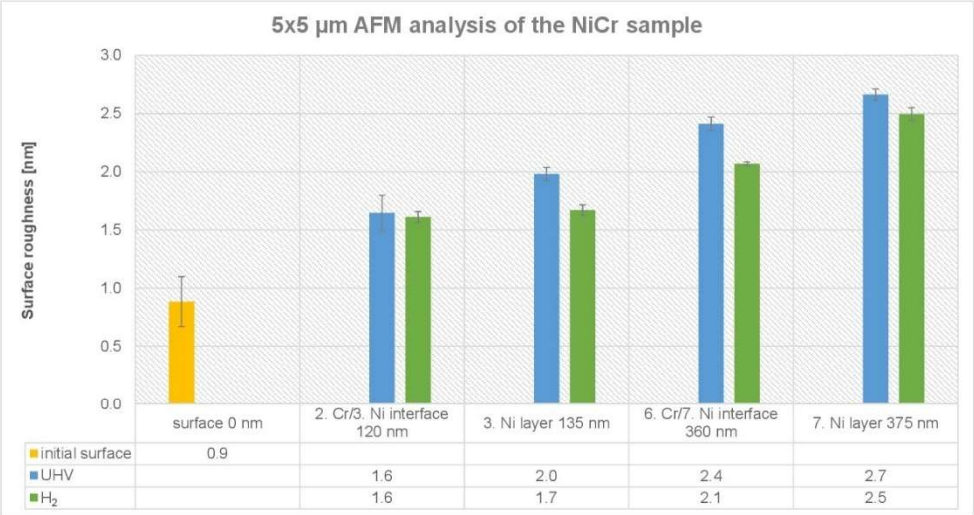

Figure S2. Surface roughness of the NiCr sample with a table of the average surface roughness values. Surface roughness was measured over the 5 µm × 5 µm area. Yellow column represents the initial surface roughness, blue columns the roughness of the craters sputtered in the UHV conditions, and green columns the roughness after sputtering in the H_2 atmosphere. Sputtering was made with the 2 keV Cs^+ ion beam.

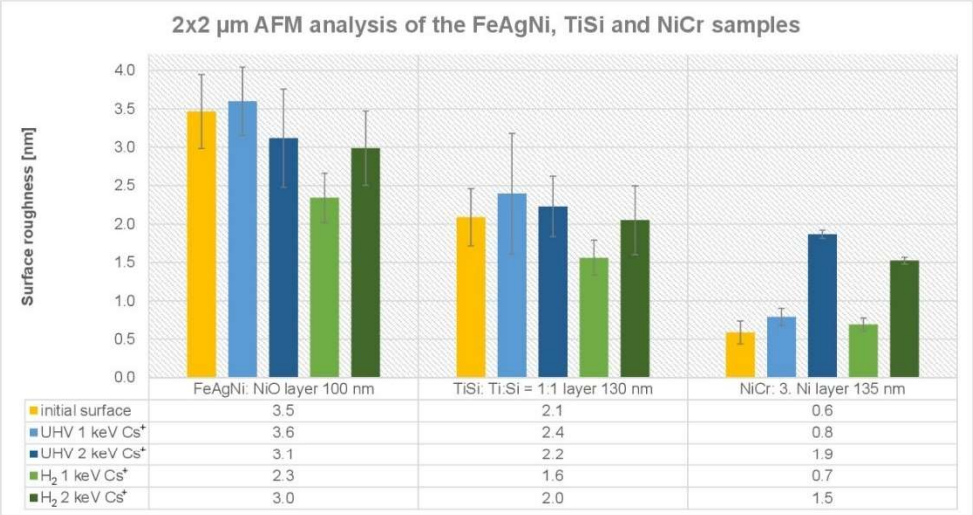

	FeAgNi: NiO layer 100 nm	TiSi: Ti:Si = 1:1 layer 130 nm	NiCr: 3. Ni layer 135 nm
initial surface	3.5	2.1	0.6
UHV 1 keV Cs^+	3.6	2.4	0.8
UHV 2 keV Cs^+	3.1	2.2	1.9
H_2 1 keV Cs^+	2.3	1.6	0.7
H_2 2 keV Cs^+	3.0	2.0	1.5

Figure S3. Surface roughness of the FeAgNi, TiSi, and NiCr samples after sputtering with the 1 and 2 keV Cs^+ ion beams. Added is the table of average surface roughness values. Surface roughness was measured over the 2 µm × 2 µm area. Yellow columns represent the initial surface roughness, light blue columns the roughness of the craters sputtered in UHV with the 1 keV Cs^+, dark blue columns the roughness of the craters sputtered in UHV with the 2 keV Cs^+, light green columns the roughness after sputtering with the 1 keV Cs^+ in the H_2 atmosphere, and dark green columns the roughness after sputtering with the 2 keV Cs^+ in the H_2 atmosphere. Analyses of the layers are assigned as "the sample: the layer of the sample being analyzed and the depth at which ion sputtering was stopped".

Chapter 7

Article 4: Improvements in Quantification by ToF-SIMS Analyses of Metals and Alloys in H_2 and O_2 Atmospheres

The matrix effect presents a significant limitation for the SIMS method to be widely used for quantitative analyses. The composition of the unknown sample can be determined by the use of the relative sensitivity factors (RSF approach) but only if the reference sample is chemically very similar to the analyzed one. This severely constricts the applicability of such an approach as a very large collection of reference materials is needed to enable the analysis of different samples. Another quantitative approach is a laser and electron beam post-ionization in the SNMS method that can be applied for chemically profoundly different samples because the ionization process happens in the gaseous plum of sputtered particles inside a vacuum and is therefore decoupled from the effects of substrate that influences ionization on the surface of the sample. However, this approach proves to be fairly complicated. Extensive instrumental changes are needed. Post-ionization is required to be complete for all emitted neutral particles. Sputtered secondary ions must be removed from sputtered neutrals. There are potential difficulties connected with the transmission to the analyzer. Finally, the mass resolution is substantially worsened as well.

Concerning the RSF approach, analysis of the MCs^+ cluster secondary ions composed of metal of interest (M) and Cs implemented into the sample during sputtering appears to be further beneficial. However, this approach was implemented and demonstrated only for the analyses of chemically very similar surfaces. Therefore, we decided to further explore the possibilities and advantages of the cluster secondary ions by performing gas flooding of reactive gases. These adsorb on the surface and form cluster ions with compounds of the sample similarly as this happened in the case of MCs^+ formation. The gases we chose for the SIMS analyses were H_2 and O_2 in the pressure range of $5 \times 10^{-7} - 1 \times 10^{-6}$ mbar and $1 - 3 \times 10^{-8}$ mbar, respectively. These pressures were chosen according to the maximum intensities of hydride and oxide secondary ions. For comparison, measurements were also performed in the ultra-high vacuum (UHV) at the pressure of approximately 2×10^{-10} mbar.

The analyzed samples were pure Al, Si, Ti, Cr, Fe, Co, and Ni and alloys composed of these metals with a presence of also V, Mn, Nb, and Mo. The alloys were profoundly different, ranging from the simple compositions of only two elements to more complex ones containing up to six different metals. Binary alloys were CoCr, AlCr, AlTi, NiTi, and SiTi

while the more complex ones were AlTiV, Fernico, Inconel, Kanthal, stainless steel, and CoCrFeMnNi. Furthermore, ratios of analyzed metals ranged from only 1 to 100% when considering all the samples included in the analysis. Measurements were performed during depth profiling with the 1 keV Cs^+ ion beam. Such an approach was implemented because hydride and oxide secondary ions ionize the most efficiently in the negative polarity and the presence of cesium enhanced the yields of the negative secondary ions. Compositions of the samples were initially determined with other quantitative methods. Bulk samples were analyzed with energy-dispersive X-ray spectroscopy (EDXS) while samples in the form of thin layers were analyzed with X-ray photoelectron spectroscopy (XPS). Results obtained with the SIMS method were compared to the results of these methods and deviations were determined. Via this, quantitative aspects of the SIMS method applied in the UHV, H_2, and O_2 atmospheres were evaluated. Before the calculations of deviations, measured intensities of secondary ions were initially normalized in three different ways: (1) by the total dose of Bi^+ primary ions, (2) by the total intensity of all secondary ions, and (3) by the intensity of the H^- ion (only H_2 atmosphere), or by the intensity of the O_2^- ion (only O_2 atmosphere). In the second step, normalized intensities of secondary ions measured in alloys were divided by normalized intensities of these same secondary ions measured in pure metals. SIMS ratios, calculated in this way, were finally compared with the true atomic ratios of different metals in alloys, providing us with the deviation values.

As expected, the worst results were obtained when analyses were done in the UHV. However, differences in results measured in UHV compared to H_2 and O_2 atmospheres were not as prominent for Al and Si as they were for Ti, Cr, Fe, Co, and Ni. Reactive gases improve quantitative aspects of the SIMS method also in the case of the analysis of p-block elements but significantly less than during analyses of transition metals. We assume the reasons for this are differences in the electronic structure connected with the valence orbitals, the reactivity of these metals towards the formation of hydride and oxide ions, and possibly also differences in the size of the atoms. Considering only transition metals, the best results were obtained when the H_2 atmosphere was applied. Combining the best results of all three types of normalization, the deviation intervals of the secondary ions, which had the smallest deviations among all secondary ions originating from the respective metal, were 23% for Ti, 46% for Cr, 22% for Fe, 31% for Co, and 39% for Ni. Deviation intervals were defined as the difference between the highest negative and the highest positive deviation of the secondary ion of interest while considering all the pure metals and all the alloys combined. In comparison, deviation intervals in the case of the O_2 atmosphere were 40% for Ti, 66% for Cr, 30% for Fe, 49% for Co, and 61% for Ni, and in the case of the UHV 69% for Ti, 76% for Cr, 44% for Fe, 92% for Co, and 228% for Ni.

These results indicate that the adsorption of the reactive gases on the surface of the sample helps to reduce the matrix effect of the substrate. Adsorbed gases form a new matrix, which is much more similar for different samples as the same gas is always used. This phenomenon reduced the effect of the initial matrix effect that was intrinsically related to the sample, therefore being significantly different for samples with different chemical compositions. Our results also indicate that cluster secondary ions are probably formed between particles constituting the sample and atoms or molecules of the adsorbed gases, and not between sputtered sample material and gaseous atmosphere. Results obtained in this study confirmed the hypothesis 1 and 2.

Contributions of the Ph.D. dissertation author: conceptualization and visualization of the experiment, methodology, investigation via ToF-SIMS measurements, performing calculations and interpreting the results, writing the original draft, reviewing and editing, project administration, and correspondence with the journal editor.

TITLE

Quantitative Aspects of ToF-SIMS Analysis of Metals and Alloys in a UHV, O_2 and H_2 Atmosphere

AUTHOR NAMES AND AFFILIATIONS

Jernej Ekar[1,2]
[1]Jožef Stefan Institute, Jamova cesta 39, SI-1000 Ljubljana, Slovenia
[2]Jožef Stefan International Postgraduate School, Jamova cesta 39, SI-1000 Ljubljana, Slovenia
email: jernej.ekar@ijs.si

Saša Kos[3,4]
[3]Geological Survey of Slovenia, Dimičeva ulica 14, SI-1000 Ljubljana, Slovenia
[4]Faculty of Civil and Geodetic Engineering, University of Ljubljana, Jamova cesta 2, SI-1000 Ljubljana, Slovenia
email: sasa.kos@geo-zs.si

Janez Kovač[1]
[1]Jožef Stefan Institute, Jamova cesta 39, SI-1000 Ljubljana, Slovenia
email: janez.kovac@ijs.si

CORRESPONDING AUTHOR

Janez Kovač (janez.kovac@ijs.si, 00386 1 477 34 03)

ABSTRACT

Although secondary ion mass spectrometry (SIMS) is a versatile method used in the fields of surface analysis, depth profiling and elemental and molecular mapping, it also lacks quantification capabilities. The main reason for this is the matrix effect, which influences the ionization yield of secondary ions with respect to the substrate from which the analyzed compounds originate. There are several approaches to reduce the matrix effect, and gas flooding is one of the easiest methods to apply. In this work, we have investigated the possibilities of the ToF-SIMS method for the quantification of selected metals and alloys containing these metals in different ratios by reducing the matrix effect in the presence of different atmospheres. The measurements were performed in the ultra-high vacuum (UHV) environment, H_2 and O_2 atmospheres. H_2 flooding shows the most significant improvements compared to the UHV analysis, while O_2 is also promising but has some limitations. Improvements are most evident for the transition metals Ti, Cr, Fe, Co and Ni employed in our study, while the p-block elements such as Al and Si do not change so extensively. The deviations from the true atomic ratios of selected transition metals in different alloys reach a maximum of only 46% when analyzed in the H_2 atmosphere. In contrast, these values are 66 and 228% for the O_2 atmosphere and UHV environment, respectively. Our results suggest that gas adsorption and consequent formation of a new matrix on the surface, especially in the case of hydrogen, reduces the differences between the different chemical environments and electronic structures of the surface. In this way, the quantitative aspects of the SIMS method can be improved.

Keywords: ToF-SIMS quantification, H_2, O_2, gas flooding, matrix effect reduction, cluster secondary ions

1. INTRODUCTION

Secondary ion mass spectrometry (SIMS) is an important analytical technique in the fields of surface and materials sciences. The information about the chemical composition and molecular structure of the sample is obtained by bombarding the surface with primary ions (e.g. Bi^+, Bi_3^+, Ar^+) and analyzing secondary ions, that is, charged sputtered particles, with a mass analyzer such as time-of-flight (ToF), magnetic sector, quadrupole, ion trap or orbitrap. [1–3] SIMS is a versatile analytical method as the sample to be analyzed is only required to be compatible with ultra-high vacuum (UHV) and, in the case of ToF-SIMS, also needs to be as flat as possible. [3,4] In addition, we can measure mass spectra, perform 2D mapping and depth profiling, and even generate 3D representations. [5] Due to these factors, SIMS can be used in many different fields such as corrosion inhibition [6,7], studies of metals, alloys and their properties [8,9], analysis of thin films and multilayers [10–12], studies of organic compounds and polymers [13,14], investigation of nanoparticles [15,16], microelectronics and photovoltaics [17,18], catalysis [19], detection of dopants and impurities [20,21], analysis of biological material including cells and tissues [22,23] and so on. However, one of the major limitations of the SIMS method is the problematic and often impossible quantification of chemical composition, mainly as a result of the matrix effect. [24–26] The intensity of the secondary ion signal (I_m) is a function of the current of the primary ions (I_p), the sputter yield (Y_m), the ionization probability ($\alpha^{+/-}$), the concentration of an analyzed compound or element (θ_m), and the transmission of the analytical system (η), as described in Equation 1. [2]

$$I_m = I_p Y_m \alpha^{+/-} \theta_m \eta \tag{1}$$

I_p and η are functions of an instrument and as such are not problematic since they can be determined and controlled, while θ_m is the concentration we are looking for in the case of quantification. Challenging in terms of quantitative analysis are Y_m and $\alpha^{+/-}$. Even the sputter yield of the element and its ionization probability influenced by its ionization energy and electron affinity are not problematic since they do not change with respect to the sample. [2] The most difficult to overcome is the influence of the substrate, i.e. the matrix effect. This is because the chemical composition of the sample has a large influence on the sputter yield and the ionization probability, and this factor changes from one sample to another, preventing and disrupting direct comparison between them. [2,24]

Various approaches have already been developed to improve and solve this issue. One possibility is the application of laser postionization of secondary neutral sputtered particles (laser-SNMS), an effective but also complicated and costly approach. [27–30] Instead of a laser, we can also use an electron beam. [31–33] Since the particles are ionized in the plum above the surface, in the gas phase, the effect of the substrate matrix is no longer present. [27,34] However, the laser must be strong enough to ionize all targeted particles, otherwise quantification is not possible. [27] We can also use the internal standard method by comparing the intensity of the signal of interest with the intensity of the reference signal and calculating the relative sensitivity factor (RSF) using Equation 2,

$$c_i / c_r = RSF\,(I_i / I_r) \tag{2}$$

where c represents the atomic or molar concentration, I the intensity of the secondary ion signal, and the subscripts i and r the element of interest and the internal reference, respectively. [25,35–37] However, this method can only be used if we have samples with a very similar matrix that all contain the element used as an internal standard. [35,36] Another approach involves reactive sputtering, mainly with Cs^+ ions. During the sputtering process, Cs^+ ions are implanted into the substrate, chemically altering it and reducing the work function, thereby promoting the formation of negative secondary ions. [24,25,38,39] In this way, we create a matrix that is more similar between different samples, as it is always based on the effect of the implanted Cs. Improved quantification can be achieved by analyzing MCs^+ or MCs_2^+ ions, where M is the metal of interest. [35,40,41]

As gaseous molecules and atoms adsorb to the surface, they also form a type of matrix, similarly as with Cs implantation, which modifies the surface even more extensively. Furthermore, a positive effect of an H_2 atmosphere on the differentiation between layers of metals, metal oxides and alloys as well as an optimized identification of interfaces has already been demonstrated by SIMS analyses. [42] Therefore, the intensities of secondary ions sputtered from different metals and alloys were measured and compared in UHV, H_2 and O_2 atmospheres.

A current study aimed to evaluate and optimize a new approach for quantification of SIMS data from metallic alloys in different atmospheres. A relative comparison between pure metal and different alloys containing this metal in different ratios was performed to find the most favorable conditions for reducing/eliminating the matrix effect while applying an H_2 or O_2 atmosphere. Significantly different samples were used so that the matrix effect would play an important role in the quantification. In the present study, we considered different ways of normalizing the acquired SIMS signals and systematically compared the quantification in the H_2 or O_2 atmosphere with the UHV. Our results improved the semi-quantitative aspect of the SIMS method by providing the possibility to compare chemically distinct alloys and metals. However, a relative comparison would still be necessary with reference materials, as a direct correlation of the intensities of the secondary ion signals with the composition of a particular alloy should not be possible. This is due to the large variations in ionization energies, electron affinities and ionization yields of cluster secondary ions between different metals. [24,43,44]

2. EXPERIMENTAL SECTION

2.1. PREPARATION OF THE SAMPLES

Co, CoCr, NiTi, AlTiV, Fernico, Inconel, Kanthal and stainless steel used in this study were in the form of bulk samples with a homogeneous composition and covered with a thin native oxide layer. They were prepared by melting the metal/alloy. If the surface was not flat enough, it was polished at the ambient conditions. Pure Al, Ti, Cr, Fe, Ni, AlCr alloy and alloys of AlTi and SiTi in two different element ratios were prepared in the form of thin films by physical vapor deposition (PVD). They were deposited in a Sputron triode sputtering system (Balzers Oerlikon). The high-purity targets used as sputtering sources for the preparation of the thin films were initially cleaned for 5 minutes with plasma inside the PVD sputtering system to remove the native oxide and other impurities on their surface. The CoCrFeMnNi alloy was prepared by the arc-melting process. The highly polished crystalline wafer was used as the pure Si sample.

2.2. EDXS MEASUREMENTS

Polished metal samples of CoCr, NiTi, AlTiV, Fernico, Inconel, Kanthal and stainless steel were analyzed for their chemical composition using the Oxford INCA PentaFET x3 energy dispersive X-ray spectrometer with Si(Li) detector coupled to the JEOL JSM 6490LV scanning electron microscope. The chemical analysis was performed at an accelerating voltage of the electron beam of 20 kV, a working distance of 10 mm and an acquisition time of 45 s over five 100 × 100 µm scanning areas. The EDS software (INCA Energy 350) was calibrated for quantification with pre-measured universal standards, according to fitted standard procedure, and referenced to Co for optimization. The EDS data was corrected using the standard ZAF-correction method, which is included in the INCA Energy software.

2.3. XPS MEASUREMENTS

X-ray photoelectron spectroscopy (XPS) was performed with the PHI-TFA XPS spectrometer from Physical Electronics, USA. The monochromatic X-ray source applied was Al using the K_α emission. The analyzed area was 0.4 mm in diameter and the depth of analysis was 3–5 nm. The XPS spectra were measured in the energy range of 0–1200 eV. The elemental composition was determined by measuring the intensity of the 2p spectra of Al, Si, Ti, Cr, Fe, Co and Ni. Depth profiling was performed with the Ar^+ ion beam with an energy of 1 keV (AlCr and both SiTi samples) or 3 keV (both AlTi and CoCrFeMnNi samples) over an area of 3 × 3 mm. The surface composition was quantified using the XPS peak intensities and considering the relative sensitivity factors specified by the instrument manufacturer [45].

2.4. SIMS MEASUREMENTS

The ToF-SIMS analyses were performed with the TOF.SIMS 5 instrument from IONTOF, Germany. Bi^+ primary ions with an energy of 30 keV were used as the analysis beam. The ion beam was pulsed with a pulse length of 6 ns and the current of the Bi^+ ions was between 1.4 and 1.6 pA. With the settings used, the mass resolution $m/\Delta m$ of the peaks of interest was mostly between 7000 and 9000, while the minimum and maximum were 5000 and 13000, respectively. The analytical depth was approximately 2 nm and the lateral resolution was around 5 µm. The analyses were performed in a dual-beam depth profiling mode using the 1 keV Cs^+ ion beam for sputtering. The current of the Cs^+ ions was between 60 and 65 nA. The analyses with the Bi^+ primary ions were performed over the 50 × 50 µm scanning area (128 × 128 pixels), which was located in the center of the 400 × 400 µm area sputtered with the Cs^+ ions. The secondary ions were analyzed over the m/z range from 0 to 400.

The analyses in the UHV environment were performed at a pressure of approximately 2×10^{-10} mbar, while the pressure during O_2 flooding ranged from 1 to 3×10^{-8} mbar and during H_2 flooding from 5×10^{-7} to 1×10^{-6} mbar. The initial pressure prior to the gas introduction was always in the 10^{-10} mbar range. The differences in the pressures of H_2 and O_2 are pressure fluctuations during a single analysis and not differences between successive measurements of different samples. The gases used during depth profiling were introduced into the analysis chamber near the analyzed region via a capillary. The purity of the gasses used was 99.9990% and 99.9950% for O_2 and H_2, respectively.

In order to minimize the effects of the measurement conditions, the samples were analyzed as similarly as possible and in the shortest feasible time span. Since H_2 and O_2 form hydride or oxide cluster ions with the metals, which ionize most effectively in the negative polarity, we only analyzed negative secondary ions. To obtain results that were as comparable as possible, the negative secondary ions were also analyzed during the measurements in the UHV as well. Cs^+ sputtering was performed simultaneously to further promote the formation of negative secondary ions. The measurement time was determined according to the thickness of the layers in the corresponding samples, so that the measurements were performed in a time interval of 150 s, during which the intensities of the signals of interest remained unchanged. An exception was Fe in the form of the thinnest layer with a measurement time of 90 s. Bulky samples analyzed with the EDXS were additionally sputtered for a longer time of approximately 10 minutes to check their homogeneity, but no fluctuations in the signal intensities were observed. Prior to the secondary ion intensity measurements, sputtering was also performed to remove the topmost oxide layer or layers above the layer of interest. The results of this process were not included in the intensity ratio calculations. The duration of sputtering prior to analysis was determined in accordance with the sample roughness and the thickness of the oxide layer or the depth at which the layer of interest was located. Depending on the sample, it lasted between 10 and 60 minutes and was done with the 1 keV Cs^+ ion beam as well.

3. RESULTS AND DISCUSSION

3.1. COMPOSITIONS OF THE SAMPLES AND QUANTIFICATION METHOD

Al, Si, Ti, Cr, Fe, Co and Ni were measured as pure metals containing only traces of the other elements. Therefore, we have considered them as 100% metals in the calculations. We must also emphasize that we are aware that Si is a semimetal, but to avoid complications in sentences, we have only used the terms metal and metals in the text. The exact compositions of alloys were determined using either EDXS or XPS measurements. EDXS was used for the bulk samples, which were CoCr, AlTiV, Fernico, Inconel, Kanthal and stainless steel. Both AlTi, AlCr, both SiTi and CoCrFeMnNi samples were in the form of layers, so they were analyzed with XPS with high surface sensitivity to avoid the influence of the underlying substrate. Only the NiTi sample was purchased with the certified composition, but it was still measured with EDXS to verify the composition. The measured atomic ratios of alloys are listed in Table 1.

Table 1: Atomic ratios of the analyzed elements in different alloys expressed in percent (%). The method used for the analyses of the referenced chemical composition is also indicated.

	method	Al	Si	Ti	V	Cr	Mn	Fe	Co	Ni	Nb	Mo
AlTi 30	XPS	30	0	70	0	0	0	0	0	0	0	0
AlTi 47	XPS	47	0	53	0	0	0	0	0	0	0	0
AlCr	XPS	37	0	1	0	62	0	0	0	0	0	0
SiTi 31	XPS	0	31	69	0	0	0	0	0	0	0	0
SiTi 51	XPS	0	51	49	0	0	0	0	0	0	0	0
CoCr	EDXS	0	1	0	0	31	1	0	63.5	0	0	3.5
NiTi	EDXS	0	0	50	0	0	0	0	0	50	0	0
AlTiV	EDXS	10	0	87	3	0	0	0	0	0	0	0
Fernico	EDXS	0	0	0	0	0	0.5	54	17.5	28	0	0
Inconel	EDXS	0	0	0	0	26	0	2	0	64.5	2.5	5
Kanthal	EDXS	10	0	0	0	22.5	0	67.5	0	0	0	0
stainless steel	EDXS	0	1	0	0	19	1.5	65	0	12	0	1.5
CoCrFeMnNi	XPS	0	0	0	0	19	19	21.5	24	16.5	0	0

Our samples differ considerably from each other and contain no common element in all of them. The application of the RSF approach and Equation 2 [35,37] was consequently not possible. Therefore, we used the atomic ratios from Table 1 to prepare our approach for quantification in different measurement conditions. The intensities of the secondary ion signals measured on different alloys were divided by the intensity values of these signals measured on the pure metal. This corresponds to normalization by the theoretical atomic ratio of 1. In this way, comparative intensity ratios between the samples were calculated for each secondary ion. Tables, presented in the Supplementary Information (SI) file and analogous to Table 1, were created from the ToF-SIMS data for all listed alloys and three different atmospheres.

To compare the quantification results, we evaluated the deviations of the intensity ratios of the SIMS secondary ion signals from the true atomic ratios of each element determined by EDXS or XPS. The deviations were calculated using Equation 3, where Δ indicates the relative errors, the R_m ratios calculated by comparing the measured SIMS intensities of the secondary ions, and the R_t true atomic ratios obtained by EDXS or XPS. The deviations of the secondary ion signals measured on pure metals are always 0 by definition. In addition, all deviation values are noted with the +/- sign, so that one can calculate the exact comparative ratios we measured with the SIMS instrument.

$$\Delta = (R_m - R_t) / R_t \quad (3)$$

Since the measurement of SIMS signals can be sensitive to small changes in the analysis conditions (ion current of the primary ion beam, efficiency of ion detection…) the measured SIMS signal

intensities were normalized in three different ways before calculating the R_m ratios. The most straightforward approach was normalization by the total dose of primary Bi^+ ions. The other option was normalization by the total intensity of all secondary ions hitting the detector. Finally, the signals from spectra measured in the H_2 and O_2 atmospheres were also normalized by the intensity of the H^- and O_2^- signals, respectively. We chose the O_2^- signal instead of the O^- signal because the latter was constantly saturated during O_2 flooding and would represent a normalization by the constant.

We also encountered some limitations in the selection of suitable metals. Mn and Mo were not analyzed as they are present in the studied alloys in too low a concentration to perform a reliable analysis, while Mn is present in only one alloy in sufficient quantity, making such an analysis deficient and inadequate. The presence in only one alloy at a low concentration was a limiting factor for V and Nb as well. Another problem with the low concentrations of some metals is the overlap of their low-intensity SIMS signals with other, more intense signals and the consequent significant errors in the readings. The Ti in the AlCr sample was not included in the calculations for this reason. Fe, on the other hand, has sufficiently strong signals for reliable analysis even when present at only 2% (Inconel), but there are limitations associated with some specific hydride and oxide signals. An example of a signal-abundant mass interval is shown in Figure 1. Superimposed are the spectra of the Fernico alloy and the metals Fe, Co and Ni it contains, measured in an H_2 atmosphere. The signals of Si in CoCr and stainless steel were also intense enough for analysis, although the proportion of Si in these alloys is only 1%. However, when the differences in the ratios of an element in different samples are as large as between 1 and 100%, this leads to problems in selecting the appropriate signals for analysis. Signals that are of ideal intensity in pure Si are extremely weak in CoCr and stainless steel and are affected by noise, while signals that are intense enough in both alloys are saturated or nearly saturated in pure Si. For this reason, we had to analyze the $^{29}Si^-$ ion instead of the Si^- ion.

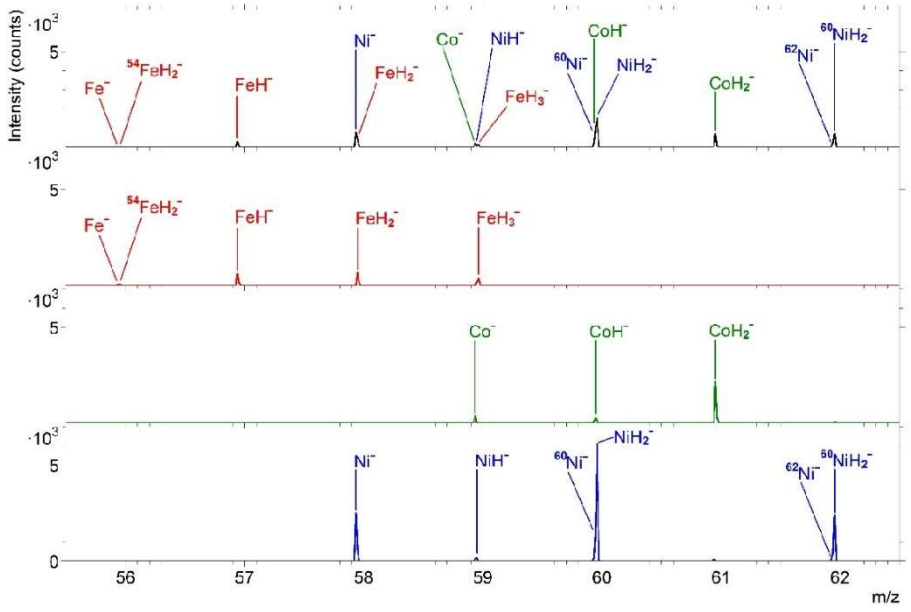

Figure 1: The SIMS spectra of the negative secondary ions from Fernico alloy (black), Fe (red), Co (green) and Ni (blue) acquired in an H_2 atmosphere. The spectral range between the masses 55.5 and 62.5 is shown, in which the signals of Fe, Co, Ni and their hydrides are present. The intensity of the signals of these secondary ions reflects the concentration of certain elements in the Fernico alloy.

Dosing the analysis chamber with different gasses and at different pressures during the SIMS analyses results in different intensities of the emitted signal of ions. In the first phase of our study, the pressures of the H_2 and O_2 atmospheres were chosen so that the analyses were carried out as much as possible in the "saturated" region. The small pressure changes in this pressure interval are not expected to cause a large difference in the intensity of the cluster secondary ions (hydrides and oxides). An example of how the intensity of the cluster secondary ions changes with increasing H_2 pressure is shown in Figure 2 for the stainless steel sample. It can be seen that the increasing pressure initially causes an increase in the intensity of the cluster secondary ions, followed by a slight plateau at approximately 1×10^{-6} mbar, and ends with a decrease in intensity. The pressure at which this plateau occurs is slightly different for the different metals, but the differences are small enough that optimal pressure can be chosen. The results of the same-approach experiment performed in the O_2 atmosphere are shown in SI in Figure 3, where it can be seen that the complexity of the intensity changes is much greater in this case. Some oxide signals show a very sharp maximum instead of a plateau, while others have a minimum at this pressure. Furthermore, maxima and plateaus can be observed at significantly different pressures and some oxides even show double maxima/plateaus depending on the O_2 pressure. These limitations compromise the ability to choose an ideal pressure and have a negative impact on the quantification results.

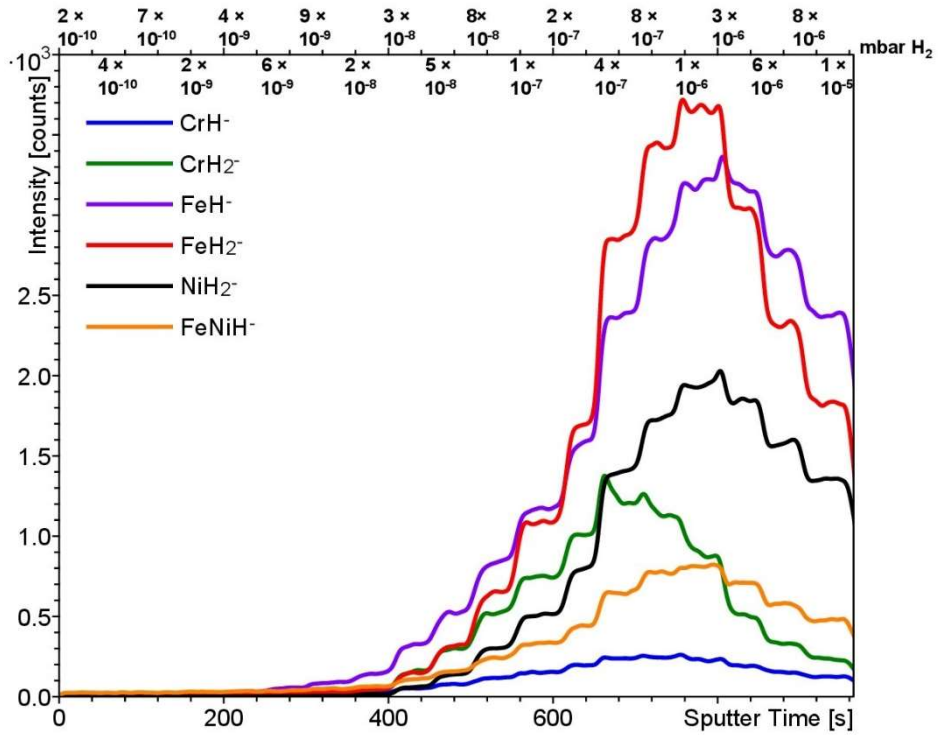

Figure 2: Changes in the intensity of metal hydride secondary ions emitted from the stainless steel sample during a steady increase of the H_2 pressure inside the analysis chamber to 1×10^{-5} mbar. For the first 50 s, the pressure was 2×10^{-10} mbar (UHV), then the leak valve was opened slightly every 50 s. The pressures measured between turns of the valve are noted on the upper x-axis, while the lower x-axis shows the time of analysis. The NiH_2^- signal was multiplied by a factor of 0.3 to avoid too large differences in the intensities of the different signals.

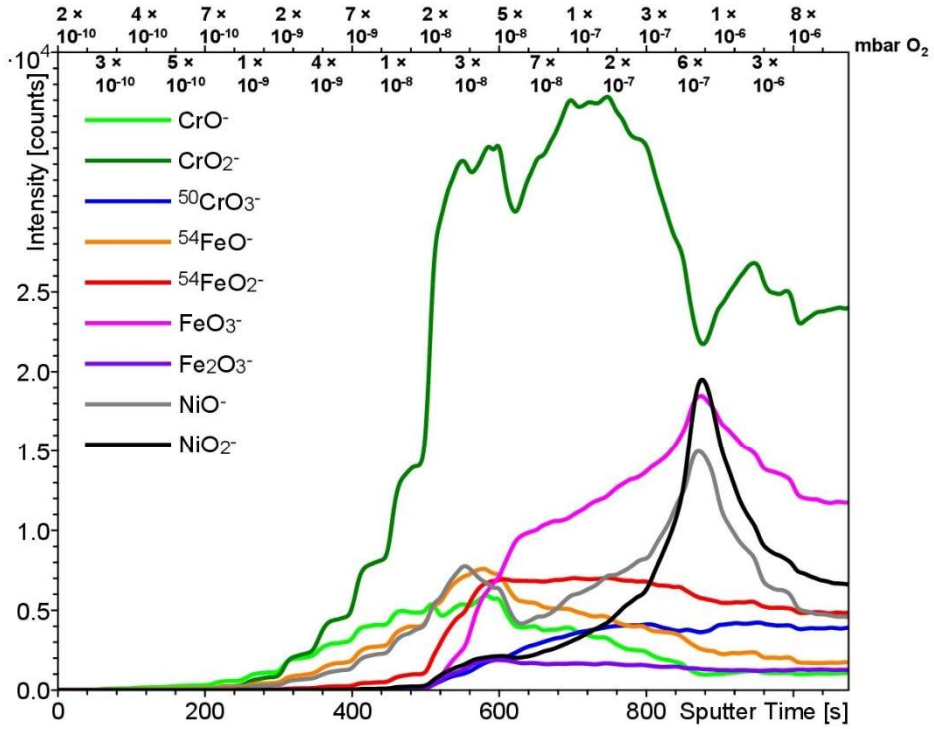

Figure 3: Changes in the intensity of metal oxide secondary ions emitted from the stainless steel sample during a steady increase of the O_2 pressure inside the analysis chamber to 8 × 10^{-6} mbar. For the first 50 s, the pressure was 2 × 10^{-10} mbar (UHV), then the leak valve was opened slightly every 50 s. The pressures measured between turns of the valve are noted on the upper x-axis, while the lower x-axis shows the time of analysis.

3.2. SIMS ANALYSES IN UHV ENVIRONMENT

The first set of results was obtained in the UHV environment, as this is the conventional way of performing SIMS measurements. In UHV, the secondary ions that were intense enough for reliable analysis were monoatomic and diatomic metal ions (M^- and M_2^-). Among diatomic secondary ions, Al_2^-, Si_2^-, Ti_2^- and Cr_2^- were suitable and intense enough for analysis, while the signals of Fe, Co and Ni had interferences mainly from mixed metal ions. Mass analyzers with a higher resolving power such as orbitrap, FT-ICR or magnetic sector are mainly able to discriminate between these ions, but ToF analyzers with the reflectron lack this capability in most cases, as the required mass resolution $m/\Delta m$ is at least 25 000. [46] Since these analyses were performed without the presence of a gas, we could only normalize the intensities of the secondary ions of interest by either the total dose of the primary Bi^+ ions or by the total intensity of all secondary ions. Deviation intervals, expressing the deviations of the comparative ratios of the secondary ion signals from the true atomic ratios, are shown in Figure 4 as intervals between the highest negative and the highest positive deviation when considering all alloys containing a metal of interest. The results are presented in separate graphs for each type of normalization and only one secondary ion represents each element. It was selected according to the criterion of the smallest deviation interval among all secondary ions analyzed. A list of all these secondary ions together with the deviation values measured separately for each alloy is presented in SI in Tables S1 and S2.

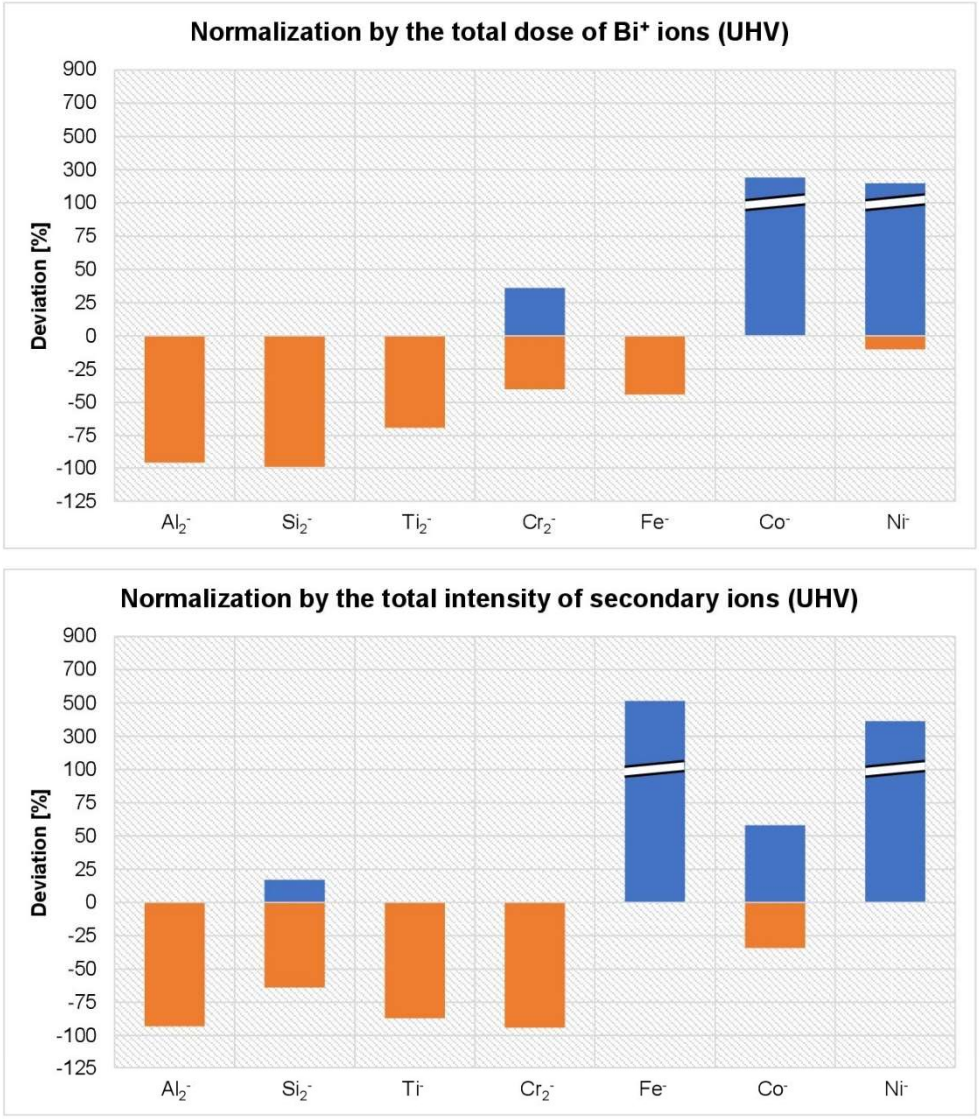

Figure 4: Deviation intervals between the highest negative and the highest positive deviation from the atomic ratios listed in Table 1 for measurements in the UHV environment. Each element is represented by one secondary ion selected on the basis of the smallest deviation interval among all secondary ions analyzed for that element.

The deviation intervals also have their uncertainties, but we can only approximate them because of their complexity. This is the reason why the columns in the diagrams are shown without error bars. The uncertainties in the deviation intervals are related to intrinsic errors of the reference techniques (EDXS and XPS), changes in Bi^+ and Cs^+ primary ion currents and gas pressure during SIMS measurements, mixing of layers in multilayered samples, determination of the signal area and repeatability errors when considering repetitions of measurements of the same sample. We assume that the relative uncertainty of the deviation intervals is between ± 30% and ± 50% of its value. Thus, if the deviation interval is 30% and the worst case scenario with the relative uncertainty of ± 50% is considered, this means that the actual deviation interval is between 15% and 45%.

The intensities of the Al_2^- signal are significantly lower than their true values for all alloys, regardless of the type of normalization, as the deviations exceed -90%. The same applies to the Si_2^- signal, which was normalized by the total dose of Bi^+ ions and even reaches a deviation of -99%. The normalization of the same signal by the total intensity of the secondary ions gives slightly better results with an error interval of 81%. Similar to Al_2^-, Ti signals show too low intensities for all alloys. The deviation intervals reach 69% (Ti_2^-) and 87% (Ti^-) for the normalization by the total dose of Bi^+ ions and the total intensity of all secondary ions, respectively. The deviations of the ratios of the Cr_2^- signal vary depending on the type of normalization used. For the normalization by the total dose of Bi^+ ions, the deviation interval is 76%, while the normalization by the total intensity of secondary ions shows worse results with a deviation interval of 94% completely in the negative direction. The results for the Fe^- signal are even more dependent on the type of normalization. The deviation interval when normalizing by Bi^+ is only 44%, while the normalization by the secondary ions gives an interval of 512%, with all the comparative ratios being higher than their true values. Contrary, in the first case, all ratios are lower than their true values. The Co^- signal also deviates strongly with an interval of 253% when normalization is performed using the total dose of Bi^+ ions. Normalization by the total intensity of the secondary ions gives slightly better results with a deviation interval of 92%. The Ni^- signal has deviation intervals of 228% when normalized by the total dose of Bi^+ and 390% when normalized by the total intensity of secondary ions.

The results measured in the UHV and normalized by the total dose of Bi^+ ions offer some potential for the quantitative analysis of Fe. Normalization by the total intensity of the secondary ions gives poorer results because no signal has satisfactory deviation intervals. We can conclude that SIMS analysis in the UHV environment is unsuitable for quantification in the vast majority of cases. Such results were to be expected as the substrate, which differs significantly between the different samples, causes a significant matrix effect that prevents successful quantification. Another substantial factor is a limited selection of signals suitable for analysis. For the signals of Fe, Co and Ni there were no alternatives as only M^- signals were an option, whereas for Al, Si, Ti and Cr we were able to choose between M^- and M_2^- ions. This issue is at least partially solved when a reactive atmosphere is introduced, as the cluster ions that are formed provide a wider range of signals that can be used for the calculations.

3.3. SIMS ANALYSES IN O_2 ATMOSPHERE

Analyses in the O_2 atmosphere are a common practice in the SIMS community to improve the detection of positive secondary ions due to the increased ionization probability in the positive polarity [47]. In our study, we were more interested in a possible quantification of the negative secondary ions, mainly oxides, measured in the O_2 atmosphere during Cs^+ sputtering. Since Cs implantation significantly improves the yield of negative secondary ions [24,25,38,39], we considered only these for analysis. In the following, we compare the quality of three types of normalization of SIMS signals measured in the O_2 atmosphere.

The secondary ions analyzed were monoatomic and diatomic metal ions (M^- and M_2^-), metal oxides, dioxides and trioxides (MO^-, MO_2^- and MO_3^-), and dimetal oxides, dioxides, trioxides and tetraoxides (M_2O^-, $M_2O_2^-$, $M_2O_3^-$ and $M_2O_4^-$). The presence of adsorbed oxygen molecules, which significantly alter the initial metallic substrate and influence the matrix effect, together with the wider arrangement of secondary ions available for analysis, led to better results than in the UHV environment. Normalization by the total dose of Bi^+ ions and the total intensity of secondary ions showed promising results for some metals, while normalization by the intensity of the O_2^- signal was not as successful. The results for all three normalizations are shown in Figure 5. Once more, only the secondary ion with the smallest deviation interval among all secondary ions originating from each element was analyzed. All analyzed signals and their deviation values for each alloy containing this element are listed in SI in Tables S3, S4 and S5.

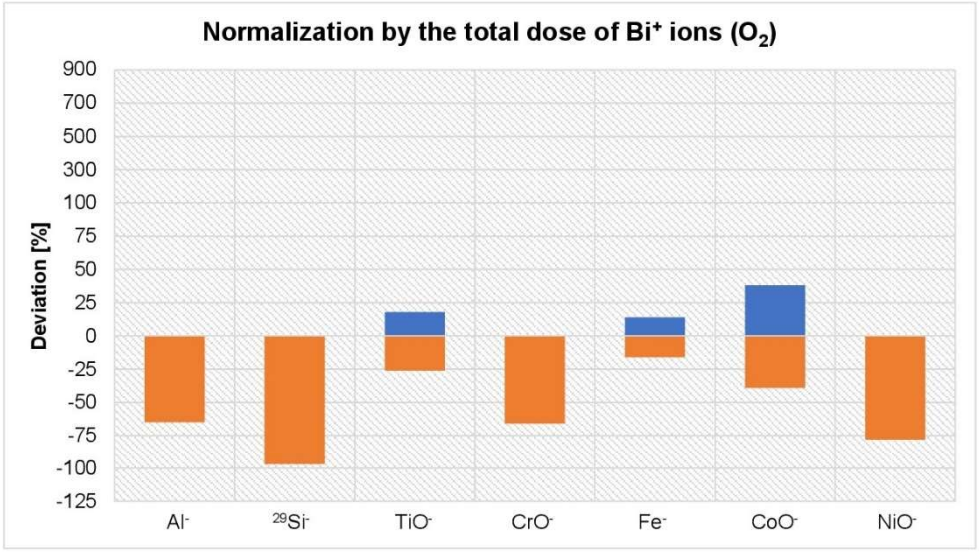
Normalization by the total dose of Bi+ ions (O2)
Deviation [%]
900
700
500
300
100
75
50
25
0
-25
-50
-75
-100
-125
Al-
29Si-
TiO-
CrO-
Fe-
CoO-
NiO-

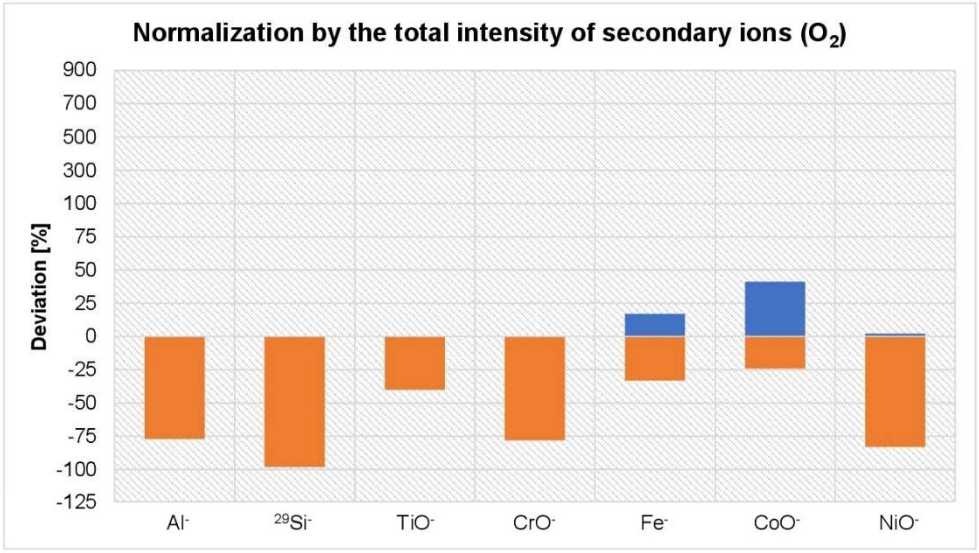
Normalization by the total intensity of secondary ions (O2)
Deviation [%]
900
700
500
300
100
75
50
25
0
-25
-50
-75
-100
-125
Al-
29Si-
TiO-
CrO-
Fe-
CoO-
NiO-

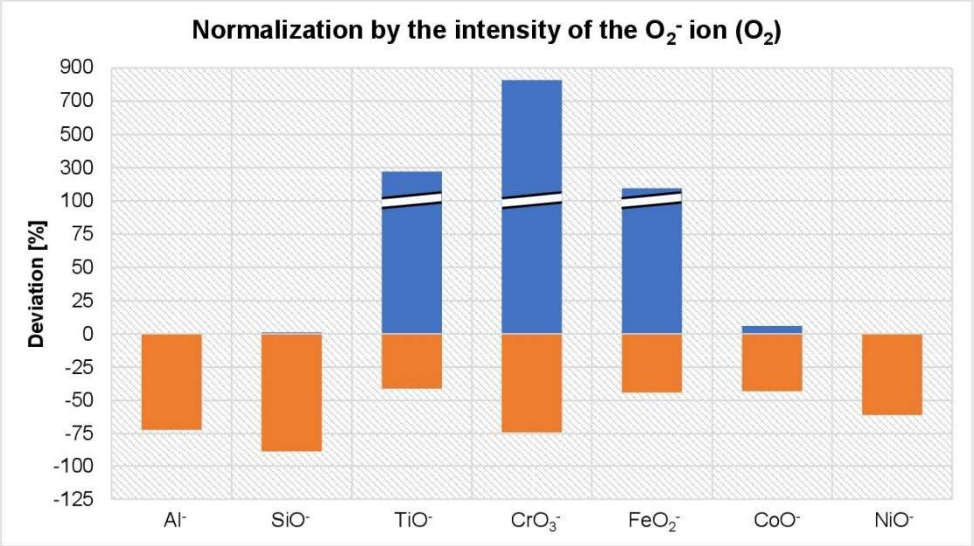

Figure 5: Deviation intervals between the highest negative and the highest positive deviation from the atomic ratios listed in Table 1 for measurements in the O_2 atmosphere in the pressure range between 1 and 3 × 10^{-8} mbar. Each element is represented by one secondary ion selected on the basis of the smallest deviation interval among all secondary ions analyzed for that element.

All comparative ratios of the Al^- signal are lower than their true values, just as in the case of the UHV analysis. However, the deviations are smaller in this case, with the best result observed when normalized by the total dose of Bi^+ ions (-65%). This is also the smallest measured deviation interval for any type of Al secondary ions that applies to all three types of atmospheres. In the case of Si, both the $^{29}Si^-$ and SiO^- signals in the alloys exhibit intensities well below their true values regardless of the type of normalization applied. The deviations reach and exceed -90% in all three cases. The only exception is the SiO^- ion in the CoCr sample with a deviation of 1% when normalized by the O_2^- signal. The results of the TiO^- signal are much better, at least when normalized by the total dose of Bi^+ ions and the intensity of all secondary ions, with deviation intervals of 44 and 40%, respectively. The deviation interval in the case of normalization by the O_2^- signal is much larger, 316%. When normalized by the total Bi^+ dose, a good result is also observed for the Ti_2O^- signal with a deviation interval of 46%. The deviation intervals of the CrO^- signal are relatively high, reaching 66 and 78% for the normalization by the total dose of Bi^+ and the total intensity of all secondary ions, respectively. All comparative ratios are lower than their true values. When normalizing by the intensity of the O_2^- signal, the smallest deviation interval was observed for the CrO_3^- ion, but the interval still reached 900%. The analysis of Fe gave similar results to Cr. The deviation intervals of the Fe^- ion are 30 and 50% for the normalization by the total dose of Bi^+ ions and the intensity of all secondary ions, respectively, while the FeO_2^- signal, normalized by the O_2^- reaches a deviation interval of 219%. On the other hand, the measurements of Co show a reversed situation. The CoO^- ion has the smallest deviation interval when normalized by the O_2^- signal, only 49%. Normalizations by the total dose of Bi^+ ions and the intensity of all secondary ions resulted in deviation intervals of 77 and 65%, respectively. The results of the NiO^- signal do not differ significantly depending on the type of normalization. The deviation intervals are 78, 85 and 61% for the normalization by the total dose of Bi^+ ions, the intensity of all secondary ions and the intensity of the O_2^- ion, respectively.

We can conclude that normalization by the intensity of the O_2^- signal is a favorable approach only for the analysis of Co with an error interval of 49%, which is a significant improvement compared to the UHV analysis. The general problem could be a diatomic form of the O_2^- ion molecule, but the O^- ion

was not an option for normalization due to the constant saturation of this ion during the analysis of all samples in the O_2 atmosphere. Normalization by the total dose of Bi^+ and the total intensity of all secondary ions gives favorable results for Ti and Fe. The deviation intervals for none of these two metals exceed 50%, which again represents a significant improvement compared to the UHV analysis, where only the Fe^- ion, normalized by the total dose of Bi^+, has an error interval below 50%. A substantial improvement compared to the UHV environment is also observed for Ni, but the error intervals remain relatively large. The analysis of Cr in the O_2 atmosphere offers almost no improvement compared to UHV, while the results for Si even deteriorate when O_2 is flooded. Finally, the error intervals for Al decrease compared to the UHV results and the normalization by the total dose of Bi^+ ions gives the smallest error interval among all three atmospheres tested, but remains relatively high with a value of 65%.

3.4. SIMS ANALYSES IN H_2 ATMOSPHERE

As a third choice of atmosphere during the SIMS analyses, H_2 flooding was applied as a novel approach. We used just under 1×10^{-6} mbar of H_2 working pressure to maximize the yield of negative metal hydride ions for a few different metals. The secondary ions available for analysis in the H_2 atmosphere were monoatomic and diatomic metal ions (M^- and M_2^-) and their mono-, di- and trihydrides (MH^-, MH_2^-, MH_3^-, M_2H^- and $M_2H_2^-$). Adsorbed hydrogen further improves the semi-quantitative nature of the SIMS method compared to oxygen, as the deviation intervals of the comparative ratios of all transition metals remain below 50%. Similar to O_2, three different types of normalization were applied. Normalization by the total dose of Bi^+ ions gives the best results for Si and Ti, while normalization by the intensity of the H^- ion gives the best results for Al, Fe, Co and Ni. Cr has practically the same deviation interval for both of these normalizations. The results for normalization by the total intensity of all secondary ions are considerably worse. The deviation intervals calculated for all three types of normalization are shown in Figure 6, while the deviations of the comparative ratios of all analyzed secondary ions for each alloy are listed in SI in Tables S6, S7 and S8.

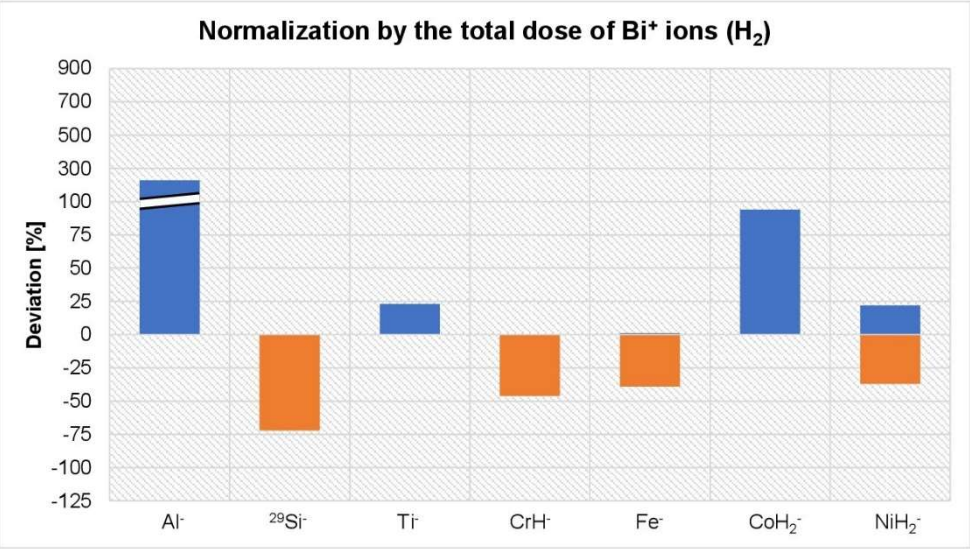

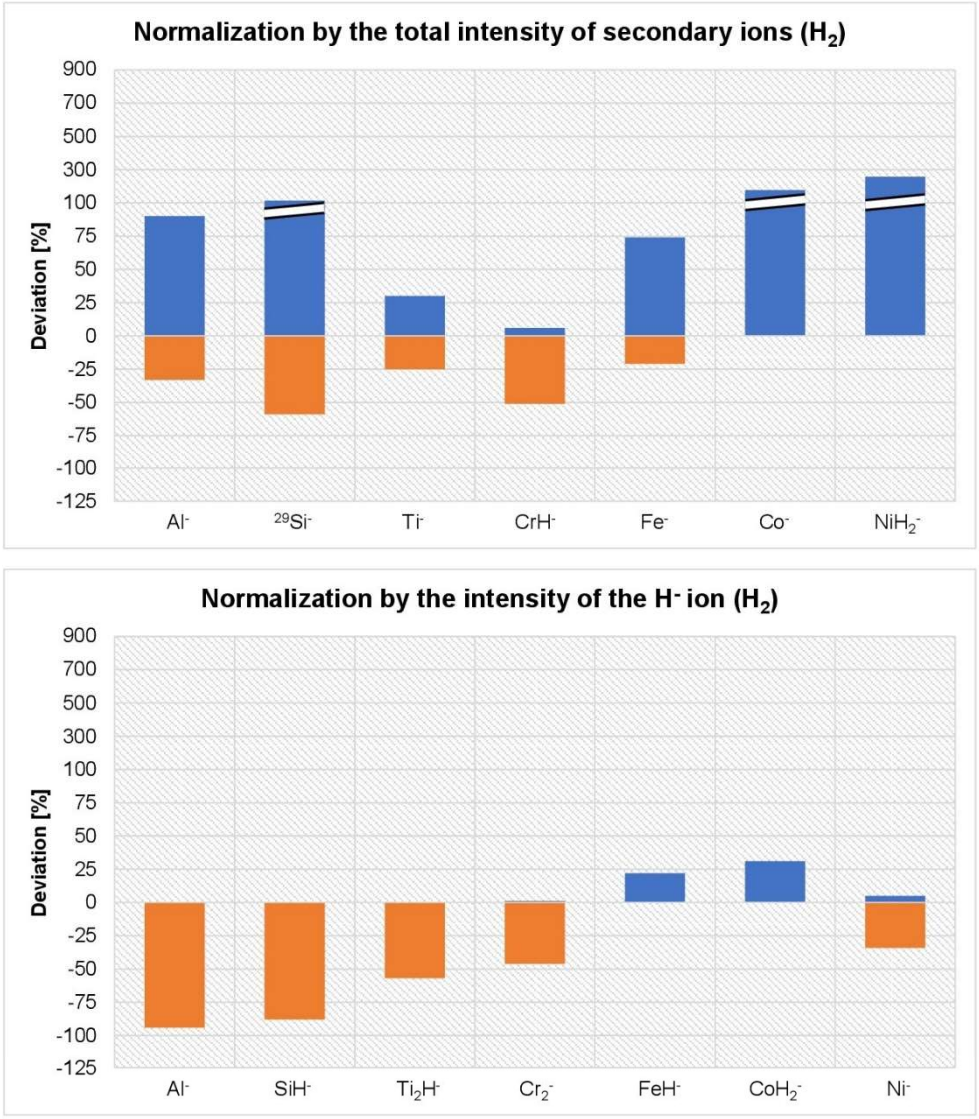

Figure 6: Deviation intervals between the highest negative and the highest positive deviation from the atomic ratios listed in Table 1 for measurements in the H_2 atmosphere in the pressure range between 5×10^{-7} and 1×10^{-6} mbar. Each element is represented by one secondary ion selected on the basis of the smallest deviation interval among all secondary ions analyzed for that element.

Al is the only metal for which all deviation intervals are larger than those measured in UHV and O_2 atmosphere. The normalization of the Al^- signal by the total dose of Bi^+ ions results in a deviation interval of 229%, the total intensity of all secondary ions in a deviation interval of 123% and the intensity of the H^- ion in a deviation interval of 94%. All other six investigated metals have the smallest deviation intervals measured during the H_2 flooding compared to the UHV and O_2 atmosphere. However, in the case of Si, it is still relatively large with a value of 72% when the $^{29}Si^-$ ion is normalized by the total dose of Bi^+ ions. The same type of normalization gives much better results for the Ti^- signal with a deviation interval of only 23%. Normalizations of the Ti^- ion by the total intensity of the

secondary ions and of the Ti_2H^- ion by the intensity of the H^- signal give slightly worse, but still good results, 55 and 57%, respectively. The deviation intervals for Cr are almost the same when normalized by the total dose of Bi^+ ions and the intensity of the H^- ion. In the first case, the CrH^- ion has a deviation interval of 46% and in the second case, the Cr_2^- ion reaches an interval of 47%. The normalization based on the intensity of the H^- ion also shows good results for the CrH^- ion with a deviation interval of 50%. The same secondary ion gives a deviation interval of 57% when normalized by the total intensity of the secondary ions. The FeH^- signal has a deviation interval of only 22% when normalized by the intensity of the H^- ion, while the Fe^- signal reaches 40% when normalized by the total dose of Bi^+ ions and 95% when normalized by the total intensity of the secondary ions. The smallest deviation of the CoH_2^- signal is observed when normalized by the intensity of the H^- ion with an interval of only 31%. The normalization of that same ion by the total dose of Bi^+ ions shows a deviation interval of 94% and the normalization of the Co^- ion by the total intensity of the secondary ions shows an interval of 177%. The normalization by the total intensity of the secondary ions also gives by far the worst result in the analysis of Ni with a deviation interval of 257%. For the other two Ni options, the deviation intervals are much smaller, 59% when normalizing NiH_2^- ion by the total dose of Bi^+ and 39% when normalizing Ni^- ion by the intensity of the H^- ion.

3.5. COMPARISON OF UHV, O_2 AND H_2 ATMOSPHERES FOR THE QUANTIFICATION ASPECT OF THE SIMS METHOD

We have shown that different secondary ions can be considered for quantification depending on the atmosphere used (oxides or hydrides) and the type of normalization. The secondary ions with the smallest deviation intervals are the same (Al_2^-, Si_2^-, Cr_2^-, Fe^-, Co^- and Ni^-), regardless of the type of normalization, when the analyses were performed in UHV. The only exception is Ti with both Ti^- and Ti_2^- ions. Differences occurred when the O_2 atmosphere was applied. Normalization by the total dose of Bi^+ ions and the total intensity of all secondary ions gives exactly the same secondary ion sets, whereas when normalized by the intensity of the O_2^- ion, changes in the optimal ions for Si, Cr and Fe can be observed. For analyses in the H_2 atmosphere, the differences are even greater, as only the Al^- ion is the same for all three types of normalization. Nevertheless, the normalizations by the total dose of Bi^+ ions and the total intensity of secondary ions remain very similar, with the only difference being Co, but everything else changes when normalizing by the intensity of the H^- ion. Even more surprising is the fact that Cr and Ni hydrides are the optimal options when normalized by total Bi^+ ion dose and total secondary ion intensity, but when normalized by H^- ion intensity, the optimal ions change to Cr_2^- and Ni^-. However, we do not have sufficient knowledge of the mechanism of secondary ion formation to explain this phenomenon, nor do we have data to elaborate why for some elements the smallest deviations are observed for oxides and hydrides, while for others for pure metal secondary ions.

Considering all three types of analytical conditions and all three types of normalizations, we found that the H_2 atmosphere gives the best results for all metals except Al. Normalization by the intensity of the H^- ion provides the smallest deviation intervals for Fe (22%), Co (31%) and Ni (39%). Cr normalized in this way has a deviation interval of 47%, while normalization by the total dose of Bi^+ ions gives an interval of 46%. This type of normalization, combined with H_2 flooding, gives the smallest deviation intervals for Si (72%) and Ti (23%). As the only exception, Al shows the best results when normalized by the total dose of Bi^+ ions after analysis in the O_2 atmosphere, with a deviation interval of 65%. As observed, the transition metals show significantly better results than Al and Si, by approximately 20% or more in absolute units. We can therefore conclude that O_2 and especially H_2 atmospheres significantly improve the quantification of transition metals in substantially different alloys, while this is not as applicable for the p-block metals and semimetals, such as Al and Si in our case. Factors that could contribute to this are the reactivities of the analyzed elements, the differences in the electronic structures

between d-orbital transition metals and p-orbital Al and Si, and the mass of these elements, with Al and Si being notably lighter.

Finally, we can compare the deviations of all elements in all alloys together for a given atmosphere and type of normalization. Due to the differences between the elements of the d-block and the p-block, we performed such an analysis only for the transition metals. This approach is illustrated in Figure 7, where the deviation intervals represent the difference between the highest negative and the highest positive deviation from the true value when all five analyzed transition metals (Ti, Cr, Fe, Co and Ni) in all alloys are considered. We regarded only the secondary ions with the smallest deviation intervals, which are shown in Figures 4, 5 and 6. Optimal results are again observed for the H_2 atmosphere, as the combined deviation interval for normalization by the intensity of the H^- ion is 88%. Normalization by the total dose of Bi^+ ions after analysis in H_2 and O_2 and normalization by the intensity of the secondary ions after analysis in O_2 give deviation intervals of 140, 116 and 124%, respectively. All other approaches have combined deviation intervals of 300% or more and even reach 900%.

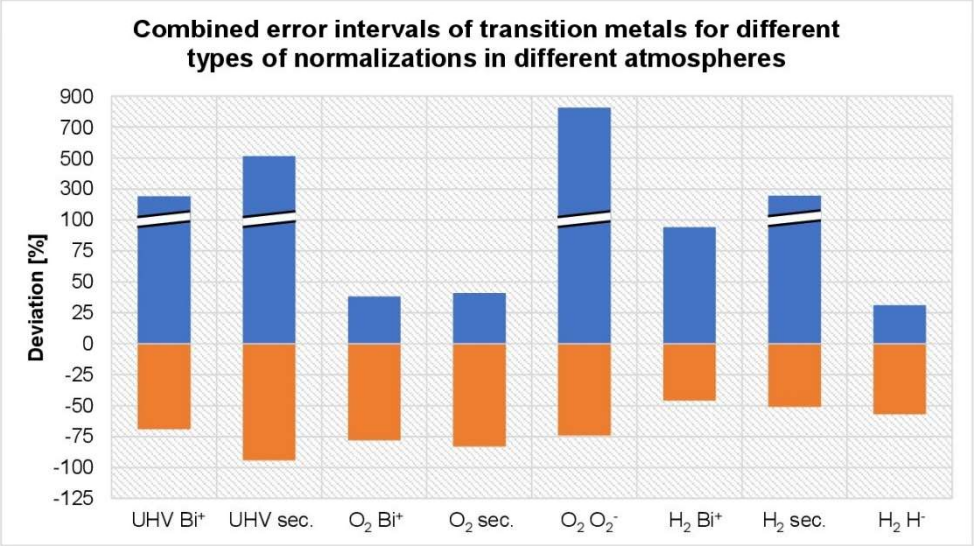

Figure 7: Combined deviation intervals between the highest negative and the highest positive deviation from the true atomic ratios listed in Table 1 when considering the transition metals (Ti, Cr, Fe, Co and Ni) in all alloys for each type of normalization in each atmosphere. Atmospheres (UHV, O_2, and H_2) and types of normalization are defined on the x-axis. Bi^+ stands for normalization by the total dose of Bi^+ ions, sec. for normalization by the intensity of all secondary ions, O_2^- for normalization by the intensity of the O_2^- ion, and H^- for normalization by the intensity of the H^- ion.

These results demonstrate a beneficial effect of the reactive atmospheres on the semi-quantitative aspect of the SIMS method, at least for the transition metals. Adsorbed gas molecules form a new matrix on the surface of the sample containing hydrogen or oxygen atoms. The matrix effect of this layer, i.e. the influence on the ionization of the emitted monoatomic and cluster secondary ions, is approximately the same regardless of the metal or alloy analyzed. In this way, the matrix effect of the original substrate, as observed prior to the exposure to the reactive gasses, is significantly reduced. This phenomenon is similar to reactive Cs^+ sputtering with implantation of Cs^+ ions [35,40,41] and metal-assisted or matrix-enhanced SIMS [48–51], while only Cs^+ enhancement and a specific approach of *in situ* metal deposition can be applied in depth profiling in the way that gas flooding can [52].

Since the best results were obtained in the H_2 atmosphere after normalization by the intensity of the H^- signal, the same could happen if normalization by the O^- ion was performed in the O_2 atmosphere.

However, such an approach would be very challenging due to the very high ionization yield of the O^- ion, resulting in very high intensity and saturation. A lower transmission to the analyzer could be effective, but only if it is applied selectively for the low-mass ions. Otherwise, the intensity of the metal and metal oxide ions would become too low for a reliable analysis. A lower O_2 pressure would be even more problematic, as small changes in O_2 pressure would cause large changes in the intensity of the oxide signals. The intensity of the metal oxide secondary ions would also decrease significantly in this case. Finally, the O_2 atmosphere could be intrinsically problematic as well, since maxima and plateaus of the different oxides differ significantly as a function of O_2 pressure (Figure 3). Our results showed a dependence of ion signal intensities on gas pressure, suggesting that recombination and cluster secondary ion formation should indeed occur at the surface of the sample or directly above it immediately after the desorption of the particles. [53–57] However, further studies on the mechanism of cluster secondary ion formation are beyond the scope of this work, but are needed to gain a deeper insight and understanding of these processes.

4. CONCLUSION

Our study shows that reactive atmospheres substantially improve the quantitative capabilities of the SIMS method. This was particularly demonstrated for the transition metals, while the improvements for the p-block elements such as Al and Si are not as significant. The best results were observed for the SIMS analyses in the H_2 atmosphere in combination with the normalizations by the intensity of the secondary H^- ion and the total dose of Bi^+ ions in the primary ion beam. The deviation intervals of the secondary ions of the analyzed transition metals, which had the smallest deviations among all secondary ions originating from the respective metal, were 23% for Ti, 46% for Cr, 22% for Fe, 31% for Co and 39% for Ni. These values are significantly better than the results measured in the UHV, where all deviation intervals except for the Fe^- ion reached 70% or more. The Fe^- signal normalized by the total dose of Bi^+ ions gave a deviation interval of 44%. The results measured during O_2 flooding showed improvements compared to the UHV environment, but not as prominent as for H_2 flooding. In the H_2 atmosphere, we improved the quantitative analysis of transition metals in significantly different alloys consisting of two to five different elements. Furthermore, the atomic ratios of these elements ranged from only a few percent to almost 100%. This is in contrast to previous SIMS studies quantifying very similar alloys and compounds, composed of the same elements with only minor differences in their relative ratios. For the application of our quantitative approach, a current of Bi^+ and Cs^+ ion beams as stable as possible and precise control of the gas pressure in the SIMS analysis chamber are crucial. To improve the proposed quantitative approach, further studies on the mechanisms of hydride and oxide cluster secondary ion formation are needed and planned.

5. CRediT AUTHOR STATEMENT

Jernej Ekar: Conceptualization, Methodology, Formal analysis, Investigation, Resources, Writing – original draft, Writing – review & editing, Visualization, Project administration. **Saša Kos:** Formal analysis, Investigation, Writing – original draft. **Janez Kovač:** Resources, Writing – review & editing, Supervision, Project administration, Funding acquisition.

6. ACKNOWLEDGMENT

The authors thank prof. Dr. Peter Panjan for preparing the multilayered samples containing Al, Si, Ti, Cr, Fe, Ni, both AlTi, AlCr, and both SiTi films. We would also like to thank the researcher Barbara Ljubec Božiček for providing the CoCrFeMnNi sample.

7. FUNDING

This work was supported by the Slovenian Research and Innovation Agency (ARIS) through the Programs P2-0082 and P1-0025 and the Project PR-09757.

8. REFERENCES

[1] P. van der Heide, Sputtering and Ion Formation, in: Second. Ion Mass Spectrom. An Introd. to Princ. Pract., John Wiley & Sons, Hoboken, New Jersey, 2014: pp. 44–143.

[2] J.C. Vickerman, Prologue: ToF-SIMS—An evolving mass spectrometry of materials, in: D. Vickerman, J. C. & Briggs (Ed.), ToF-SIMS Mater. Anal. by Mass Spectrom. 2nd Ed., IM Publications LLP and SurfaceSpectra Limited, Chichester, Manchester, 2013: pp. 1–37.

[3] P. van der Heide, Instrumentation Used in SIMS, in: Second. Ion Mass Spectrom. An Introd. to Princ. Pract., John Wiley & Sons, Hoboken, New Jersey, 2014: pp. 147–194.

[4] B.W. Schueler, Time-of-flight mass analysers, in: D. Vickerman, J. C. & Briggs (Ed.), ToF-SIMS Mater. Anal. by Mass Spectrom. 2nd Ed., IM Publications LLP and SurfaceSpectra Limited, Chichester, Manchester, 2013: pp. 247–270.

[5] P. van der Heide, The Art of Measurement, in: Second. Ion Mass Spectrom. An Introd. to Princ. Pract., John Wiley & Sons, Hoboken, New Jersey, 2014: pp. 195–208.

[6] Y. Abe, M. Komatsu, H. Okuhira, Estimation of ToF-SIMS information depth in micro-corrosion analysis, Appl. Surf. Sci. 203–204 (2003) 859–862. https://doi.org/10.1016/S0169-4332(02)00824-3.

[7] D.K. Kozlica, J. Ekar, J. Kovač, I. Milošev, Roles of Chloride Ions in the Formation of Corrosion Protective Films on Copper, J. Electrochem. Soc. 168 (2021) 031504. https://doi.org/10.1149/1945-7111/abe34a.

[8] P. Jovičević-Klug, N. Lipovšek, M. Jovičević-Klug, M. Mrak, J. Ekar, B. Ambrožič, G. Dražić, J. Kovač, B. Podgornik, Assessment of deep cryogenic heat-treatment impact on the microstructure and surface chemistry of austenitic stainless steel, Surfaces and Interfaces. 35 (2022) 102456. https://doi.org/10.1016/J.SURFIN.2022.102456.

[9] X. Xu, C. Jiao, K. Li, M. Hao, K.L. Moore, T.L. Burnett, X. Zhou, Application of high-spatial-resolution secondary ion mass spectrometry for nanoscale chemical mapping of lithium in an Al-Li alloy, Mater. Charact. 181 (2021) 111442. https://doi.org/10.1016/J.MATCHAR.2021.111442.

[10] J. Kovač, J. Ekar, M. Čekada, L. Zajíčková, D. Nečas, L. Blahová, J. Yong Wang, M. Mozetič, Depth profiling of thin plasma-polymerized amine films using GDOES in an Ar-O_2 plasma, Appl. Surf. Sci. 581 (2022) 152292. https://doi.org/10.1016/J.APSUSC.2021.152292.

[11] M. Holzweber, A.G. Shard, H. Jungnickel, A. Luch, W.E.S. Unger, Dual beam organic depth profiling using large argon cluster ion beams, Surf. Interface Anal. 46 (2014) 936–939. https://doi.org/10.1002/SIA.5429.

[12] E.I. Vasilkova, A.N. Klochkov, A.N. Vinichenko, N.I. Kargin, I.S. Vasil'evskii, Comparison of the thermal interdiffusion phenomena in InGaAs/GaAs and InGaAs/AlGaAs strained heterostructures, Surfaces and Interfaces. 29 (2022) 101766. https://doi.org/10.1016/J.SURFIN.2022.101766.

[13] J. Bailey, R. Havelund, A.G. Shard, I.S. Gilmore, M.R. Alexander, J.S. Sharp, D.J. Scurr, 3D ToF-SIMS imaging of polymer multilayer films using argon cluster sputter depth profiling, ACS Appl. Mater. Interfaces. 7 (2015) 2654–2659. https://doi.org/10.1021/AM507663V/SUPPL_FILE/AM507663V_SI_001.PDF.

[14] A.G. Shard, R. Havelund, M.P. Seah, S.J. Spencer, I.S. Gilmore, N. Winograd, D. Mao, T. Miyayama, E. Niehuis, D. Rading, R. Moellers, Argon cluster ion beams for organic depth profiling: Results from a VAMAS interlaboratory study, Anal. Chem. 84 (2012) 7865–7873. https://doi.org/10.1021/AC301567T/ASSET/IMAGES/LARGE/AC-2012-01567T_0006.JPEG.

[15] R.M. Patil, P.P. Deshpande, M. Aalhate, S. Gananadhamu, P.K. Singh, An Update on Sophisticated and Advanced Analytical Tools for Surface Characterization of Nanoparticles, Surfaces and Interfaces. 33 (2022) 102165. https://doi.org/10.1016/J.SURFIN.2022.102165.

[16] A. Gulin, A. Shakhov, A. Vasin, A. Astafiev, O. Antonova, S. Kochev, Y. Kabachii, A. Golub, V. Nadtochenko, ToF-SIMS depth profiling of nanoparticles: Chemical structure of core-shell quantum dots, Appl. Surf. Sci. 481 (2019) 144–150. https://doi.org/10.1016/J.APSUSC.2019.03.097.

[17] G. Guryanov, T.P. St. Clair, R. Bhat, C. Caneau, S. Nikishin, B. Borisov, A. Budrevich, SIMS quantitative depth profiling of matrix elements in semiconductor layers, Appl. Surf. Sci. 252 (2006) 7208–7210. https://doi.org/10.1016/J.APSUSC.2006.02.254.

[18] K. Brecl, M. Jošt, M. Bokalič, J. Ekar, J. Kovač, M. Topič, Are Perovskite Solar Cell Potential-Induced Degradation Proof?, Sol. RRL. 6 (2022) 2100815. https://doi.org/10.1002/SOLR.202100815.

[19] A. Omerzu, R. Peter, D. Jardas, I. Turel, K. Salamon, M. Podlogar, D. Vengust, I. Jelovica Badovinac, I. Kavre Piltaver, M. Petravic, Large enhancement of photocatalytic activity in ZnO thin films grown by plasma-enhanced atomic layer deposition, Surfaces and Interfaces. 23 (2021) 100984. https://doi.org/10.1016/J.SURFIN.2021.100984.

[20] F. Hölzel, D. Rolón, J. Bauer, J. Kober, S. Kühne, F. Pietag, D. Oberschmidt, T. Arnold, Reactive ion beam smoothing of rapidly solidified aluminum (RSA) 501 surfaces for potential visible and ultraviolet light applications, Surfaces and Interfaces. 38 (2023) 102784. https://doi.org/10.1016/J.SURFIN.2023.102784.

[21] M. Sumiya, A. Tsukazaki, S. Fuke, A. Ohtomo, H. Koinuma, M. Kawasaki, SIMS analysis of ZnO films co-doped with N and Ga by temperature gradient pulsed laser deposition, Appl. Surf. Sci. 223 (2004) 206–209. https://doi.org/10.1016/S0169-4332(03)00923-1.

[22] P. Agüi-Gonzalez, S. Jähne, N.T.N. Phan, SIMS imaging in neurobiology and cell biology, J. Anal. At. Spectrom. 34 (2019) 1355–1368. https://doi.org/10.1039/C9JA00118B.

[23] J. Brison, N. Mine, N. Wehbe, X. Gillon, T. Tabarrant, R. Sporken, L. Houssiau, Molecular depth profiling of model biological films using low energy monoatomic ions, Int. J. Mass Spectrom. 321–322 (2012) 1–7. https://doi.org/10.1016/J.IJMS.2012.04.001.

[24] P. van der Heide, Secondary Ion Yields, in: Second. Ion Mass Spectrom. An Introd. to Princ. Pract., John Wiley & Sons, Hoboken, New Jersey, 2014: pp. 93–121.

[25] M. Grasserbauer, Quantitative Secondary Ion Mass Spectrometry, J. Res. Natl. Bur. Stand. 93 (1988) 510. https://doi.org/10.6028/JRES.093.140.

[26] A. Priebe, T. Xie, G. Bürki, L. Pethö, J. Michler, The matrix effect in TOF-SIMS analysis of two-element inorganic thin films, J. Anal. At. Spectrom. 35 (2020) 1156–1166. https://doi.org/10.1039/c9ja00428a.

[27] A. Wucher, Laser post-ionisation—fundamentals, in: D. Vickerman, J. C. & Briggs (Ed.), ToF-SIMS Mater. Anal. by Mass Spectrom. 2nd Ed., IM Publications LLP and SurfaceSpectra Limited, Chichester, Manchester, 2013: pp. 217–246.

[28] L. Breuer, P. Ernst, M. Herder, F. Meinerzhagen, M. Bender, D. Severin, A. Wucher, Mass spectrometric investigation of material sputtered under swift heavy ion bombardment, Nucl. Instruments Methods Phys. Res. Sect. B Beam Interact. with Mater. Atoms. 435 (2018) 101–110. https://doi.org/10.1016/j.nimb.2017.10.019.

[29] L. Breuer, N.J. Popczun, A. Wucher, N. Winograd, Reducing the Matrix Effect in Molecular Secondary Ion Mass Spectrometry by Laser Post-Ionization, J. Phys. Chem. C. 121 (2017) 19705–19715. https://doi.org/10.1021/acs.jpcc.7b02596.

[30] N.P. Lockyer, Laser post-ionisation for elemental and molecular surface analysis, in: D. Vickerman, J. C. & Briggs (Ed.), ToF-SIMS Mater. Anal. by Mass Spectrom. 2nd Ed., IM Publications LLP and SurfaceSpectra Limited, Chichester, Manchester, 2013: pp. 361–396.

[31] R. Wilson, J.A. Van Den Berg, J.C. Vickerman, Quantitative surface analysis using electron beam SNMS: Calibrations and applications, Surf. Interface Anal. 14 (1989) 393–400. https://doi.org/10.1002/sia.740140617.

[32] M. Kopnarski, H. Jenett, Electron-Impact (EI) Secondary Neutral Mass Spectrometry (SNMS), in: Surf. Thin Film Anal., Wiley-VCH Verlag GmbH & Co. KGaA, Weinheim, Germany, 2011: pp. 161–177.

[33] H. Oechsner, Electron Gas SNMS, in: Second. Ion Mass Spectrom. SIMS V, Springer, Berlin, 1986: pp. 70–74.

[34] L. Breuer, H. Tian, A. Wucher, N. Winograd, Molecular SIMS Ionization Probability Studied with Laser Postionization: Influence of the Projectile Cluster, J. Phys. Chem. C. 123 (2019) 565–574. https://doi.org/10.1021/acs.jpcc.8b10245.

[35] V. Karki, M. Singh, Quantitative depth distribution analysis of elements in high alloy steel using MCs^+-SIMS approach, Int. J. Mass Spectrom. 430 (2018) 22–30. https://doi.org/10.1016/J.IJMS.2018.04.001.

[36] P. van der Heide, Data Processing, in: Second. Ion Mass Spectrom. An Introd. to Princ. Pract., John Wiley & Sons, Hoboken, New Jersey, 2014: pp. 248–268.

[37] H. Satoh, M. Owari, Y. Nihei, Relative sensitivity factors for submicron secondary ion mass spectrometry with gallium primary ion beam, Jpn. J. Appl. Phys. 32 (1993) 3616. https://doi.org/10.1143/JJAP.32.3616/XML.

[38] Y. Kudriatsev, A. Villegas, S. Gallardo, G. Ramirez, R. Asomoza, V. Mishurnuy, Cesium ion sputtering with oxygen flooding: Experimental SIMS study of work function change, Appl. Surf. Sci. 254 (2008) 4961–4964. https://doi.org/10.1016/j.apsusc.2008.01.145.

[39] Z. Cong, X. Fu, S. Liu, W. Wang, H. Liu, G. Lei, B. Zhao, H. Wu, C. Gao, Enhancing the organic solar cells performances by elevating cesium carboxylate content of graphene oxide based cathode interface layer, Surfaces and Interfaces. 31 (2022) 102068. https://doi.org/10.1016/J.SURFIN.2022.102068.

[40] C. Hongo, M. Tomita, M. Suzuki, Quantitative secondary ion mass spectrometry analysis of impurities in GaN and $Al_xGa_{1-x}N$ films using molecular ions MCs^+ and MCs_2^+, Appl. Surf. Sci. 144–145 (1999) 306–309. https://doi.org/10.1016/S0169-4332(98)00815-0.

[41] Y.J. Jang, S.H. Kim, K.J. Kim, D. Kim, Y. Lee, Comparison of quantitative analyses using SIMS, atom probe tomography, and femtosecond laser ablation inductively coupled plasma mass spectrometry with $Si_{1-X}Ge_X$ and $Fe_{1-X}Ni_X$ binary alloys, J. Vac. Sci. Technol. B. 38 (2020) 034009. https://doi.org/10.1116/6.0000101/591706.

[42] J. Ekar, P. Panjan, S. Drev, J. Kovač, ToF-SIMS Depth Profiling of Metal, Metal Oxide, and Alloy Multilayers in Atmospheres of H_2, C_2H_2, CO, and O_2, J. Am. Soc. Mass Spectrom. 33 (2022) 31–44. https://doi.org/10.1021/JASMS.1C00218/ASSET/IMAGES/LARGE/JS1C00218_0008.JPEG.

[43] P. van der Heide, Electronic Structure of Atoms and Ions, in: Second. Ion Mass Spectrom. An Introd. to Princ. Pract., John Wiley & Sons, Hoboken, New Jersey, 2014: pp. 27–42.

[44] A. Priebe, I. Utke, L. Pethö, J. Michler, Application of a Gas-Injection System during the FIB-TOF-SIMS Analysis - Influence of Water Vapor and Fluorine Gas on Secondary Ion Signals and Sputtering Rates, Anal. Chem. 91 (2019) 11712–11722. https://doi.org/10.1021/acs.analchem.9b02287.

[45] J.F. Moulder, W.F. Stickle, P.E. Sobol, K.D. Bomben, Handbook of X-Ray Photoelectron Spectroscopy, Physical Electronics Inc., Eden Prairie, Minnesota, 1995.

[46] P. van der Heide, Secondary Ion Columns, in: Second. Ion Mass Spectrom. An Introd. to Princ. Pract., John Wiley & Sons, Hoboken, New Jersey, 2014: pp. 167–191.

[47] D. Sykes, A. Chew, M. Crapper, R. Valizadeh, The effect of oxygen flooding on the secondary ion yield of Cs in the Cameca IMS 3f, Vacuum. 43 (1992) 159–162. https://doi.org/10.1016/0042-207X(92)90204-A.

[48] J.D. Debord, A. Prabhakaran, M.J. Eller, S. V. Verkhoturov, A. Delcorte, E.A. Schweikert, Metal-assisted SIMS with hypervelocity gold cluster projectiles, Int. J. Mass Spectrom. 343–344 (2013) 28–36. https://doi.org/10.1016/j.ijms.2013.03.012.

[49] S.J.B. Dunham, T.J. Comi, K. Ko, B. Li, N.F. Baig, N. Morales-Soto, J.D. Shrout, P.W. Bohn, J. V. Sweedler, Metal-assisted polyatomic SIMS and laser desorption/ionization for enhanced small molecule imaging of bacterial biofilms, Biointerphases. 11 (2016) 02A325. https://doi.org/10.1116/1.4942884.

[50] J.J.D. Fitzgerald, P. Kunnath, A. V. Walker, Matrix-enhanced secondary ion mass spectrometry (ME SIMS) using room temperature ionic liquid matrices, Anal. Chem. 82 (2010) 4413–4419. https://doi.org/10.1021/ac100133c.

[51] L. Cai, L. Sheng, M. Xia, Z. Li, S. Zhang, X. Zhang, H. Chen, Graphene Oxide as a Novel Evenly Continuous Phase Matrix for TOF-SIMS, J. Am. Soc. Mass Spectrom. 28 (2017) 399–408. https://doi.org/10.1007/S13361-016-1557-Z.

[52] A. Yamazaki, T. Tobe, S. Akiba, M. Owari, Metal-Assisted SIMS for three-dimensional analysis using shave-off section processing, Surf. Interface Anal. 46 (2014) 1215–1218. https://doi.org/10.1002/sia.5589.

[53] H.M. Urbassek, Status of cascade theory, in: D. Vickerman, J. C. & Briggs (Ed.), ToF-SIMS Mater. Anal. by Mass Spectrom. 2nd Ed., IM Publications LLP and SurfaceSpectra Limited, Chichester, Manchester, 2013: pp. 67–86.

[54] F. Honda, G.M. Lancaster, Y. Fukuda, J.W. Rabalais, SIMS study of the mechanism of cluster formation during ion bombardment of alkali halides, J. Chem. Phys. 69 (1978) 4931–4937. https://doi.org/10.1063/1.436480.

[55] G.M. Lancaster, F. Honda, Y. Fukuda, J.W. Rabalais, Secondary Ion Mass Spectrometry of Molecular Solids. Cluster Formation During Ion Bombardment of Frozen Water, Benzene, and Cyclohexane, J. Am. Chem. Soc. 101 (1979) 1951–1958. https://doi.org/10.1021/JA00502A004/ASSET/JA00502A004.FP.PNG_V03.

[56] J. Vlekken, M. D'Olieslaeger, G. Knuyt, W. Vandervorst, L. De Schepper, Investigation of the formation process of MCs^+-molecular ions during sputtering, J. Am. Soc. Mass Spectrom. 11 (2000) 650–658. https://doi.org/10.1016/S1044-0305(00)00130-6.

[57] B. Saha, P. Chakraborty, Secondary ion mass spectrometry of MCs_n^+ molecular ion complexes, Nucl. Instruments Methods Phys. Res. Sect. B Beam Interact. with Mater. Atoms. 258 (2007) 218–225. https://doi.org/10.1016/J.NIMB.2006.12.172.

Supplementary information

Quantitative Aspects of ToF-SIMS Analysis of Metals and Alloys in a UHV, O_2 and H_2 Atmosphere

Jernej Ekar,[1,2] Saša Kos,[3,4] Janez Kovač[1,*]

[1]Jožef Stefan Institute, Jamova cesta 39, SI-1000 Ljubljana, Slovenia
[2]Jožef Stefan International Postgraduate School, Jamova cesta 39, SI-1000 Ljubljana, Slovenia
[3]Geological Survey of Slovenia, Dimičeva ulica 14, SI-1000 Ljubljana, Slovenia
[4]Faculty of Civil and Geodetic Engineering, University of Ljubljana, Jamova cesta 2, SI-1000 Ljubljana, Slovenia

Corresponding author: *Janez Kovač (janez.kovac@ijs.si, 00386 1 477 34 03)

Table S1: Deviations of the comparative ratios of the measured secondary ions from their true atomic ratios for analyzed alloys. The measurements were performed in the UHV environment and the intensities of the secondary ions were normalized by the total dose of Bi^+ ions.

	Al^-	Al_2^-	$^{29}Si^-$	Si_2^-	Ti^-	Ti_2^-	Cr^-	Cr_2^-	Fe^-	Co^-	Ni^-
AlTi 30	0.46	-0.92			0.14	-0.33					
AlTi 47	0.99	-0.71			0.20	-0.27					
AlCr	-0.38	-0.82					0.91	-0.16			
SiTi 31			0.47	-0.77	1.48	-0.02					
SiTi 51			-0.01	-0.14	0.89	-0.69					
CoCr			-0.81	-0.99			2.03	-0.15		0.76	
NiTi					0.38	-0.54					2.18
AlTiV	1.13	-0.95			0.09	0.00					
Fernico									-0.35	2.53	0.28
Inconel							2.45	-0.40	-0.02		-0.10
Kanthal	-0.01	-0.96					2.40	0.36	-0.33		
stainless steel			-0.61	-0.98			2.93	0.18	-0.26		0.26
CoCrFeMnNi							2.70	-0.04	-0.44	1.15	0.16

Table S2: Deviations of the comparative ratios of the measured secondary ions from their true atomic ratios for analyzed alloys. The measurements were performed in the UHV environment and the intensities of the secondary ions were normalized by the total intensity of all secondary ions.

	Al^-	Al_2^-	$^{29}Si^-$	Si_2^-	Ti^-	Ti_2^-	Cr^-	Cr_2^-	Fe^-	Co^-	Ni^-
AlTi 30	2.58	-0.81			-0.45	-0.67					
AlTi 47	3.51	-0.34			-0.46	-0.67					
AlCr	-0.12	-0.75					-0.86	-0.94			
SiTi 31			1.34	-0.64	-0.80	-0.92					
SiTi 51			0.36	0.17	-0.87	-0.98					
CoCr			5.99	-0.56			0.44	-0.60		0.58	
NiTi					-0.55	-0.85					2.21
AlTiV	8.73	-0.77			-0.01	-0.09					
Fernico									2.09	0.27	1.86
Inconel							-0.61	-0.93	1.78		0.19
Kanthal	0.49	-0.93					-0.74	-0.90	0.28		
stainless steel			9.00	-0.40			0.31	-0.61	5.12		3.90
CoCrFeMnNi							-0.40	-0.84	1.30	-0.34	1.23

Table S3: Deviations of the comparative ratios of the measured secondary ions from their true atomic ratios for analyzed alloys. The measurements were performed in the O_2 atmosphere and the intensities of the secondary ions were normalized by the total dose of Bi^+ ions.

	Al^-	Al_2^-	AlO_2^-	AlO_3^-	$Al_2O_3^-$	$Al_2O_4^-$	$^{29}Si^-$	SiO^-	Si_2^-	SiO_2^-
AlTi 30	-0.56	-0.99	0.23	-0.14	-0.48	-0.63				
AlTi 47	-0.26	-0.85	0.28	-0.16	-0.29	-0.53				
AlCr	-0.65	-0.98	3.10	3.22	3.83	4.01				
SiTi 31							-0.61	1.26	-0.81	0.24
SiTi 51							-0.45	1.41	-0.38	0.77
CoCr							-0.86	2.66	-0.99	15.56
NiTi										
AlTiV	-0.23	-0.96	0.43	0.69	-0.64	-0.69				
Fernico										
Inconel										
Kanthal	-0.62	-1.00	10.60	15.47	10.18	20.50				
stainless steel							-0.97	1.64	-1.00	39.40
CoCrFeMnNi										

	Ti^-	TiO^-	TiO_2^-	Ti_2^-	TiO_3^-	Ti_2O^-	$Ti_2O_2^-$	$Ti_2O_3^-$
AlTi 30	-0.13	-0.17	0.29	-0.48	1.46	-0.42	-0.34	-0.09
AlTi 47	0.18	0.18	0.05	0.27	0.54	-0.08	-0.44	-0.58
AlCr								
SiTi 31	0.25	-0.13	0.57	-0.47	1.97	-0.46	-0.19	0.32
SiTi 51	0.94	-0.26	0.49	-0.37	2.80	-0.39	-0.24	0.13
CoCr								
NiTi	-0.12	-0.23	0.72	-0.02	1.29	-0.19	0.48	3.84
AlTiV	-0.06	-0.01	0.76	-0.29	5.48	-0.43	-0.36	-0.04
Fernico								
Inconel								
Kanthal								
stainless steel								
CoCrFeMnNi								

	Cr^-	CrO^-	CrO_2^-	CrO_3^-	$Cr_2O_3^-$	$Cr_2O_4^-$	Fe^-	FeO^-	FeO_2^-
AlTi 30									
AlTi 47									
AlCr	0.08	-0.66	-0.88	-0.97	-0.93	-0.99			
SiTi 31									
SiTi 51									
CoCr	0.22	-0.41	-0.42	-0.89	0.67	-0.85			
NiTi									
AlTiV									
Fernico							-0.16	0.26	-0.23
Inconel	-0.51	-0.64	0.20	-0.28	3.85	0.19	0.04	-0.10	-0.34
Kanthal	-0.07	-0.32	-0.08	-0.51	-0.03	-0.78	0.14	0.16	-0.62
stainless steel	-0.22	-0.36	0.61	0.06	1.10	-0.34	-0.02	0.26	-0.28
CoCrFeMnNi	0.03	-0.14	0.87	0.12	2.27	-0.14	0.03	0.44	-0.15

	Co^-	CoO^-	CoO_2^-	Ni^-	NiO^-	NiO_2^-
AlTi 30						
AlTi 47						
AlCr						
SiTi 31						
SiTi 51						
CoCr	0.67	-0.39	-0.82			
NiTi				1.68	-0.78	-0.99
AlTiV						
Fernico	0.85	0.35	0.14	0.24	-0.39	-0.83
Inconel				-0.54	-0.71	-0.86
Kanthal						
stainless steel				0.33	-0.06	-0.72
CoCrFeMnNi	0.65	0.38	0.35	0.67	-0.03	-0.68

Table S4: Deviations of the comparative ratios of the measured secondary ions from their true atomic ratios for analyzed alloys. The measurements were performed in the O_2 atmosphere and the intensities of the secondary ions were normalized by the total intensity of all secondary ions.

	Al^-	Al_2^-	AlO_2^-	AlO_3^-	$Al_2O_3^-$	$Al_2O_4^-$	$^{29}Si^-$	SiO^-	Si_2^-	SiO_2^-
AlTi 30	-0.59	-0.99	0.16	-0.19	-0.51	-0.65				
AlTi 47	-0.35	-0.87	0.13	-0.26	-0.38	-0.59				
AlCr	-0.73	-0.99	2.20	2.29	2.76	2.92				
SiTi 31							-0.55	1.67	-0.77	0.47
SiTi 51							-0.33	1.92	-0.24	1.17
CoCr							-0.78	4.67	-0.99	24.92
NiTi										
AlTiV	-0.27	-0.96	0.37	0.61	-0.65	-0.70				
Fernico										
Inconel										
Kanthal	-0.77	-1.00	6.10	9.04	5.78	12.11				
stainless steel							-0.98	1.45	-1.00	36.50
CoCrFeMnNi										

	Ti^-	TiO^-	TiO_2^-	Ti_2^-	TiO_3^-	Ti_2O^-	$Ti_2O_2^-$	$Ti_2O_3^-$
AlTi 30	-0.30	-0.34	0.04	-0.58	0.97	-0.54	-0.47	-0.27
AlTi 47	-0.12	-0.11	-0.21	-0.05	0.16	-0.31	-0.57	-0.68
AlCr								
SiTi 31	-0.02	-0.32	0.23	-0.58	1.35	-0.57	-0.36	0.04
SiTi 51	0.56	-0.40	0.21	-0.49	2.08	-0.50	-0.38	-0.08
CoCr								
NiTi	-0.15	-0.25	0.68	-0.05	1.24	-0.21	0.45	3.74
AlTiV	-0.23	-0.20	0.44	-0.42	4.30	-0.53	-0.47	-0.22
Fernico								
Inconel								
Kanthal								
stainless steel								
CoCrFeMnNi								

	Cr^-	CrO^-	CrO_2^-	CrO_3^-	$Cr_2O_3^-$	$Cr_2O_4^-$	Fe^-	FeO^-	FeO_2^-
AlTi 30									
AlTi 47									
AlCr	0.05	-0.67	-0.88	-0.97	-0.93	-0.99			
SiTi 31									
SiTi 51									
CoCr	0.85	-0.11	-0.12	-0.84	1.52	-0.77			
NiTi									
AlTiV									
Fernico							0.14	0.73	0.05
Inconel	-0.70	-0.78	-0.28	-0.57	1.93	-0.28	-0.33	-0.42	-0.57
Kanthal	-0.30	-0.48	-0.30	-0.63	-0.26	-0.83	-0.08	-0.06	-0.69
stainless steel	-0.30	-0.43	0.44	-0.06	0.87	-0.41	-0.07	0.21	-0.30
CoCrFeMnNi	0.09	-0.09	0.99	0.19	2.48	-0.09	0.17	0.64	-0.03

	Co^-	CoO^-	CoO_2^-	Ni^-	NiO^-	NiO_2^-
AlTi 30						
AlTi 47						
AlCr						
SiTi 31						
SiTi 51						
CoCr	1.09	-0.24	-0.78			
NiTi				2.75	-0.70	-0.99
AlTiV						
Fernico	0.94	0.41	0.19	0.56	-0.23	-0.78
Inconel				-0.73	-0.83	-0.92
Kanthal						
stainless steel				0.17	-0.17	-0.75
CoCrFeMnNi	0.44	0.20	0.18	0.74	0.02	-0.67

Table S5: Deviations of the comparative ratios of the measured secondary ions from their true atomic ratios for analyzed alloys. The measurements were performed in the O_2 atmosphere and the intensities of the secondary ions were normalized by the intensity of the O_2^- ion.

	Al^-	Al_2^-	AlO_2^-	AlO_3^-	$Al_2O_3^-$	$Al_2O_4^-$	$^{29}Si^-$	SiO^-	Si_2^-	SiO_2^-
AlTi 30	-0.61	-0.99	0.11	-0.23	-0.54	-0.67				
AlTi 47	-0.18	-0.84	0.42	-0.07	-0.22	-0.48				
AlCr	-0.55	-0.98	4.27	4.41	5.20	5.44				
SiTi 31							-0.98	-0.87	-0.99	-0.93
SiTi 51							-0.94	-0.75	-0.93	-0.81
CoCr							-0.96	0.01	-1.00	3.58
NiTi										
AlTiV	-0.64	-0.98	-0.32	-0.20	-0.83	-0.85				
Fernico										
Inconel										
Kanthal	-0.72	-1.00	7.67	11.28	7.33	14.99				
stainless steel							-1.00	-0.89	-1.00	0.74
CoCrFeMnNi										

	Ti^-	TiO^-	TiO_2^-	Ti_2^-	TiO_3^-	Ti_2O^-	$Ti_2O_2^-$	$Ti_2O_3^-$
AlTi 30	-0.01	-0.06	0.47	-0.40	1.80	-0.34	-0.25	0.04
AlTi 47	0.64	0.65	0.46	0.77	1.16	0.28	-0.21	-0.42
AlCr								
SiTi 31	0.60	0.11	1.00	-0.31	2.82	-0.31	0.04	0.69
SiTi 51	3.43	0.69	2.43	0.45	7.73	0.41	0.75	1.58
CoCr								
NiTi	3.26	2.75	7.40	3.76	10.21	2.97	6.25	22.62
AlTiV	-0.44	-0.41	0.05	-0.58	2.89	-0.66	-0.61	-0.43
Fernico								
Inconel								
Kanthal								
stainless steel								
CoCrFeMnNi								

	Cr^-	CrO^-	CrO_2^-	CrO_3^-	$Cr_2O_3^-$	$Cr_2O_4^-$	Fe^-	FeO^-	FeO_2^-
AlTi 30									
AlTi 47									
AlCr	8.99	2.15	0.10	-0.74	-0.38	-0.93			
SiTi 31									
SiTi 51									
CoCr	40.96	19.08	18.83	2.64	56.12	4.23			
NiTi									
AlTiV									
Fernico							2.01	3.53	1.75
Inconel	4.98	3.34	13.47	7.73	57.99	13.45	2.51	2.02	1.22
Kanthal	3.96	2.65	3.93	1.62	4.21	0.18	0.69	0.71	-0.44
stainless steel	3.13	2.37	7.48	4.58	10.03	2.46	0.43	0.84	0.06
CoCrFeMnNi	7.52	6.10	14.44	8.26	26.04	6.08	1.36	2.30	0.94

	Co^-	CoO^-	CoO_2^-	Ni^-	NiO^-	NiO_2^-
AlTi 30						
AlTi 47						
AlCr						
SiTi 31						
SiTi 51						
CoCr	1.88	0.06	-0.69			
NiTi				7.22	-0.34	-0.98
AlTiV						
Fernico	0.20	-0.13	-0.26	0.77	-0.13	-0.76
Inconel				-0.38	-0.61	-0.81
Kanthal						
stainless steel				-0.22	-0.46	-0.83
CoCrFeMnNi	-0.31	-0.43	-0.44	0.52	-0.11	-0.71

Table S6: Deviations of the comparative ratios of the measured secondary ions from their true atomic ratios for analyzed alloys. The measurements were performed in the H_2 atmosphere and the intensities of the secondary ions were normalized by the total dose of Bi^+ ions.

	Al^-	AlH^-	AlH_2^-	$^{29}Si^-$	SiH^-	Ti^-	TiH^-	TiH_2^-	TiH_3^-
AlTi 30	1.26	48.43	10.41			0.07	-0.25	-0.31	-0.25
AlTi 47	1.78	54.11	12.53			0.13	-0.20	-0.28	-0.10
AlCr	0.43	26.82	24.78						
SiTi 31				-0.58	5.78	0.23	-0.31	-0.37	-0.25
SiTi 51				-0.43	1.85	0.19	-0.78	-0.88	-0.88
CoCr				-0.72	1.43				
NiTi						0.05	-0.54	-0.65	-0.77
AlTiV	2.29	80.95	15.71			0.05	0.02	-0.27	-0.36
Fernico									
Inconel									
Kanthal	0.21	43.63	17.90						
stainless steel				-0.50	2.33				
CoCrFeMnNi									

	Ti_2H^-	$Ti_2H_2^-$	Cr^-	CrH^-	$^{50}CrH_2^-$	Cr_2^-	Cr_2H^-	Fe^-	FeH^-
AlTi 30	-0.38	-0.38							
AlTi 47	-0.35	-0.34							
AlCr			1.21	-0.29	-0.38	-0.01	-0.62		
SiTi 31	-0.56	-0.54							
SiTi 51	-0.87	-0.90							
CoCr			0.64	-0.46	-0.68	-0.62	-0.87		
NiTi	-0.76	-0.79							
AlTiV	-0.17	-0.24							
Fernico								-0.39	-0.42
Inconel			1.85	-0.43	-0.74	-0.58	-0.89	-0.14	-0.41
Kanthal			1.09	-0.01	-0.22	-0.41	-0.77	0.01	0.31
stainless steel			0.94	-0.31	-0.54	-0.51	-0.85	-0.23	-0.19
CoCrFeMnNi			1.39	-0.35	-0.60	-0.43	-0.84	-0.10	-0.22

	Co^-	CoH_2^-	Ni^-	NiH_2^-
AlTi 30				
AlTi 47				
AlCr				
SiTi 31				
SiTi 51				
CoCr	0.66	0.94		
NiTi			1.84	-0.13
AlTiV				
Fernico	1.18	0.68	-0.21	-0.13
Inconel			-0.10	-0.37
Kanthal				
stainless steel			-0.19	-0.04
CoCrFeMnNi	1.30	0.69	0.22	0.22

Table S7: Deviations of the comparative ratios of the measured secondary ions from their true atomic ratios for analyzed alloys. The measurements were performed in the H_2 atmosphere and the intensities of the secondary ions were normalized by the total intensity of all secondary ions.

	Al^-	AlH^-	AlH_2^-	$^{29}Si^-$	SiH^-	Ti^-	TiH^-	TiH_2^-	TiH_3^-
AlTi 30	0.46	31.01	6.36			0.16	-0.18	-0.25	-0.18
AlTi 47	0.90	36.84	8.28			0.30	-0.07	-0.16	0.04
AlCr	0.22	22.80	21.13						
SiTi 31				-0.59	5.52	-0.25	-0.58	-0.61	-0.54
SiTi 51				-0.34	2.32	-0.12	-0.83	-0.91	-0.91
CoCr				0.04	7.95				
NiTi						0.24	-0.46	-0.58	-0.73
AlTiV	0.89	46.33	8.60			0.02	-0.02	-0.29	-0.38
Fernico									
Inconel									
Kanthal	-0.33	23.77	9.47						
stainless steel				1.13	13.01				
CoCrFeMnNi									

	Ti_2H^-	$Ti_2H_2^-$	Cr^-	CrH^-	$^{50}CrH_2^-$	Cr_2^-	Cr_2H^-	Fe^-	FeH^-
AlTi 30	-0.33	-0.32							
AlTi 47	-0.25	-0.24							
AlCr			0.82	-0.41	-0.49	-0.18	-0.69		
SiTi 31	-0.73	-0.72							
SiTi 51	-0.90	-0.93							
CoCr			1.18	-0.27	-0.57	-0.50	-0.83		
NiTi	-0.72	-0.75							
AlTiV	-0.20	-0.27							
Fernico								0.02	-0.03
Inconel			1.47	-0.51	-0.77	-0.63	-0.91	0.09	-0.25
Kanthal			0.11	-0.47	-0.58	-0.69	-0.88	-0.21	0.02
stainless steel			1.98	0.06	-0.29	-0.25	-0.77	0.74	0.82
CoCrFeMnNi			1.43	-0.34	-0.59	-0.42	-0.84	0.34	0.15

	Co^-	CoH_2^-	Ni^-	NiH_2^-
AlTi 30				
AlTi 47				
AlCr				
SiTi 31				
SiTi 51				
CoCr	1.45	1.86		
NiTi			3.66	0.43
AlTiV				
Fernico	1.77	1.13	1.20	1.43
Inconel			0.89	0.33
Kanthal				
stainless steel			2.03	2.57
CoCrFeMnNi	1.59	0.90	1.99	2.02

Table S8: Deviations of the comparative ratios of the measured secondary ions from their true atomic ratios for analyzed alloys. The measurements were performed in the H_2 atmosphere and the intensities of the secondary ions were normalized by the intensity of the H^- ion.

	Al^-	AlH^-	AlH_2^-	$^{29}Si^-$	SiH^-	Ti^-	TiH^-	TiH_2^-	TiH_3^-
AlTi 30	-0.94	0.27	-0.71			0.23	-0.13	-0.21	-0.13
AlTi 47	-0.94	0.30	-0.68			0.19	-0.15	-0.23	-0.04
AlCr	-0.85	1.94	1.72						
SiTi 31				-0.99	-0.88	0.46	-0.17	-0.24	-0.10
SiTi 51				-0.97	-0.87	2.75	-0.29	-0.61	-0.62
CoCr				-0.97	-0.73				
NiTi						2.47	0.52	0.17	-0.23
AlTiV	-0.93	0.78	-0.64			0.03	-0.01	-0.29	-0.38
Fernico									
Inconel									
Kanthal	-0.87	3.99	1.11						
stainless steel				-0.94	-0.58				
CoCrFeMnNi									

	Ti_2H^-	$Ti_2H_2^-$	Cr^-	CrH^-	$^{50}CrH_2^-$	Cr_2^-	Cr_2H^-	Fe^-	FeH^-
AlTi 30	-0.28	-0.29							
AlTi 47	-0.31	-0.30							
AlCr			1.05	-0.34	-0.42	-0.08	-0.65		
SiTi 31	-0.48	-0.45							
SiTi 51	-0.57	-0.68							
CoCr			1.38	-0.21	-0.53	-0.46	-0.81		
NiTi	-0.21	-0.31							
AlTiV	-0.19	-0.26							
Fernico								0.11	0.06
Inconel			4.64	0.13	-0.48	-0.16	-0.79	0.50	0.03
Kanthal			1.07	-0.02	-0.23	-0.41	-0.77	-0.12	0.15
stainless steel			2.26	0.16	-0.22	-0.18	-0.75	0.14	0.21
CoCrFeMnNi			3.24	0.15	-0.28	0.01	-0.71	0.42	0.22

	Co^-	CoH_2^-	Ni^-	NiH_2^-
AlTi 30				
AlTi 47				
AlCr				
SiTi 31				
SiTi 51				
CoCr	-0.09	0.06		
NiTi			-0.12	-0.73
AlTiV				
Fernico	0.71	0.31	-0.21	-0.13
Inconel			-0.14	-0.40
Kanthal				
stainless steel			-0.34	-0.22
CoCrFeMnNi	0.55	0.14	0.05	0.05

Chapter 8

Conclusions

In the frame of this thesis, we studied the reactive gas flooding approach to address different aspects of the matrix effect during the SIMS depth profiling and quantification. The largest improvements were observed in the field of depth profiling of metals, metal oxides, and chemically similar alloys in the form of both thin and thick films. The main advances of a new approach are related to the improved identification, determination, and differentiation of thin layers, enhanced resolving power, and reduced surface roughening. Furthermore, significant progress was made in the direction of quantitative SIMS analyses of metals and alloys. The improvements were the most successful during the H_2 flooding. Another positive aspect of the gas flooding approach is its simplicity as it does not require either expensive instrumentation or extensive modifications of the SIMS instrument. As such, it can be implemented in any type of SIMS.

SIMS depth profiling of thin films and multilayers composed of metals and their oxides can be challenging as clear differentiation between these layers can be difficult. Similar issues can be observed when analyzing alloys composed of the same metals in different concentrations. Precise SIMS analysis many times requires measuring depth profiles of the same sample using different primary ions and analytical conditions. This process is time-consuming. SIMS depth profiling combined with reactive gas flooding provides the possibility of avoiding these problems. In our case, H_2, C_2H_2, CO, and O_2 gases were applied and cluster secondary ions in the form of metal hydrides, carbides, and oxides were formed and analyzed. As they most efficiently ionize in the negative polarity, depth profiling was performed with the Cs^+ ion beam, which appears to be a proper choice for achieving good depth resolution. Application of C_2H_2, CO, and O_2 improved SIMS depth profiling results in comparison to the UHV conditions, but not uniformly and rather selectively for only specific aspects of different samples. The best results were obtained with the H_2 atmosphere. The most important aspects of the H_2 flooding that we found are the formation of the metal hydride (MH_n^-) secondary ions which exclusively form in the layers of unoxidized metals, the presence of intense but not saturated H^- signal, which can be used for the normalization, and the introduction of only one new element from the reactive gas molecule which does not complicate the results of the analysis extensively.

Application of the proper atmosphere and the optimized parameters allowed us a clear differentiation between successive layers of different metals, metals and their oxides, and alloys composed of the same elements in different ratios. In the cases of TiSi alloys, an unambiguous determination was possible as intensities of cluster secondary ions correctly represented changes in atomic ratios of constituting elements. Furthermore, good depth resolution was maintained even after prolonged sputtering providing the possibility of unequivocal separation for thin layers of thickness below 5 nm. Interfaces were sharp as well. Finally, the H_2 atmosphere causes no reduction in the sputter rate. Therefore, there

is no prolongation in the analysis time. On the other hand, C_2H_2, CO, and O_2 flooding reduces the sputter rate significantly concerning the UHV environment. The positive aspects of the H_2 atmosphere were, considering common samples, analyzed with the SIMS depth profiling, the most extensively applied for the cases of the oxidized surfaces. Oxide layers analyzed were formed spontaneously in the ambient conditions, synthesized intentionally as a part of passivation and corrosion inhibition as well as covered with additional layers of organic or inorganic compounds.

Further studies of the effects of the H_2 flooding proved the positive effect on the reduction of the surface roughness development during ion sputtering. Prolonged bombardment with the ions induces extensive damage accumulation resulting in surface roughening which is an unwanted process as it worsens depth resolution. It was found that the presence of H_2 during depth profiling causes a reduction of surface roughness after prolonged sputtering in comparison to the UHV profiling. For the initially smooth samples with a surface roughness average (S_a) of approximately 1 nm, the improvements were proven to be statistically significant. On the other hand, samples with larger initial surface roughness average S_a between 3 and 5 nm exhibit extensive scattering of the measured S_a. We related this with the presence of randomly distributed trench and ripple-like structures probably formed during sample preparation. Because of this, improvements observed during H_2 flooding were in these cases mostly statistically insignificant. An interesting result of our study was that some specific initially rough samples with the S_a between 3 and 5 nm can become smoother after sputtering with the Cs^+ ion beam with the energy of 1 keV. This indicates the presence of smoothing, a reversed process from what is generally expected. It was also observed that the positive effects of the H_2 flooding become more pronounced after prolonged sputtering, that is when deeper craters are etched. We anticipate that the most probable reason for the H_2-induced improvement is a reduced degree of recrystallization taking place in the H_2 atmosphere. Since amorphous materials more easily relax, they generally tend to form less topographical structures on the surface, and ion sputtering is known to cause amorphization of the material. If recrystallization is limited, a larger amount of the surface material will stay in the amorphous form and this can consequently reduce surface roughness.

A similar approach as described above was also used in the quantification studies where results obtained in UHV were compared with those measured in the H_2 and O_2 atmospheres. The reason for conducting the analyses in the depth profiling regime was once more enhanced ionization of hydride and oxide negative secondary ions caused by the implantation of cesium during Cs^+ ion bombardment. Pure metals Al, Si, Ti, Cr, Fe, Co, and Ni, as well as their alloys with profoundly different compositions, were analyzed. Alloys were composed of between two and six different metals with the atomic percentage of these elements ranging from only a few percent in some alloys to 100% in pure metals. In this way, a quantitative comparison of samples with significant differences in chemical composition was performed, which is uncommon for the SIMS analyses. For example, the approach of the relative sensitivity factors (RSF) is mostly used when samples are composed of the same elements with only slight differences in their atomic ratios. Our results indicate that the presence of H_2 or O_2 significantly improves the quantification capabilities of the SIMS method in comparison with the UHV. The most significant improvements were made with the transition metals, while both p-block elements, like Al and Si, show limited possibility for quantification. For all five analyzed transition metals, the smallest deviations of measured signals of the secondary ions from their true atomic ratios were obtained during H_2 flooding while normalizing secondary ion signals by the intensity of the H^- ion and the total dose of Bi^+ ions. The deviation intervals of their secondary ions, which have the smallest deviations among all secondary ions originating from the respective transition metal, are 23% for Ti, 46% for Cr, 22% for Fe, 31% for Co,

and 39% for Ni. O_2 flooding provides notable improvements in comparison to the UHV as well, but deviation intervals still reach values of up to 66%. For the UHV measurements, the maximal deviation interval reaches even 228%. Our results indicate that atmospheres of reactive gases substantially improve the quantitative capabilities of the SIMS method even when profoundly different samples are compared. This can be explained by the formation of the new matrix on the freshly sputtered surface which mainly depends on the type of the gas and not the composition of the sample. The new matrix effect consequently remains mostly the same for different analyses while the initial matrix effect caused by the sample substrate is reduced and suppressed.

With the results described above, we almost fully confirmed our hypotheses. Hypothesis 1, describing the formation of the cluster secondary ions, was completely confirmed in Articles 1, 2, and 4 (Chapters 4, 5, and 7). Improvements in the quantitative aspects of the SIMS method stated in Hypothesis 2 were achieved partially as described in Article 4 (Chapter 7). However, the method could be improved further both regarding the breadth of the applicability and additional reduction in deviations of the measured ratios from their true values. Hypotheses 3 and 4 related to the depth profiling optimization and polarity of the secondary ions, respectively, were confirmed fully and successfully as shown in Articles 1 and 2 (Chapters 4 and 5). Finally, Hypothesis 5 stating the reduction in surface roughening caused by the gas flooding was confirmed partially via the study presented in Article 3 (Chapter 6). The lack of statistical significance observed in the cases of rougher samples represents a challenge for further studies and improvements.

Therefore, research in the field of reactive gas flooding applied during SIMS analyses still offers a lot of potential for further optimization of quantification and reduction in surface roughening. Different primary ions can be used especially during quantification studies. The quantification method can be further developed by analyzing more metals or even molecular materials and a comparison of the results obtained with the hydride, oxide, and MCs^+ cluster secondary ions can be performed. The use of standards and better control of instrumental parameters would be also beneficial for the confirmation of the quantification aspects. Further systematic studies are needed to determine the mechanism of the formation process of the cluster secondary ions in more detail. The influence of the ratio of gas adsorption and its removal caused by the ion sputtering can give us information about the gas monolayer formation and consequently about the correlation between the amount of adsorbed gases and the intensity of their cluster secondary ions. Such research would be beneficial for the explanation of the mechanism of the formation of cluster ions composed of atoms from the sample and the reactive gas applied. Finally, the effects of some other experimental conditions, such as the temperature of the sample, could be explored as well.

References

[1] J. I. Goldstein *et al.*, "The SEM and Its Modes of Operation," in *Scanning Electron Microscopy and X-ray Microanalysis*, Boston, MA: Springer US, 2003, pp. 21–60.

[2] C. Y. Tang and Z. Yang, "Transmission Electron Microscopy (TEM)," in *Membrane Characterization*, Elsevier Inc., 2017, pp. 145–159.

[3] G. W. Grime, "Proton Microprobe (Method and Background)," in *Encyclopedia of Spectroscopy and Spectrometry, Second Edition*, Academic Press, 1999, pp. 2296–2300.

[4] C. Bai, *Scanning Tunneling Microscopy and its Application*, vol. 9, no. 4. Springer-Verlag Berlin Heidelberg, 1998.

[5] D. A. Bonnell, "Scanning Tunneling Microscopy," in *Encyclopedia of Materials: Science and Technology*, Elsevier, 2001, pp. 8269–8281.

[6] C. J. Chen, *Introduction to Scanning Tunneling Microscopy: Second Edition*. Oxford: Oxford University Press, 2007.

[7] P. J. Bryant, R. G. Miller, and R. Yang, "Scanning tunneling and atomic force microscopy combined," *Appl. Phys. Lett.*, vol. 52, no. 26, pp. 2233–2235, 1988.

[8] Y. Gan, "Atomic and subnanometer resolution in ambient conditions by atomic force microscopy," *Surf. Sci. Rep.*, vol. 64, no. 3, pp. 99–121, Mar. 2009.

[9] H. J. Mathieu, "Auger Electron Spectroscopy," in *Surface Analysis - The Principal Techniques: Second Edition*, John Wiley and Sons, 2009, pp. 9–45.

[10] F. Hofer, F. P. Schmidt, W. Grogger, and G. Kothleitner, "Fundamentals of electron energy-loss spectroscopy," *IOP Conf. Ser. Mater. Sci. Eng.*, vol. 109, no. 1, Feb. 2016.

[11] B. Fultz, "Introduction," in *Transmission Electron Energy Loss Spectrometry in Materials Science and The EELS Atlas*, Wiley-VCH Verlag GmbH & Co. KGaA, 2005, pp. 1–19.

[12] J. I. Goldstein et al., "X-Ray Spectral Measurement: EDS and WDS," in *Scanning Electron Microscopy and X-ray Microanalysis*, Boston, MA: Springer US, 2003, pp. 297–353.

[13] J. I. Goldstein et al., "Special Topics in Scanning Electron Microscopy," in *Scanning Electron Microscopy and X-ray Microanalysis*, Boston, MA: Springer US, 2003, pp. 195–270.

[14] D. P. Woodruff, "Low Energy Electron Diffraction," in *Reference Module in Materials Science and Materials Engineering*, Elsevier, 2016.

[15] E. Taglauer, "Low-Energy Ion Scattering and Rutherford Backscattering," in *Surface Analysis - The Principal Techniques: Second Edition*, John Wiley and Sons, 2009, pp. 269–331.

[16] K. Ishii, "PIXE and Its Applications to Elemental Analysis," *Quantum Beam Sci.*, vol. 3, no. 2, pp. 12–25, Jun. 2019.

[17] A. G. Karydas et al., "3D Micro PIXE - A new technique for depth-resolved elemental analysis," *J. Anal. At. Spectrom.*, vol. 22, no. 10, pp. 1260–1265, 2007.

[18] B. D. Ratner and D. G. Castner, "Electron Spectroscopy for Chemical Analysis," in *Surface Analysis - The Principal Techniques: Second Edition*, John Wiley and Sons, 2009, pp. 47–112.

[19] J. E. Whitten, "Ultraviolet photoelectron spectroscopy: Practical aspects and best practices," *Appl. Surf. Sci. Adv.*, vol. 13, p. 100384, Feb. 2023.

[20] H. Yoshida, "Principle and application of low energy inverse photoemission spectroscopy: A new method for measuring unoccupied states of organic semiconductors," *J. Electron Spectros. Relat. Phenomena*, vol. 204, pp. 116–124, Oct. 2015.

[21] M. Schmeling, "X-Ray Fluorescence and Emission | Total Reflection X-Ray Fluorescence," in *Encyclopedia of Analytical Science*, Academic Press, 2019, pp. 449–458.

[22] D. M. Wong, A. A. Bol'shakov, and R. E. Russo, "Laser Induced Breakdown Spectroscopy," in *Encyclopedia of Spectroscopy and Spectrometry*, Academic Press, 2017, pp. 533–538.

[23] J. Koch and D. Günther, "Laser Ablation ICP-MS," in *Encyclopedia of Spectroscopy and Spectrometry*, Second Edition, Academic Press, 2010, pp. 1262–1269.

[24] J. C. Vickerman, "Prologue: ToF-SIMS—An evolving mass spectrometry of materials," in *ToF-SIMS: Materials Analysis by Mass Spectrometry 2nd Edition*, D. Vickerman, J. C. & Briggs, Eds. Chichester, Manchester: IM Publications LLP and SurfaceSpectra Limited, 2013, pp. 1–37.

[25] E. Claude, E. A. Jones, and S. D. Pringle, "DESI mass spectrometry imaging (MSI)," in *Methods in Molecular Biology*, vol. 1618, Totowa: Humana Press Inc., 2017, pp. 65–75.

[26] D. Parrot, S. Papazian, D. Foil, and D. Tasdemir, "Imaging the Unimaginable: Desorption Electrospray Ionization - Imaging Mass Spectrometry (DESI-IMS) in Natural Product Research," *Planta Med.*, vol. 84, no. 9–10, pp. 584–593, Jul. 2018.

[27] M. Karas and R. Krüger, "Ion formation in MALDI: The cluster ionization mechanism," *Chem. Rev.*, vol. 103, no. 2, pp. 427–439, Feb. 2003.

[28] D. M. Parees, S. D. Hanton, P. A. Cornelio Clark, and D. A. Willcox, "Comparison of mass spectrometric techniques for generating molecular weight information on a class of ethoxylated oligomers," *J. Am. Soc. Mass Spectrom.*, vol. 9, no. 4, pp. 282–291, 1998.

[29] P. van der Heide, "The Art of Measurement," in *Secondary Ion Mass Spectrometry: An Introduction to Principles and Practices*, Hoboken, New Jersey: John Wiley & Sons, 2014, pp. 195–208.

[30] P. Jovičević-Klug et al., "Assessment of deep cryogenic heat-treatment impact on the microstructure and surface chemistry of austenitic stainless steel," *Surfaces and Interfaces*, vol. 35, p. 102456, Dec. 2022.

[31] X. Xu et al., "Application of high-spatial-resolution secondary ion mass spectrometry for nanoscale chemical mapping of lithium in an Al-Li alloy," *Mater. Charact.*, vol. 181, p. 111442, Nov. 2021.

[32] Y. Abe, M. Komatsu, and H. Okuhira, "Estimation of ToF-SIMS information depth in micro-corrosion analysis," *Appl. Surf. Sci.*, vol. 203–204, pp. 859–862, Jan. 2003.

[33] D. K. Kozlica, J. Ekar, J. Kovač, and I. Milošev, "Roles of Chloride Ions in the Formation of Corrosion Protective Films on Copper," *J. Electrochem. Soc.*, vol. 168, no. 3, p. 031504, Feb. 2021.

[34] J. Y. Xu et al., "Accurate and Efficient SIMS Oxygen Isotope Analysis of Composition-Variable Minerals: Online Matrix Effect Calibration for Dolomite," *Anal. Chem.*, vol. 94, no. 22, pp. 7944–7951, Jun. 2022.

[35] S. He, Y. Li, L. G. Wu, D. F. Guo, Z. Y. Li, and X. H. Li, "High precision zircon SIMS Zr isotope analysis," *J. Anal. At. Spectrom.*, vol. 36, no. 10, pp. 2063–2073, Oct. 2021.

[36] J. Kovač et al., "Depth profiling of thin plasma-polymerized amine films using GDOES in an Ar-O_2 plasma," *Appl. Surf. Sci.*, vol. 581, p. 152292, Apr. 2022.

[37] M. Holzweber, A. G. Shard, H. Jungnickel, A. Luch, and W. E. S. Unger, "Dual beam organic depth profiling using large argon cluster ion beams," *Surf. Interface Anal.*, vol. 46, no. 10–11, pp. 936–939, Oct. 2014.

[38] E. I. Vasilkova, A. N. Klochkov, A. N. Vinichenko, N. I. Kargin, and I. S. Vasil'evskii, "Comparison of the thermal interdiffusion phenomena in InGaAs/GaAs and InGaAs/AlGaAs strained heterostructures," *Surfaces and Interfaces*, vol. 29, p. 101766, Apr. 2022.

[39] R. M. Patil, P. P. Deshpande, M. Aalhate, S. Gananadhamu, and P. K. Singh, "An Update on Sophisticated and Advanced Analytical Tools for Surface Characterization of Nanoparticles," *Surfaces and Interfaces*, vol. 33, p. 102165, Oct. 2022.

[40] A. Gulin et al., "ToF-SIMS depth profiling of nanoparticles: Chemical structure of core-shell quantum dots," *Appl. Surf. Sci.*, vol. 481, pp. 144–150, Jul. 2019.

[41] G. Guryanov et al., "SIMS quantitative depth profiling of matrix elements in semiconductor layers," *Appl. Surf. Sci.*, vol. 252, no. 19, pp. 7208–7210, Jul. 2006.

[42] K. Brecl, M. Jošt, M. Bokalič, J. Ekar, J. Kovač, and M. Topič, "Are Perovskite Solar Cell Potential-Induced Degradation Proof?," *Sol. RRL*, vol. 6, no. 2, p. 2100815, Feb. 2022.

[43] T. Lombardo et al., "ToF-SIMS in battery research: Advantages, limitations, and best practices," *J. Vac. Sci. Technol. A*, vol. 41, no. 5, p. 53207, Sep. 2023.

[44] T. Sui, B. Song, J. Dluhos, L. Lu, and A. M. Korsunsky, "Nanoscale chemical mapping of Li-ion battery cathode material by FIB-SEM and TOF-SIMS multi-modal microscopy," *Nano Energy*, vol. 17, pp. 254–260, Oct. 2015.

[45] J. T. Li et al., "XPS and ToF-SIMS study of Sn–Co alloy thin films as anode for lithium ion battery," *J. Power Sources*, vol. 195, no. 24, pp. 8251–8257, Dec. 2010.

[46] A. Omerzu et al., "Large enhancement of photocatalytic activity in ZnO thin films grown by plasma-enhanced atomic layer deposition," *Surfaces and Interfaces*, vol. 23, p. 100984, Apr. 2021.

[47] T. Stephan and I. C. Lyon, "Application of ToF-SIMS in cosmochemistry," in *ToF-SIMS: Materials Analysis by Mass Spectrometry 2nd Edition*, J. C. Vickerman and D. Briggs, Eds. Chichester, Manchester: IM Publications LLP and SurfaceSpectra Limited, 2013, pp. 709–723.

[48] P. Hoppe, "NanoSIMS: A new tool in cosmochemistry," *Appl. Surf. Sci.*, vol. 252, no. 19, pp. 7102–7106, Jul. 2006.

[49] D. S. McPhail, "Some applications of SIMS in conservation science, archaeometry and cosmochemistry," *Appl. Surf. Sci.*, vol. 252, no. 19, pp. 7107–7112, Jul. 2006.

[50] J. Bailey et al., "3D ToF-SIMS imaging of polymer multilayer films using argon cluster sputter depth profiling," *ACS Appl. Mater. Interfaces*, vol. 7, no. 4, pp. 2654–2659, Feb. 2015.

[51] A. G. Shard et al., "Argon cluster ion beams for organic depth profiling: Results from a VAMAS interlaboratory study," *Anal. Chem.*, vol. 84, no. 18, pp. 7865–7873, Sep. 2012.

[52] L. Van Vaeck, Y. Vercammen, J. Lenaerts, R. De Mondt, J. Van Luppen, and F. Vangaever, "Photographic and digital graphic materials," in *ToF-SIMS: Materials Analysis by Mass Spectrometry 2nd Edition*, J. C. Vickerman and D. Briggs, Eds. Chichester, Manchester: IM Publications LLP and SurfaceSpectra Limited, 2013, pp. 685–708.

[53] F. Hölzel et al., "Reactive ion beam smoothing of rapidly solidified aluminum (RSA) 501 surfaces for potential visible and ultraviolet light applications," *Surfaces and Interfaces*, vol. 38, p. 102784, Jun. 2023.

[54] M. Sumiya, A. Tsukazaki, S. Fuke, A. Ohtomo, H. Koinuma, and M. Kawasaki, "SIMS analysis of ZnO films co-doped with N and Ga by temperature gradient pulsed laser deposition," *Appl. Surf. Sci.*, vol. 223, no. 1–3, pp. 206–209, Feb. 2004.

[55] P. Agüi-Gonzalez, S. Jähne, and N. T. N. Phan, "SIMS imaging in neurobiology and cell biology," *J. Anal. At. Spectrom.*, vol. 34, no. 7, pp. 1355–1368, Jul. 2019.

[56] J. Brison et al., "Molecular depth profiling of model biological films using low energy monoatomic ions," *Int. J. Mass Spectrom.*, vol. 321–322, pp. 1–7, May 2012.

[57] P. van der Heide, "Sputtering," in *Secondary Ion Mass Spectrometry: An Introduction to Principles and Practices*, Hoboken, New Jersey: John Wiley & Sons, 2014, pp. 46–88.

[58] P. van der Heide, "Ionization/Neutralization," in *Secondary Ion Mass Spectrometry: An Introduction to Principles and Practices*, Hoboken, New Jersey: John Wiley & Sons, 2014, pp. 88–138.

[59] C. M. Mahoney and G. Gillen, "An Introduction to Cluster Secondary Ion Mass Spectrometry (Cluster SIMS)," in *Cluster Secondary Ion Mass Spectrometry: Principles and Applications*, C. M. Mahoney, Ed. New Jersey: John Wiley and Sons, 2013, pp. 1–11.

[60] P. van der Heide, "Secondary Ion Columns," in *Secondary Ion Mass Spectrometry: An Introduction to Principles and Practices*, Hoboken, New Jersey: John Wiley & Sons, 2014, pp. 167–191.

[61] B. W. Schueler, "Time-of-flight mass analysers," in *ToF-SIMS: Materials Analysis by Mass Spectrometry 2nd Edition*, J. C. Vickerman and D. Briggs, Eds. Chichester, Manchester: IM Publications LLP and SurfaceSpectra Limited, 2013, pp. 247–270.

[62] A. Benninghoven, "The history of Static SIMS—A personal perspective," in *ToF-SIMS: Materials Analysis by Mass Spectrometry 2nd Edition*, J. C. Vickerman and D. Briggs, Eds. Chichester, Manchester: IM Publications LLP and SurfaceSpectra Limited, 2013, pp. 39–66.

[63] C. M. Mahoney, "Surface Analysis of Organic Materials with Polyatomic Primary Ion Sources," in *Cluster Secondary Ion Mass Spectrometry: Principles and Applications*, C. M. Mahoney, Ed. New Jersey: John Wiley and Sons, 2013, pp. 77–116.

[64] P. van der Heide, "Vacuum," in *Secondary Ion Mass Spectrometry: An Introduction to Principles and Practices*, Hoboken, New Jersey: John Wiley & Sons, 2014, pp. 152–159.

[65] P. van der Heide, "Ion Sources," in *Secondary Ion Mass Spectrometry: An Introduction to Principles and Practices*, Hoboken, New Jersey: John Wiley and Sons, 2014, pp. 161–167.

[66] E. Niehuis and T. Grehl, "Depth profiling of inorganic materials," in *ToF-SIMS: Materials Analysis by Mass Spectrometry 2nd Edition*, J. C. Vickerman and D. Briggs, Eds. Chichester, Manchester: IM Publications LLP and SurfaceSpectra Limited, 2013, pp. 613–635.

[67] R. Steinberger *et al.*, "XPS study of the effects of long-term Ar^+ ion and Ar cluster sputtering on the chemical degradation of hydrozincite and iron oxide," *Corros. Sci.*, vol. 99, pp. 66–75, Oct. 2015.

[68] N. Wehbe and L. Houssiau, "Comparative study of the usefulness of low energy Cs^+, Xe^+, and O_2^+ ions for depth profiling amino-acid and sugar films," *Anal. Chem.*, vol. 82, no. 24, pp. 10052–10059, Dec. 2010.

[69] X. L. Yan, M. M. Duvenhage, J. Y. Wang, H. C. Swart, and J. J. Terblans, "Evaluation of sputtering induced surface roughness development of Ni/Cu multilayers thin films by Time-of-Flight Secondary Ion Mass Spectrometry depth profiling with different energies O_2^+ ion bombardment," *Thin Solid Films*, vol. 669, pp. 188–197, Jan. 2019.

[70] A. Theodosiou, B. F. Spencer, J. Counsell, and A. N. Jones, "An XPS/UPS study of the surface/near-surface bonding in nuclear grade graphites: A comparison of monatomic and cluster depth-profiling techniques," *Appl. Surf. Sci.*, vol. 508, p. 144764, Apr. 2020.

[71] A. Delcorte, O. A. Restrepo, and B. Czerwinski, "Cluster SIMS of Organic Materials: Theoretical Insights," in *Cluster Secondary Ion Mass Spectrometry: Principles and Applications*, C. M. Mahoney, Ed. New Jersey: John Wiley and Sons, 2013, pp. 13–55.

[72] H. Tian, D. Maciążek, Z. Postawa, B. J. Garrison, and N. Winograd, "CO_2 Cluster Ion Beam, an Alternative Projectile for Secondary Ion Mass Spectrometry," *J. Am. Soc. Mass Spectrom.*, vol. 27, no. 9, pp. 1476–1482, Sep. 2016.

[73] S. Holzer, S. Krivec, S. Kayser, J. Zakel, and H. Hutter, "Large O_2 Cluster Ions as Sputter Beam for ToF-SIMS Depth Profiling of Alkali Metals in Thin SiO_2 Films," *Anal. Chem.*, vol. 89, no. 4, pp. 2377–2382, Feb. 2017.

[74] C. M. Mahoney and A. Wucher, "Molecular Depth Profiling with Cluster Ion Beams," in *Cluster Secondary Ion Mass Spectrometry: Principles and Applications*, C. M. Mahoney, Ed. New Jersey: John Wiley and Sons, 2013, pp. 117–205.

[75] J. S. Fletcher and C. Szakal, "Cluster and polyatomic primary ion beams," in *ToF-SIMS: Materials Analysis by Mass Spectrometry 2nd Edition*, J. C. Vickerman and D. Briggs, Eds. Chichester, Manchester: IM Publications LLP and SurfaceSpectra Limited, 2013, pp. 291–310.

[76] R. Hill, "Analysis beams used in ToF-SIMS," in *ToF-SIMS: Materials Analysis by Mass Spectrometry 2nd Edition*, J. C. Vickerman and D. Briggs, Eds. Chichester, Manchester: IM Publications LLP and SurfaceSpectra Limited, 2013, pp. 271–290.

[77] C. Noël and L. Houssiau, "Hybrid Organic/Inorganic Materials Depth Profiling Using Low Energy Cesium Ions," *J. Am. Soc. Mass Spectrom.*, vol. 27, no. 5, pp. 908–916, May 2016.

[78] L. Houssiau, B. Douhard, and N. Mine, "Molecular depth profiling of polymers with very low energy ions," *Appl. Surf. Sci.*, vol. 255, no. 4, pp. 970–972, Dec. 2008.

[79] J. S. Fletcher, X. A. Conlan, N. P. Lockyer, and J. C. Vickerman, "Molecular depth profiling of organic and biological materials," *Appl. Surf. Sci.*, vol. 252, no. 19, pp. 6513–6516, Jul. 2006.

[80] B. Jenčič *et al.*, "MeV-SIMS TOF Imaging of Organic Tissue with Continuous Primary Beam," *J. Am. Soc. Mass Spectrom.*, vol. 30, no. 9, pp. 1801–1812, Sep. 2019.

[81] Z. Siketić, I. Bogdanović Radović, M. Barac, M. Brajković, and M. Popović Hadžija, "Chemical Imaging of Organic Materials by MeV SIMS Using a Continuous Collimated Ion Beam," *Anal. Chem.*, vol. 95, no. 5, pp. 3069–3074, Feb. 2023.

[82] M. Barac *et al.*, "Depth profiling of Cr-ITO dual-layer sample with secondary ion mass spectrometry using MeV ions in the low energy region," *Sci. Reports 2022 121*, vol. 12, no. 1, pp. 1–6, Jul. 2022.

[83] T. Seki, T. Nonomura, T. Aoki, and J. Matsuo, "MeV-SIMS measurement of lithium-containing electrolyte," *Nucl. Instruments Methods Phys. Res. Sect. B Beam Interact. with Mater. Atoms*, vol. 479, pp. 229–232, Sep. 2020.

[84] B. Jenčič *et al.*, "Stigmatic imaging of secondary ions in MeV-SIMS spectrometry by linear Time-of-Flight mass spectrometer and the TimePix detector," *Nucl. Instruments Methods Phys. Res. Sect. B Beam Interact. with Mater. Atoms*, vol. 452, pp. 1–6, Aug. 2019.

[85] M. Brajković, M. Barac, I. Bogdanović Radović, and Z. Siketić, "Dependence of Megaelectron Volt Time-of-Flight Secondary Ion Mass Spectrometry Secondary Molecular Ion Yield from Phthalocyanine Blue on Primary Ion Stopping Power," *J. Am. Soc. Mass Spectrom.*, vol. 31, no. 7, pp. 1518–1524, Jul. 2020.

[86] P. van der Heide, "Primary Ion Columns," in *Secondary Ion Mass Spectrometry: An Introduction to Principles and Practices*, Hoboken, New Jersey: John Wiley & Sons, 2014, pp. 159–167.

[87] P. van der Heide, "SIMS in its various forms," in *Secondary Ion Mass Spectrometry: An Introduction to Principles and Practices*, Hoboken, New Jersey: John Wiley & Sons, 2014, pp. 148–151.

[88] A. Wucher, G. L. Fisher, and C. M. Mahoney, "Three-Dimensional Imaging with Cluster Ion Beams," in *Cluster Secondary Ion Mass Spectrometry: Principles and Applications*, C. M. Mahoney, Ed. New Jersey: John Wiley and Sons, 2013, pp. 207–246.

[89] J. Vickerman and N. Winograd, "Cluster TOF-SIMS Imaging and the Characterization of Biological Materials," in *Cluster Secondary Ion Mass Spectrometry: Principles and Applications*, C. M. Mahoney, Ed. New Jersey: John Wiley and Sons, 2013, pp. 269–312.

[90] A. Shard, I. Gilmore, and A. Wucher, "Molecular depth profiling," in *ToF-SIMS: Materials Analysis by Mass Spectrometry 2nd Edition*, D. Vickerman, J. C. & Briggs, Eds. Chichester, Manchester: IM Publications LLP and SurfaceSpectra Limited, 2013, pp. 311–334.

[91] I. Gilmore, "Role of operating conditions in ToF-SIMS," in *ToF-SIMS: Materials Analysis by Mass Spectrometry 2nd Edition*, D. Vickerman, J. C. & Briggs, Eds. Chichester, Manchester: IM Publications LLP and SurfaceSpectra Limited, 2013, pp. 335–359.

[92] P. Van der Heide, "Mass Spectra," in *Secondary Ion Mass Spectrometry: An Introduction to Principles and Practices*, Hoboken, New Jersey: John Wiley & Sons, 2014, pp. 197–201.

[93] A. Delcorte, "Fundamentals of organic SIMS: insights from experiments and models," in *ToF-SIMS: Materials Analysis by Mass Spectrometry 2nd Edition*, D. Vickerman, J. C. & Briggs, Eds. Chichester, Manchester: IM Publications LLP and SurfaceSpectra Limited, 2013, pp. 87–123.

[94] F. Reich, "Sample handling for ToF-SIMS," in *ToF-SIMS: Materials Analysis by Mass Spectrometry 2nd Edition*, J. C. Vickerman and D. Briggs, Eds. Chichester, Manchester: IM Publications LLP and SurfaceSpectra Limited, 2013, pp. 397–416.

[95] B. J. Tyler, "ToF-SIMS image analysis," in *ToF-SIMS: Materials Analysis by Mass Spectrometry 2nd Edition*, D. Vickerman, J. C. & Briggs, Eds. Chichester, Manchester: IM Publications LLP and SurfaceSpectra Limited, 2013, pp. 485–502.

[96] P. Van der Heide, "Imaging," in *Secondary Ion Mass Spectrometry: An Introduction to Principles and Practices*, Hoboken, New Jersey: John Wiley & Sons, 2014, pp. 204–208.

[97] E. Niehuis, "Depth profiling in organic electronics," in *ToF-SIMS: Materials Analysis by Mass Spectrometry 2nd Edition*, J. C. Vickerman and D. Briggs, Eds. Chichester, Manchester: IM Publications LLP and SurfaceSpectra Limited, 2013, pp. 637–660.

[98] Y. Abe, "Evaluation of Damage Cross Sections by Au Cluster Ion Bombardment," *J. Surf. Anal.*, vol. 12, no. 2, 2005.

[99] Y. H. Chu *et al.*, "Improvement of the gas cluster ion beam-(GCIB)-based molecular secondary ion mass spectroscopy (SIMS) depth profile with O_2^+ cosputtering," *Analyst*, vol. 141, no. 8, pp. 2523–2533, Apr. 2016.

[100] P. Van der Heide, "Depth Profiling," in *Secondary Ion Mass Spectrometry: An Introduction to Principles and Practices*, Hoboken, New Jersey: John Wiley & Sons, 2014, pp. 201–204.

[101] P. Van der Heide, "Matrix Effect," in *Secondary Ion Mass Spectrometry: An Introduction to Principles and Practices*, Hoboken, New Jersey: John Wiley & Sons, 2014, pp. 97–113.

[102] B. Hagenhoff, "Cationisation," in *ToF-SIMS: Materials Analysis by Mass Spectrometry 2nd Edition*, D. Vickerman, J. C. & Briggs, Eds. Chichester, Manchester: IM Publications LLP and SurfaceSpectra Limited, 2013, pp. 193–216.

[103] P. Williams and C. M. Mahoney, "Future Challenges and Prospects of Cluster SIMS," in *Cluster Secondary Ion Mass Spectrometry: Principles and Applications*, C. M. Mahoney, Ed. New Jersey: John Wiley and Sons, 2013, pp. 313–327.

[104] P. Van der Heide, "Ionization Potential and Electron Affinity," in *Secondary Ion Mass Spectrometry: An Introduction to Principles and Practices*, Hoboken, New Jersey: John Wiley & Sons, 2014, pp. 95–97.

[105] N. J. Popczun, L. Breuer, A. Wucher, and N. Winograd, "Ionization Probability in Molecular Secondary Ion Mass Spectrometry: Protonation Efficiency of Sputtered Guanine Molecules Studied by Laser Postionization," *J. Phys. Chem. C*, vol. 121, no. 16, pp. 8931–8937, 2017.

[106] A. Wucher, "Molecular ionization probability in cluster-SIMS," *J. Vac. Sci. Technol. B, Nanotechnol. Microelectron. Mater. Process. Meas. Phenom.*, vol. 36, no. 3, p. 03F123, 2018.

[107] N. J. Popczun, L. Breuer, A. Wucher, and N. Winograd, "On the SIMS Ionization Probability of Organic Molecules," *J. Am. Soc. Mass Spectrom.*, vol. 28, no. 6, pp. 1182–1191, Jun. 2017.

[108] L. Van Vaeck, "Molecular speciation analysis of inorganic compounds," in *ToF-SIMS: Materials Analysis by Mass Spectrometry 2nd Edition*, J. C. Vickerman and D. Briggs, Eds. Chichester, Manchester: IM Publications LLP and SurfaceSpectra Limited, 2013, pp. 125–149.

[109] A. Wucher, "Laser post-ionisation—fundamentals," in *ToF-SIMS: Materials Analysis by Mass Spectrometry 2nd Edition*, D. Vickerman, J. C. & Briggs, Eds. Chichester, Manchester: IM Publications LLP and SurfaceSpectra Limited, 2013, pp. 217–246.

[110] N. P. Lockyer, "Laser post-ionisation for elemental and molecular surface analysis," in *ToF-SIMS: Materials Analysis by Mass Spectrometry 2nd Edition*, D. Vickerman, J. C. & Briggs, Eds. Chichester, Manchester: IM Publications LLP and SurfaceSpectra Limited, 2013, pp. 361–396.

[111] H. F. Arlinghaus, "Laser Secondary Neutral Mass Spectrometry (Laser-SNMS)," in *Surface and Thin Film Analysis: A Compendium of Principles, Instrumentation, and Applications, Second Edition*, Weinheim, Germany: Wiley-VCH, 2011, pp. 179–189.

[112] M. Kopnarski and H. Jenett, "Electron-Impact (EI) Secondary Neutral Mass Spectrometry (SNMS)," in *Surface and Thin Film Analysis*, Weinheim, Germany: Wiley-VCH Verlag GmbH & Co. KGaA, 2011, pp. 161–177.

[113] M. Franzmann, H. Bosco, L. Hamann, C. Walther, and K. Wendt, "Resonant laser–SNMS for spatially resolved and element selective ultra-trace analysis of radionuclides," *J. Anal. At. Spectrom.*, vol. 33, no. 5, pp. 730–737, 2018.

[114] R. Wilson, J. A. Van Den Berg, and J. C. Vickerman, "Quantitative surface analysis using electron beam SNMS: Calibrations and applications," *Surf. Interface Anal.*, vol. 14, no. 6–7, pp. 393–400, 1989.

[115] R. Wilson, J. A. Van den Berg, and J. C. Vickerman, "Surface analysis using electron beam SNMS, applications and investigations of sputter yields," *Vacuum*, vol. 39, no. 11–12, pp. 1089–1093, Jan. 1989.

[116] H. Oechsner, "Electron Gas SNMS," in *Secondary Ion Mass Spectrometry SIMS V*, 1986, pp. 70–74.

[117] D. Lipinsky *et al.*, "Performance of a new ion optics for quasisimultaneous secondary ion, secondary neutral, and residual gas mass spectrometry," *J. Vac. Sci. Technol. A*, vol. 3, no. 5, pp. 2007–2017, Sep. 1985.

[118] K. J. Wu and R. W. Odom, "Matrix-enhanced secondary ion mass spectrometry: A method for molecular analysis of solid surfaces," *Anal. Chem.*, vol. 68, no. 5, pp. 873–882, Jan. 1996.

[119] J. E. Locklear, C. Guillermier, S. V. Verkhoturov, and E. A. Schweikert, "Matrix-enhanced cluster-SIMS," *Appl. Surf. Sci.*, vol. 252, no. 19, pp. 6624–6627, Jul. 2006.

[120] J. J. D. Fitzgerald, P. Kunnath, and A. V. Walker, "Matrix-enhanced secondary ion mass spectrometry (ME SIMS) using room temperature ionic liquid matrices," *Anal. Chem.*, vol. 82, no. 11, pp. 4413–4419, Jun. 2010.

[121] J. D. Debord, A. Prabhakaran, M. J. Eller, S. V. Verkhoturov, A. Delcorte, and E. A. Schweikert, "Metal-assisted SIMS with hypervelocity gold cluster projectiles," *Int. J. Mass Spectrom.*, vol. 343–344, pp. 28–36, Jun. 2013.

[122] S. J. B. Dunham *et al.*, "Metal-assisted polyatomic SIMS and laser desorption/ionization for enhanced small molecule imaging of bacterial biofilms," *Biointerphases*, vol. 11, no. 2, p. 02A325, Jun. 2016.

[123] A. Yamazaki, T. Tobe, S. Akiba, and M. Owari, "Metal-Assisted SIMS for three-dimensional analysis using shave-off section processing," in *Surface and Interface Analysis*, 2014, vol. 46, no. 12–13, pp. 1215–1218.

[124] A. M. Piwowar and N. Winograd, "Application of SIMS to study of biological systems," in *ToF-SIMS: Materials Analysis by Mass Spectrometry 2nd Edition*, J. C. Vickerman and D. Briggs, Eds. Chichester, Manchester: IM Publications LLP and SurfaceSpectra Limited, 2013, pp. 553–582.

[125] B. Jenčič *et al.*, "Cationization of organic molecules under keV and MeV primary ion bombardment," *Int. J. Mass Spectrom.*, vol. 484, p. 116983, Feb. 2023.

[126] Y. Kudriatsev, A. Villegas, S. Gallardo, G. Ramirez, R. Asomoza, and V. Mishurnuy, "Cesium ion sputtering with oxygen flooding: Experimental SIMS study of work function change," *Appl. Surf. Sci.*, vol. 254, no. 16, pp. 4961–4964, 2008.

[127] P. Williams, K. Franzreb, R. C. Sobers, and J. Lörinčík, "On the effect of oxygen flooding on the detection of noble gas ions in a SIMS instrument," *Nucl.*

Instruments Methods Phys. Res. Sect. B Beam Interact. with Mater. Atoms, vol. 268, no. 17–18, pp. 2758–2765, 2010.

[128] C. M. Ng, A. T. S. Wee, C. H. A. Huan, and A. See, "Effects of oxygen flooding on crater bottom composition and roughness in ultrashallow secondary ion mass spectrometry depth profiling," *J. Vac. Sci. Technol. B Microelectron. Nanom. Struct.*, vol. 19, no. 3, pp. 829–835, 2001.

[129] A. Priebe, I. Utke, L. Pethö, and J. Michler, "Application of a Gas-Injection System during the FIB-TOF-SIMS Analysis - Influence of Water Vapor and Fluorine Gas on Secondary Ion Signals and Sputtering Rates," *Anal. Chem.*, vol. 91, no. 18, pp. 11712–11722, Sep. 2019.

[130] A. Hong, S. Ju Lee, C. Min Choi, J. Young Baek, and M. Choul Choi, "Neutral gas effect on the surface potential and charge compensation of an insulating sample," *Appl. Surf. Sci.*, vol. 572, p. 151338, Jan. 2022.

[131] Y. Kudriavtsev, R. Asomoza, M. Mansurova, L. A. Perez, and V. M. Korol', "Sputtering of the target surface by Cs^+ ions: Steady-state concentration of implanted cesium and emission of CsM^+ cluster ions," *Tech. Phys.*, vol. 58, no. 5, pp. 735–743, May 2013.

[132] J. Brison and L. Houssiau, "Study of ionization processes during TOF-SIMS analysis by co-sputtering cesium and xenon," *Nucl. Instruments Methods Phys. Res. Sect. B Beam Interact. with Mater. Atoms*, vol. 259, no. 2, pp. 984–988, 2007.

[133] J. Brison, R. G. Vitchev, and L. Houssiau, "Cesium/xenon co-sputtering at different energies during ToF-SIMS depth profiling," *Nucl. Instruments Methods Phys. Res. Sect. B Beam Interact. with Mater. Atoms*, vol. 266, no. 24, pp. 5159–5165, 2008.

[134] H. Tian, A. Wucher, and N. Winograd, "Dynamic Reactive Ionization with Cluster Secondary Ion Mass Spectrometry," *J. Am. Soc. Mass Spectrom.*, vol. 27, no. 2, pp. 285–292, 2016.

[135] H. Tian, A. Wucher, and N. Winograd, "Reduce the matrix effect in biological tissue imaging using dynamic reactive ionization and gas cluster ion beams," *Biointerphases*, vol. 11, no. 2, p. 02A320, 2016.

[136] H. Tian, A. Wucher, and N. Winograd, "Reducing the Matrix Effect in Organic Cluster SIMS Using Dynamic Reactive Ionization," *J. Am. Soc. Mass Spectrom.*, vol. 27, no. 12, pp. 2014–2024, 2016.

[137] S. Hofmann, H. Yang, J. Kovač, J. Ekar, Y. B. Song, and J. Y. Wang, "Artifacts in multilayer depth profiling: Origin and quantification of a double peak layer profile of Ag in ToF-SIMS depth profiles of an Ag/Ni multilayer," *Mater. Charact.*, vol. 171, p. 110774, Jan. 2021.

[138] S. Y. Lian, K. J. Kim, T. G. Kim, S. Hofmann, and J. Y. Wang, "Prediction and experimental determination of the layer thickness in SIMS depth profiling of Ge/Si multilayers: Effect of preferential sputtering and atomic mixing," *Appl. Surf. Sci.*, vol. 481, pp. 1103–1108, Jul. 2019.

[139] L. D. Gelb and A. V. Walker, "Toward understanding weak matrix effects in TOF SIMS," *J. Vac. Sci. Technol. B, Nanotechnol. Microelectron. Mater. Process. Meas. Phenom.*, vol. 36, no. 3, p. 03F127, 2018.

[140] P. Van der Heide, "Quantification of the Concentration Scale," in *Secondary Ion Mass Spectrometry: An Introduction to Principles and Practices*, Hoboken, New Jersey: John Wiley & Sons, 2014, pp. 259–268.

[141] M. Grasserbauer, "Quantitative Secondary Ion Mass Spectrometry," *J. Res. Natl. Bur. Stand. (1934).*, vol. 93, no. 3, p. 510, 1988.

[142] V. Karki and M. Singh, "Quantitative depth distribution analysis of elements in high alloy steel using MCs^+-SIMS approach," *Int. J. Mass Spectrom.*, vol. 430, pp. 22–30, Jul. 2018.

[143] H. Satoh, M. Owari, and Y. Nihei, "Relative sensitivity factors for submicron secondary ion mass spectrometry with gallium primary ion beam," *Jpn. J. Appl. Phys.*, vol. 32, no. 8 R, p. 3616, Aug. 1993.

[144] B. Jenčič *et al.*, "Molecular imaging of cannabis leaf tissue with MeV-SIMS method," *Nucl. Instruments Methods Phys. Res. Sect. B Beam Interact. with Mater. Atoms*, vol. 371, pp. 205–210, Mar. 2016.

[145] U. Valbusa, C. Boragno, and F. B. De Mongeot, "Nanostructuring surfaces by ion sputtering," *J. Phys. Condens. Matter*, vol. 14, no. 35, pp. 8153–8175, Aug. 2002.

[146] E. Chason, T. M. Mayer, B. K. Kellerman, D. T. McIlroy, and A. J. Howard, "Roughening instability and evolution of the Ge(001) surface during ion sputtering," *Phys. Rev. Lett.*, vol. 72, no. 19, pp. 3040–3043, 1994.

[147] A. Barna, B. Pécz, and M. Menyhard, "Amorphisation and surface morphology development at low-energy ion milling," *Ultramicroscopy*, vol. 70, no. 3, pp. 161–171, Jan. 1998.

[148] J. Kozole, A. Wucher, and N. Winograd, "Energy deposition during molecular depth profiling experiments with cluster ion beams," *Anal. Chem.*, vol. 80, no. 14, pp. 5293–5301, Jul. 2008.

[149] A. Zalar and S. Hofmann, "Influence of ion energy, incidence angle and surface roughness on depth resolution in AES sputter profiling of multilayer Cr/Ni thin films," *Nucl. Instruments Methods Phys. Res. Sect. B Beam Interact. with Mater. Atoms*, vol. 18, no. 1–6, pp. 655–658, Jan. 1986.

[150] S. Hofmann, A. Zalar, E. -H Cirlin, J. J. Vajo, H. J. Mathieu, and P. Panjan, "Interlaboratory comparison of the depth resolution in sputter depth profiling of Ni/Cr multilayers with and without sample rotation using AES, XPS, and SIMS," *Surf. Interface Anal.*, vol. 20, no. 8, pp. 621–626, Jul. 1993.

[151] S. W. MacLaren, J. E. Baker, N. L. Finnegan, and C. M. Loxton, "Surface roughness development during sputtering of GaAs and InP: Evidence for the role of surface diffusion in ripple formation and sputter cone development," *J. Vac. Sci. Technol. A Vacuum, Surfaces, Film.*, vol. 10, no. 3, pp. 468–476, May 1992.

[152] R. M. Bradley and J. M. E. Harper, "Theory of ripple topography induced by ion bombardment," *J. Vac. Sci. Technol. A Vacuum, Surfaces, Film.*, vol. 6, no. 4, pp. 2390–2395, Jul. 1988.

[153] A. Zalar, "Improved depth resolution by sample rotation during Auger electron spectroscopy depth profiling," *Thin Solid Films*, vol. 124, no. 3–4, pp. 223–230, Feb. 1985.

[154] R. M. Bradley and E. H. Cirlin, "Theory of improved resolution in depth profiling with sample rotation," *Appl. Phys. Lett.*, vol. 68, no. 26, pp. 3722–3724, 1996.

[155] M. E. E. Carbone, J. E. Castle, R. Ciriello, A. M. Salvi, J. Treacy, and P. Zhdan, "In Situ Electrochemical-AFM and Cluster-Ion-Profiled XPS Characterization of an Insulating Polymeric Membrane as a Substrate for Immobilizing Biomolecules," *Langmuir*, vol. 33, no. 10, pp. 2504–2513, Mar. 2017.

[156] C. M. Mahoney, A. J. Fahey, G. Gillen, C. Xu, and J. D. Batteas, "Temperature-Controlled Depth Profiling of Poly(methyl methacrylate) Using Cluster Secondary Ion Mass Spectrometry. 2. Investigation of Sputter-Induced Topography, Chemical Damage, and Depolymerization Effects," *Anal. Chem.*, vol. 79, pp. 837–845, 2007.

[157] C. M. Mahoney, A. J. Fahey, G. Gillen, C. Xu, and J. D. Batteas, "Temperature-controlled depth profiling in polymeric materials using cluster secondary ion mass spectrometry (SIMS)," *Appl. Surf. Sci.*, vol. 252, no. 19, pp. 6502–6505, Jul. 2006.

[158] M. Wolff, J. W. Schultze, and H. -H Strehblow, "Low-energy implantation and sputtering of TiO_2 by nitrogen and argon and the electrochemical reoxidation," *Surf. Interface Anal.*, vol. 17, no. 10, pp. 726–736, Sep. 1991.

[159] Z. Chen, J. Luo, I. Doudevski, S. Erten, and S. H. Kim, "Atomic Force Microscopy (AFM) Analysis of an Object Larger and Sharper than the AFM Tip," *Microsc. Microanal.*, vol. 25, no. 5, pp. 1106–1111, Oct. 2019.

[160] C. Y. Poon and B. Bhushan, "Comparison of surface roughness measurements by stylus profiler, AFM and non-contact optical profiler," *Wear*, vol. 190, no. 1, pp. 76–88, Nov. 1995.

[161] D. Semnani, "Geometrical characterization of electrospun nanofibers," in *Electrospun Nanofibers*, M. Afshari, Ed. Sawston: Woodhead Publishing, 2017, pp. 151–180.

Bibliography

Original Scientific Articles Related to the Thesis

1. J. Ekar, P. Panjan, S. Drev, and J. Kovač, "ToF-SIMS depth profiling of metal, metal oxide, and alloy multilayers in atmospheres of H_2, C_2H_2, CO, and O_2," *J. Am. Soc. Mass Spectrom.*, vol. 33, iss. 1, pp. 31–44, 2022.

2. J. Kovač, J. Ekar, M. Čekada, L. Zajíčková, D. Nečas, L. Blahová, J. Y. Wang, and M. Mozetič, "Depth profiling of thin plasma-polymerized amine films using GDOES in an Ar-O_2 plasma," *Appl. Surf. Sci.*, vol. 581, pp. 152292-1–152292-10, 2022.

3. J. Ekar, and J. Kovač, "AFM study of roughness development during ToF-SIMS depth profiling of multilayers with a Cs^+ ion beam in a H_2 atmosphere," *Langmuir*, vol. 38, no. 42, pp. 12871–12880, 2022.

Other Original Scientific Articles

4. B. Jenčič, J. Ekar, M. Vasić, Ž. Barba, M. Kelemen, P. Vavpetič, J. Kovač, and P. Pelicon, "Cationization of organic molecules under keV and MeV primary ion bombardment," *Int. J. Mass Spectrom.*, vol. 484, pp. 1–8, 2023.

5. J. Olenik, V. Shvalya, M. Modic, J. Ekar, J. Kovač, U. Cvelbar, and J. L. Walsh, "Plasma-induced interfacial processes in metal halides FTIR gas cell windows," *J. Anal. Test.*, vol. 7, iss. 4, pp. 392–404, 2023.

6. D. Paul, M. Mozetič, R. Zaplotnik, J. Ekar, A. Vesel, G. Primc, and D. Đonlagić, "Loss of oxygen atoms on well-oxidized cobalt by heterogeneous surface recombination," *Materials*, vol. 16, iss. 17, pp. 1–14, 2023.

7. Ž. Jelen, M. Krajewski, F. Zupanič, P. Majerič, T. Švarc, I. Anžel, J. Ekar, S.-C. Liou, J. Kubacki, M. Tokarczyk, and R. Rudolf, "Melting point of dried gold nanoparticles prepared with ultrasonic spray pyrolysis and lyophilization," *Nanotechnol. Rev.*, vol. 12, iss. 1, pp. 1–12, 2023.

8. A. Uccello, F. Ghezzi, J. Kovač, J. Ekar, T. Filipič, I. Bogdanović Radović, D. Dellasega, V. Mellera, M. Pedroni, D. Ricci, and GyM Team, "Study the erosion of Eurofer-97 steel with the linear plasma device GyM," *Nucl. Mater. Energy.*, vol. 35, pp. 101422-1–101422-13, 2023.

9. D. Paul, M. Mozetič, R. Zaplotnik, J. Ekar, A. Vesel, G. Primc, and D. Đonlagić, "Recombination of oxygen atoms on the surface of oxidized polycrystalline nickel—temperature and pressure dependences," *Plasma Sources Sci. Technol.*, vol. 32, pp. 1–13, 2023.

10. M. Barac, M. Brajković, Z. Siketić, J. Ekar, I. Bogdanović Radović, I. Šrut Rakić, and J. Kovač, "Depth profiling of Cr-ITO dual-layer sample with secondary ion mass spectrometry using MeV ions in the low energy region," *Sci. Rep.*, vol. 12, no. 1, pp. 11611-1–11611-6, 2022.

11. K. Brecl, M. Jošt, M. Bokalič, J. Ekar, J. Kovač, and M. Topič, "Are perovskite solar cell potential-induced degradation proof?," *Solar RRL*, vol. 6, iss. 2, pp. 2100815-1–2100815-10, 2022.

12. P. Jovičević Klug, N. Lipovšek, M. Klug Jovičević, M. Mrak, J. Ekar, B. Ambrožič, G. Dražič, J. Kovač, and B. Podgornik, "Assessment of deep cryogenic heat-treatment impact on the microstructure and surface chemistry of austenitic stainless steel," *Surf. Interfaces.*, vol. 35, article 102456, pp. 1–12, 2022.

13. D. Kozlica, J. Ekar, J. Kovač, and I. Milošev, "Roles of chloride ions in the formation of corrosion protective films on copper," *J. Electrochem. Soc.*, vol. 168, no. 3, pp. 031504-1–031504-18, 2021.

14. M. Resnik, E. Levičnik, Ž. Gosar, R. Zaplotnik, J. Kovač, J. Ekar, M. Mozetič, and I. Junkar, "The oleofobization of paper via plasma treatment," *Polymers*, vol. 13, no. 13, pp. 2148-1–2148-16, 2021.

15. J. Ekar, and K. Kranjc, "Synthesis of hydrazinylpyridines via nucleophilic aromatic substitution and further transformation to bicyclo[2.2.2]octenes fused with two N-aminosuccinimide moieties," *Synthesis*, vol. 53, iss. 6, pp. 1112–1120, 2021.

16. S. Hofmann, H. Yang, J. Kovač, J. Ekar, J. B. Song, and J. Y. Wang, "Artifacts in multilayer depth profiling: origin and quantification of a double peak layer profile of Ag in ToF-SIMS depth profiles of an Ag/Ni multilayer," *Mater. Charact.*, vol. 171, p. 110774, 2021.

17. A. Vesel, D. Lojen, R. Zaplotnik, G. Primc, M. Mozetič, J. Ekar, J. Kovač, M. Gorjanc, M. Kurečič, and K. Stana-Kleinschek, "Defluorination of polytetrafluoroethylene surface by hydrogen plasma," *Polymers*, vol. 12, no. 12, pp. 2855-1–2855-14, 2020.

Published Scientific Papers at the Conferences

18. T. Sotelšek, J. Kovač, J. Ekar, S. Šturm, and M. Vrabec, "Sestava vključkov v granatih iz pohorskih gnajsov," in *Treatises, reports: 26th Meeting of Slovenian Geologists*, Ljubljana, Slovenia: Univerza v Ljubljani, Naravoslovnotehniška fakulteta, Oddelek za geologijo, 2023.

Published Abstracts of the Scientific Papers at the Conferences (Invited Lecture)

19. J. Ekar, and J. Kovač, "TOF-SIMS and H_2 atmosphere: reduction of matrix effect and improvements in depth profiling," in *29th International Scientific Meeting on Vacuum Science and Techniques*, Gozd Martuljek, Slovenia: Slovenian Society for Vacuum Technique, 2023.

20. D. Lojen, R. Zaplotnik, A. Vesel, J. Ekar, G. Primc, and M. Mozetič, "Low pressure plasma functionalization of fluoropolymers," in *28th International Scientific Meeting on Vacuum Science and Technology*, Crikvenica, Croatia: Croatian Vacuum Society, 2022.

21. J. Ekar, and J. Kovač, "TOF-SIMS depth profiling in the H_2, C_2H_2, CO and O_2 atmosphere and during water flooding combined with a sample cooling," in *27th International Scientific Meeting on Vacuum Science and Techniques*, Gozd Martuljek, Slovenia: Slovenian Society for Vacuum Technique, 2021.

Published Abstracts of the Scientific Papers at the Conferences

22. J. Ekar, and J. Kovač, "Chemical analysis of surfaces and thin multilayers," in *15th Jožef Stefan International Postgraduate School Students' Conference*, Kamnik, Slovenia: Jožef Stefan Institute: Jožef Stefan International Postgraduate School, 2023.

23. J. Ekar, and J. Kovač, "ToF-SIMS analyses in an H_2 atmosphere: Improvements in depth profiling and reduction of matrix effect," in *SIMS Europe 2023, European Workshop on Secondary Ion Mass Spectrometry*, Nottingham, UK, 2023.

24. D. Kozlica, J. Ekar, J. Kovač, and I. Milošev, "Revealing the formation of corrosion protective films on copper through the role of chloride ions," in *8th Regional Symposium on Electrochemistry of South-East Europe together with the 9th Kurt Schwabe Symposium*, Graz, Austria: Verlag der Technischen Universität, 2022.

25. K. Brecl, M. Jošt, M. Bokalič, J. Ekar, J. Kovač, and M. Topič, "The impact of high negative bias on perovskite solar cells in PID testing," in *8th World Conference on Photovoltaic Energy Conversion: proceedings of the international conference*, München, Germany: WIP, 2022.

26. B. Podgornik, P. Jovičević Klug, J. Ekar, and J. Kovač, "Impact of deep cryogenic treatment on nitridability and properties of nitrided hot work tool steel," in *27th IFHTSE Congress & European Conference on heat treatment*, Salzburg, Austria, 2022.

27. J. Kovač, J. Ekar, M. Čekada, L. Zajíčková, D. Nečas, L. Blahová, J. Y. Wang, and M. Mozetič, "GDOES, ToF-SIMS and XPS depth profiling of polyamine films," in *28th International Scientific Meeting on Vacuum Science and Technology*, Crikvenica, Croatia: Croatian Vacuum Society, 2022.

28. J. Ekar, J. Kovač, K. Brecl, and M. Jošt, "TOF-SIMS 3D analysis of solar cells," in *28th International Scientific Meeting on Vacuum Science and Technology*, Crikvenica, Croatia: Croatian Vacuum Society, 2022.

29. J. Kovač, J. Ekar, M. Čekada, L. Zajíčková, D. Nečas, L. Blahová, J. Y. Wang, and M. Mozetič, "Depth profiling of thin plasma-polymerized polyamine films using GDOES, ToF-SIMS and XPS techniques," in *ECASIA 2022, 19th European Conference on Applications of Surface and Interface Analysis*, Limerick, Ireland, 2022.

30. J. Ekar, and J. Kovač, "Reduction of matrix effect in ToF-SIMS depth profiling via H_2 flooding," in *ECASIA 2022, 19th European Conference on Applications of Surface and Interface Analysis*, Limerick, Ireland, 2022.

31. J. Ekar, and J. Kovač, "Effects of gas flooding and temperature manipulation on ionisation efficiency and SIMS depth profiling," in *18th International Conference on Thin Films & 18th Joint Vacuum Conference*, Budapest, Hungary, 2020.

32. J. Kovač, S. Hofmann, Z. Gang, S. Drev, J. Ekar, S. Y. Lian, B. Lin, and J. Y. Wang, "Preferential sputtering and depth resolution in profiling of multilayers with SIMS, XPS and AES," in *18th International Conference on Thin Films & 18th Joint Vacuum Conference*, Budapest, Hungary, 2020.

33. J. Ekar, T. Filipič, and J. Kovač, "ToF-SIMS analyses of thin oxide layers by dual beam depth profiling," in *27th International Conference on Materials and Technology*, Portorož, Slovenia: The Institute of Metals and Technology, 2019.

34. J. Ekar, P. Podbevšek, and J. Plavec, "Oxidation of guanine nucleos(t)ides with peroxynitrite," in *Scientific Conference for Young Researchers*, Ljubljana, Slovenia: Faculty of Chemistry and Chemical Technology, 2017.

Independent Scientific Compositions or Chapters in Monographic Publications

35. A. Vesel, D. Lojen, R. Zaplotnik, G. Primc, M. Mozetič, J. Ekar, J. Kovač, M. Gorjanc, M. Kurečič, and K. Stana-Kleinschek, "Defluorination of polytetrafluoroethylene surface by hydrogen plasma," in *Advances in plasma processes for polymers*, Basel: MDPI, 2022, pp. 347–360.

Master's Thesis

36. J. Ekar, "Synthesis of the Hydrazinylpyridines and Binding of Substituted Hydrazines to the Bicyclo[2.2.2]octene Base," *Master's Thesis, Master's Study program Chemistry*, Ljubljana, 2019, 71 pages.

Conference Papers Without Print

37. J. Ekar, and D. Paul, *Delavnica Vakuum in plazma: Noč raziskovalk in raziskovalcev*, 2023.

Invited Conference Lectures Without Print

38. J. Ekar, and J. Kovač, "ToF-SIMS analyses in an H_2 atmosphere: Improvements in depth profiling and reduction of matrix effect," in *ECOSS36, European Conference on Surface Science*, Lodz, Poland, 2023.

Mentor – Other

39. J. Mihelčič, and A. Mundjar, "Izdelava detektorja kozmičnih delcev," *Research project*, Šolski center Postojna, gimnazija, 2019, prize: Silver Award.

Biography

Jernej Ekar was born on Friday, July 3rd 1992. He spent his childhood mostly at his home in the small village of Čelje. At that time, he was attending the Dragotin Kette primary school in Ilirska Bistrica. After finishing his primary education, he entered Gimnazija Ilirska Bistrica where he graduated in the year 2011. He continued his education at the Faculty of Chemistry and Chemical Technology, University of Ljubljana, where he got his bachelor's degree in chemistry in the year 2014. The work he performed for the degree is titled *Nitro Hydroxy Disubstituted Curcumin Analogs: Synthesis, Bromination and Preparation of BF_2 Complexes*. During his high school and bachelor years, he was also a recipient of the Zois scholarship for talented students. He continued his master's study at the same faculty, receiving the title of Master of Chemistry in the year 2019. The title of his master's degree thesis is *Synthesis of the Hydrazinylpyridines and Binding of Substituted Hydrazines to the Bicyclo[2.2.2]octene Base*. During his master's studies, he also finished an additional one-year program of pedagogy and andragogy for professionals working in elementary and high schools which was run by the Faculty of Arts, University of Ljubljana. His diploma thesis in this program is titled *Education and Punishment*.

The author of the doctoral desertion started gaining work experience during his studies in Ljubljana. As a master's degree student, he was a tutor of his younger colleagues for three years, between 2014 and 2017. He was also working as a student researcher at the National Institute of Chemistry in the field of NMR. This work lasted from the end of the year 2014 to the summer of 2017 when he finished all of his exams in the master's degree study. Shortly after this, he started working at the Šolski center Postojna and Gimnazija Ilirska Bistrica as a professor of chemistry. He worked there for two school years until the summer of 2019 and during this time he also co-mentored a research project in the field of astronomy that received a silver award at the state competition.

In the autumn of 2019, Jernej Ekar began his Ph.D. study in the field of surface analysis. He took a position as a young researcher at the Jožef Stefan Institute, Department of Surface Engineering (F4) under the supervision of Prof. Dr. Janez Kovač. He enrolled in the program Nanosciences and Nanotechnologies at the Jozef Stefan International Postgraduate School where he finished all his exams with an average of 10. The main field of his research was the optimization of the ToF-SIMS method mostly concerning the reduction of the matrix effect, enhancement of secondary ion yields, and improvement of depth profiling via the introduction of reactive gases during measurements. The reactive gas flooding approach also led to the improvements in quantitative aspects of the SIMS compositional analyses. During his Ph.D. studies, he received a Student Travel Grand Award for one of the three best presentations made by young researchers at the 19th European Conference on Applications of Surface and Interface Analysis (ECASIA 2022). He participated in nine scientific conferences in Slovenia and abroad, attended schools on surface science analytical methods in Poland and England, and went to Japan as a part of a bilateral project. He is also an author or co-author of seventeen published original scientific articles and the author of one scientific paper that is currently in the process of publishing.

Jernej Ekar is also a member of the Slovenian Society for Vacuum Techniques and the MENSA organization of people scoring top 2% on the official standardized IQ test.